METALLOPHTHALOCYANINES AS ELECTROCATALYSTS AND SUPEROXIDE DISMUTASE MIMICS

A thesis submitted in fulfillment of the
requirements for the degree of

DOCTOR OF PHILOSOPHY

of

RHODES UNIVERSITY

by

FUNGISAI MATEMADOMBO

July 2009

Acknowledgment

They destroyed the status quo and challenged the sport.

ABSTRACT

Syntheses, spectral, electrochemical, and spectroelectrochemical studies of iron, cobalt, and manganese phthalocyanines are reported.

The novel coordination of cobalt tetracarboxy metallophthalocyanine to an electrode pre-modified with aryl radicals and its use in the detection of thiocyanate are reported.

This work describes the catalytic activity of cobalt phthalocyanine (CoPc) derivatives adsorbed onto glassy carbon electrodes for the electrocatalytical detection of nitrite, L-cysteine, and melatonin. The modified electrodes efficiently detected nitrite. The CoPc derivative modified electrodes proficiently detected L-cysteine whereas an un-modified electrode could not. This work presents the innovative electrochemical detection of melatonin using electrodes adsorbed with CoPc derivatives. These electrodes detected melatonin at more favorable electrochemical parameters relative to an un-modified gold electrode. The limits of melatonin detection of the modified electrodes lay in the 10^{-7} to 10^{-6} M region. The modified electrodes accurately detected capsule melatonin concentrations as specified by the supplier and could differentiate between a mixture of melatonin, tryptophan, and ascorbic acid. They reliably detected nitrite, L-cysteine, and melatonin in the 10^{-4} to 10^{-2} M region.

Metallophthalocyanine complexes substituted with thio groups were employed as self assembled monolayers (SAMs). Voltammetry, impedance, atomic force microscopy, and scanning electrochemical microscopy proved that the SAMs all act as selective and efficient barriers to ion permeability. All the SAMs in this work can be used as effective electrochemical sensors of nitrite and L-cysteine in the 10^{-4} to 10^{-2} M region with competitive limits of detection whereas an un-modified electrode cannot detect L-cysteine. The manganese phthalocyanine SAM modified electrodes are arguably better nitrite and L-cysteine electrocatalysts relative to their iron and cobalt counterparts.

Manganese phthalocyanines were used as superoxide dismutase (SOD) mimics. All manganese phthalocyanine complexes in this work acted as SOD mimics in an enzymatic system of superoxide production. From cellular studies, complexes **6d, 6e, 8d, 8e** act as intracellular SOD mimics and are without significantly high cellular toxicity.

CONTENTS

List of Abbreviations

AA	Ascorbic acid
AFM	Atomic force microscopy
AIDS	Acquired immune deficiency syndrome
Ar	Aryl group
AU	Arbitrary unit
bp	Boiling point
CME	Chemically modified electrode
C_o	Concentration of the electroactive reactant
CE	Counter electrode
cytc	Cytochrome c
CV	Cyclic voltammetry or cyclic voltammogram
D	Diffusion coefficient
DBU	1,8-diazabicyclo(5.4.0)undec-7-ene
DBN	1,5-diazabicyclo(4.3.0)non-5-ene
DCM	Dichloromethane
DHE	Dihydroethidium
DMF	Dimethylformamide
DMSO	Dimethylsulfoxide
DNA	Deoxyribonucleic acid
DTSP	Dthiobis(*N*-succinimidyl propionate)
EDC	1-Ethyl-3-(3-dimethylaminopropyl)-carbodiimide
Eq.	Equation
ESR or EPR	Electron spin (paramagnetic) resonance
f	Frequency
FBS	Fetal bovine serum
GCE	Glassy carbon electrode
HIV	Human immunodeficiency virus
HL-60	Human promyelocytic leukemia cells
HOMO	Highest occupied molecular orbital

HPLC	High performance liquid chromatography
^{1}H NMR	Proton nuclear magnetic resonance
I_p(corr)	Background corrected current
IR	Infrared
LMCT	Ligand to metal charge transfer
LSWV	Linear square wave voltammogram
LUMO	Lowest unoccupied molecular orbital
ME	Melatonin
MeOH	Methanol
MPc	Metallophthalocyanine
NADPH	Nicotinamide adenine dinucleotide phosphate-oxidase
NHE	Normal hydrogen reference electrode
NHS	*N*-hydroxysuccinimide
NOS	Nitric oxide synthase
MLCT	Metal to ligand charge transfer
MALDI-TOF	Matrix Assisted Laser Desorption /Ionization - Time Of Flight
MTT	3-(4,5-dimethylthiazol-2-yl)-2,5-diphenyltetrazolium bromide
OTTLE	Optically transparent thin layer electrode
P	Porphine
PA	*meso*-tetraazaporphine or porphyrazine
PBS	Phosphate buffer saline solution
Pc	Phthalocyanine
Pc(COOH)$_4$	Tetracarboxyphthalocyanine
Pc(COOH)$_8$	Octacarboxyphthalocyanine
Pc(SCH$_2$Ph)$_8$	Octabenzylthiophthalocyanine
PDT	Photodynamic therapy
Ph	Phenyl group
PMA	Phorbol 12-myristate 13-acetate
PVC	Polyvinyl chloride
RE	Reference electrode

Redox	Reduction/oxidation
Ref.	Reference
RPMI	Roswell Park Memorial Institute
RSH	L-cysteine
RSSR	Cystine
SAM	Self assembled monolayer
SCE	Saturated calomel electrode
SDS	Sodium dodecyl sulfate
SECM	Scanning electrochemical microscopy
SEM	Standard error of the mean
SOD	Superoxide dismutase
SPM	Scanning probe microscopy
STM	Scanning tunneling microscopy
SWV	Square wave voltammetry or square wave voltammogram
TBABF$_4$	Tetrabutylammonium tetrafluoroborate
TBAP	Tetrabutylammonium perchlorate
THF	Tetrahydrofuran
TMPyPc	Tetra-(2-mercaptopyridine)phthalocyanine
Tryp	Tryptophan
UME	Ultramicroelectrode
U.mL^{-1}	Units per millilitre
UPD	Underpotential deposition
UV-visible	Ultraviolet-visible
vs.	Versus
W	Watts
WE	Working electrode
XOD	Xanthine oxidase
$|Z|$	Total impedance
Z'	Real impedance component
Z''	Imaginary impedance component

List of Symbols

Δ	Heat or change
α	Transfer coefficient
ε	Extinction coefficient
θ	Phase-shift
Γ	Surface coverage
Γ_{ibf}	Ion barrier factor
λ	Wavelength
A	Electrode Area
C	Capacitance
C_s	Interfacial capacitance
D	Diffusion coefficient
e^-	Electron
E_{pa}	Anodic peak potential
E_{pc}	Cathodic peak potential
E	Potential
$E_{1/2}$	Half wave potential
ΔE	Anodic-to-cathodic peak potential separation
F	Faraday constant
IC50	Concentration of putative SOD mimic that induces a 50 % inhibition of the reduction of cytochrome c
i_{ch}	Charging current
I	Peak current
I_{pa}	Anodic peak current
I_{pc}	Cathodic peak current
$I_p.v^{-1/2}$	Sweep-rate normalized current density
$\%I$	Percent inhibition
k_{cat}	Apparent catalytic rate constant for the dismutation of superoxide
k_{Cytc}	Rate constant of the bimolecular reaction between $O_2^{\cdot-}$ and cytochrome c
λ_{max}	Wavelength of maximum absorbance

mV.dec^{-1}	mV.decade (millivolts per decade)
n	Moles of electrons, number of electrons, or number of times experiment done
n_t	Total number of electrons involved
$O_2^{\cdot-}$	Superoxide radical
Q	Electrical charge
Q_{Bare}	Total charge under the peak of a bare gold electrode
Q_{SAM}	Total charge under the peak of a SAM modified gold electrode
R	Gas constant
T	Temperature
μ	Micro
v	Volume
ν	Scan rate
V	Volts

List of Figures

CHAPTER 1: INTRODUCTION

The key aim of this work is to use metallophthalocyanines as electrochemical sensors (electrocatalysts) and superoxide dismutase mimics.

Phthalocyanines (Pcs) and metallophthalocyanines (MPcs) are macrocyclic π-electron conjugated molecules. MPcs and Pcs, primarily due to their π-electron conjugation, may exhibit a series of electrochemical processes and can consequently be used as efficient electron mediators. Therefore, this work uses MPcs attached to electrodes as electrochemical sensors; an electrochemical sensor being a measurement device which uses an electrical and chemical reaction to detect and quantify a specific substance.

Reactive oxygen species, such as the superoxide radical ($O_2^{\cdot-}$), are created by several biological pathways. Accumulation of these oxygen species in organisms may cause several pathological conditions such as enzyme inactivation, but antioxidant defence systems can minimize the harmful effects of reactive oxygen species. An example of such an antioxidant defence system is superoxide dismutase (SOD), an enzyme that catalyzes the removal of $O_2^{\cdot-}$. This work uses MPcs, containing Mn as a central metal, as SOD mimics; Mn being vital for superoxide dismutation (a process of simultaneous oxidation and reduction - used especially of compounds taking part in biological processes).

1.1. Phthalocyanines

1.1.1. An overview

Phthalocyanines were accidentally discovered in 1907. Four chemists (Dandridge, Drescher, Dunworth, and Thomas), at Scottish Dyes Ltd, noticed an insoluble blue material during the routine manufacture of phthalimide from phthalic anhydride (both of which are white solids) [1]. Analysis proved this material to be an iron organic compound. Its structure was elucidated as iron phthalocyanine by Linstead *et al* [2-7] and later confirmed by Robertson [8-12]. Linstead conceived the term 'phthalocyanine' from two Greeks terms relating to the compound: naptha (rock oil) to emphasize the Pc association with its various phthalic acid derived precursors, and cyanine (blue).

Chapter 1: Introduction

Substitution of the four *meso*-CH bridges in porphine (H$_2$P, **1**, Fig 1.1) with four *meso*-nitrogen atoms forms a porphyrazine (*meso*-tetraazaporphine, H$_2$PA, **2**). Addition of a benzene unit to the porphyrazine (**2**) forms a phthalocyanine (tetrabenzoporphyrazine, H$_2$Pc, **3**). Phthalocyanines are planar macrocyclic aromatic compounds consisting of four isoindoline units linked together by nitrogen atoms [13].

1   **2**   **3**
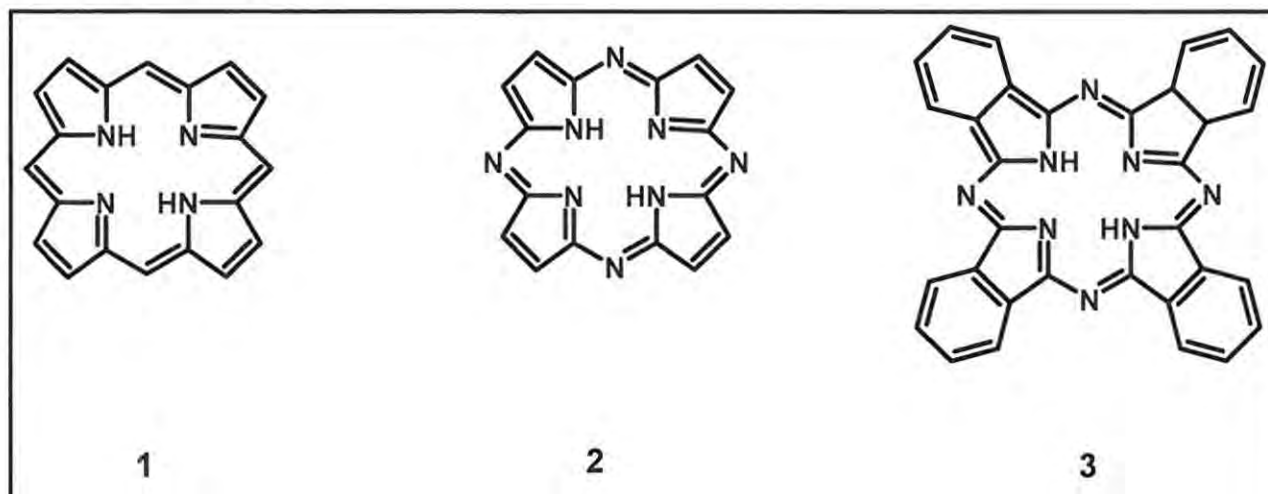
Fig. 1.1 Porphine (**1**, H$_2$P), porphyrazine (**2**, H$_2$PA) and phthalocyanine (**3**, H$_2$Pc) structures

H$_2$Pc (**3**) can thus act as a ligand to most metal and metalloid elements [14-17]. Fig. 1.2 shows the Periodic Table in which the shaded boxes indicate elements coordinated by the Pc ring inside its central cavity [17].

Chapter 1: Introduction

Fig. 1.2 Periodic Table: the shaded boxes indicate elements coordinated by the Pc ring inside its central cavity

The standard oxidation state of Pc is -2, and therefore it can coordinate a central atom M (with oxidation state +2). Thus, from Fig. 1.2, the oxidation state of the central atom can range between +1 (e.g. for Li) and +5 (e.g. for W). So, for ions with a charge of +2, a simple and stable MPc complex is usually obtained because there is no need for additional ligands to retain neutrality; but neutral ligands such as pyridine or water can be incorporated. Metal ions of charge +3 (e.g. manganese Pcs of this work), or higher, require additional 'axial' ligands, which may be attached to the MPc structure as shown in Fig. 1.3.

L-MPc

4
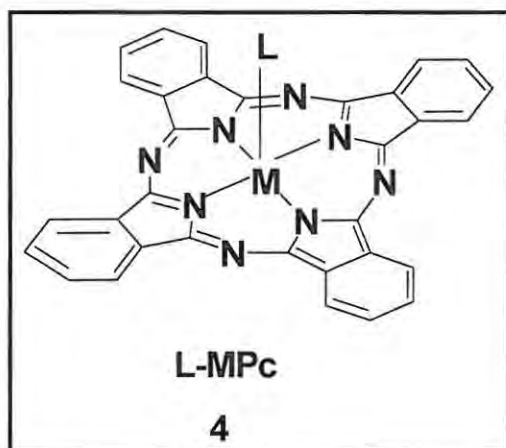
Fig. 1.3 Axial ligand (L) attachment to an MPc

This work uses MPcs containing Co^{II}, Fe^{II}, and Mn^{III} in the central cavity.

Furthermore, Fig. 1.4 shows possible substitution positions on Pcs; these positions are labelled 1-25 in red on complex **5**.
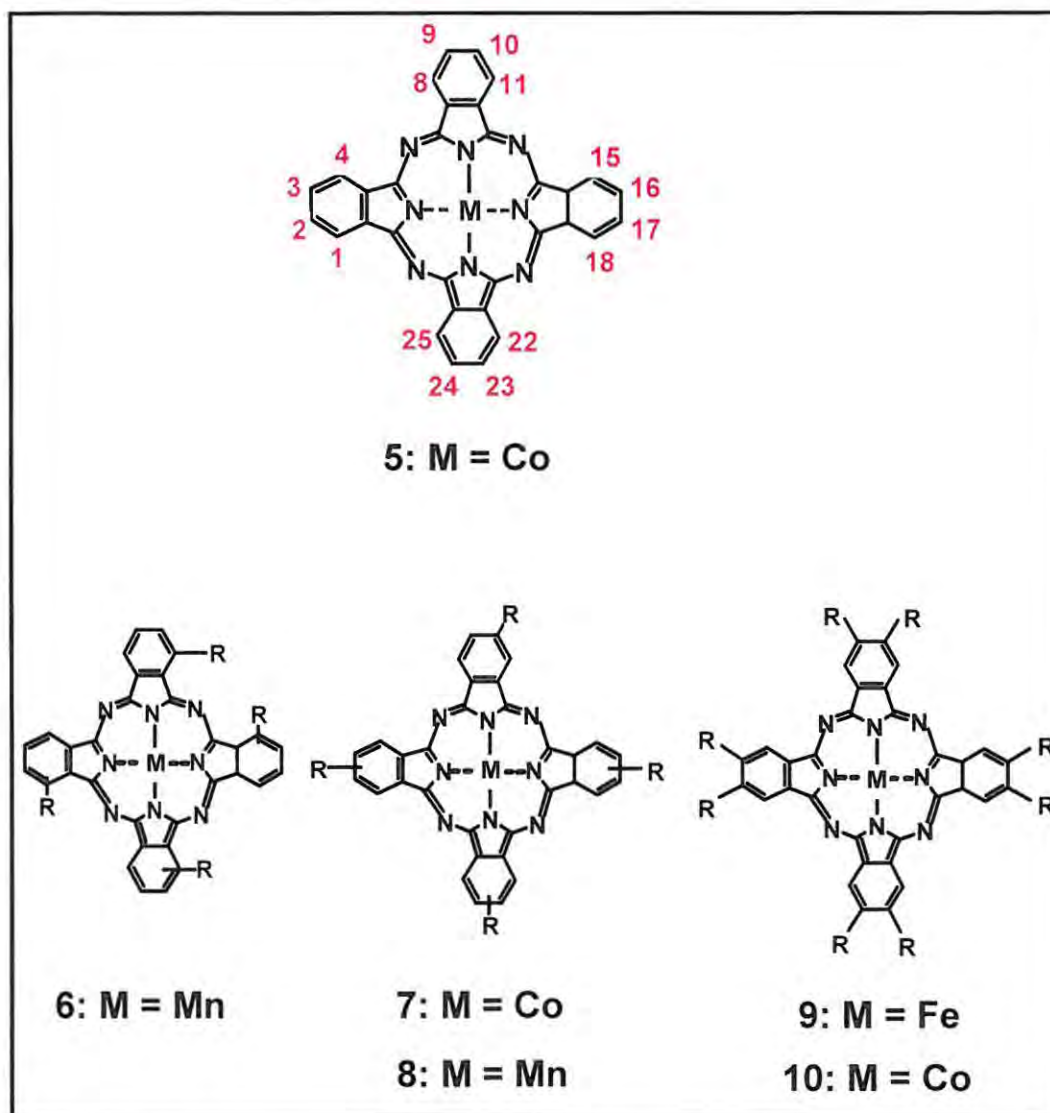
Fig. 1.4 Possible substitution positions on Pcs, labelled

Pcs can have substituents at the α, non-peripheral (complex **5**: carbon number 1, 4, 8, 11, 15, 18, 22, 25, Fig. 1.4) and/or β, peripheral (complex **5**: carbon number 2, 3, 9, 10, 16, 17, 23, 24, Fig. 1.4) positions of the four benzene rings [18]. Complexes employed in this work (**5-10**) are either substituted at four α (**6**) or β (**7, 8**), or all β (**9, 10**) positions, Fig. 1.4. The two types of tetrasubstituted Pcs (α and β), complexes **6 - 8**, were studied in this work primarily to compare the effect of point of substitution on electrocatalytic or SOD mimic behaviour. Similarly,

Chapter 1: Introduction
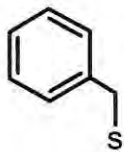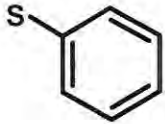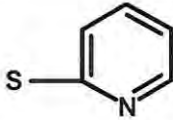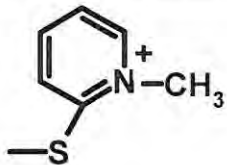
octasubstituted Pcs, complexes **9** and **10**, were studied to compare their activity to their tetrasubstituted counterparts. Complexes used in this work are named in Table 1.1.

Table 1.1a Complexes used in this work

Substitution	Metal	Identity	Name of complex
Un-substituted	Co	**5g**	Cobalt phthalocyanine: CoPc
α-tetrasubstituted	Mn	**6c**	Manganese (III) 2,(3)-tetraphenylthiophthalocyanine: $(OH)MnPc(SPh)_4$
		6d	Manganese (III) 1,(4)-tetra-(2-mercaptopyridine)phthalocyanine: α-(OH)MnTMPyPc
		6e	Quaternized manganese (III) 1,(4)-tetra-(2-mercaptopyridine)phthalocyanine: α-Q-(OH)MnTMPyPc
β-tetrasubstituted	Co	**7a**	Cobalt tetracarboxyphthalocyanine: $CoPc(COOH)_4$
	Mn	**8b**	Manganese (III) tetrakis (benzyl-mercapto) phthalocyanine: $(OH)MnPc(SCH_2Ph)_4$
		8d	Manganese (III) 2,(3)-tetra-(2-mercaptopyridine)phthalocyanine: β-(OH)MnTMPyPc
		8e	Quaternized manganese (III) 2,(3)-tetra-(2-mercaptopyridine)phthalocyanine: β-Q-(OH)MnTMPyPc
		8f	Manganese (III) tetrasulfonatedphthalocyanine: $(Na)_4(OH)MnPc(SO_3)_4$
Octasubstituted	Fe	**9b**	Iron octabenzylthiophthalocyanine: $FePc(SCH_2Ph)_8$
	Co	**10a**	Cobalt octacarboxyphthalocyanine: $CoPc(COOH)_8$
	Co	**10b**	Cobalt octabenzylthiophthalocyanine: $CoPc(SCH_2Ph)_8$

Table 1.1b Ring substituent structures

Identity	Ring substituent
a	COOH
b	
c	
d	
e	
f	SO_3^-
g	H

Transition metals (Fe, Co, and Mn) were used because they display the electrochemical activity [19-24] necessary for the electrocatalytic studies reported in this work. Complexes **7a** and **10a** are well known [25,26] but their use in electrocatalysis has not been fully explored. Complex **8b** has been reported before [27] but this work presents its novel use as a superoxide dismutase (SOD) mimic. Complex **8f** was synthesized and characterized using methods reported in literature [28,29]. Pc ring system **c** has been reported for titanium Pc [30] but is reported here as a manganese Pc for the first time. The pyridine substituted complexes (**6d, e** and **8d, e**) and their quaternized derivatives have recently been reported by our group [31]. The syntheses of **6c, 9b,** and **10b** are reported here for the first time.

Chapter 1: Introduction

Carboxy complexes (**a**) were used in this work because they form good adsorbates on glassy carbon electrodes and therefore have potential as electrochemical sensors. In a related vein, thio-derivatised Pcs, i.e. those bearing SR substituents (S = sulfur, R = organic group) were used in this work primarily because the S moiety can attach to gold electrodes resulting in a potential electrochemical sensor. Table 1.2 lists several known thio-derivatised MPcs [23,32-37]. Use of thio-derivatised Pcs is still limited and hence is part of this work. The synthesis of SH-substituted Pcs is lengthy and complicated mostly due to the S-S bond formation between Pcs. But when self assembled monolayers (SAMs) are terminated with an R group, such as the phenyls in this work, the synthesis is more feasible because the R groups effectively prevent the sulfur moieties from forming links with each other. Mn was chosen as the metal for superoxide dismutase (SOD) studies because it is the metal used by most natural superoxide dismutase systems [38,39]. Aryl groups were mostly chosen as substituents to increase Pc solubility, especially for biological compatibility.

Chapter 1: Introduction

Table 1.2 Examples of known thio-derivatised MPcs[a]

MPc	Reference
FeTBMPc	32
FeTDMPc	32
$FePc(SC_4H_9)_8$	33
$FePc(SC_2H_4OH)_8$	23
CoTBMPc	32
CoTDMPc	32
$CoPc(SC_4H_9)_8$	34
$CoPc(SC_2H_4OH)_8$	23
MnTBMPc	32
MnTDMPc	32
$MnPc(SC_5H_{11})_8$	35
Zn(obtPc)	36
Zn(htPc)	37
Cu(htPc)	37

[a]TB = tetrakis (benzylmercapto); TD = tetrakis (dodecylmercapto); obt = octabutylthio; ht = octakis (hexylthio)

The heteroaromatic π-system and central metal primarily give Pcs their brightness and diverse electrochemistry [15,40-42]. Also, the four peripheral benzene groups and *meso*-nitrogen atoms enhance the chemical and thermal stabilities of Pcs, especially in comparison to their porphine (**1**, H_2P) counterparts. It is principally for these reasons (i.e. electrochemical capacity and stability) that complexes **5-10** (Table 1.1) were used in this work as electrochemical sensors and/or SOD mimics.

Traditionally, Pcs are used as blue and green pigments (e.g. for automotive paints) and as blue/cyan dyes (e.g. for textiles) because they possess high tinctorial strength (being durable to light, heat, and most chemicals), are cheap (especially as they can be synthesised from low-cost raw materials), and are bright [43]. This combination of properties is rare, e.g. natural dyes such as chlorophyll and haemin are easily destroyed by light, heat, and mild chemical reagents. While

the use of Pcs as pigments relies on their insolubility to ensure fixation to material and durability against light, heat, and chemicals to avoid fading, most Pc applications require solubility in water or a common organic solvent. To increase solubility, a number of functional groups have been added to the Pc framework via attachment to the benzene rings on the periphery of these macrocycles. Simple functional groups such as alkyl chains, aromatics, and aryl thio have been added to improve the overall properties of Pcs. The central metal in MPc complexes may influence the type of dye: Pcs that absorb in the ultra violet-visible (UV-visible) region, such as the Fe and Co complexes (**5, 7, 9, 10**), are mostly limited to blue, cyan, and green colors [44]; but in MnPc complexes (**6, 8**), where the absorption may be extended into the near infrared and by appropriate design, it is possible to fingerprint the 700 - 1000 nm region. The properties and effects of these infrared-absorbing phthalocyanines are diverse and cover many important high-technology applications e.g. photodynamic therapy (PDT) for cancer [45], photosensitizers in the conversion of solar energy to chemical or electrochemical energy [44,46], and sensor applications [47] (alarms, environmental) amongst others [15].

This work aims to develop Pcs for use as electrochemical sensors and/or SOD mimics.

1.1.2. Synthesis

1.1.2.1. Synthesis of un-substituted phthalocyanines

A Pc is formed from the cyclotetramersation of its precursor units so the synthetic strategy starts from the molecules which make up these units. MPcs can form from precursors through a metal-templated cyclotetramerization reaction. Typical precursors are phthalic acid (**11**), phthalonitrile (**12**), phthalic anhydride (**13**), phthalimide (**14**), diiminoisoindoline (**15**), and *o*-cyanobenzamide (**16**), Scheme 1.1 [29,48-72].
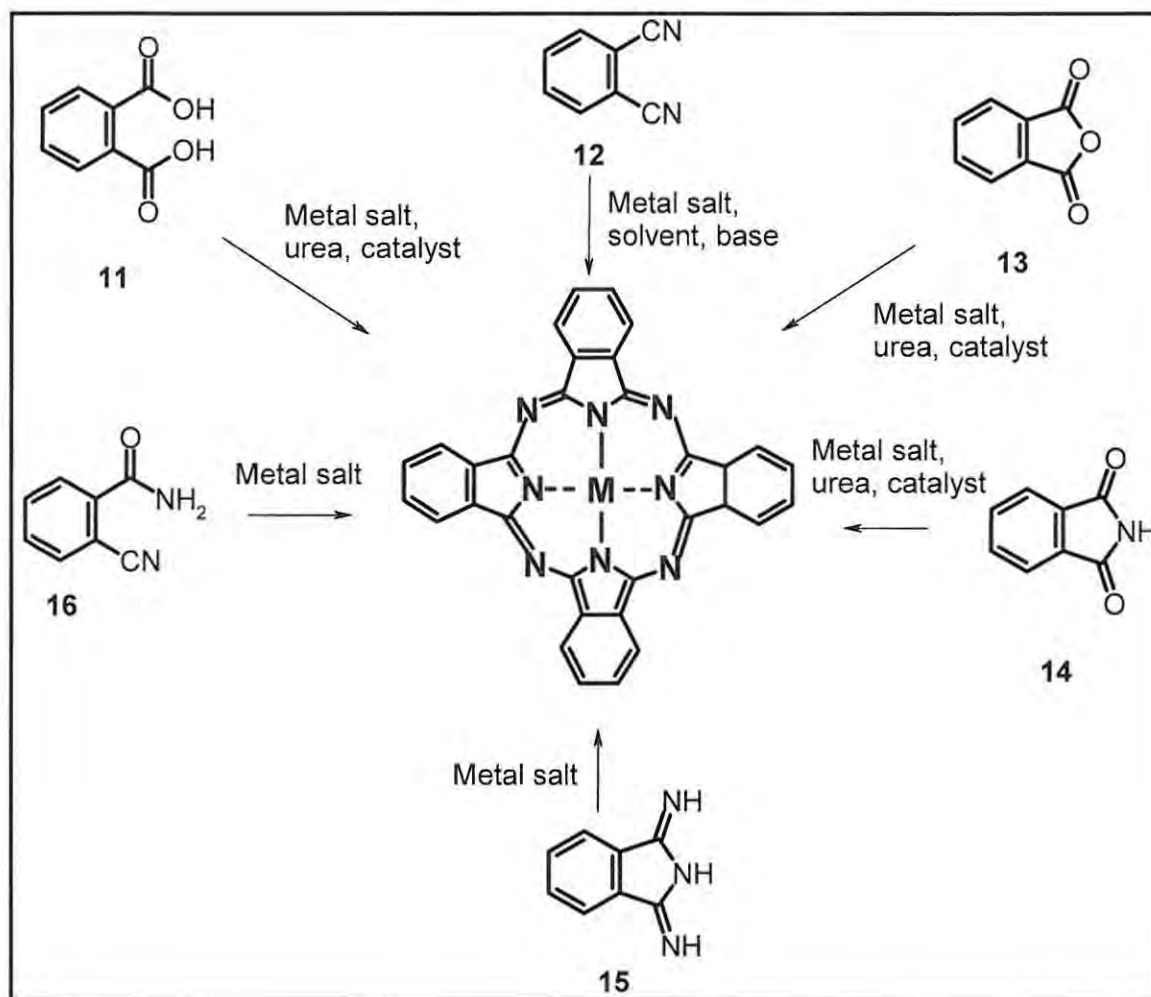
Scheme 1.1 Various MPc synthetic routes

The variety of starting materials for Pc synthesis and the diversified methods for their preparation, Scheme 1.1, allow Pcs to fulfill their promise.

The most useful of the un-substituted MPc precursors is phthalonitrile (**12**). This compound readily gives MPc complexes in good yields with most metals except silver and mercury [48]. Reactions often involve simply heating the phthalonitrile in the presence of a metal-ion source and base as either a melt of reagents or in a suitable high boiling point solvent. Phthalonitrile (**12**) as a precursor leads to products of high purity but, because phthalonitriles are generally more expensive, their use tends to be restricted to high-technological applications (e.g. electrophotography) and small scale syntheses (e.g. laboratory synthesis) where quality, and not cost, is the main consideration.

11

Chapter 1: Introduction

Un-substituted MPcs commonly exhibit poor solubility in most organic solvents and water due to the molecular interactions between their π-systems. These interactions lead to the Pcs stacking upon themselves to form a strong and hydrophobic crystal lattice. This insolubility significantly limits the usefulness of un-substituted Pcs.

1.1.2.2. Synthesis of tetrasubstituted phthalocyanines

For most of their applications, substituted Pcs have to be prepared in order to improve their usefulness by, for example, enabling coupling to other entities [73] like gold electrode surfaces or enhancing their solubility. Substituents may alter the intrinsic properties of Pcs by changing the electronic distribution [74] so that molecules may be tailored to required needs. This tailoring (i.e. substitution onto a Pc) is usually done by one of two basic methods. The first involves the direct substitution onto a pre-existing Pc. An example of this is sulfonation of Pcs [75], which can be accomplished by heating a Pc macrocycle in oleum. While direct substitution is the preferred method for adding substituents to Pcs for the dye industry [43], the harsh reaction conditions used result in complex isomeric mixtures and erratic degrees of substitution. Furthermore, isolation and purification of the desired product is extremely difficult. This greatly limits this methodology in applications needing well-defined Pcs. The second basic method, used in this work, involves condensation of substituted precursors. This leads to much cleaner reactions in terms of the degree of substitution, with, for example, monosubstituted precursors leading to tetrasubstituted Pcs.

Tetrasubstituted Pcs are usually prepared by the condensation of an aptly substituted pre-cursor e.g. phthalonitrile (**12**). This method may result in undesirable constitutional isomers of tetrasubstituted Pcs due to the symmetry involved in the condensation reaction used in the Pc synthesis. While it is theoretically possible to separate these isomers using their differing geometries, this has only been accomplished for very specific Pcs, using specially designed high performance liquid chromatography (HPLC) columns [55], but the results are often unsatisfactory. The MPcs used in this work did not require distinct molecular geometries and hence the presence of isomers is not important for the reported applications. Furthermore, this synthetic method is clean and it is possible to control the formation of specifically substituted

products through phthalonitrile substitution at the 1,4- (α) or 2,3- (β) position. Both types of MPcs (α and β) were synthesised in this work.

1.1.2.2.1. Synthesis of non-peripherally (α) tetrasubstituted phthalocyanines

A synthesis of non-peripherally tetrasubstituted phthalocyanines (alias 1,4- tetrasubstituted or α-substituted phthalocyanines) is outlined in Scheme 1.2.
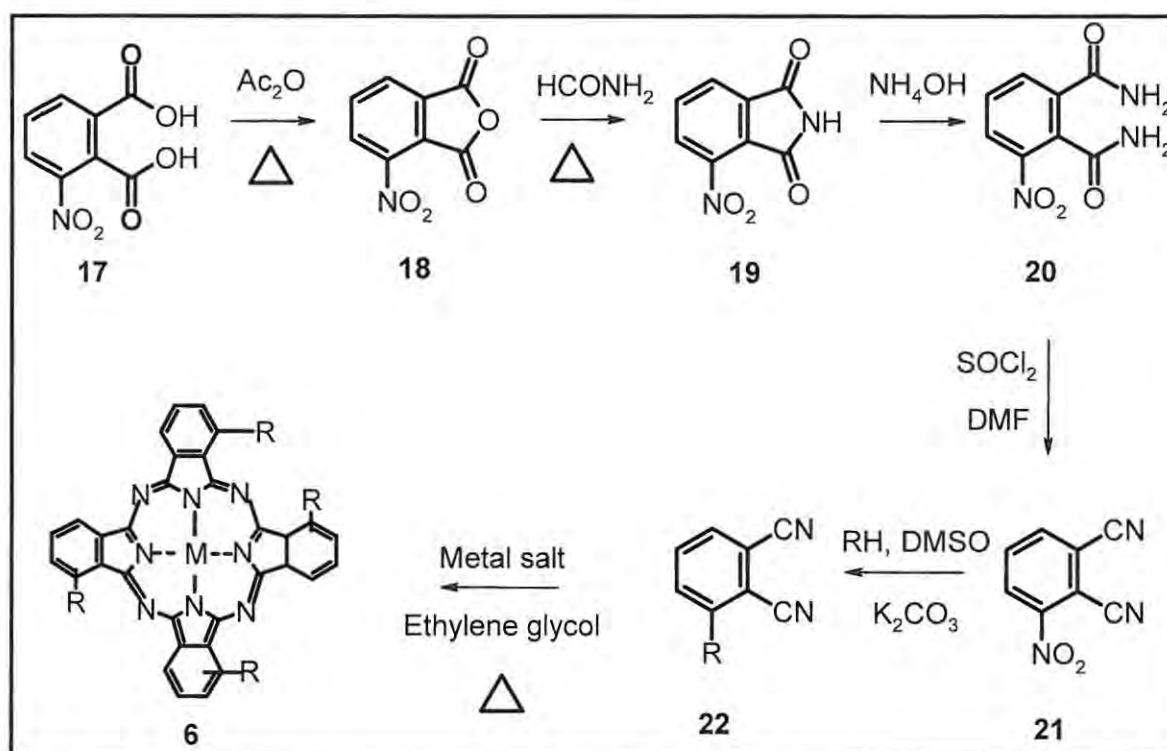
Scheme 1.2 Synthesis of a non-peripherally tetrasubstituted phthalocyanine (**6**)

Scheme 1.2 shows a synthesis of a non-peripherally tetrasubstituted phthalocyanine (**6**) involving the nucleophilic aromatic substitution of 3-nitrophthalonitrile (**21**). This method is advantageous in that the phthalonitrile derivative (**21**) is commercially available or can be prepared easily. Initially 3-nitrophthalic acid (**17**) is transformed to 3-nitrophthalonitrile (**21**), Scheme 1.2 [76]. Nucleophilic aromatic substitution of 3-nitrophthalonitrile (**21**) results in the substituted phthalonitrile (**22**). In this nucleophilic aromatic substitution, a strong nucleophile (e.g. thiolate) [77,78] effectively displaces the good leaving nitro group (of **21**) from its activated aromatic substituent in the presence of a base (for catalysis) [79] and dry polar aprotic solvents (e.g. dimethylformamide (DMF) or dimethylsulfoxide (DMSO)). Reaction of the substituted

13

phthalonitrile (**22**) with a metal salt in the presence of ethylene glycol gives, through a metal assisted cyclotetramerisation process, the non-peripherally tetrasubstituted phthalocyanine (**6**). This work describes the synthesis and/or use of non-peripherally tetrasubstituted phthalocyanines **6 c** to **e**.

1.1.2.2.2. Synthesis of peripherally (β) tetrasubstituted phthalocyanines

The synthesis of peripherally tetrasubstituted phthalocyanines is similar to that of their non-peripherally substituted counterparts except for the initial steps, as outlined in Scheme 1.3.
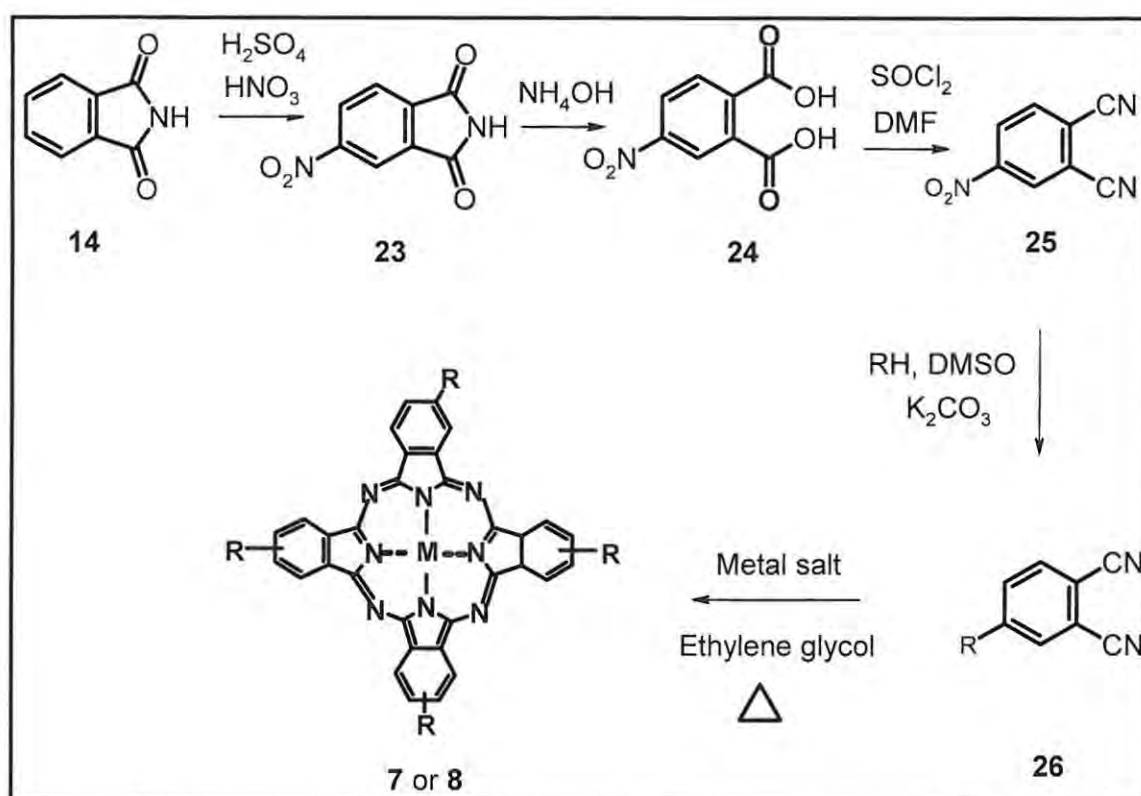
Scheme 1.3 Synthesis of a peripherally tetrasubstituted phthalocyanine (**7** or **8**)

Peripherally tetrasubstituted phthalocyanine synthesis involves the nucleophilic aromatic substitution of 4-nitrophthalonitrile (**25**). Again, the phthalonitrile derivative is commercially available or may be synthesized through the steps shown in Scheme 1.3 [80] and can be transformed into substituted phthalonitrile (**26**) as explained above. The peripherally substituted Pc is then formed by cyclotetramerisation of substituted phthalonitrile **26** as described for α Pcs.

Monosubstitution at the 4-position of phthalonitrile leads to four single isomers of (C_{4h}) 2,9,16,23-, (C_{2v}) 1,9,17,24-, (C_s) 2,9,16,24-, and (D_{2h}) 2,10,16,24- tetrasubstituted Pcs, Fig. 1.5, close to the statistical ratio of 1:1:2:4 respectively.
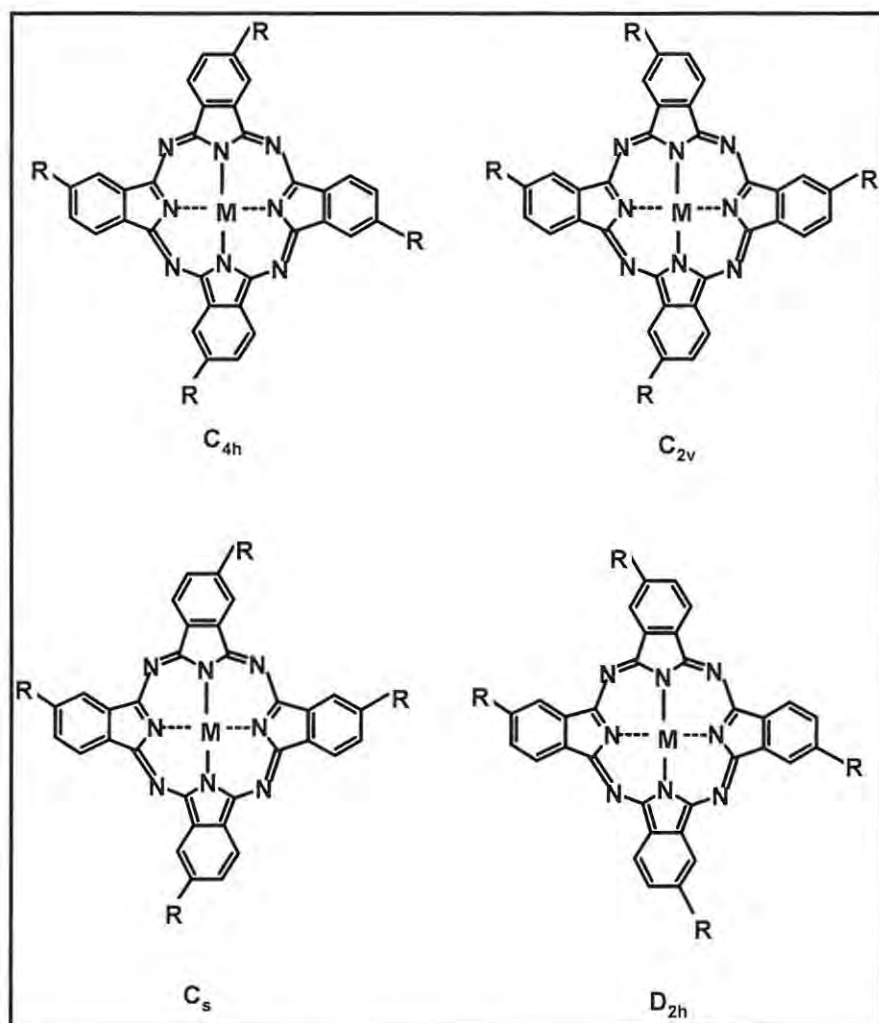
Fig. 1.5 Constitutional isomers (labelled with their geometries) possible for a peripherally tetrasubstituted phthalocyanine

Long chain or bulky substituents, such as those employed for MPcs in this work, improve the solubility of Pcs by causing substantial disruption of the strong Pc ring interactions. Tetrasubstituted Pcs are more soluble than their corresponding octasubstituted counterparts due to their lower degree of order in the solid state and also due to the presence of constitutional isomers and the high dipole moment that results from the unsymmetrical arrangement of the

substuituents at the periphery [81-83]. This work describes the use of peripherally tetrasubstituted phthalocyanines **7a**, **8b**, **8d**, **8e**, and **8f**.

1.1.2.3. Synthesis of octasubstituted phthalocyanines

Symmetrically substituted precursors either form 1,4,8,11,15,18,22,25- (non-peripherally) or 2,3,9,10,16,17,23,24- (peripherally) octasubstituted Pcs. Peripherally octasubstituted Pcs were studied in this work and are described in detail. Numerous methods can be used for the synthesis of peripherally octasubstituted Pcs [69,84]. Scheme 1.4 shows the octasubstituted Pc synthetic method used in this work.
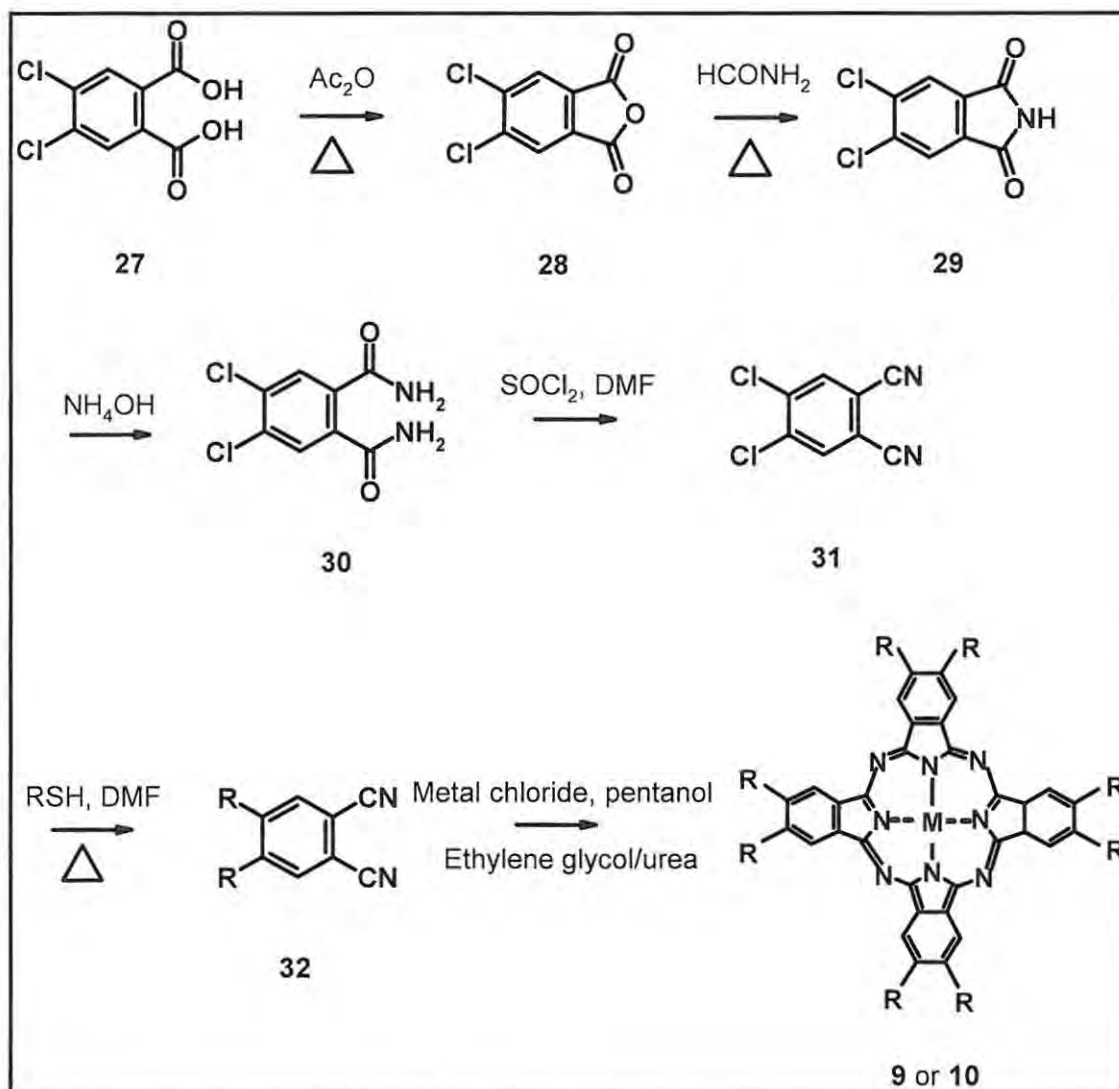
Scheme 1.4 Synthesis of octasubstituted Pc (**9** or **10**)

The inexpensive, commercially available reagent, 1,2-dichlorophthalic acid (**27**) is commonly used in the preparation of 4,5-disubstituted phthalonitriles (**32**) [69] and is therefore important in the synthesis of octasubstituted Pcs. Complex **31**, an important intermediate, is prepared from complex **27** in a manner similar to that of complex **22** (Scheme 1.2), as shown in Scheme 1.4. Reaction of **31** with a substituent such as thiol (RSH) leads to a nucleophilic displacement reaction producing the 4,5-disubstituted phthalonitrile (**32**), Scheme 1.4. The final step involves reacting the 4,5-disubstituted phthalonitrile (**32**) with a metal salt in the presence of 1,8-diazabicyclo-[5.4.0]-undec-7-ene (DBU) and solvent (or urea) to yield the peripherally

octasubstituted MPc (**9** or **10**), Scheme 1.4. The reaction shown in Scheme 1.4 can occur under different conditions. For various substituted dinitriles, the reaction in the presence of strong non-nucleophilic bases (e.g. 1,8-diazabicyclo[4.3.0]non-5-ene (DBN)) and/or a solvent is efficient (e.g. high yields) in comparison to other methods [61,64,85]. Furthermore, these reactions are easily done under relatively mild conditions and yield pure Pcs.

An advantage of octasubstituted Pc synthesis, especially in comparison to that for tetrasubstituted Pcs, is that isomerically pure products are obtained (making their purification easier). Also, the basic position of these substitutents is known because, for example, 4,5-disubstituted phthalonitriles condense to form 2,3,9,10,16,17,23,24-octasubstituted Pcs. In comparison to tetrasubstituted Pcs, an important disadvantage of octasubstituted Pcs is their insolubility. But the octasubstituted Pcs used in this work were rendered comparably soluble by introducing bulky peripheral substituents to the Pc core.

This work develops octasubstituted Pcs **9b**, **10a**, and **10b**.

1.1.3. UV-visible spectra

Classical (e.g. infra-red (IR) spectroscopy) and recent (e.g. matrix-assisted laser desorption ionisation (MALDI)) methods have been used for characterization of Pcs [16,41,86]. The most common method is by UV-visible spectroscopy.

The UV-visible spectral range is between 200 - 700 nm (where maximum absorption by FePcs and CoPcs commonly occurs) whilst the near-infrared range is 700 - 1000 nm (where maximum absorption by MnPcs usually occurs). The UV-visible spectra of MPcs usually consist of the following absorption bands [87]:

- an intense absorption band in the visible region (near 690 nm) called the Q band
- charge transfer bands (between the central metal and Pc ring)
- the superimposition of two bands, B_1 and B_2, giving a weak band near 350 nm called the Soret or B band.

The Q and B bands are those occurring most frequently in all Pcs. Fig. 1.6 shows a typical MPc UV-visible spectrum with the described absorption bands [14].
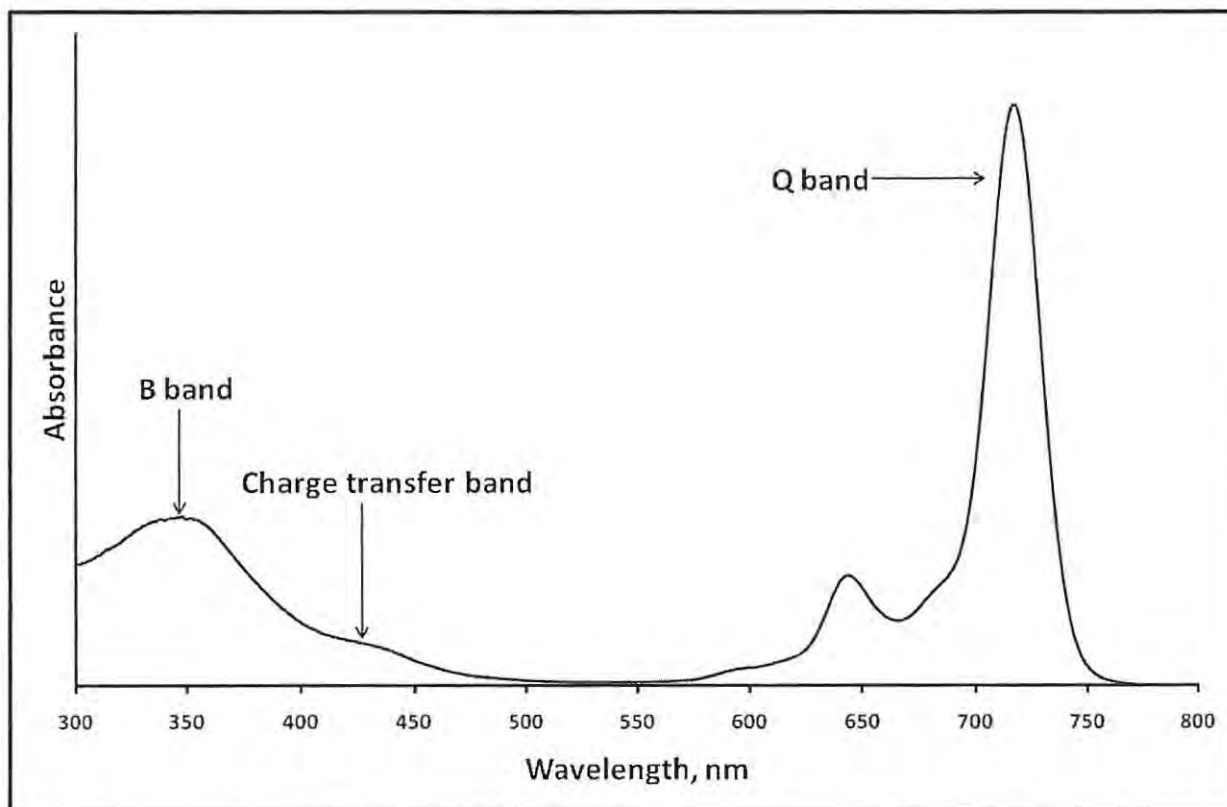
Fig. 1.6 MPc classic electronic absorption spectra showing the common absorption bands

The Q band originates from the π-π^* electronic transitions from the highest occupied molecular orbital (HOMO) to the lowest unoccupied molecular orbital (LUMO) of the Pc^{2-} ring whilst the B bands occur as a result of deeper π levels to LUMO transitions, Fig. 1.7.

19
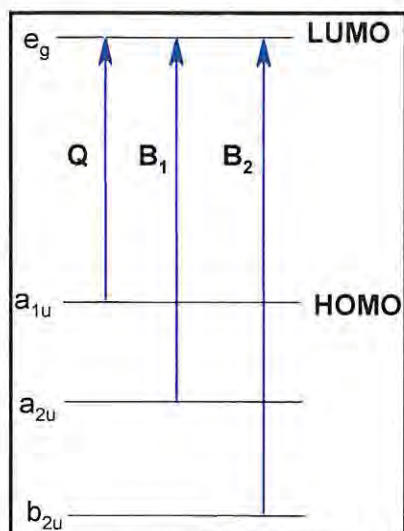
Fig. 1.7 Pc electronic transitions showing the origin of the Q and B absorption bands

From Fig. 1.7, the Q, B_1, and B_2 bands are shown as due to: a_{1u} to e_g; a_{2u} to e_g; b_{2u} to e_g electronic transitions respectively.

The spectral position and intensity of the Q band are important in tailoring new Pc types for particular applications. The positions of the Pc spectral absorption bands, especially the Q band, are affected by factors such as central metal, symmetry, substituents, aggregation, and solvents [88,89].

A non-metallated Pc displays a split Q band, whereas a MPc displays one Q band, Fig. 1.8a.
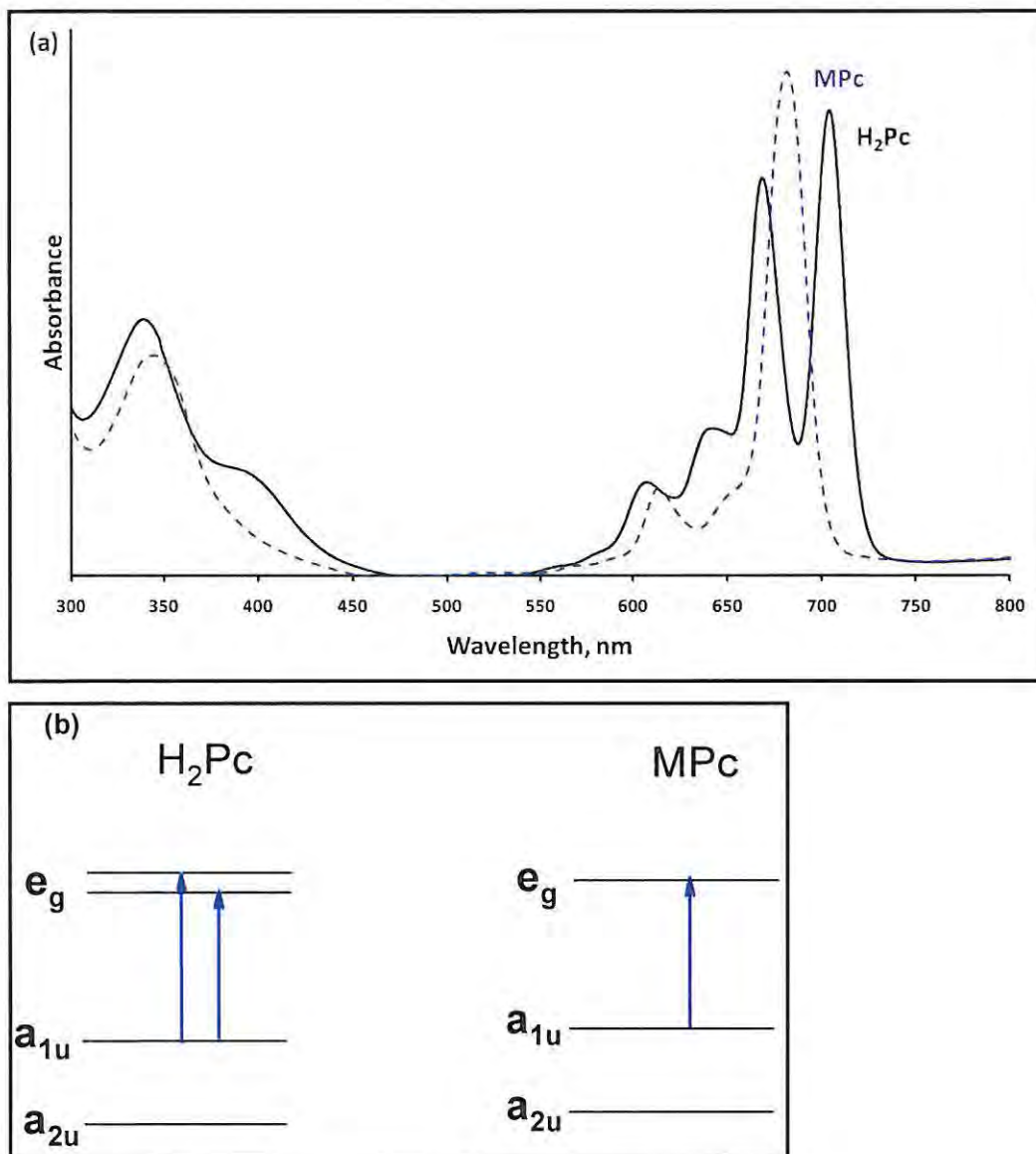
Fig. 1.8 (a) UV visible spectrums of non-metallated (H$_2$Pc) and metallated (MPc) Pcs. (b) Their Q band electronic transitions

The differences in absorption displayed between non-metallated and metallated Pcs, Fig. 1.8, is primarily due to symmetry. A non-metallated Pc has a D$_{2h}$ symmetry but, upon substitution of a metal, the MPc changes to a D$_{4h}$ symmetry. This increase in symmetry occurs because the change in geometry (once the Pc has been metallated) reduces the number of allowed transitions as shown in Fig. 1.8b.

Chapter 1: Introduction

Pcs are mostly blue/green in colour [90,91] because the intense Q band usually lies at the red end of the visible spectrum. In MnPcs the Q band is shifted out of the visible region into the near-infrared region so that the color of the complex is now determined by the absorption at the blue end of the spectrum and MnPcs consequently appear red or brown. Absorption can be moved into the near-infrared region by appropriate substitution of the Pc ring and by varying the central metal atom. The effect of the central Pc metal atom on the absorption maximum is especially significant for the Q band spectral position (λ_{max}), Table 1.3, spanning from the most hypsochromic metal, iron, to the most bathochromic metal, manganese [92-94].

Table 1.3 Q band positions of selected MPcs in dimethylformamide

Complex	λ_{max}, nm	Reference
FePc	~650	92
CoPc	667	93
MnPc	706	94

The effects of non-peripheral substitution of a Pc on its Q band position are larger than observed for peripheral substitution [89]. Peripherally substituted derivatives also have a stronger tendency to aggregate [95,96] and show a broader Q band than non-peripherally substituted complexes [97]. Furthermore, the consequence of incorporating sulfur donors, as was done in this work, is to shift the Q-band to the longer (near-infrared) wavelengths [98] essential for high-technology applications, such as PDT and near-infrared detection.

Aggregation in MPc complexes is characterized by a broadened or split Q band, with the high energy band being due to the aggregate and the low energy band due to the monomer. The use of dilute solutions and the addition of coordinating solvents can help avoid aggregation problems.

Dimeric (or polymeric) species can be formed as a result of direct linkages between two phthalocyanine rings [99], through covalent bonding involving the metal [100], when two Pc rings share one central metal [101], or through weak association where peripheral substitution holds two rings adjacent in space (where solvent polarity affects the monomer-dimer equilibrium) [102,103]. Higher aggregation in hexane than in chloroform was attributed to the

lower permittivity of hexane resulting in a weaker screening effect to disrupt Pc-Pc interactions [104].

Charge transfer transitions located between the Q and B bands, Fig. 1.6, are frequently used in identifying metal oxidation states in MPc complexes. For example, $Co^{I}Pc$ species show a band near 500 nm due to a metal to ligand charge transfer (MLCT) transition. $Mn^{III}Pc$ species [105] show a band in the same region due to ligand to metal charge transfer (LMCT) transitions. Fig. 1.9 shows the origins for the charge transfer transitions between the central metal and the ligand (Pc ring).
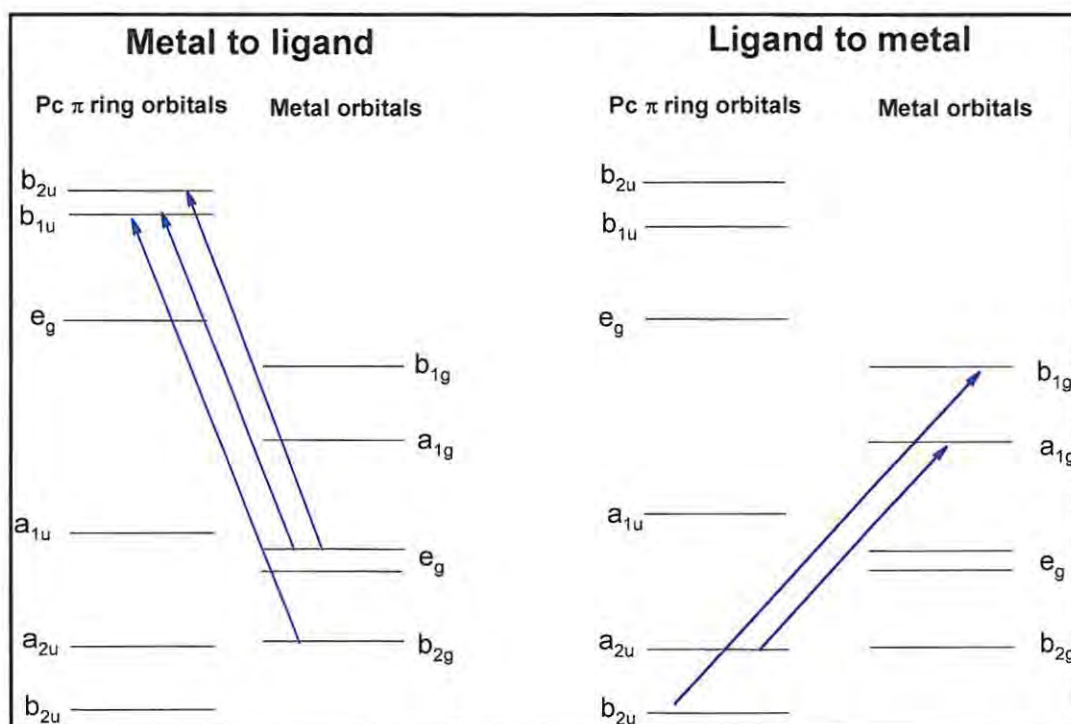
Fig. 1.9 Probable directions for charge transfer transitions between the central metal and ligand

1.2. Electrochemistry

1.2.1. Voltammetry

A three-electrode electrochemical cell, shown in Fig. 1.10, is often used in dynamic electrochemical experiments and was used for this thesis. The electrochemical reaction occurs at the working electrode (WE) which is commonly made of mercury, carbon, or noble metals (especially platinum and gold) [106-108].
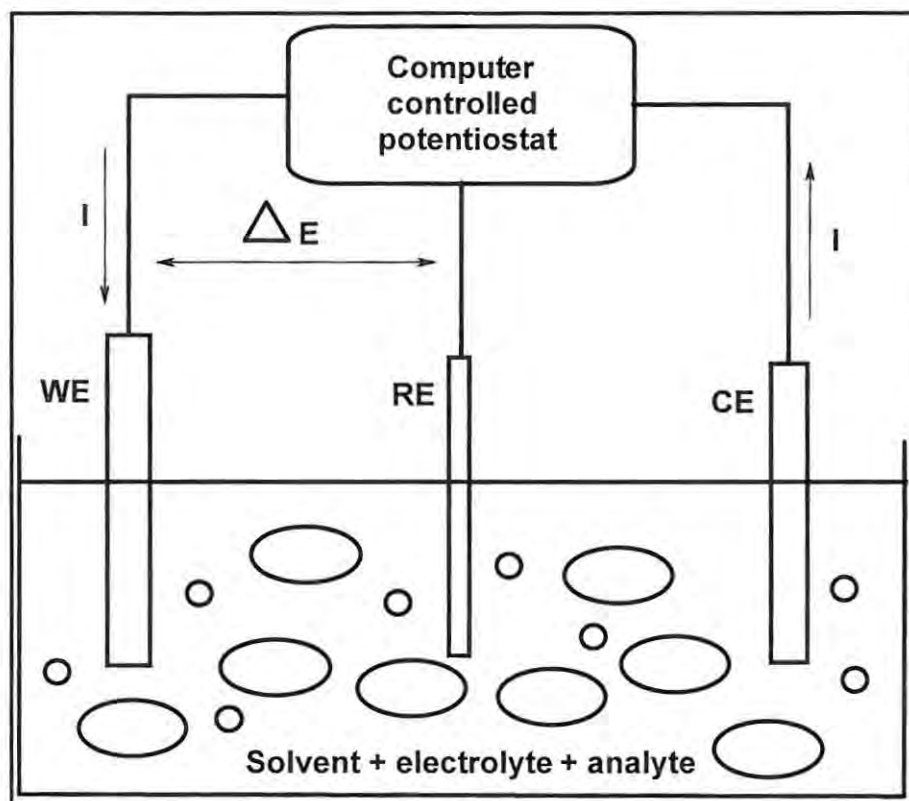
Fig. 1.10 A conventional three-electrode cell: WE = working electrode; RE = reference electrode; CE = counter electrode; I = current

Cyclic voltammetry is a common technique used in electrochemistry. During cyclic voltammetry, the potential is ramped from an initial potential E_1 to a second potential E_2. On reaching E_2, the direction of the potential scan is reversed, usually stopping at the initial potential E_1, Fig. 1.11.
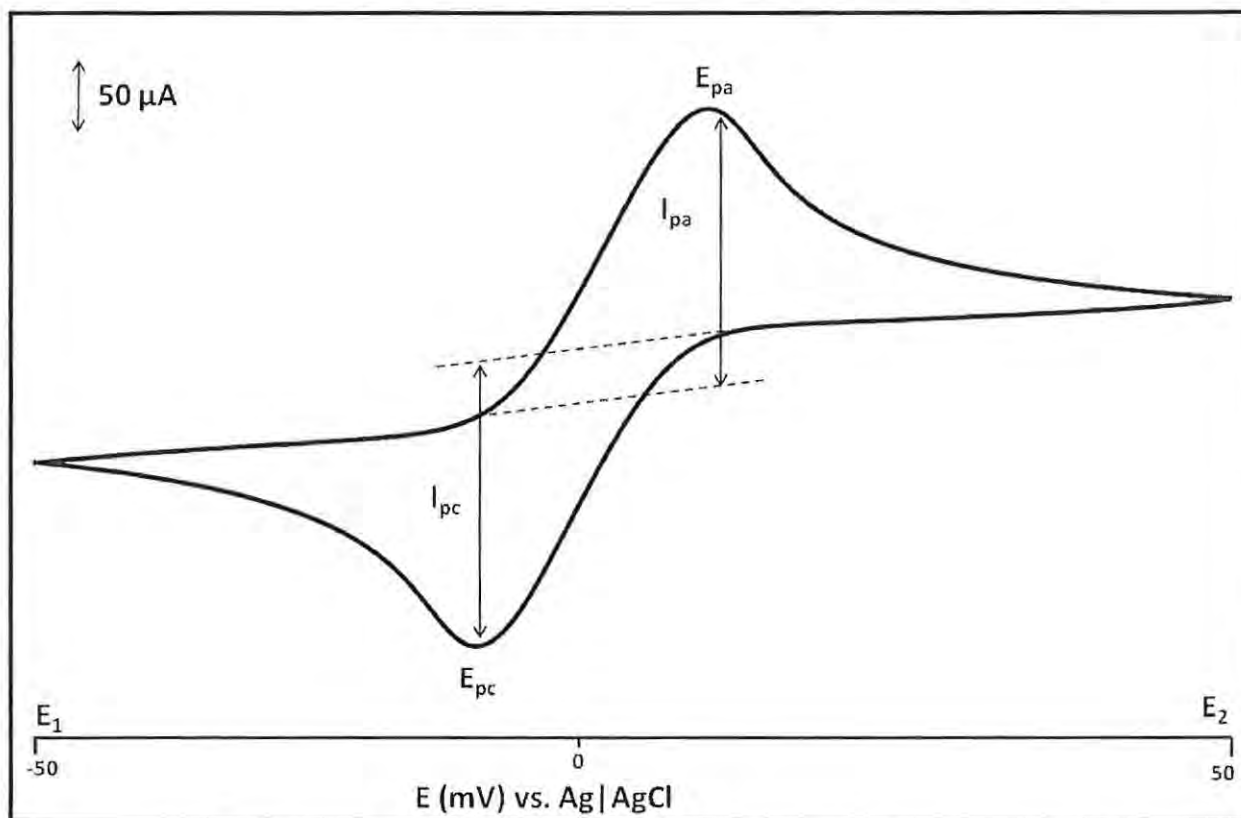
Fig. 1.11 Typical cyclic voltammogram

Several important parameters can be obtained from the cyclic voltammogram, Fig. 1.11: E_{pa}, the anodic peak potential; E_{pc}, the cathodic peak potential; I_{pa}, the anodic peak current; I_{pc}, the cathodic peak current. These parameters and their derivatives are used to identify the reduction/oxidation (redox) reactions. Another important parameter is the half-wave potential, $E_{1/2}$:

$$E_{1/2} = \frac{E_{pa} + E_{pc}}{2} \qquad\qquad 1.1$$

$E_{1/2}$ is used to identify a particular electrochemical process and the position where it occurs.

A reversible reaction is one in which the redox system remains in equilibrium throughout a potential scan i.e. the electrode surface concentrations of the oxidized (O) and reduced (R) species are maintained at the Nernst equation values. Under these conditions, the following parameters characterize the cyclic voltammogram of the reversible redox process:

25

Chapter 1: Introduction

- the peak potential separation (E_{pa} - E_{pc}) is equal to 59/n mV for all scan rates where n is the number of electrons transferred during the redox process
- the peak current ratio (I_{pa}/I_{pc}) is equal to 1 for all scan rates
- the peak current function increases linearly as a function of the square root of the scan rate (ν).

For reversible systems (like Fig. 1.11) the Nernst equation can be used. The current of reversible reactions may be represented by the Randles-Sevcik equation, Eq. 1.2:

$$i_p = 2.69 \times 10^5 n^{3/2} A D^{1/2} c \nu^{1/2} \qquad 1.2$$

where i_p is the peak current, n is the moles of electrons, A is the electrode area, D is the diffusion coefficient, c is the analyte concentration, and ν is the scan rate.

An irreversible reaction is one where the electrode reaction cannot be reversed. Slow electron exchange or chemical reactions at the electrode surface may result in irreversibility. Cyclic voltammograms showing a single oxidation or reduction peak signify an irreversible system. A large peak current separation (> 200 mV) also indicates irreversibility.

Quasi-reversible reactions exhibit behaviours intermediate between reversible and irreversible reactions [107]. Quasi-reversibility is observed when the return peak is smaller than the forward peak and/or a larger peak potential separation is observed in comparison to reversible systems. A peak separation of 80 to 200 mV is characteristic of a quasi-reversible system.

Linear sweep voltametry, commonly used in conjunction with cyclic voltammetry, is cyclic voltammetry without the return scan.

1.2.2. Spectroelectrochemistry

Spectroelectrochemistry allows the simultaneous acquisition of electrochemical and spectroscopic data [109-114]. In spectroelectrochemistry, the current and spectral absorbance bands are concurrently monitored [115-119].

The main problem encountered in *in situ* spectroelectrochemical experiments is that light must be able to pass through the electroanalysis cell, so everything (cell walls, solution, and electrode) must be highly transparent. To construct a cell from quartz or silica is simple, and to work with transparent solutions is generally problem-free, but transparent electrodes are a greater challenge. Nevertheless, the use of a wire mini-grid optically transparent electrode (OTE) overcomes this challenge. Modern methods commonly use a relatively cheap, thin (~0.3 μm) film of a

semiconductor: either tin oxide doped with fluoride (SnO_2:F) or indium doped with tin oxide [115] otherwise known as indium-tin oxide (ITO).

Fig. 1.12 gives an example of a MPc UV-visible spectroelectrochemistry study [120], where the application of potential results in spectral changes.
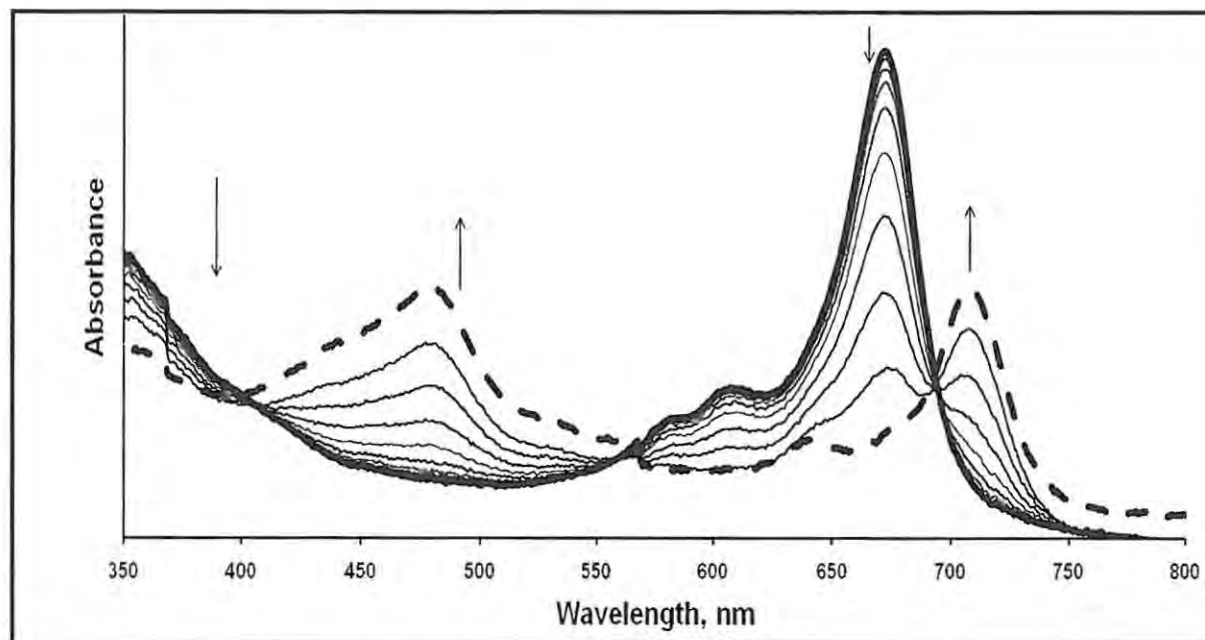
Fig. 1.12 Typical MPc UV-visible spectroscopy spectral study

1.2.3. Phthalocyanine electrochemistry

MPc electrochemistry in the solution phase is typified by multiple and often reversible redox processes localized on the metal centre and the Pc ring [15,16,121,122]. The standard oxidation state is -2 (Pc^{-2}) and the ring can be singly or doubly oxidized: $Pc^{-2} \rightarrow Pc^{-1} \rightarrow Pc^0$; and can be sequentially reduced at least four times through: $Pc^{-2} \rightarrow Pc^{-3} \rightarrow Pc^{-4} \rightarrow Pc^{-5} \rightarrow Pc^{-6}$ [121]. These redox pathways may be influenced by the solvent and the axial ligand [121] and are important in natural and industrial catalytic reactions of phthalocyanines. Fig. 1.13 shows the energy level diagrams of neutral, one-electron ring reduced, and one-electron ring oxidized MPc complexes. A small black arrow represents electrons in Fig. 1.13.

27

Neutral: MPc^{-2}   **Ring-oxidized: MPc^{-1}**   **Ring-reduced: MPc^{-3}**

e_g e_g e_g

Q B_1 B_2

a_{1u}

a_{2u}

b_{2u}
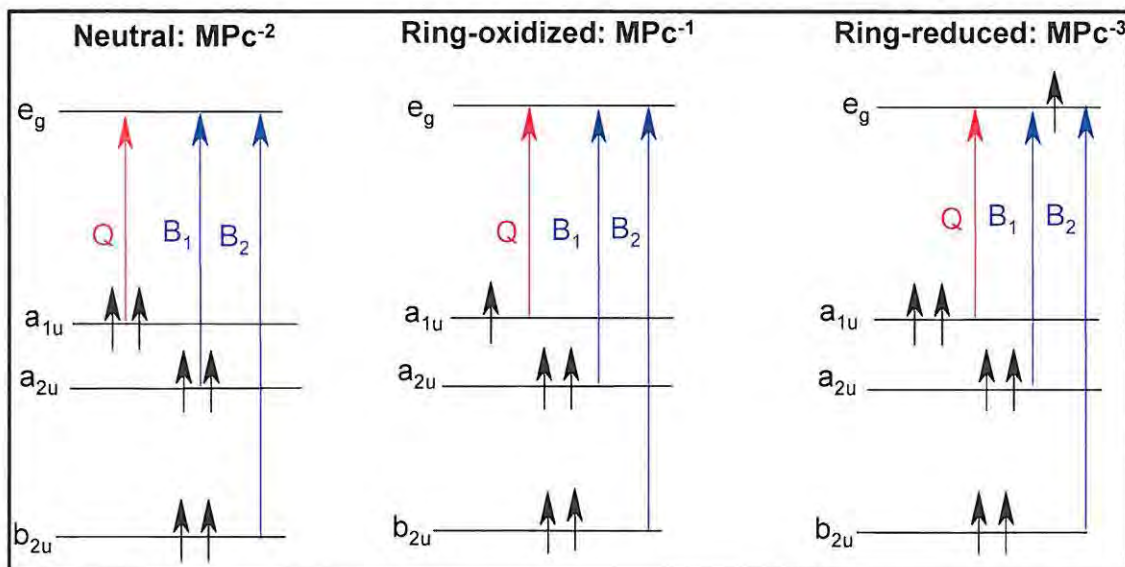
Fig. 1.13 Energy level diagrams of neutral, one-electron ring reduced, and one-electron ring oxidized MPc complexes

As stated, Pcs can form stable complexes with a variety of metal ions. MPcs which have been studied electrochemically are shown in Fig. 1.14 [123].

Fig. 1.14 MPcs electrochemically studied (shaded) and not studied (not shaded)

28

Chapter 1: Introduction

Non-transition metals do not have d-orbitals between the HOMO and LUMO gap of the Pc ligand and therefore only ring processes occur in these phthalocyanines. First row transition metals have d-orbitals situated between the HOMO and LUMO gap of the Pc ligand [124-127] and consequently show electrochemical reactivity. Electrochemical processes occurring on the metal in the Pc are expected especially for Fe, Co, and Mn derivatives [128,129], and hence such derivatives were used in this work. M^{II}/M^{I} and M^{III}/M^{II} couples are observed for Fe and Co Pcs whilst only the M^{III}/M^{II} couple is commonly observed for MnPcs [130]. Furthermore, the redox potentials of the MPcs frequently depend on the central metal ion, the nature of the macrocycle and its susbtituents, the axial ligand, and the solvent conditions. Fine tuning of the redox potentials is often achieved by varying these factors [16,121,122] as was done in this work. Table 1.4 shows a selection of reported redox potentials for various MPc (M = Fe, Co, Mn) complexes [22,23,27,131-134].

Table 1.4 $E_{1/2}$ potentials (V vs. Ag|AgCl) for selected MPc processes in dimethylformamide unless otherwise stated

MPc[a]	M^IPc^{-2} $/M^IPc^{-3}$	$M^{II}Pc^{-2}$ $/M^{II}Pc^{-3}$	$M^{II}Pc^{-2}$ $/M^IPc^{-2}$	$M^{III}Pc^{-2}$ $/M^{II}Pc^{-2}$	$M^{IV}Pc^{-2}$ $/M^{III}Pc^{-2}$	$M^{IV}Pc^{-1}$ $/M^{III}Pc^{-2}$	$M^{III}Pc^{-1}$ $/M^{III}Pc^{-2}$	Ref.
FePc	-1.17	-	-0.55	0.37	-	-	-	131
FePc(Cl)$_{16}$	-1.11	-	-	0.73	-	-	-	132
FeOBTPc	-1.00	-	-0.49	0.26	-	-	0.91	132
FeOHETPc	-1.01	-	-0.54	0.31	-	-	0.90	23
CoPc	-1.40	-	-0.37	-	-	-	-	131
CoOBTPc	-1.07	-	-0.38	0.40	-	-	0.77	133
CoHETPc[b]	-1.22	-	-0.34	0.43	-	-	-	134
MnTBMPc[c]	-	-0.84	-	-0.08	0.3	0.87	-	27
MnTDMPc[c]	-	-0.98	-	-0.26	0.3	0.83	-	27
MnPc(NH$_2$)$_4$	-	-0.98	-	-0.30	0.58	0.75	-	22

[a]OBTPc = octabutylthiometallophthalocyanine; OHETPc = octa(hydroxyethylthio) phthalocyanine; TBMPc = tetrakis(benzylmercapto)phthalocyanine; TDMPc = tetrakis(dodecyl-mercapto)phthalocyanine

[b]In dimethylsulfoxide

[c]In dichloromethane

1.3. Chemically modified electrodes

A good electrochemical catalyst (electrocatalyst) is ultimately a good electrosensor hence, in this work, both terms have the same meaning. Many electrode reactions occur, if at all, only at very high overpotentials in the absence of a catalyst with low current responses because of poor kinetics. Un-modified electrodes are also susceptible to fouling. Electrochemical catalysis (electrocatalysis) provides lower energy of activation pathways and hence allows electrode reactions to occur at low overpotentials with high current densities. The electrocatalyst must be stable, resistant to corrosion, and maintain its catalytic activity for a long period. Pcs have the potential to exhibit these properties and hence were used in this work.

Chapter 1: Introduction

A chemically modified electrode (CME) is a device where a chemical substance has been attached to an electrode surface; the chemical substance acts as a catalyst so the modification enhances electrochemical processes occurring at the electrode surface. Modification of electrode surfaces with MPcs for electrocatalysis began with oxygen reduction mediated by CoPc [19,20] and is a developing field [21,106,135-137]. Electrocatalysis using modified electrodes is especially advantageous in that it provides desirable qualities such as sensitivity, speed, miniaturization, and reliability. In this work MPc electrocatalysts have been used as electrochemical sensors for various analytes.

The CMEs catalyse electrochemical reactions by facilitating electron transfer between the electrode and an analyte [138-140]. This reaction sequence is usually described by Eq. 1.3 and 1.4 for reduction using MPcs as electrocatalysts [106]:

$$MPc_{Ox} + e^- \rightarrow MPc_{Red} \qquad\qquad 1.3$$

$$MPc_{Red} + A_{Ox} \rightarrow MPc_{Ox} + A_{Red} \qquad\qquad 1.4$$
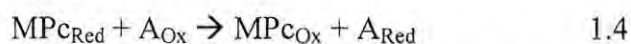
where MPc_{Ox} = oxidised form of MPc; e^- = electron; MPc_{Red} = reduced form of MPc; A_{Ox} = oxidised form of analyte; A_{Red} = reduced form of analyte.

Electron transfer occurs between the electrode and the mediator (e.g. MPc) and not directly between the electrode and the analyte. The electron shuttling represented by Eqs. 1.3 and 1.4 results in a lowering of overpotentials (i.e. less energy is necessary for electrochemical reactions to occur) and higher current density (i.e. increase in electrochemical response). These factors are the most important for efficient electrochemical sensing [138-140] such as done in this work. Eq. 1.3 and 1.4 are represented diagrammatically in Scheme 1.5 [115,141].

Chapter 1: Introduction
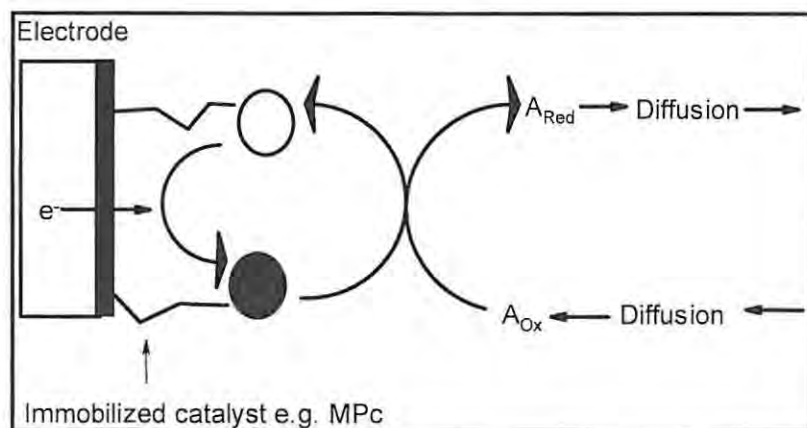
Scheme 1.5 Schematic illustration of modified electrode used for electrocatalysis in solution: $\circ$ = oxidised form of catalyst (e.g. MPc_{Ox}); $\bullet$ = reduced form of catalyst (e.g. MPc_{Red}); A_{Ox} = oxidised form of analyte; A_{Red} = reduced form of analyte (i.e. the product)

Scheme 1.5 illustrates the design for accelerating electrochemical reactions with an immobilized mediator catalyst. The oxidized form of the mediator catalyst is rapidly reduced by the electrode, and then its reduced form reacts with the analyte species (A_{ox}) in solution. The analyte is consequently reduced (giving A_{Red}, i.e. the product) and then diffuses back into solution, whilst the mediator catalyst is simultaneously oxidized to regenerate its (original) oxidised form. In mediator catalyst processes, such as represented in Scheme 1.5, the electron transfer reaction is ideally fast and simple whilst both catalyst redox states should be chemically stable and undergo little or no structural or bonding changes during reaction [142]. A good choice of a mediator requires the electrode potential of the mediator to 'couple' with the redox state of the analyte.

1.3.1. Electrodes used in this work

This work uses glassy carbon and gold electrodes, described in this section.

1.3.1.1. Glassy carbon electrodes

Electrocatalytic reactions have been performed on various electrodes modified by the application of MPcs, but carbon is the most widely used electrode material. Glassy carbon, carbon fibres, or graphite electrode surfaces have been treated with MPcs by coating, adsorption, or chemical bonding [143-145].

Chapter 1: Introduction

The disadvantages of carbon electrodes are that carbon has a high surface activity so it is susceptible to poisoning by organic compounds, and electron transfer rates at carbon surfaces are often slower than those at metal surfaces. Electron transfer rates are also greatly influenced by the carbon surface structure [146]. Nevertheless, a number of electrode pre-treatment procedures have been proposed to increase the electron-transfer rates and ultimately the analytical performance of carbon electrodes. The advantages of carbon electrodes are that they [106]: may be used for broad potential window studies; have low background currents; are cheap; are chemically inert; are suitable for various sensing and detecting applications. Carbon electrodes have been used in biomedical fields because of their good conductivity, chemical inertness, and mechanical stability [147]. A model for a glassy carbon electrode is shown in Fig. 1.15 [148].
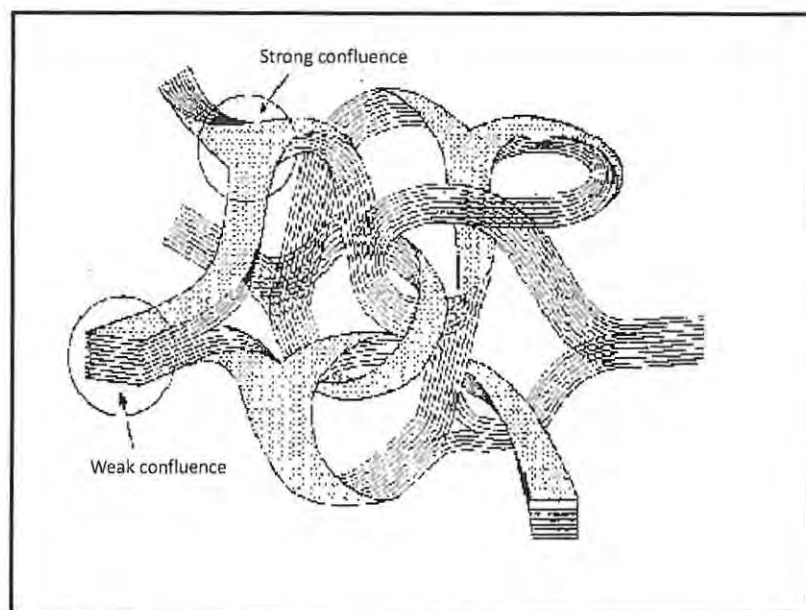
Fig. 1.15 Model for a glassy carbon electrode

The model consists of entangled ribbons of polymeric graphite molecules, Fig. 1.15. The strength of glassy carbon is attributed to the entanglement of the ribbons [149,150]. Its chemical inertness is regarded as being due to the ribbons having no ends, but rather merging and separating at 'confluences' as shown in Fig. 1.15. Glassy carbon is popular because of its wide range of usable potential, its relatively reproducible performance, and low cost in comparison to

gold or platinum electrodes [106,151]. Glassy carbon also exhibits a much lower oxidation rate at elevated temperatures suggesting a greater inertness to chemical attack than other types of carbons such as graphite.

1.3.1.2. Gold electrodes

Gold is most commonly used as an electrode material due largely to its variety of configurations, widespread commercial availability in various formats, and high purity [151]. One disadvantage of gold electrodes, like any metal electrode, is that they may be corroded or passivated by e.g. salt film formation on the surface and other reactions dependent upon the medium and experimental conditions [107]. Nonetheless, gold electrodes display negligible background currents due to their high resistivity, are sensitive, exhibit good reproducibility, are easy to clean, and allow for SAM formation. Thus they were used in this work.

1.3.2. Methods of electrode modification using metallophthalocyanines

Literature methods of modifying electrodes with MPcs are varied [22,152-159] and include direct deposition of MPc on the electrode through adsorption [137,160-165], mixing the MPc with carbon paste to make a conductive carbon cement [166], electropolymerization [167], electrodeposition [168], spin coating [162], self-assembled monolayer [133,162,169-174] and Langmuir-Blodgett films [175]. Consequently, there is considerable versatility in the construction of electrochemical sensors [106,151,176-178]. This section describes the methods used in this work to modify electrodes with MPcs; these methods are: electrode modification using aryl radicals (grafting), adsorption, and self assembled monolayers (SAMs).

1.3.2.1. Electrode modification using aryl radicals (grafting)

This section presents a new approach for the modification of a glassy carbon electrode (GCE) using a simple MPc complex, such as a carboxyphthalocyanine.

Immobilization of MPcs on electrodes by polymerization or by the formation of self assembled monolayers results in reproducible thin films, b ut their formation requires the synthesis of particular ring substituted MPc complexes, which is very time consuming [33,179,180].

Oxidation of carbon surfaces results in oxygen functional groups (e.g. carboxyl or hydroxyl) [181-184]. The precise nature of these oxygen functionalized groups has proven problematic to

study, aggravated by carbon surface corrosion [185-187]. It is consequently necessary to develop convenient and efficient modification techniques for the augmentation of glassy carbon surfaces such as by using aryl radicals, Scheme 1.6 [188-190].
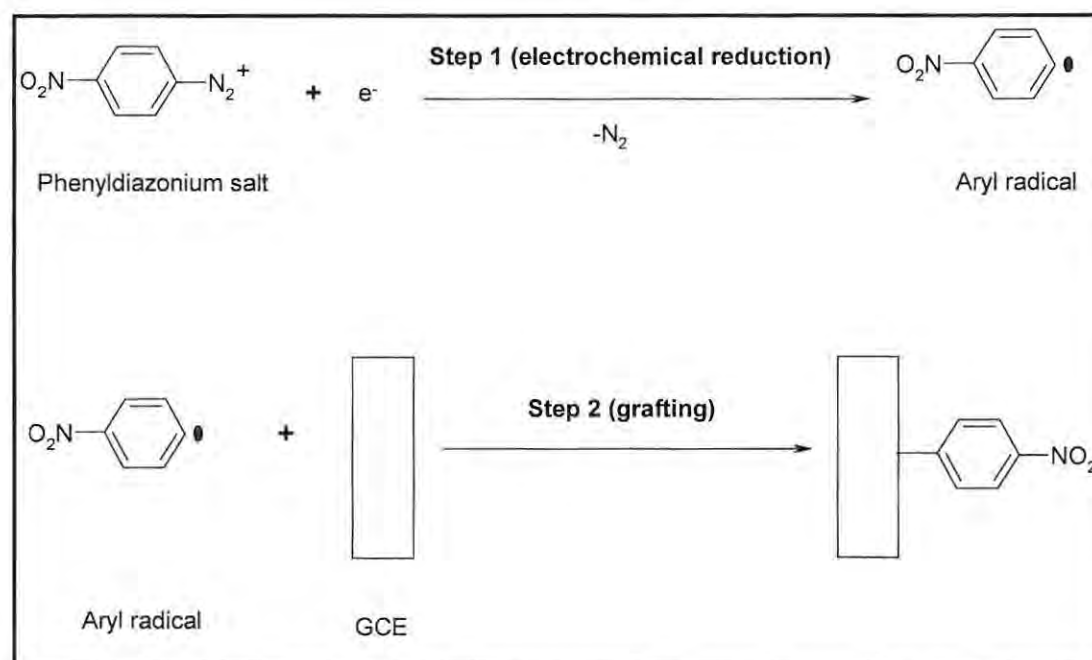
Scheme 1.6 Steps in the formation of a phenyldiazonium salt radical attached to a GCE

Scheme 1.6 represents the formation of a phenyldiazonium salt radical through the electrochemical reduction of a phenyldiazonium salt derivative (Step 1, Scheme 1.6) followed by the formation of a covalent bond between the phenyldiazonium salt radical (aryl radical) and the carbon surface (Step 2, Scheme 1.6). The generation of the aryl radical is a concerted process involving electron transfer and cleavage of the di-nitrogen (of the diazonmium salt) before the formation of the covalent bond [191]. The NO_2 is then reduced to NH_2, followed by attachment of a carboxyphthalocyanine.

Factors influencing the film structure formed on the carbon surfaces by the electrochemical reduction of an aryl diazonium salt include [192]: the carbon substrate type (aryl diazonium derivative or aryl diazonium salt concentration), the applied potential [193], and the modification time [193]. Even though the diazonium salt surface coverage on carbon substrates may be

controlled by varying the described factors, a saturation value comparable to a compactly packed monolayer is achieved [190].

The carbon surface modification technique described by Scheme 1.6 provides advantages in that specific functional groups, on the aryl group, may further enhance the properties of the modified electrode [194,195]. Thus, in this work a GCE was grafted with a phenyldiazonium salt followed by the attachment of **7a**; this CME was used as an electrocatalyst.

1.3.2.2. Adsorption

If a glassy carbon surface is exposed to a solution of MPc, adsorption of the MPc onto the glassy carbon surface can occur [137,161]. This CME can then be studied in a solution in which the MPc is insoluble but, even when in an MPc soluble solution, the MPc may still remain attached to the glassy carbon surface due to the strong bonding. The interaction between the adsorbate and the electrode surface may be electrostatic (e.g. the adsorption of ions on a surface of opposite charge), charge-dipole (e.g. the adsorption of benzene), or due to the formation of a covalent bond. Great variations occur in the strength of the bonding and the reversibility of the adsorption process.

CMEs formed by adsorption have displayed electrochemical catalytic activity [196-200]. Carbon electrodes are especially effective at adsorbing reagents that have extended π-bond systems such as MPcs. This is why glassy carbon electrodes and MPcs were used in this work for adsorption studies.

1.3.2.3. Self assembled monolayers

A self assembled monolayer (SAM) is a self-organized array of molecules chemically bonded onto a solid substrate [201,202]. A self assembled monolayer consists of molecules with recognizable head and tail groups, Fig. 1.16.
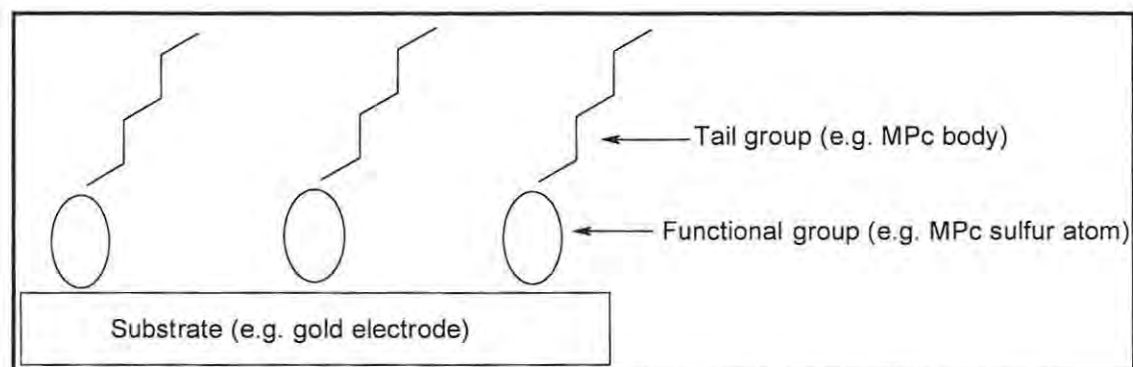
Fig. 1.16 Diagrammatic representation of a SAM

SAMs are formed spontaneously on immersing a solid substrate into a solution containing a species with an appropriate functional group. SAMs have been formed on electrode surfaces (the substrate, Fig. 1.16) such as gold, silver, platinum, mercury, or graphite but the most common ones are those formed by reactions of thiols or aryl thios (the functional group, Fig. 1.16) on gold or silver surfaces, or silanes on silica surfaces [34,170,171,203-206].

The affinity of sulfur for the coinage metals has resulted in the synthesis of Pc molecules containing sulfur substituents [23,33,34,133,162,169,172,207-210] for possible use in SAMs. SAM formation using sulfur functional groups and gold substrates may be understood in terms of the 'hard and soft acids and bases' (HSAB) theory. The S^{2-} anion is an example of a monodentate Lewis base because it is a ligand that donates one electron pair to one acid ion or molecule. Gold, functioning as a Lewis acid, forms strong covalent bonds with the Lewis base S^{2-}. The Lewis HSAB theory hence explains why the SAM bonding between thiols and gold is so favourable and strong. This work used SAMs formed by arylthio MPc on gold electrode surfaces for electrochemical catalysis.

The orientation of SAMs on gold, which influences their electrocatalytic behaviour [170,171], is affected by factors such as the number of substituents on the Pc ring, the chain length of the substituents, and axial substitution. The various MPc SAM orientations (vertical, umbrella, and octopus) are shown in Fig. 1.17.
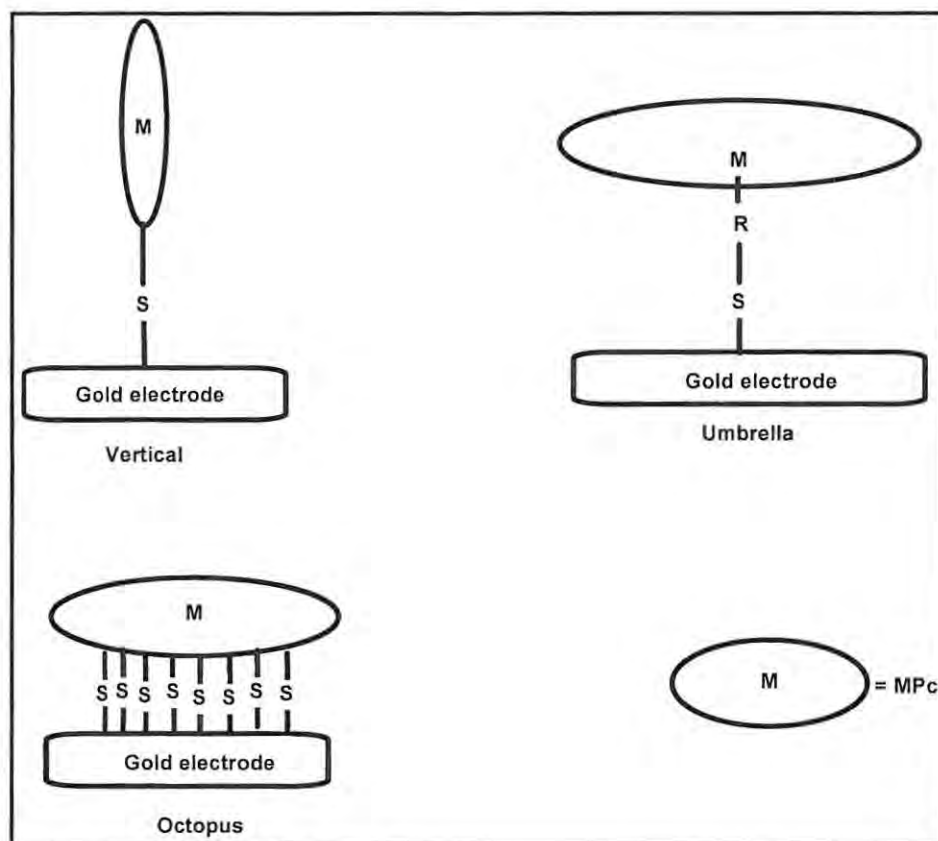
Fig. 1.17 MPc SAM orientations

Factors affecting SAM formation include [211]:

- substrate morphology: irregular substrate morphology leads to an irregular packing of self assembled monolayers on the surface. A rough substrate surface may lead to a higher density of self assembled monolayers due to an increase in available surface area [212]

- deposition solvent: solvent choice depends on several factors which may include solvent toxicity levels, solvent purity, and adsorbate solubility (1×10^{-3} M concentrations are preferred for MPcs). Common organic solvents may be used appropriately for self assembled monolayer deposition

- deposition concentration, time, and temperature: all three factors are inter-related. A high deposition concentration (e.g. ~1×10^{-3} M) allows for a lower deposition time and also possibly a lower temperature environment. Lower concentrations may require longer deposition times due to mass transport limitations of the adsorbate to the substrate [213].

Chapter 1: Introduction

The substrate is usually left in the deposition solvent for times ranging from 30 minutes to 24 hours, though longer deposition times have been reported [214].

Disadvantages of SAMs are that these layers are mostly limited to specific functional groups (e.g. thiols or aryl thios) and, in most cases, are restricted to metal surface substrates (e.g. gold). Conversely, SAMs are advantageous in that their formation is spontaneous, fast, and simple [132].

Even though SAMs have been used as metal ion sensors [215], immunosensors [216], and biosensors [217], few MPc complexes tetrasubstituted with thiols or aryl thios have been used as electrochemical sensors and their orientation on substrates still needs to be explored.

1.4. Characterization of chemically modified electrodes

The chemically modified electrodes (CMEs) of this work were characterized using the following techniques: voltammetry, impedance, atomic force microscopy (AFM), and scanning electrochemical microscopy (SECM). These techniques are detailed in this section.

1.4.1. Voltammetry

Voltammetry techniques for characterization of SAMs are based on the principle that SAMs block a number of Faradic processes [23].

1.4.1.1. Ion barrier factor (Γ_{ibf})

In SAM studies, an exposed site on the electrode surface is called a pinhole [218]. Therefore, at such a site, self assembled molecules are absent and nearby molecular tails do not block the site. A pinhole may therefore be considered a defect in the SAM surface. Numerically, the extent of pinhole presence is indicated by the ion barrier factor, Γ_{ibf}. The ion barrier factor (Γ_{ibf}) is obtained by a comparison of the total charge under the gold redox peak of a SAM-modified electrode (Q_{SAM}) with that of an un-modified electrode (Q_{Bare}), Eq. 1.5:

$$\Gamma_{ibf} = 1 - \frac{Q_{SAM}}{Q_{Bare}} \qquad 1.5$$

An ion barrier factor of one indicates no pinholes and therefore the SAM is an ideal barrier to ion and solvent permeability [132,218].

Chapter 1: Introduction

1.4.1.2. Interfacial capacitance (C_s)

The interfacial capacitance, C_s, is a measure of ion permeability through the SAM because it indicates how close packed and defect-free the SAM is [132,219]. A defined cyclic voltammogram potential window, in which no peaks are observed for both un-modified and SAM-modified gold electrodes, will have a charging current (i_{ch}) whose value may be used to calculate the interfacial capacitance (C_s) using Eq. 1.6:

$$C_s = \frac{i_{ch}}{\nu A} \qquad\qquad 1.6$$

where ν is the scan rate ($V.s^{-1}$) and A is the electrode surface area (cm^2).

The lower the C_s value, the fewer are the defects present in the SAM and so the electrode surface is less permeable to electrolyte ions [132,219]. Therefore, a SAM-modified gold electrode should display a lower C_s value relative to an un-modified gold electrode.

1.4.1.3. Inhibition of redox couples

A SAM-modified gold electrode inhibits metal deposition on the gold electrode [218]. An un-modified gold electrode, recorded in a Cu^{2+} aqueous solution, displays a cyclic voltammogram where Cu deposition onto the electrode begins near the standard potential of Cu^{2+} (0.10 V vs. Ag|AgCl) during the negative-going scan. On the return scan there is a prominent stripping peak of the copper metal (at ~0.15 V vs. Ag|AgCl). An ideal SAM-modified gold electrode will block the metal deposition and, therefore, the stripping processes [218].

SAM-modified gold electrodes also inhibit Faradic processes of a soluble analyte such as $Fe(NH_4)(SO_4)_2$. The SAM ability to act as a barrier to the $[Fe(H_2O)_6]^{3+}/[Fe(H_2O)_6]^{2+}$ redox couple is an excellent indication that the SAM film is compact and/or that the pinholes are smaller than the electroactive probe ions.

1.4.1.4. Surface coverage (Γ)

Surface concentration may be estimated from the charge produced by a metal Pc couple (e.g. $M^{III}Pc/M^{II}Pc$) on an electrode, obtained in a suitable aqueous analyte. Surface coverage (Γ) may then be calculated using Eq. 1.7:

$$i_p = \frac{n^2 F^2 A \Gamma(\nu)}{4RT} \qquad\qquad 1.7$$

where i_p is the peak current (amps), n is the number of electrons, F is the Faraday constant (F = 96485 $C.mol^{-1}$), A is the electrode surface area (cm^2), ν is the scan rate ($V.s^{-1}$), R is the gas constant (R = 8.314 $J.K^{-1}.mol^{-1}$), and T is the temperature in Kelvin.

The value of Γ gives an estimate of monolayer coverage with Pcs lying flat given $\Gamma \approx 1 \times 10^{-10}$ $mol.cm^{-2}$ [220,221].

1.4.2. Impedance

Measurement of impedance is non-invasive and can be used for investigating bulk, as well as interfacial, processes [222-224]. Impedance has an advantage over chronoamperometry and cyclic voltammetry in the study of SAMs because the effects of solution resistance and currents due to diffusion or other processes occurring in the SAM are observed more explicitly [225].

1.4.2.1. Nyquist plot

The Nyquist (Argand or Cole-Cole) plot is a popular format for plotting complex impedances [115,224-236]. In the Nyquist plot, the imaginary impedance component (Z") is plotted against the real impedance component (Z') at each excitation frequency (input signal). The total impedance |Z| (output response) is then calculated from Pythagorian mathematics. Fig. 1.18 gives examples of Nyquist plots [236].
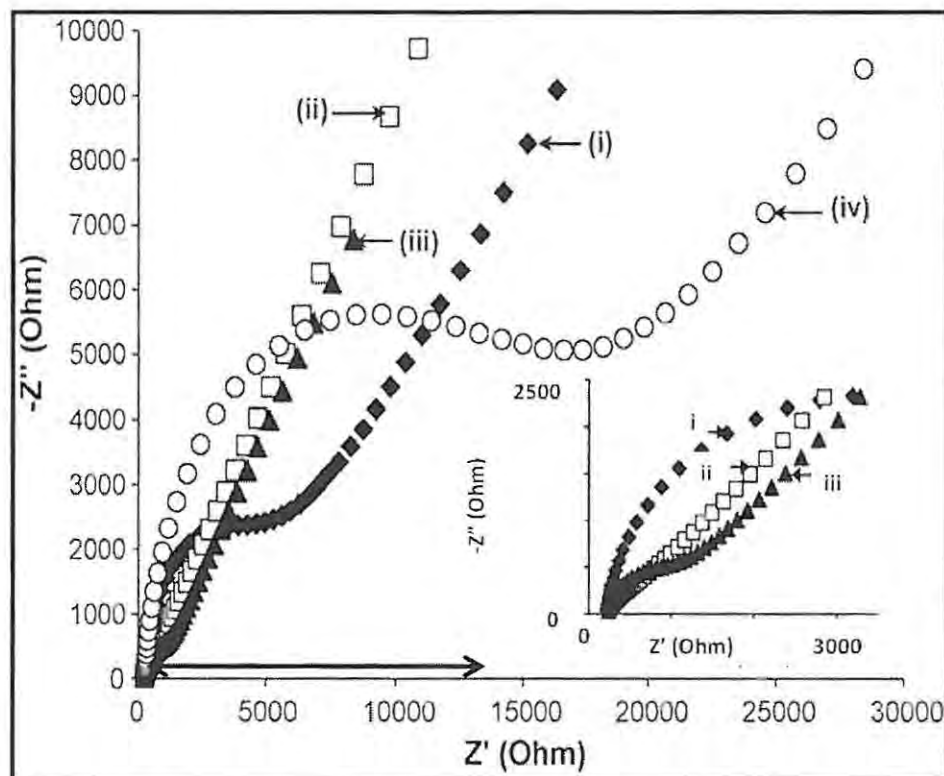
Fig. 1.18 Nyquist plots for actual chemical systems. The double-headed arrow on plot iv indicates its charge transfer resistance R_{ct}

This work uses Nyquist plots to calculate charge transfer resistance (R_{ct}) values of CMEs. The R_{ct} is calculated from the diameter of the semi-circular part of the Nyquist plot (indicated by the double headed arrow in Fig. 1.18, plot iv). The dynamics of R_{ct} are strongly influenced by the nature of the electrode surface and the structure of the electrical double layer [214,229-233] and R_{ct} is therefore a useful characterisation technique. In SAM studies, a large R_{ct} means that the monolayer is compact and acts as a barrier to the solution species and/or that the pinholes are smaller than the electrochemical solution species.

1.4.2.2. Bode plot

The Bode plot allows the examination of the absolute impedance ($|Z|$) and the phase shift (θ) of the impedance, each as a function of frequency [237]. The impedance is represented as $|Z|$ or log $|Z|$. Theta (θ) represents the time lag experienced between the input signal (e.g. current) and output response (e.g. voltage). The Bode plot has some distinct advantages over the Nyquist plot. Because frequency appears as one of the axes, it is easy to see from the plot how the impedance

depends on the frequency [238]. The plot also uses the logarithm of frequency so a very wide frequency range can be plotted on one graph. Fig. 1.19 shows, as an example, Bode plots of SAM-modified electrodes (Au SAM) relative to an un-modified (Au-bare) electrode recorded in 1 mM $[Fe(CN)_6]^{3-}/[Fe(CN)_6]^{4-}$ in 0.1 M KCl as a supporting electrolyte [88]. The non-labelled arrow in Fig. 1.19 indicates increasing SAM deposition time.
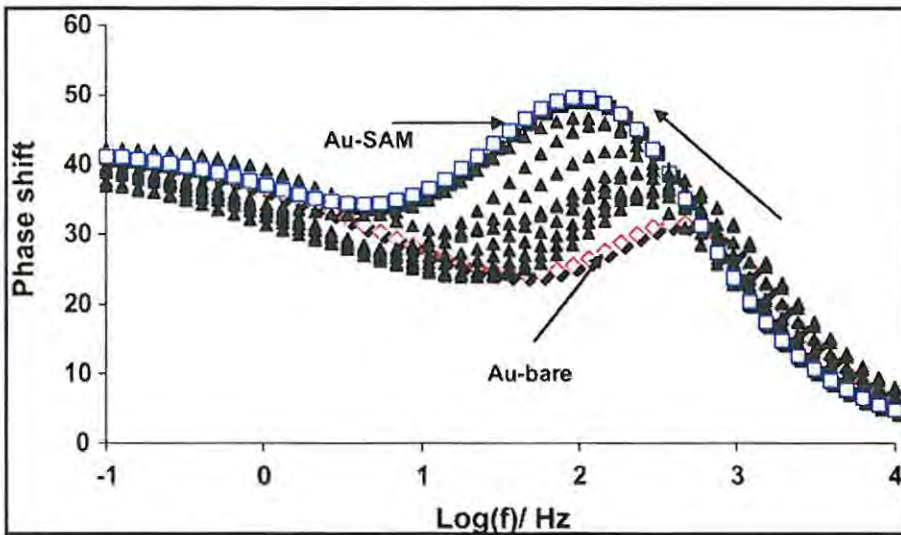
Fig. 1.19 Bode plots of SAM-modified electrodes (Au SAM) relative to an un-modified (Au-bare) electrode recorded

From Fig. 1.19, the Bode plots show that as the SAM deposition time increases lower peak frequencies are obtained, proving that the $[Fe(CN)_6]^{3-}/[Fe(CN)_6]^{4-}$ redox process occurs at the modifying film rather than directly on the un-modified gold [88].

1.4.3. Atomic force microscopy

Scanning probe microscopy (SPM) is a general term used to describe techniques that use a sharp probe to image and measure surface properties. SPM techniques include scanning tunneling microscopy (STM) and atomic force microscopy (AFM).

STM was first developed in 1982 by Binnig *et al* [239]. Though useful, STM has a major drawback: it can only image conducting or semiconducting surfaces. This led to the development, in 1986, of the atomic force microscope by Binnig, Quate, and Gerber [240].

Chapter 1: Introduction

AFM finds a variety of applications that range from nanofabrication (e.g. semi-conductors) to biological materials (e.g. studying DNA structure) [241-243]. AFM has also been used for SAM characterisation, Fig. 1.20 [88].
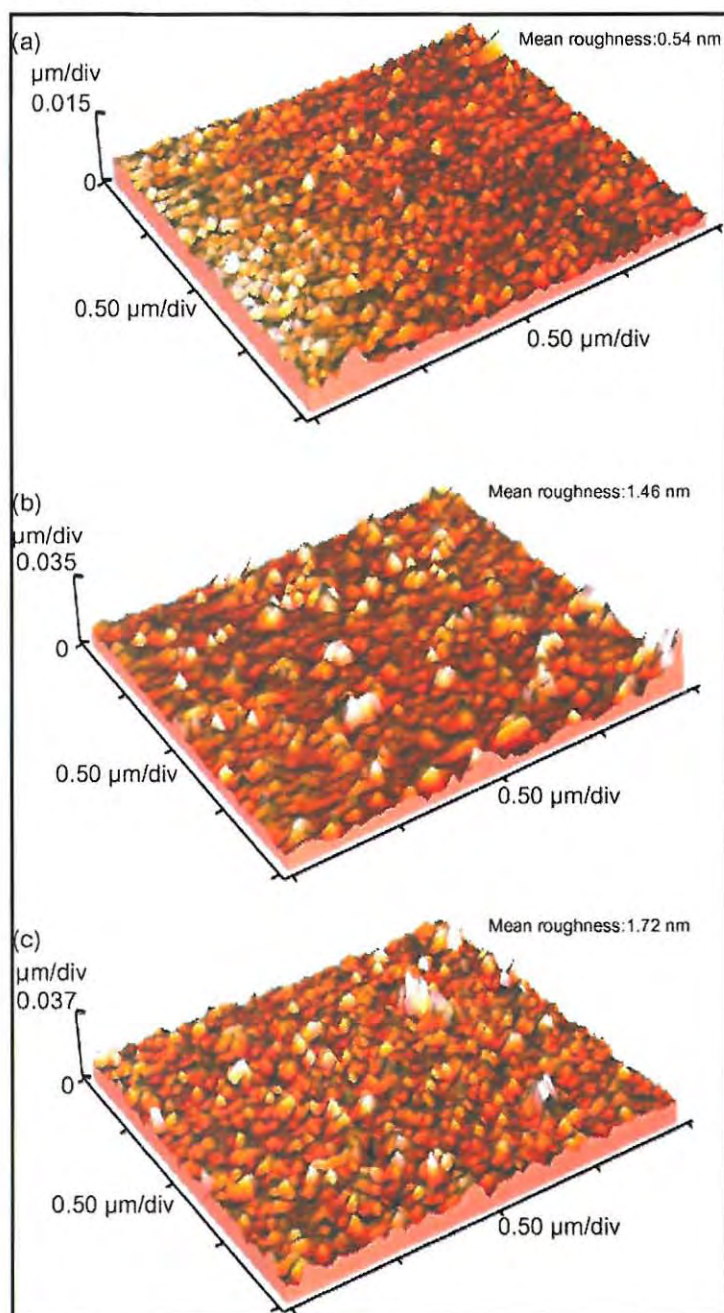
Fig. 1.20 AFM images of gold surfaces before (a) and after modification with the SAM of two different MPc complexes (b and c)

Chapter 1: Introduction

The AFM images of Fig. 1.20 show clear differences in morphology and roughness factor between an un-modified gold surface and MPc SAM surfaces [88] proving that AFM is useful for SAM characterisation.

1.4.4. Scanning electrochemical microscopy

Scanning electrochemical microscopy (SECM) is a scanning probe technique based on changes in Faradic current when an ultramicroelectrode (UME) tip is moved across the surface of a sample [244]. SECM provides good sensitivity in obtaining topographic and surface electrochemical information [245,246].

SECM involves the flow of current through a very small electrode tip (e.g. an UME with a tip diameter of ~10 µm) near a conductive, semiconductive or insulating sample (or 'substrate') immersed in solution. This current is used to characterize processes and structural features at the sample's surface as the tip is moved near the surface. A basic SECM setup is shown in Fig. 1.21.
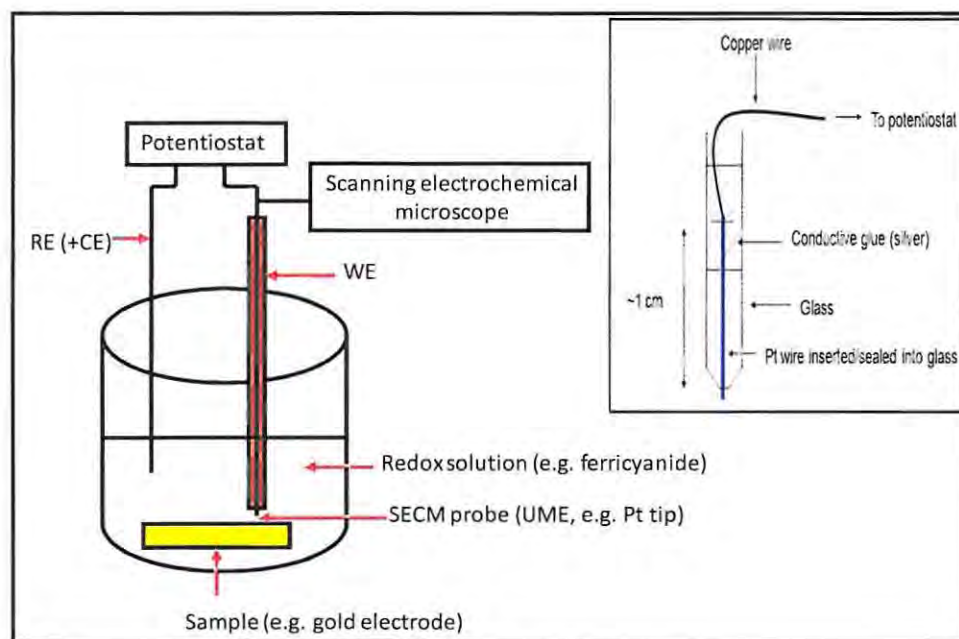
Fig. 1.21 Basic SECM setup also showing ultramicroelectrode (UME) magnification (insert)

The basic SECM setup, Fig. 1.21, consists of a redox solution such as ferricyanide. An advantage of using UMEs is that the electrolyte is unnecessary due to the small currents involved. The

Chapter 1: Introduction

reference electrode also serves as the counter electrode for the same reason. The SECM working electrode is shown in greater detail as Fig. 1.21 insert. This electrode is a fine wire encased within a non-reactive sheath, thus ensuring that only one end is in contact with the redox solution. This exposed end, typically flat and circular with a diameter of ~10 µm (i.e. the actual UME), is the SECM probe and is often called a 'tip' [115]. The tip can be moved normal to the sample surface (the z direction) or scanned at constant z across the surface (the x and y directions). The device uses piezoelectric elements, or stepping motors driving differential springs, to enable such movements. The term SECM is used interchangeably both for the technique and the instrument.

SECM images depend on the sample topography and the surface conductivity. The resolution of SECM images largely depends upon the tip radius and the distance between the tip and the sample, but the resistance of the solution and the rates of mass and charge transfer processes that affect the current density distribution are also important factors.

SECM modes of operation include:

- collection mode: where products electrochemically generated at the sample are detected at the tip
- feedback mode: where the effect of the sample on the tip current is monitored.

The feedback mode is used in this work especially because it can be used with conductive or insulating samples and is less sensitive to disruptive electrical coupling between the sample and the tip. Also, in the feedback mode, as the tip is scanned over a sample, the disturbance of the sample by the tip is minimal because the diffusion layer of interest in the measurement originates at the tip rather than at the sample.

Applications of SECM to thin films, modified electrodes, and conductive polymers have been reported [247,248] in areas of general interest such as batteries, sensors, and display devices [249-251]. Other uses of SECM include studies of: heterogeneous electron-transfer reactions [252,253]; molecular transport across membranes [254,255]; adsorption/desorption processes [256,257]; corrosion processes [258,259]; charge transfer at liquid-liquid interfaces [260,261]; and imaging of surface and electrochemical systems [245,262-267].

This work uses SECM to study SAMs. In SECM experiments on SAMs the sample is either the un-modified gold electrode or the SAM-modified gold electrode. Inhibition of electron transfer is

46

a basis for imaging SAMs on gold electrodes by SECM [252,268-274]. Generally a defect-free SAM passivates the gold electrode so strongly that it behaves like an insulator. Alternatively, the SECM signal sensitively responds to pinholes where higher current values result because no passivation occurs. SECM shows a good contrast between SAM and un-modified gold electrode surfaces, thereby proving the low defect density on the SAM-covered areas. In comparison to cyclic voltammetry, which is often used to characterize SAM passivating behaviour, the application of extreme (and therefore possibly SAM-disrupting) potentials can be avoided in SECM investigations of SAMs [271]. Fig. 1.22 shows a SECM image of a GCE, a part of it covered with insulating Teflon® recorded in phosphate buffer solution containing 5 mM $Ru(NH_3)_6^{3+}$ as redox mediator [275]. It can be seen, as expected, that the insulating Teflon® has a much lower current output relative to the un-modified GCE [275].
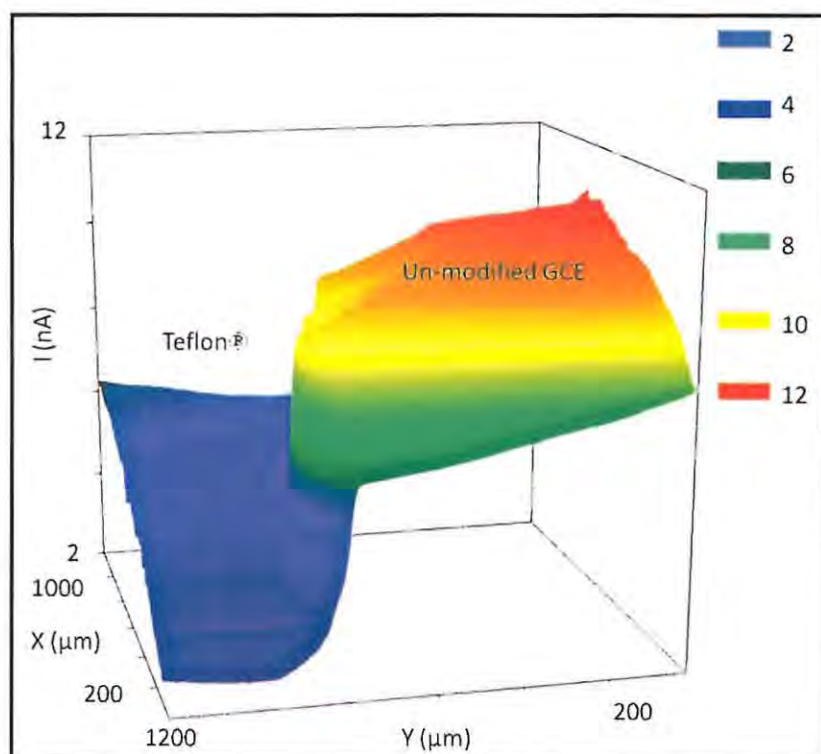
Fig. 1.22 SECM image of a GCE, a part of it covered with insulating Teflon®

Chapter 1: Introduction

1.5. Metallophthalocyanines as electrocatalysts

A good electrocatalyst must be chemically and physically stable during electron transfer, lower the electrochemical detection potential, and increase the sensitivity and selectivity for a particular analyte. Metallophthalocyanines display most of these characteristics and are therefore renowned catalysts [276-279] especially in comparison to their metal and metal oxide counterparts. Furthermore, the flexibility involved in the synthesis of MPcs, their rich redox chemistry, and their abundant coordination chemistry explains their use as catalysts [41,42,135,280] and electrochemical sensors [41,281].

Two factors primarily determine the electrochemical properties of MPcs: substituent type and central metal. The central metal is often the playmaker in electrocatalysis. The potentials at which catalytic currents are observed are closely related to the redox potentials of the central metal [21,167,168,282-287] so Pcs with low potentials should be used as electrocatalysts. Catalytic activity occurs mainly for MPcs containing electrochemically active central metals such as Fe, Co, Mn, or Cr [21,288]. Pcs containing Fe, Co, or Mn central metals have shown the best electrocatalytic activity and that is why they were used in this work.

MPc uses axial co-ordination sites between the metal and analyte for catalysis. For this to happen, the MPc metal needs an empty or half-filled 2_{a1g} orbital with proper symmetry to interact with the analyte. This is characteristic of Fe, Co, and Mn, Table 1.5. This also explains why Fe, Co, and Mn Pcs exhibit higher catalytic activity relative to other metals and why they were used in this work. ZnPc, for example, has a completely filled 2_{a1g} orbital, Table 1.5, which does not favor axial ligation to the analyte for catalytic purposes. Therefore, ZnPc is a weak catalyst with electrochemical processes occuring on the ring rather than on the central metal atom.

Table 1.5 Electronic configurations of selected MPc metal ions

$M^{II}Pc$	d-electrons	Electronic configuration
MnPc	d^5	$(b_{2g})^2(6_{eg})^2(2_{a1g})^1$
FePc	d^6	$(b_{2g})^2(6_{eg})^3(2_{a1g})^1$
CoPc	d^7	$(b_{2g})^2(6_{eg})^4(2_{a1g})^1$
ZnPc	d^{10}	$(b_{2g})^2(6_{eg})^4(2_{a1g})^2(2_{b1g})^2$

When using MPc modified electrodes the analyte is electrocatalytically oxidized or reduced and it is the resultant electrocatalytic current that is detected. Frequently, metal based redox processes mediate MPc catalytic reactions [19-21,136,289-292] but ring based catalysis has been reported [293-297]. The mechanism for the electrochemical oxidation using the metal of MPc as a catalyst is shown in Eqs. 1.8 - 1.9:

$$M^{II}Pc^{2-} \rightarrow M^{III}Pc^{2-} + e^- \qquad\qquad 1.8$$

$$M^{III}Pc^{2-} + A \rightarrow M^{II}Pc^{2-} + P \qquad\qquad 1.9$$

whilst that of ring-based catalysis is shown in Eqs. 1.10-1.11:

$$M^{II}Pc^{2-} \rightarrow M^{II}Pc^- + e^- \qquad\qquad 1.10$$

$$M^{II}Pc^- + A \rightarrow M^{II}Pc^{2-} + P \qquad\qquad 1.11$$

where A = analyte and P = product.

Metal (Eq. 1.8) or ring (Eq. 1.10) oxidation occurs first, followed by a chemical process leading to oxidation of the analyte by the reactive oxidised catalyst, whilst the original form of the catalyst is regenerated. One important way in which the catalysis proceeds is by stabilizing the transition state through electrostatics. By lowering the energy of the transition state, the catalysis allows a greater population of the starting material to attain the energy needed to overcome the transition energy and proceed to product.

MPc electrocatalysis can be observed by comparing the cyclic voltammogram of an analyte recorded by an un-modified electrode with that recorded by a MPc modified electrode. The higher current and/or a shift to a less positive peak potential displayed by the cyclic voltammogram of the MPc modified electrode compared to the un-modified electrode is an indication of electrocatalysis of the analyte, Fig. 1.23 [298].
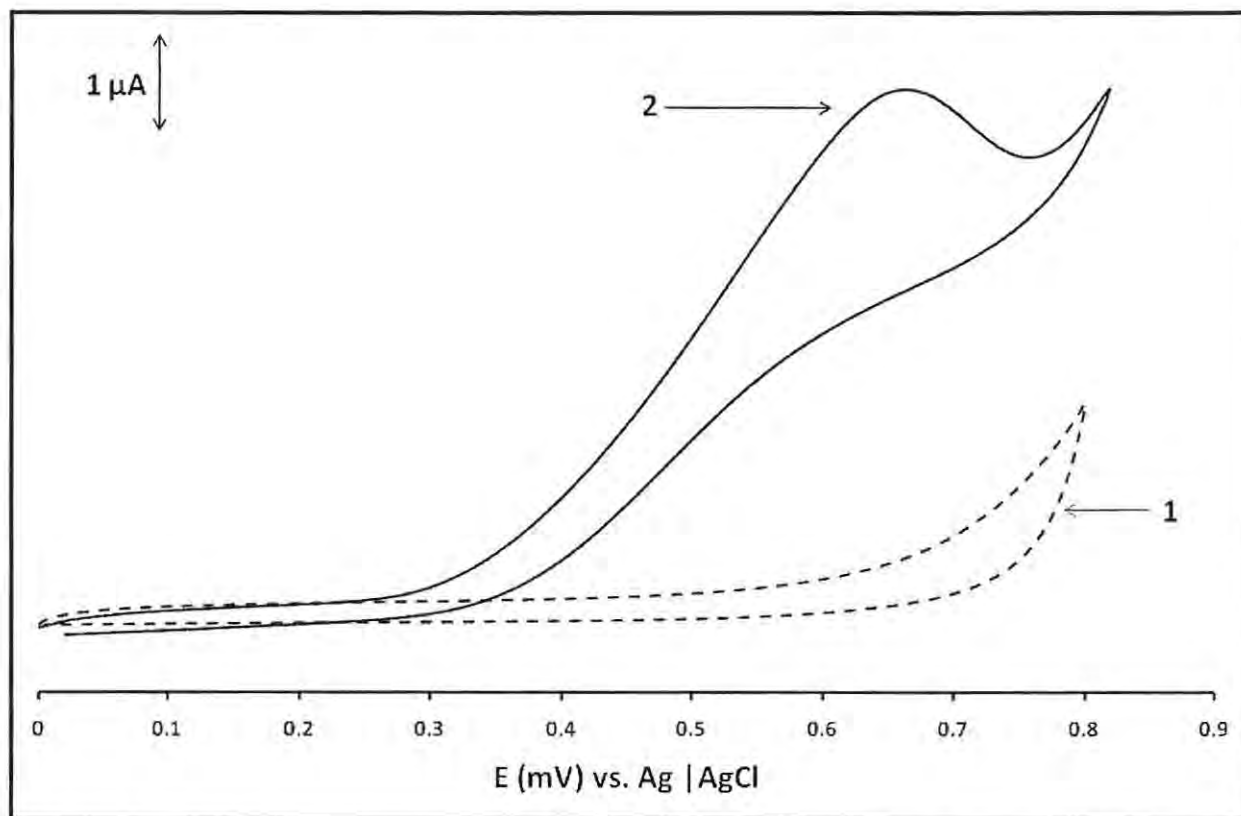
Fig. 1.23 Cyclic voltammograms of un-modified (1) and MPc modified (2) electrodes recorded in 1 μM L-cysteine in pH 4 buffer

In Fig. 1.23, MPc modified electrode electrocatalysis is shown by its higher cyclic voltammogram amperometric response in comparison to the un-modified electrode.

When MPcs act as mediator catalysts in chemically modified electrodes, as in this work, catalytic activity is determined primarily by the MPc central metal and substituent type [299]. Therefore, this work used a selection of MPc metals (Fe, Co, Mn) with a variety of substituents to create chemically modified electrodes.

1.6. Analytes employed in this work

This work used electrodes modified with various MPcs to electrochemically detect a number of analytes. The analytes, described in this section, are: melatonin; nitrite; thiocyanate; cysteine. This wide range was chosen to demonstrate the versatility of the MPc modified electrodes.

Chapter 1: Introduction

1.6.1. Melatonin

Melatonin (**33**), a hormone produced in the human brain, is vital primarily in regulating sleep patterns [300] and as an anti-oxidant [301,302]. Melatonin has therefore been used to treat insomnia and to enhance the immune system [303]. As an anti-oxidant, melatonin also protects deoxyribonucleic acid (DNA) [304,305] and is believed to aid in the treatment of diseases [306] such as human immunodeficiency virus (HIV) or acquired immune deficiency syndrome (AIDS) and other viral diseases [307], cancer [308], Parkinson's, and Alzheimer's [309]. Abnormal concentrations of melatonin enhance the risk of associated diseases [310] and so, in this work, electrochemical sensors for melatonin were sought. The principal aims are to lower the melatonin oxidation potential and to eliminate interferences in melatonin detection. This may be achieved using electrodes modified with sensitive and selective catalysts as presented in this work. Melatonin oxidation has been reported to occur weakly on un-modified glassy carbon electrodes [311], and the reported mechanism is shown in Scheme 1.7 [312].
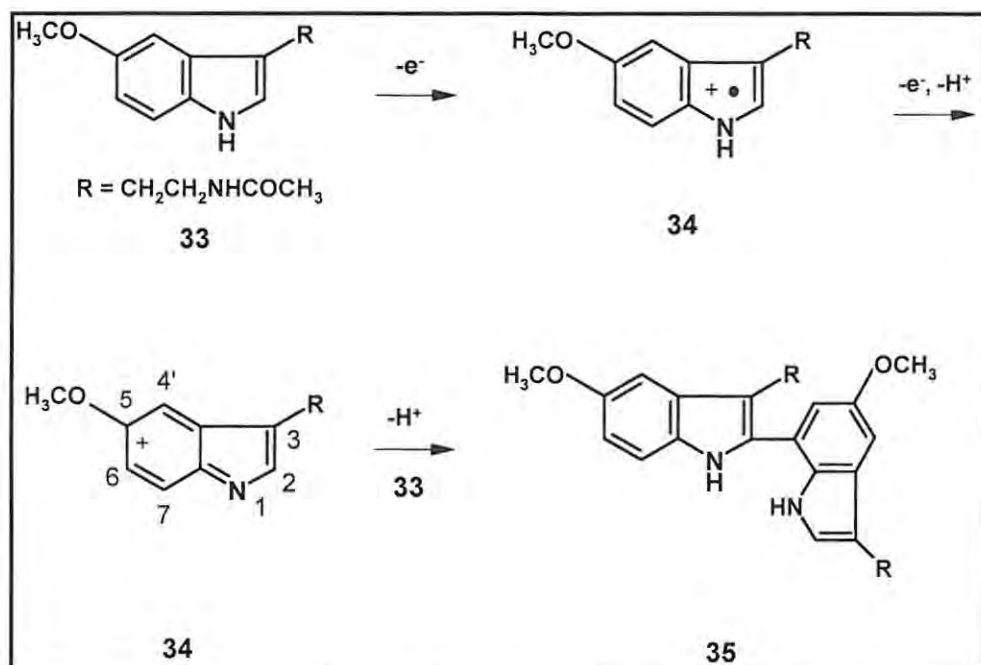
Scheme 1.7 Mechanism of melatonin (**33**) oxidation at carbon electrodes

From Scheme 1.7, the crucial electrode process involves one-electron oxidation from melatonin (**33**) to generate a radical cation (**34**). This is further oxidized by the loss of a second electron and

51

proton to give a complex (34) which is susceptible to nucleophilic attack at positions 4 and 7 [313]. Nucleophilic attack by another melatonin molecule leads to different carbon-carbon linked dimers such as complex 35, shown in Scheme 1.7 [312].

Even though detection of melatonin at carbon electrodes has been reported to be satisfactory, the electrodes are most susceptible to poisoning by melatonin oxidation products rendering them useless [312]. Although phthalocyanines are well known electrocatalysts, their use for melatonin detection has not been explored.

1.6.2. Nitrite

Nitrites are prevalent within the environment, food (nitrites are vital as food additives [314] e.g. in curing meat products) and industry (e.g. to prevent corrosion). Environmentally, nitrate (NO_3^-) is reduced by bacteria to nitrite (NO_2^-), and nitrite produces carcinogenic nitrosamines. Furthermore, excess nitrites in food have been found to be toxic and carcinogenic [315-317]. Physiologically, nitrite can oxidize haemoglobin Fe^{II} to Fe^{III} resulting in methemoglobin; this leads to a disorder called methemoglobinemia. The detection of nitrite is therefore important.

Most methods of nitrite detection, e.g. spectrophotometric [318], reported in literature are complex and slow. Electrochemical methods of nitrite detection have been limited by slow electron transfer kinetics and poisoning of electrodes leading to a decreased sensitivity and accuracy [319]. It is also necessary to lower the overpotentials of nitrite oxidation and increase the oxidation currents.

The mechanism for the electrochemical detection of nitrite using MPc modified electrodes has been proposed as [319]:

$$M^{II}Pc + NO_2^- \rightarrow [(NO_2^-)M^{II}Pc]^- \qquad 1.12$$

$$[(NO_2^-)M^{II}Pc]^- \rightarrow (NO_2^-)M^{III}Pc + e^- \qquad 1.13$$

$$(NO_2^-)M^{III}Pc \rightarrow M^{II}Pc + NO_2 \qquad 1.14$$
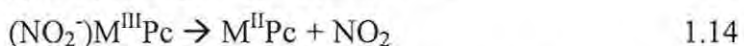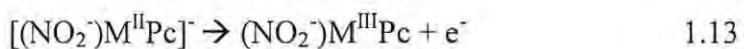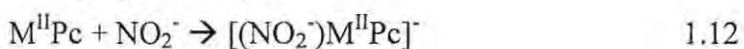
Eq. 1.12 is proposed on the basis of coordination of nitrite to MPc complexes proven spectroscopically. Eq. 1.13 is proposed because the catalytic oxidation of nitrite is within the range where $M^{III}Pcs$ exists (especially when M = Fe or Co) and is catalyzed by this couple. Eq. 1.14 represents the regeneration of the MPc catalyst and, in order to account for a total of one

Chapter 1: Introduction

electron transferred (calculated from kinetics), the most likely product is NO_2. The NO_2 species may then disproportionate to give nitrite and nitrate, Eq. 1.15:

$$2NO_2 + H_2O \rightarrow NO_2^- + NO_3^- + 2H^+ \qquad 1.15$$
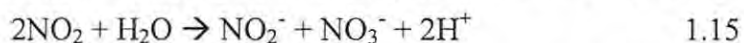
A few methods for nitrite detection by MPc SAMs (where M = Fe, Co, or Mn) have been reported, but detection potentials are undesirably high, Table 1.6 [32]. Some MPc SAMs used for nitrite detection are also unstable [320]. This work reports MPc SAMs used for improved detection of nitrite.

Table 1.6 Electrochemical detection of nitrite using MPc SAM-modified gold electrodes [32]

MPc[a]	E_p (V) vs. Ag|AgCl
FeTDMPc	0.71
CoTBMPc	0.75
CoTDMPc	0.77
MnTBMPc	0.76
MnTDMPc	0.79

[a]TD = tetrakis (dodecylmercapto); TB = tetrakis (benzylmercapto)

1.6.3. Thiocyanate

Thiocyanate (SCN⁻) is a vital biological and environmental thiol ion [321-324]. Medically, thiocyanates interfere with thyroxine synthesis in the thyroid gland thereby hindering its uptake of iodine. Thiocyanate levels may also be used to detect the extent of cigarette smoking [321,323]. Environmentally, thiocyanate levels are also used to monitor HCN from fire atmospheres. Thiocyanate is also harmful to aquatic life. The detection of thiocyanate is therefore important. Thiocyanate is rarely detected by un-modified electrodes, hence the use of CMEs in this work as thiocyanate sensors.

MPc complexes containing an electroactive central metal show good catalytic activity for the oxidation (therefore detection) of sulfur containing compounds [21,289,325]. Furthermore, the most active complexes, such as CoPc, interact much more strongly with the thiol than those exhibiting lower activity (e.g. Cr and Ni derivatives). Thiocyanate detection by Co phthalocyanine modified electrodes has been reported, Table 1.7 [23].

Table 1.7 Electrochemical detection of thiocyanate using selected Co phthalocyanine SAM-modified gold electrodes [23]

MPc^a	E$_p$ (V) vs. Ag|AgCl
CoOBTPc	0.74
CoPc(SC$_2$H$_4$OH)$_8$	0.75
CoPc(SC$_4$H$_9$)$_8$	0.78

^{a}OBTPc = octabutylthiometallophthalocyanine

The accepted mechanism for the oxidation of SCN$^-$ in alkaline media involves the formation of an adduct between the metal centre in the complex (which acts as the active site) and thiocyanate. The mechanism can be represented as [326]:

$$M^{II}Pc \rightarrow M^{III}Pc + e^- \qquad 1.16$$

$$M^{III}Pc + SCN^- \rightarrow [SCN\text{-}M^{III}Pc]^- \qquad 1.17$$

$$[SCN\text{-}M^{III}Pc]^- \rightarrow [SCN\text{-}M^{III}Pc] + e^- \qquad 1.18$$

$$[SCN\text{-}M^{III}Pc] \rightarrow M^{II}Pc + {^\bullet}SCN \qquad 1.19$$

$${^\bullet}SCN + {^\bullet}SCN \rightarrow (SCN)_2 \qquad 1.20$$

$$(SCN)_2 + H_2O \rightarrow \text{reaction products} \qquad 1.21$$
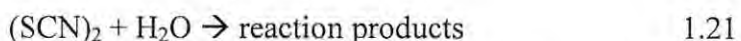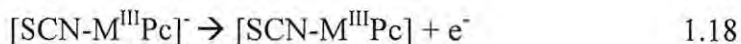
Eq. 1.16 represents the oxidation of M^{II}Pc to M^{III}Pc. This is followed by axial ligation of the M^{III}Pc to SCN$^-$, Eq. 1.17. Eq. 1.18 is the rate determining step. Then the ligated complex dismantles regenerating M^{II}Pc and a SCN radical, Eq. 1.19. The SCN radical quickly combines with another SCN radical forming (SCN)$_2$, Eq. 1.20. The (SCN)$_2$ may combine with H$_2$O to form reaction products, Eq. 1.21.

1.6.4. Cysteine

The structure of cysteine (**36**), an amino acid thiol, is shown in Fig. 1.24.

Chapter 1: Introduction
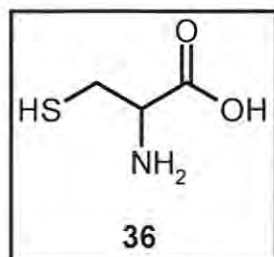
Fig. 1.24 Cysteine structure

Cysteine plays vital roles as a substrate for protein and antioxidant (glutathione) synthesis [327]. Cysteine is also a precursor in the food, pharmaceutical, and personal care industries. Cysteine is believed to aid in the remedy of hangover symptoms by counteracting the poisonous effects of acetaldehyde [328], a major by-product of alcohol metabolism. Cysteine is required by sheep in order to produce wool and is an essential amino acid which must be taken in as food from grass. Therefore, the detection of L-cysteine is of both biological and environmental importance.

Some Pcs and related macrocycles have been used in the electrochemical sensoring of cysteine [138,160,279,329-332]. The mechanism proposed for the electrochemical sensoring of cysteine by Pcs in basic media is as shown by Eqs. 1.22 - 1.25 [160,333]:

$$RSH + OH^- \leftrightarrow RS^- + H_2O \qquad\qquad 1.22$$

$$M^{II}Pc + RS^- \leftrightarrow [R\text{-}S \bullet\bullet\bullet M^IPc]^- \qquad\qquad 1.23$$

$$[R\text{-}S \bullet\bullet\bullet M^IPc]^- \rightarrow M^{II}Pc + RS^\bullet + e^- \qquad\qquad 1.24$$

$$RS^\bullet + RS^\bullet \rightarrow RS\text{-}SR \qquad\qquad 1.25$$
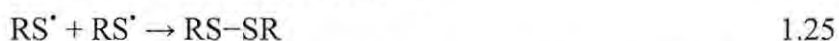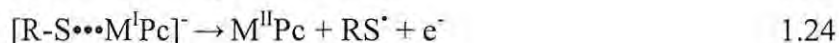
From the mechanism, the thiolate initially dissociates in solution to form the RS⁻ moiety, Eq. 1.22. An important step is Eq. 1.23, which involves a partial reduction of the metal centre in the catalyst and partial oxidation of the bound thiol molecule. The redox potential can be used as a parameter of reactivity because reduction of the metal centre is involved (Eq. 1.23) [21,135,325]. Therefore, the formal potential is related to the reactivity of the metal centre towards the thiol through adduct formation and to the thermodynamics of this process (Eq. 1.23). The catalytic oxidation potentials of thiols can be related to the pH of the media: the $M^{III}Pc/M^{II}Pc$ couple was found to be active in acid media, whilst the $M^{II}Pc/M^IPc$ couple was active in basic media [283,333]. Eq. 1.24 is the rate determining step whilst Eq. 1.25 is fast and irreversible.

Chapter 1: Introduction

The redox potential of the MPc can be 'tuned' to achieve best electrochemical sensoring of thiols (like cysteine) by varying the MPc design (Pc metal and substituents) [325,333]. This work therefore uses a wide variety of MPcs to obtain cysteine sensors. The nature of the metal plays an important role in determining the catalytic activity. Fe and Co complexes show the best electrocatalytic activity [334-343] and that is why they were used in this work. Mn complexes also display good activity, in some cases comparable to those of iron [344], but their activity has been found to diminish with time [345,346].

Electrochemical detection of cysteine on un-modified electrodes has been limited by factors such as high overpotentials and low detection limits [347-349]. Modified electrodes, including those modified using SAMs, have been found to enhance the electrochemical oxidation of cysteine. Reported electrochemical detection parameters of cysteine using selected MPc modified electrodes are given in Table 1.8 [23,33,34,160,205,350-352].

Table 1.8 Electrochemical detection of cysteine using selected MPc modified electrodes

MPc[a]	Electrode[b]	Modification method	E_p (V) vs. Ag|AgCl	Reference
FePc	4-MPy-Au	SAM	0.185	352
FePc(SO$_3$)$_4$	Graphite	Adsorption/drip dry	0.195	160
CoPc(COCl)$_4$	2-ME-Au	SAM	0.405,0.675	205
CoPc(SC$_4$H$_9$)$_8$	Au	SAM	0.465	34
CoTEThPc	Au	SAM	0.535,0.775	351
CoPc(SC$_2$H$_4$OH)$_8$	Au	SAM	0.545	23
FePc(SC$_4$H$_9$)$_8$	Au	SAM	0.38	33
FePc(SC$_2$H$_4$OH)$_8$	Au	SAM	0.43	23
MnPc	4-MPy-Au	SAM	0.205	352
MnPc(COOH)$_4$	ME-Au	SAM	0.52	350

[a]TEThPc = tetraethoxythiophene phthalocyanine

[b]4-MPy-Au = pre-formed SAM on gold using 4-mercaptopyridine, 2-ME-Au = pre-formed SAM on gold using 2-mercaptoethanol, ME-Au = pre-formed SAM on gold using mercaptoethanol

Chapter 1: Introduction

Even though some overpotentials for cysteine electrochemical detection are lower for the FePc complexes compared to the corresponding CoPcs (Table 1.8), the latter were found to be less susceptible to fouling [23].

1.7. Superoxide dismutation studies

Reactive oxygen species, such as superoxide ($O_2^{\cdot-}$, which is very selective in its reactivity and therefore possibly most damaging [38]), hydrogen peroxide (H_2O_2), and hydroxyl radicals ($^\cdot OH$) are created by several biological pathways [353]. Damage caused by these active oxygen species in aerobic organisms may cause DNA strand breakage, destruction of membrane lipids, and inactivation of enzymes, amongst other pathological conditions [39,354-360]. Defence systems derived from enzymatic and non-enzymatic antioxidants in living organisms can minimize the harmful effects of oxygen free radicals. Vital antioxidant systems include superoxide dismutase (SOD, for $O_2^{\cdot-}$), catalase (for H_2O_2), and peroxidase (for peroxides) [355].

This work used MPcs as superoxide dismutase (SOD) mimics. This section describes SODs and their related studies.

1.7.1. Superoxide dismutase mechanism

Superoxide dismutases (SODs) are enzymes, containing metal-active sites, that catalyze the removal of the superoxide radical. Normally, they contain either copper/zinc (CuZnSOD, usually tetrameric), manganese (MnSOD, usually homodimeric), iron (FeSOD, usually homodimeric), or nickel (NiSOD) in the active site of each subunit [38,39]. They provide protection against oxidative stress in physiological systems by specifically catalyzing the dismutation of the superoxide radical to hydrogen peroxide and molecular oxygen via a catalytic cycle of alternating reduction and oxidation of the active-site metal in the protein, such as in Eqs. 1.26 - 1.27 for MnSOD:

$$O_2^{\cdot-} + Mn^{III}SOD^+ \rightarrow O_2 + Mn^{II}SOD \qquad\qquad 1.26$$
$$O_2^{\cdot-} + Mn^{II}SOD + 2H^+ \rightarrow H_2O_2 + Mn^{III}SOD \qquad\qquad 1.27$$
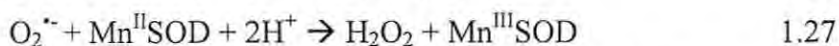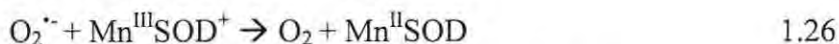
The overall redox reaction for the dismutation of superoxide by SOD is thus Eq. 1.28:

$$2O_2^{\cdot-} + 2H^+ \rightarrow O_2 + H_2O_2 \qquad\qquad 1.28$$

The oxidation of $O_2^{\cdot-}$ (Eq. 1.26) is slower than its reduction and therefore is considered to be the rate-limiting step [361].

Chapter 1: Introduction

Mitochondria are the major source of superoxide in the cell under physiological conditions. Approximately 1 - 2 % of the total oxygen uptake is estimated to be used to generate either superoxide or hydrogen peroxide [362]. Other sources of superoxide include xanthine oxidase and nicotinamide adenine dinucleotide phosphate (NADPH) oxidase, which cause an acute elevation of superoxide formation in the extracellular compartment [363]. Nitric oxide synthase (NOS) has also been proposed as an intracellular source of superoxide under pathological conditions [364].

Rate constants of CuZnSOD, MnSOD, and FeSOD are pH dependent and in the region of 10^8 - 10^9 $M^{-1}.s^{-1}$ [365-369].

1.7.2. Superoxide dismutase structure

SOD and its enzymatic activity were discovered by various groups in the 20th century [370-378]. The structure of human mitochondrial MnSOD (37) is shown in Fig. 1.25 [379].
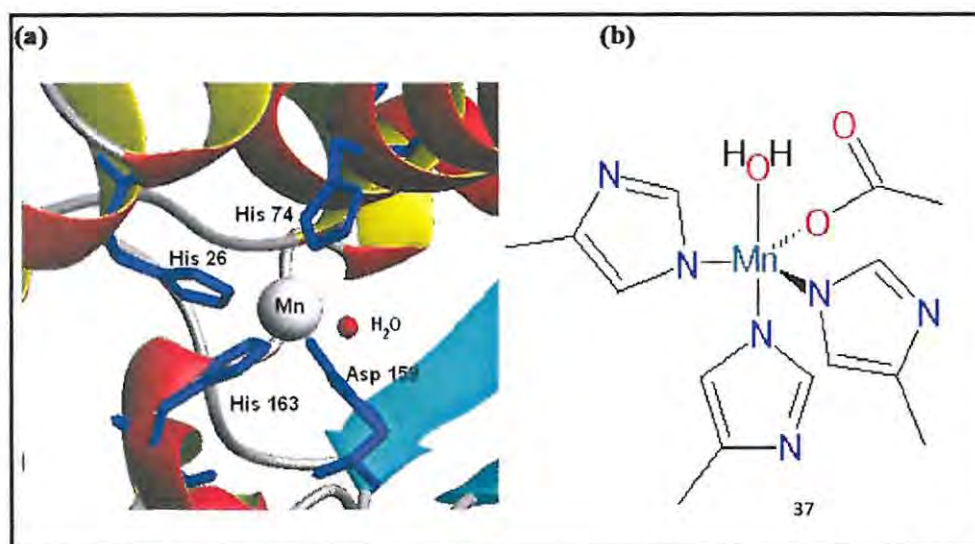
Fig. 1.25 Molecular model (a) and chemical structure (b) of active site of human mitochondrial MnSOD. His = histidine, Asp = aspartate

The human mitochondrial MnSOD, Fig. 1.25, is a homotetramer whose active metal (Mn) ion site is attached to the following ligands: either a water molecule or a hydroxyl ligand, depending on the oxidation state of manganese (III/II)), three histidine side chains, and an aspartate side chain [379].

Chapter 1: Introduction

The kinetics and mechanisms of SOD activity have been characterized using various techniques [380-384]. SOD has a net negative charge at physiological pH which varies with the species. However, the deep and active narrow channel above the catalytic binding site shows a highly positive charge which is able to electrostatically attract and guide negatively charged $O_2^{\cdot-}$ to reach the catalytic metal at the bottom of the active channel [385].

1.7.3. Superoxide dismutase mimics

There is a pharmaceutical requirement for molecules that could scavenge or, even better, catalytically dismutate superoxide [386-396] i.e. SOD mimics.

The design of low molecular mass SOD mimics requires greater understanding of the effect of the metal environment on the SOD-like activity. A transition metal complex must meet the following criteria to be an effective SOD mimic:

- have low molecular mass and high cell permeability. Because native SOD enzymes cannot penetrate the cell membranes, low molecular mass complexes that can be handled endogenously or exogenously (and therefore penetrate the cell membranes) are more ideal as SOD mimics

- be water soluble

- be stable

- be substrate ($O_2^{\cdot-}$) specific

- have a reduction potential between approximately -0.4 V (the standard reduction potential of the $O_2/O_2^{\cdot-}$ couple) and +0.65 V (the standard reduction potential of the $H_2O_2/O_2^{\cdot-}$ couple) so that catalysis can occur efficiently [361,397-401]. As an example, the catalysis of superoxide dismutation by Mn complexes is a redox process involving both Mn^{II} and Mn^{III} oxidation states (Eqs. 1.26 and 1.27). To make this redox catalysis efficient, the redox potential of the $Mn^{III/II}$ couple should be, as encountered in SODs, between the potential of the two couples $O_2/O_2^{\cdot-}$ and $H_2O_2/O_2^{\cdot-}$, that is (at pH 7) -0.4 V and +0.65 V vs. saturated calomel electrode (SCE), respectively. Theoretically, the closer the potential of the two couples, the faster the reaction between them. Therefore, the value, optimizing the kinetics of both oxidation and reduction, is the midway potential, i.e. +0.12 V vs. SCE

- be non-toxic

- possess a catalytic rate constant between 10^8 - 10^9 $M^{-1}.s^{-1}$ [397]

In the field of superoxide dismutase mimics, copper, iron, manganese, and cobalt complexes have been described [361,367,381,395,396,402-425]. Mn is the least toxic of these metal ions, is stable, and is well characterized [404-407,423], hence the use of Mn SOD mimics in this work. Also, manganese was chosen as the metal centre due to its biocompatibility, while the cyclic structure of the ligand offers high metal-ligand stability [419]. This work investigates the use of phthalocyanines as SOD mimics, especially as they present structural similarities with porphyrins which have been successfully used as SOD mimics [361,409,410,413,418,426,427].

1.7.4. The McCord-Fridovich assay

The McCord-Fridovich assay, used in this work, is a technique for the evaluation of superoxide. Common assays for the detection of superoxide are based on the reduction of cytochrome c (Fe^{III}) to generate cytochrome c (Fe^{II}), which is analyzed using UV-visible spectrophotometry [428,429]. The McCord-Fridovich assay is a test developed for superoxide monitoring [361,409,410,413,418,419,421]. Reactivity towards the superoxide can be investigated in an aqueous buffer (pH = 7.8) using the xanthine-xanthine oxidase system to produce the superoxide. The McCord-Fridovich test is based on the kinetic competition for the superoxide reduction between the putative superoxide scavenger and cytochrome c (Fe^{III}) [369,371,388,408,430,431]. The concentration of superoxide is based on the spectrophotometric measurement of the amount of cytochrome c (Fe^{III}) reduced by $O_2^{\cdot-}$, Eq. 1.29:

Cytochrome c (Fe^{III}) + $O_2^{\cdot-}$ → cytochrome c (Fe^{II}) + O_2 1.29
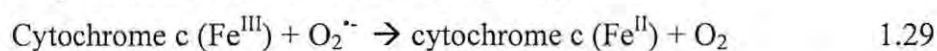
This reduction is monitored spectrophotometrically at 550 nm because that is where cytochrome c (Fe^{II}) exhibits a strong absorbance.

An example of such a study, where the evolution of the absorbance at 550 nm of cytochrome c (Fe^{III}) + xanthine after the injection of xanthine oxidase (XOD) and then superoxide dismutase (SOD), is shown in Fig. 1.26 [432].
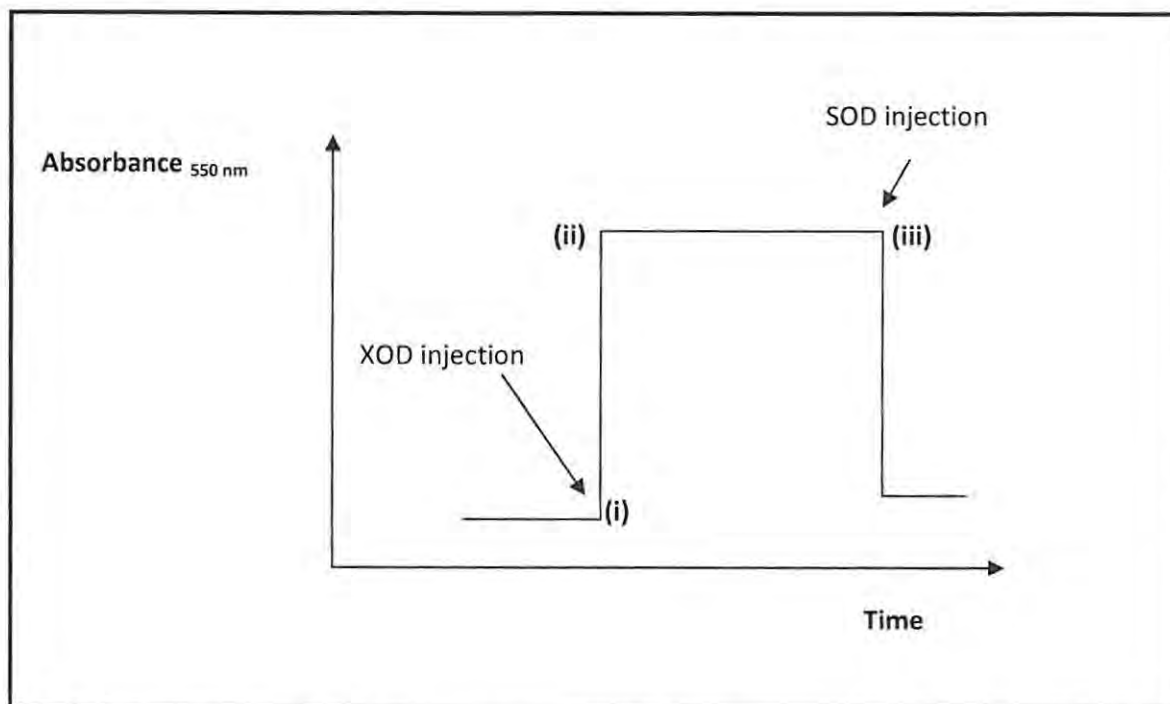
Fig. 1.26 Absorbance at 550 nm of cytochrome c (Fe^{III}) + xanthine after the injection of XOD and then SOD

Fig. 1.26 shows the change in the absorbance at 550 nm of cytochrome c (Fe^{III}) + xanthine after the injection of xanthine oxidase (XOD) (i, forming Fe^{II} by Eq. 1.29) and then SOD (iii, removing $O_2^{\cdot -}$ so no Fe^{II} is produced). The measured absorbance increases and reaches a plateau (ii - iii, Fig. 1.26) due to the kinetic equilibrium between the formation of superoxide by the enzymatic path and the degradation of superoxide by its natural disproportionation. The specificity of SOD is also directly tested on the cytochrome c (Fe^{III}) reduction as shown, where, after the SOD injection, there is a dramatic decrease in the absorbance (iii, Fig. 1.26), i.e. superoxide is being dismutated by SOD and is no longer 'available' for the cytochrome c (Fe^{III}) reduction (Eq. 1.29). It should be noted that cytochrome c (Fe^{III}) is a non-specific electron acceptor.

In summary, the McCord-Fridovich assay is amongst the most developed test for superoxide monitoring [361,409,410,413,418,419,421,433]. It is based on a kinetic competition for superoxide reduction between the SOD mimic and cytochrome c (Fe^{III}) [369,430]. In this assay, the xanthine-xanthine oxidase reaction is used to produce the superoxide, which then reduces cytochrome c (Fe^{III}) to cytochrome c (Fe^{II}). The latter is then measured using UV-visible

spectrophotometry at 550 nm. If SOD is added, the superoxide produced by the xanthine-xanthine oxidase reaction reduces the SOD, and not the cytochrome c (Fe^{II}), and hence there is less cytochrome c (Fe^{II}) as evidenced by the decrease in absorbance at 550 nm compared to that in the absence of SOD.

Other superoxide evaluation techniques, not employed in this work, include electrochemical [432,434-452], chemiluminescence [450,451] and electron spin (paramagnetic) resonance (ESR or EPR) [452].

This work used the McCord-Fridovich assay to determine the SOD activity of MnPcs and to compare their activity to a commercially available SOD mimic. The prepared putative Mn SOD mimics used in this work are: **6c**; **6d**; **6e**; **8b**; **8d**; **8e**; **8f**, while manganese (III) tetrakis (1-methyl-4-pyridyl)porphyrin (**38**) is a commercially available SOD mimic, Fig. 1.27.

38
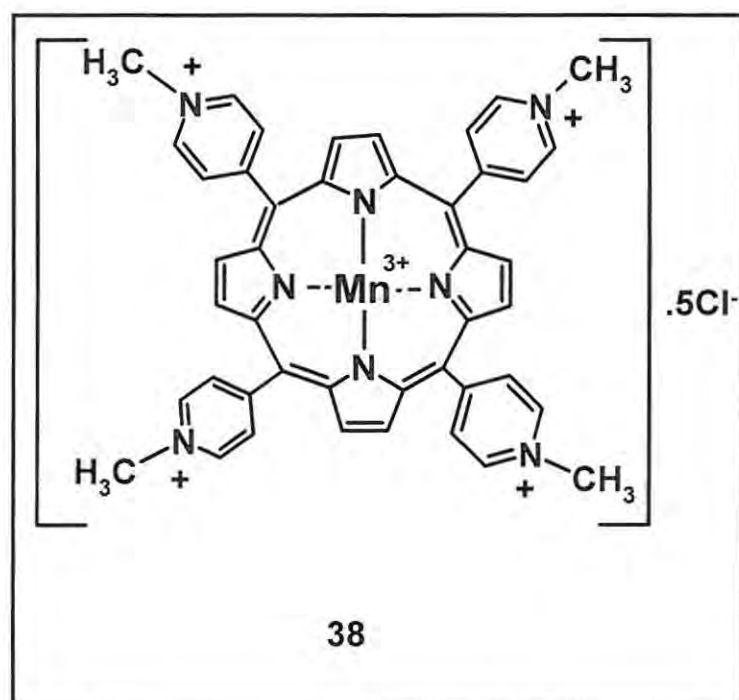
Fig. 1.27 Manganese (III) tetrakis (1-methyl-4-pyridyl)porphyrin (**38**)

Chapter 1: Introduction

1.8. Thesis aims

The principal aim of this work is to use phthalocyanines as efficient electrochemical sensors and as superoxide dismutase mimics. This includes:

- synthesis of Fe, Co, and Mn octa- and tetra-substituted phthalocyanines
- characterization of these phthalocyanines using: UV-visible spectrophotometry, infra-red spectroscopy, spectroelectrochemistry, and cyclic voltammtetry
- use of these phthalocyanines in the development of chemically modified electrodes by means of grafting (**7a**: CoPc(COOH)$_4$), adsorption (**5g** (CoPc), **7a** (CoPc(COOH)$_4$), **10a** (CoPc(COOH)$_8$)), and self assembled monolayer (**6c** (OH)MnPc(SPh)$_4$, **6d** (α-(OH)MnTMPyPc), **6e** (α-Q-(OH)MnTMPyPc), **8d** (β-(OH)MnTMPyPc), **8e** (β-Q-(OH)MnTMPyPc), **9b** (FePc(SCH$_2$Ph)$_8$), **10b** (CoPc(SCH$_2$Ph)$_8$)) techniques. The chemically modified electrodes are characterized using: voltammetry, impedance, atomic force microscopy, and scanning electrochemical microscopy
- use of th e chemically modified electrodes as electrochemical sensors for m elatonin, nitrite, thiocyanate, and cysteine
- use of manganese phthalocyanines (**6c** (OH)MnPc(SPh)$_4$, **6d** (α-(OH)MnTMPyPc), **6e** (α-Q-(OH)MnTMPyPc), **8b** ((OH)MnPc(SCH$_2$Ph)$_4$), **8d** (β-(OH)MnTMPyPc), **8e** (β-Q-(OH)MnTMPyPc), **8f** ((Na)$_4$(OH)MnPc(SO$_3$)$_4$)) as novel superoxide dismutase mimics.

CHAPTER 2: EXPERIMENTAL

2.1. Materials

2.1.1. Synthesis materials

Anhydrous manganese (II) acetate, manganese (II) chloride, 4,5-dichlorophthalic acid, sodium hydride, benzene-1,2,4,5-tetracarboxylic dianhydride, K_2CO_3, and urea were purchased from Aldrich. 4-sulfophthalic acid was purchased from Sigma. Iron (II) chloride hexahydrate, ammonium molybdate, ammonium chloride, and cobaltous chloride hexahydrate were procured from Saarchem. Benzyl mercaptan was purchased from Fluka. Nitrogen gas was purchased from Afrox.

2.1.2. Solvents

Acetic anhydride was obtained from Merck. Thionyl chloride, acetonitrile, and 1,8-diazabicyclo-[5.4.0]-undec-7-ene (DBU) were purchased from Aldrich. Petroleum ether (bp 40 - 60 °C), formamide, ammonium hydroxide (25 and 35% solutions), dimethylformamide (DMF), dimethylsulfoxide (DMSO), tetrahydofuran (THF), glacial acetic acid, H_2SO_4, $HClO_4$, H_3PO_4, $HClO_4$, and nitric acid (55%) were procured from Saarchem. Absolute methanol, chloroform, *n*-hexane, ethyl acetate, and acetone were provided by Protea Chemicals and distilled before use. Ethanol, also distilled before use, was obtained from NCP Alcohols. 1-Pentanol and pH 12 buffer solution were purchased from Fluka. Ethylene glycol was obtained from NT Laboratory. Deionised water was obtained from a Millipore-Q-system.

2.1.3. Electrochemical materials

Tetrabutylammonium tetrafluoroborate (TBABF₄) was purchased from Aldrich. Buffer (pH 4 and 7) tablets, sodium sulfate anhydrous, copper (II) sulfate, potassium ferricyanide ($K_3Fe(CN)_6$), NaOH, NaH_2PO_4, $Fe(NH_4)SO_4$, KCl, ascorbic acid, and KOH pellets were procured from Saarchem. Tetrabut ylammonium perchlorate (TBAP) was recrystallized from ethanol before use. Na_2HPO_4 was purchased from PAL Chemicals. 1-Ethyl-3-(3-dimethylaminopropyl)-carbodiimide (EDC), *N*-hydroxysuccinimide (NHS), and DL-tryptophan were purchased from Fluka. KH_2PO_4 was purchased from Associated Chemical Enterprises. Potassium thiocyanate was purchased from Riedel-de Haën. Sodium nitrite was purchased from BDH Chemical Co. (UK). L-cysteine, melatonin (N-acetyl-5-methoxytryptamine), and 4-

Chapter 2: Experimental

nitrobenzenediazonium tetrafluoroborate were purchased from Sigma. Phosphate buffer saline solution (PBS, 1×10^{-2} M, pH 7.4) was employed for melatonin studies. Melatonin capsules, each containing 3 mg melatonin, were procured from Holistix Products and Services and were dissolved in PBS (pH 7.4), filtered, and the solution containing melatonin was then analyzed.

2.1.4. Superoxide dismutase materials

Xanthine, xanthine oxidase (from bovine milk), cytochrome c (Fe^{III}) (practical grade from bovine heart), phorbol 12-myristate 13-acetate (PMA), superoxide dismutase (SOD bovine, 4140 units.mg^{-1} protein), 3-(4,5-dimethylthiazol-2-yl)-2,5-diphenyltetrazolium bromide (MTT), RPMI 1640 (RPMI = Roswell Park Memorial Institute), fetal bovine serum (FBS), sodium dodecyl sulfate (SDS) and dihydroethidium (DHE) were purchased from Sigma. Human leukemia cells (HL-60 cells, CCL240) were from The American Type Culture Collection (ATCC). Manganese (III) tetrakis (1-methyl-4-pyridyl)porphyrin (**38**) was purchased from Alexis Biochemicals and used as received.

2.2. Equipment

IR spectra (in KBr pellets) were recorded on a Perkin-Elmer Spectrum 2000 FTIR spectrometer or a Bio-Rad FTS 175C FT-IR spectrometer.

^{1}H-nuclear magnetic resonance (NMR) spectra were recorded in CDCl$_3$ or DMSO-d$_6$ solutions using a Varian 500 MHz or Bruker EMX 400 NMR (400 MHz) spectrometer.

Elemental analyses were obtained with a Thermo Finnigan Flash 1112 Instrument.

MALDI-TOF spectra were obtained with Perspective Biosystems Voyager DE-PRO Biospectrometry Workstation possessing delayed extraction at the University of Cape Town (South Africa).

UV-visible spectra were recorded on a Shimadzu 2001 UV-Vis spectrophotometer or on a Cary 500 UV-visible/NIR spectrophotometer. Spectroelectrochemical data were recorded using an optically transparent thin-layer electrochemical (OTTLE) cell connected to a BioAnalytical System (BAS) 27 voltammogram.

An AUTOLAB PGSTAT30 potential/galvanostat, connected to a computer and controlled by GPES and FRA software, was used for acquisition and analysis of impedance data. Cyclic voltammetry studies were recorded using a Bio-Analytical System (BAS) B/W 100

Chapter 2: Experimental

Electrochemical Workstation. All impedance measurements were conducted at 100 mV in potassium ferricyanide solutions of pH 8.26.

SECM experiments were done using homemade 10 or 25 μm Pt ultramicroelectrodes.

Atomic force microscopy (AFM) images were recorded using a CP-11 Scanning Probe Microscope from Veeco Instruments (Carl Zeiss, South Africa); a gold-coated crystal (Q-Sense®, Sweden) was used for the formation of SAM.

Raman data of SAMs on gold was recorded using a Bruker RAM II FT-Raman spectrometer by excitation with a Nd:YAG laser source (1064 nm). Estimation of the area of the MPc molecules was done using GaussView, Version 4.1.

2.3. Synthesis

2.3.1. Synthesis of substituted phthalonitriles

Synthesis of phthalonitriles: dichlorophthalonitrile [69], 3-nitrophthalonitrile [76] and 4-nitrophthalonitrile [80] is routine and the complexes may be purchased, hence their synthetic details are not repeated here. 1,2-Bis(S-benzylthio)-4,5-dicyanobenzene (**39**) was synthesized according to the literature [453]. Phenylthiophthalonitrile (**41**) has been synthesized before [30].

2.3.1.1. Synthesis of complex 39 (Scheme 3.1)

Complex **31** was synthesized according to the literature [69]; then complex **39** was synthesized as follows. To a suspension of sodium hydride (3 g, 124 mmol) in dry DMF (80 ml), benzyl mercaptan (15 ml) was added under N_2 while keeping the temperature between 10 and 15 °C. The mixture was brought to room temperature and **31** (12 g, 61 mmol) was then added in small portions. The reaction mixture was left overnight under N_2 while stirring. The product was collected by filtration and recrystallized from $CHCl_3$/MeOH. Compound **39** was dissolved in MeOH and heated under reflux, then $CHCl_3$ was added to the mixture and heating under reflux continued. This procedure was repeated once. Finally the product was recrystallized from methanol to give **39** as a pale yellow powder, which was dried in vacuum. Yield: 39 %. IR [(KBr) v_{max}/cm^{-1}]: 3033(Ar-CH), 2227(C≡N), 1561(C=C). ^{1}H NMR (DMSO-d$_6$) [δ (ppm)]: 8.20 (s, 2 H, benzyl), 7.30 (m, 10 H, phenyl), 4.30 (s, 4 H, methylene).

2.3.2. Synthesis of arylthio substituted phthalocyanines

Complexes **6 d, e** and **8 d, e** were available from a previous study [31].

2.3.2.1. Synthesis of FePc(SCH$_2$Ph)$_8$ (9b, Scheme 3.2)

A mixture of **39** (1.52 g, 4 mmol), FeCl$_2$.4H$_2$O (0.21 g, 1 mmol), and urea (0.386 g, 6.25 mmol) was heated and stirred at 150 °C for 90 minutes. After cooling to room temperature, the reaction mixture was heated with hot ethanol and filtered. The dark green crude product was purified by treating with CHCl$_3$ followed by Soxhlet extraction with ethanol, methanol, and acetone. Complex **9b** was then treated with hot methanol, ethanol, and acetone then dried in vacuum. Yield: 55 %. IR [(KBr) v_{max}/cm^{-1}]: 3676 (Ar-CH), 1653 (C=C), 694 (C-S-C) . ^{1}H NMR (DMSO-d$_6$) [δ (ppm)]: 8.00 (s, 8 H, Pc), 7.50 (m, 40 H, phenyl), 4.50 (m, 16 H, methylene). UV-visible (DMF): λ_{max}, nm (log ε): 359(4.80), 451(4.33), 623(4.29), 690(4.80). MS (MALDI-TOF), C$_{88}$H$_{64}$FeN$_8$S$_8$: m/z, calcd. for [FePc(SCH$_2$Ph)$_8$ + H]$^+$ 1546.8, found 1546.4.

2.3.2.2. Synthesis of CoPc(SCH$_2$Ph)$_8$ (10b, Scheme 3.2)

A mixture of **39** (2.5 g, 6.7 mmol), anhydrous CoCl$_2$ (0.22 g, 1.7 mmol), and ethylene glycol (13 ml) was heated and stirred at 200 °C for 4 hours under N$_2$. After cooling to room temperature, the reaction mixture was treated with ethanol to precipitate the dark green product and then filtered. The precipitate **10b** was intensively washed with acetone and hexane. Yield: 55 %. IR [(KBr) v_{max}/cm^{-1}]: 3852 (Ar-CH), 1561 (C=C), 687 (C-S-C). ^{1}H NMR (DMSO-d$_6$) [δ (ppm)]: 8.20 (s, 8 H, Pc), 7.20 (m, 40 H, phenyl), 4.60 (m, 16 H, methylene). UV-visible (DMF): λ_{max}, nm(log ε): 327(4.61), 619(4.31), 686(4.45). MS (MALDI-TOF), C$_{88}$H$_{64}$CoN$_8$S$_8$: m/z, calcd. for [CoPc(SCH$_2$Ph)$_8$ + H]$^+$ 1549.8, found 1549.7.

2.3.2.3. Synthesis of (OH)MnPc(SPh)$_4$ (6c, Scheme 3.4)

The synthesis of metal 1,(4)-(tetraphenylthiophthalocyaninato) (MPc(SPh)$_4$) has been reported before [30]. Briefly, **41** (0.7 g, 4 mmol) was mixed with 0.182 g (1.05 mmol) anhydrous manganese (II) acetate and 6 mL ethylene glycol then refluxed for 5 hours at 200 °C under nitrogen atmosphere. The mixture was allowed to cool to room temperature and then excess methanol was added to precipitate out the crude reddish brown solid product which was then

treated in a Soxhlet extraction apparatus with ethanol for 48 hours. The product was purified using silica gel column chromatography eluting twice with chloroform and tetrahydrofuran. The pure complex was a deep red solid. Yield: 71 %. UV-visible (DMF): λ_{max}, nm(log ε): 360(2.37), 511(3.36), 681(4.47), 764(5.02). IR [(KBr) ν_{max}/cm^{-1}]: 1382 (C=C), 1106 (Mn-OH), 681(C-S-C). Anal. Calcd. For (OH)$C_{56}H_{32}N_8S_4$Mn.7(C_4H_8O).$CHCl_3$: C, 62.94; H, 5.53; N, 6.83; S, 7.81 %. Found: C, 63.68; H, 5.30; N, 6.94; S, 7.74.

2.3.2.4. Synthesis of (OH)MnPc(SCH$_2$Ph)$_4$ (8b, Scheme 3.5)

Synthesis of **8b** has been reported [27] but was synthesized again in this work for superoxide dismutase studies. 3-Benzylthiophthalonitrile (**40**, 0.7 g, 4 mmol) was mixed with 0.182 g (1.05 mmol) anhydrous manganese (II) acetate and 6 mL ethylene glycol (anhydrous) then refluxed for 5 hours at 200 °C under nitrogen atmosphere. The mixture was allowed to cool to room temperature when excess methanol was added to precipitate out the crude reddish brown solid product which was then treated in a Soxhlet extraction apparatus with ethanol for 48 hours. The product was purified using silica gel column chromatography eluting twice with chloroform and tetrahydrofuran. The pure complex was a deep red solid. Yield: 80 %. UV-visible (DMF): λ_{max}, nm(log ε): 360(4.09), 507(3.14), 709(3.36), 763(3.98). IR [(KBr) ν_{max}/cm^{-1}]: 1382 (C=C), 832 (Mn-OH), 625 (C-S-C). Anal. Calcd. For (OH)$C_{60}H_{40}N_8S_4$Mn.9(C_4H_8O): C, 66.95; H, 6.61; N, 6.51; S, 7.45 %. Found: C, 67.44; H, 7.062; N, 7.06; S, 6.762.

2.3.3. Synthesis of cobalt octacarboxy (CoPc(COOH)$_8$) (10a, Scheme 3.6)

The cobalt complexes **5g**, **7a**, and **10a** were synthesized according to reported procedures [25,26,454]. Complexes **5g** and **7a** were available in our laboratory. The synthesis of **10a**, which not available in our laboratory, was done and shall be described.

Benzene-1,2,4,5-tetracarboxylic dianhydride (**42**, 2.50 g, 11.5 mmol), 13.0 g (0.22 mol) of urea, 3.05 g (23.5 mmol) of $CoCl_2$, and 100 μL DBU was heated to 250 °C until the reaction mixture fused. The product was washed with water, acetone, and 6 M HCl. After drying, the solid obtained was hydrolyzed. The crude product (1.6 g), 1.6 g KOH, and 90 mL of water were then heated for 8 hours at 100 °C. The mixture was diluted with 200 mL water then filtered. The filtrate was acidified to pH 2 with concentrated HCl. The product, which precipitated as a blue

solid, was separated from the solution using centrifugation. The solid was washed with water three times then dried.

Yield: 76.5 %. UV-visible (DMF): λ_{max}, nm(log ε): 350(4.50), 620(4.28), 689(4.43). IR [(KBr) ν_{max}/cm^{-1}]: 1650 (C=C).

2.3.4. Synthesis of $(Na)_4(OH)MnPc(SO_3)_4$ (8f, Scheme 3.7)

Synthesis of $(Na)_4(OH)MnPc(SO_3)_4$ (8f) was prepared according to reported procedures of similar compounds [28]. A mixture of 4-sulfophthalic acid (4 g, 8.1 mmol), urea (1.5 g, 24.3 mmol), manganese (II) chloride (0.81 g, 4.1 mmol), ammonium chloride (1.56 g, 29 mmol), and ammonium molybdate (0.17 g, 0.138 mmol) was placed in a microwave oven and irradiated at 1000 W for 5 minutes. The completeness of the reaction was determined using thin layer chromatography. Complex 8f was then purified according to literature [29].

Yield: 50.5 %. UV-visible (DMF): λ_{max}, nm(log ε): 360(1.67), 490(1.02), 630(0.75), 725(3.01). IR [(KBr) ν_{max}/cm^{-1}]: 1637 (C=C).

2.4. Electrode modification of this work

This section describes the methods, used in this work, to modify electrodes with MPcs. These methods are: electrode modification using aryl radicals (grafting); adsorption; self assembled monolayers (SAMs).

2.4.1. Electrode modification using aryl radicals (grafting)

The glassy carbon electrode (GCE) was cleaned by polishing, using aqueous slurries of alumina (< 10 micron), on a SiC-emery paper (type 2400 grit), and then to a mirror finish on a Buehler-felt pad. Finally, the glassy carbon electrode was rinsed in copious amounts of ultra pure Millipore water and acetone to remove residual alumina particles trapped at the surface.

For the formation of the nitrophenyl grafted GCE (GCE-2, Scheme 4.1), cyclic voltammograms of the un-modified GCE were recorded in a fresh solution of 0.01 M phenyldiazonium salt in acetonitrile containing 0.1 M TBABF$_4$. To transform NO$_2$ to NH$_2$, the cyclic voltammogram of GCE-2 was recorded in a protic aqueous solution containing 0.1 M KCl in EtOH:H$_2$O (1:9, v:v). This was followed by continuous cyclic voltammetry multi-cycling (52 scans) in the same protic aqueous solution resulting in GCE-3. Finally, the attachment of CoPc(COOH)$_4$ to GCE-3

Chapter 2: Experimental

(forming **GCE-4**, Scheme 4.1), was performed by immersing **GCE-3** into a solution of 1 mM CoPc(COOH)$_4$ containing 5 mM EDC and 12.5 mM NHS in EtOH:DMSO (1:1, v:v) solution for 24 hours to form **GCE-4**.

2.4.2. Adsorption (drop dry method)

1 mM CoPc derivative (10 μL in DMF) was placed onto a cleaned glassy carbon electrode surface for 30 minutes to dry.

2.4.3. Self assembled monolayers

The gold electrode was cleaned by immersing it for approximately 2 minutes in a hot solution of 1:3 (v:v) nitric acid (55%) and concentrated H$_2$SO$_4$. This procedure removes organic impurities on the electrode. This was then followed by polishing the gold electrode, using aqueous slurries of alumina (< 10 micron), on a SiC-emery paper (type 2400 grit), and then to a mirror finish on a Buehler-felt pad. Finally the Au electrode was rinsed in copious amounts of ultrapure Millipore water and acetone to remove residual alumina particles trapped at the surface.

This cleaning was followed by placing the electrode in a DMF solution of 1 mM thiol-derivatised MPc for 24 hours at room temperature. Upon removal from the deposition solution, the electrode was rinsed with buffer solution before any electrochemical analysis.

2.5. Electrochemical methods

The electrodes of this work are characterized using: voltammetry, impedance, atomic force microscopy (AFM), scanning electrochemical microscopy (SECM). These methods are described below.

2.5.1. Voltammetry

A conventional three electrode system consisting of a glassy carbon (1.5 mm radius) or gold electrode (0.8 mm radius) as working electrode, Ag|AgCl pseudo reference electrode, and a platinum wire counter electrode were employed. The potential response of the Ag|AgCl pseudo-reference electrode was less than that of the Ag|AgCl (3 M KCl) by 0.015±0.003 V. For SOD studies, the given potentials were recalculated vs. normal hydrogen reference electrode (NHE) [455] in order to allow accurate comparison between experimentally obtained data and reported

Chapter 2: Experimental

data. Electrochemical experiments were performed at 25.0±1.0 °C using freshly distilled solvents. All electrochemical solutions were purged of oxygen by bubbling pure nitrogen or argon through them prior to experiments and the electrochemical cell was kept under nitrogen throughout the analyses.

2.5.2. Impedance

The impedance measurements for modified electrodes were performed using potassium ferricyanide in 0.1 M KCl solutions at the potential of the Fe^{III}/Fe^{II} couple (100 mV) on a Au electrode.

2.5.3. Scanning electrochemical microscopy

For scanning electrochemical microscopy (SECM) studies, the gold electrode (square shaped 1×1 cm) was positioned in a small well containing potassium ferricyanide solution (5 mM in phosphate buffer solution pH 7.4). SECM experiments were done using homemade 10 or 25 μm Pt ultramicroelectrodes. Tip approach curves were recorded by holding the ultramicroelectrodes at a fixed x/y position and monitoring changes in the steady-state current of $[Fe(CN)_6]^{4-}$ oxidation at 440 mV vs. Ag|AgCl (using TBABF$_4$ as an electrolyte) as the ultramicroelectrode tip travels (5 μm.s^{-1}) in the z direction from the bulk of the solution to the gold sample surface. The difference in $[Fe(CN)_6]^{4-}$ potential between impedance and SECM studies is due to the fact a gold electrode is used as a working electrode for the former whilst a platinum tip is used as the working electrode for the latter (Fig. 1.21). SECM images were then obtained by maintaining the ultramicroelectrode tip at a constant z-position and scanning in the x/y plane over the desired area (SECM constant-height mode).

2.6. Superoxide dismutation studies

2.6.1. Urate assay

To check that the putative superoxide scavengers (or SOD mimics) do not inhibit the production of superoxide by xanthine oxidase, the rate of conversion of xanthine to urate was determined by measuring the change in absorbance at 290 nm (where urate absorbs) over two minutes. All urate assays were done at 25±1 °C in a 50 mM PBS (pH 7.8) solution containing xanthine (35 μM) +

xanthine oxidase (0.01 U.mL^{-1}) and the putative SOD mimic. All MnPcs of this work were initially dissolved in DMSO (the final percentage of DMSO ranges from 0.02 to 0.08 %), except water soluble complexes **6e**, **8e**, and **8f** which were initially dissolved in 50 mM PBS.

2.6.2. McCord-Fridovich assay

Rates of cytochrome c (Fe^{III}) reduction were followed at 550 nm with a Varian Cary 1000 scan UV-visible spectrophotometer (DSI-476). Rate constants for reaction of the putative scavengers with O$_2^{•-}$ were based on their competition with cytochrome c (Fe^{III}) for reaction with O$_2^{•-}$, using $k_{Cytc} = 2.6 \times 10^5$ M^{-1}.s^{-1} [431]. All McCord-Fridovich assays were done at 25±1 °C in a 50 mM PBS (pH 7.8) solution containing cytochrome c (Fe^{III}) (10 µM) + xanthine (20 µM) without and with different concentrations of putative SOD mimic. Then xanthine oxidase (0.01 U.mL^{-1}) was added. Although the use of ethylenediaminetetraacetic acid (EDTA) to prevent the inactivation of the xanthine oxidase by trace metals during the assay is reported in some assays, it was not used in this work. Its absence in all the experiments creates a control by itself. Also, determinations of the IC50 were made over the first minute where the plots are linear. All studies were done in duplicate. Solutions of MPcs derivatives were prepared as stated in Section 2.6.1.

2.6.3. Dihydroethidium assay

HL-60 cells (CCL240), from ATCC, were cultured in RPMI 1640 with Glutamax, supplemented with 20% FBS, penicillin (100 U.mL^{-1}), streptomycin (100 µg.mL^{-1}), and non essential amino acids. To induce differentiation to granulocyte-like cells, HL-60 cell suspensions were incubated with 1.3% (v:v) DMSO for 6 days [456]. To induce extracellular superoxide production, differentiated cells were incubated with PMA (100 ng.mL^{-1}) for 15 minutes at 37 °C. DMSO-differentiated cells were washed with cell culture medium and re-suspended in the same medium. Cells (200 µL, approximately 5 $\times$ 10^5 cells/well) were dispensed into each well of a 96-well black plate. DHE was added to a final concentration of 25 µM. HL-60 cells were exposed to increasing amounts of SOD mimics or cell impermeable SOD protein in 5 µL. Each treatment was performed in triplicate and fluorescence was recorded after 2 hours using a microplate reader Victor 2 (Perkin Elmer), equipped for fluorescence with excitation and emission

wavelengths of 485 and 570 nm, respectively, to monitor hydroxyethidium from each well. For the determination of the non-activated cells, the curve was linear over 2 hours.

Each experiment was repeated 3 times. The concentrations of MnPcs tested ranged from 0.01 to 50 μM.

2.6.4. Cell viability

Cells (200 μL, approximately 5×10^5 cells/well) were dispensed into 1.5 mL tubes. Superoxide scavenger solution (10 μL, final concentration 50 μM) was added to the cells (in triplicate) and incubated at room temperature for 2 hours. Cell viability was assayed using the MTT test. The MTT assay is a standard colorimetric assay for measuring the activity of mitochondrial enzymes that reduce MTT to formazan, giving a purple color. It can also be used to determine cytotoxicity of various agents and toxic materials because those agents could cause cell toxicity and metabolic dysfunction resulting in decreased assay performance. Briefly, cells were washed once in PBS by centrifugation, and re-suspended in a culture medium containing MTT (0.5 mg.mL^{-1}) and incubated in their culture medium for 2 hours at 37 °C under 5% CO_2. After centrifugation, the cell pellet was lysed in 100 μL isopropanol containing 0.06 M HCl and 0.5% sodium dodecyl sulfate (SDS). The intensity of color was measured spectrophotometrically in a microplate reader at 562 nm (BioKinetics Reader, EL340). Appropriate controls with only 10% DMSO, without cells, etc, were run to subtract background absorbance. Results are presented as a percentage of non-treated cells.

Publications

PUBLICATIONS

Some of the results described in this thesis have been, or are being, published in the following peer reviewed journals:

1. Fungisai Matemadombo, Mahmut Durmuş, V. Escriou, S. Griveau, D. Scherman, F. Bedioui, Tebello Nyokong. **Evaluation of the performance of manganese phthalocyanines as superoxide dismutase mimics** *Current Analytical Chemistry* (In press)

2. Fungisai Matemadombo, Mahmut Durmuş, Chamunorwa Togo, Janice Limson, Tebello Nyokong. **Characterization of manganese tetraalkylthiosubstituted phthalocyanines self assembled monolayers** *Electrochimica Acta* (In press)

3. Fungisai Matemadombo, Nthapo Sehlotho, Tebello Nyokong. **Effect of number of ring substituents of cobalt carboxyphthalocyanines on the electrocatalytic detection of nitrite, cysteine and melatonin** *Journal of Porphyrins and Phthalocyanines* (In press)

4. Fungisai Matemadombo, Sophie Griveau, Fethi Bedioui, Tebello Nyokong. **Electrochemical characterization of self-assembled monolayer of a novel manganese tetrabenzylthiosubstituted phthalocyanine and its use in nitrite oxidation** *Electroanalysis* 2008; 20: 1863 - 1872.

5. Fungisai Matemadombo, Philippe Westbroek, Tebello Nyokong. **Electroanalysis of thiocyanate using a novel glassy carbon electrode modified by aryl radicals and cobalt tetracarboxyphthalocyanine** *Electrochimica Acta* 2007; 53: 480 - 486.

6. Fungisai Matemadombo and Tebello Nyokong. **Characterization of self-assembled monolayers of iron and cobalt octaalkylthiosubstituted phthalocyanines and their use in nitrite electrocatalytic oxidation** *Electrochimica Acta* 2007; 52: 6856 - 6864.

7. Fungisai Matemadombo, M. David Maree, Kenneth I. Ozoemena, Philippe Westbroek, Tebello Nyokong. **Synthesis, electrochemical and spectroelectrochemical studies of octaalkylthiosubstituted phthalocyanines** *Journal of Porphyrins and Phthalocyanines* 2005; 9: 484 - 490.

CHAPTER 3: SYNTHESIS AND CHARACTERIZATION

3.1. Synthesis of arylthio substituted phthalocyanines

3.1.1. FePc(SCH$_2$Ph)$_8$ (9b) and CoPc(SCH$_2$Ph)$_8$ (10b)

3.1.1.1. Synthesis and spectral characterization

Because complexes **9b** and **10b** have been synthesized for the first time, their synthesis and characterization are explicitly discussed.

Phthalonitrile **39** was synthesized as outlined in Scheme 3.1.
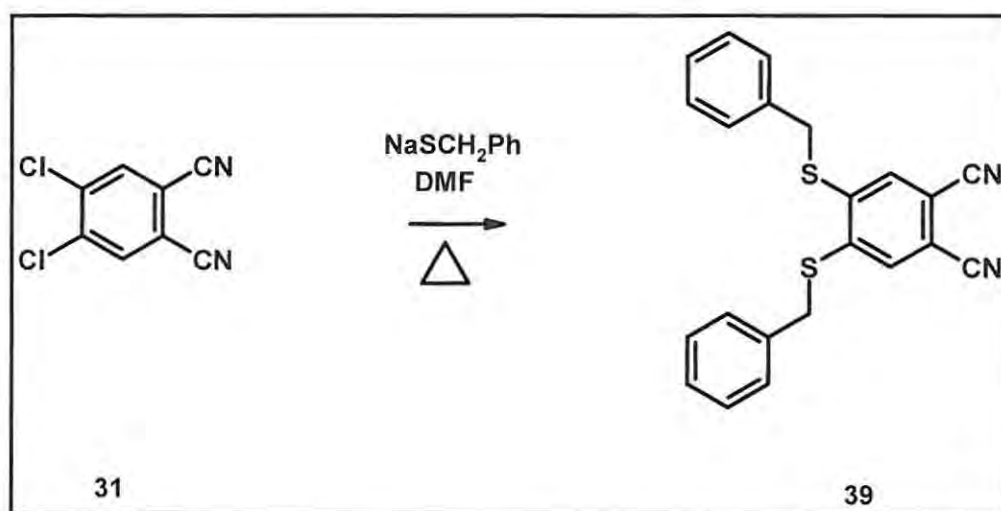
Scheme 3.1 Synthesis of **39**

The synthesis of the aromatic 1,2-bis(*S*-benzylthio)-4,5-dicyanobenzene (**39**) was done according to reported procedures [453] from the dichlorophthalonitrile (**31**) in a 39 % yield. Synthesis of **39** using sodium hydride (used as a strong base) and benzyl mercaptan proved to be more successful (especially with respect to a purer product) as opposed to the nucleophillic displacement reaction using an excess of thiols in the presence of an excess of potassium carbonate [69].

The CN band in the infrared (IR) spectrum of **39** was observed at 2227 cm^{-1}, Fig. 3.1.

75
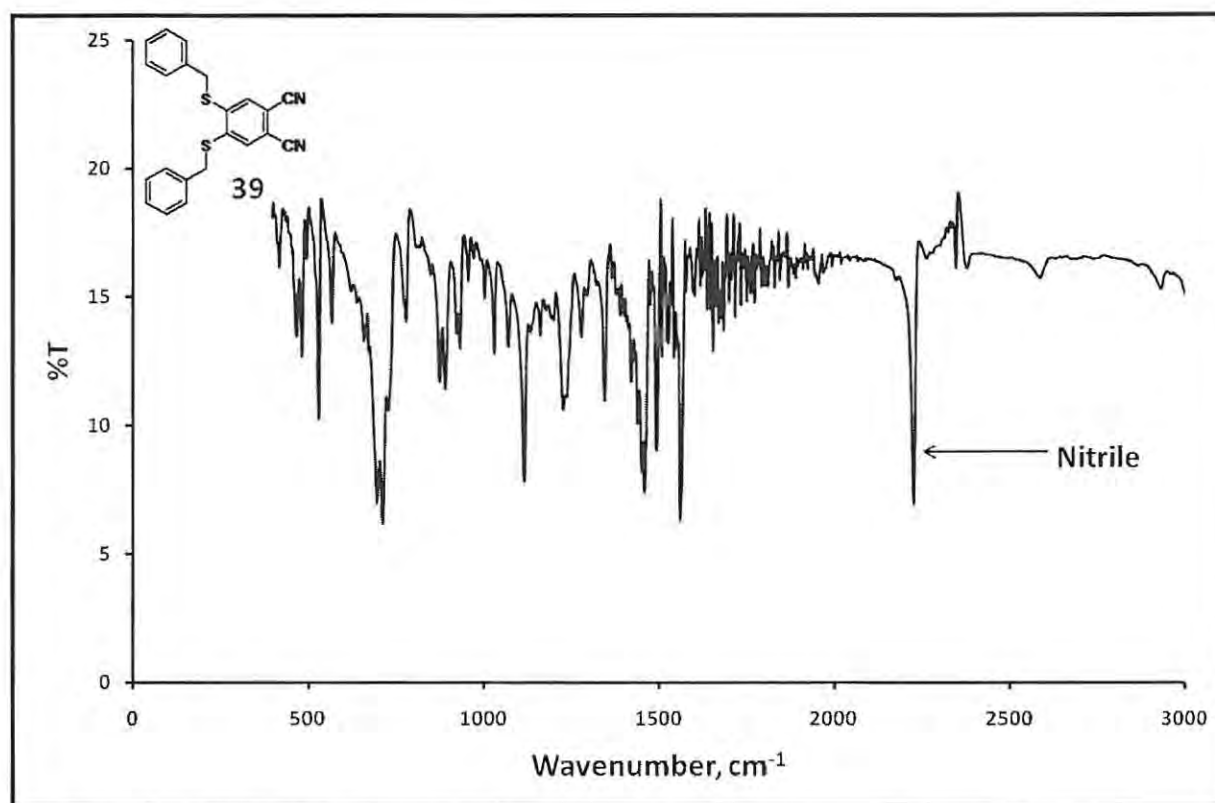
Fig. 3.1 Infrared spectrum of complex **39**

The benzyl protons of **39** appeared as a singlet integrating for 10 at 8.20 ppm in the ^{1}H NMR spectrum, Fig. 3.2. A multiplet, integrating for 2, pertaining to the phenyl protons of **39** at 7.30 ppm also appeared, and the methylene protons were found as a singlet integrating for 4 at 4.30 ppm.
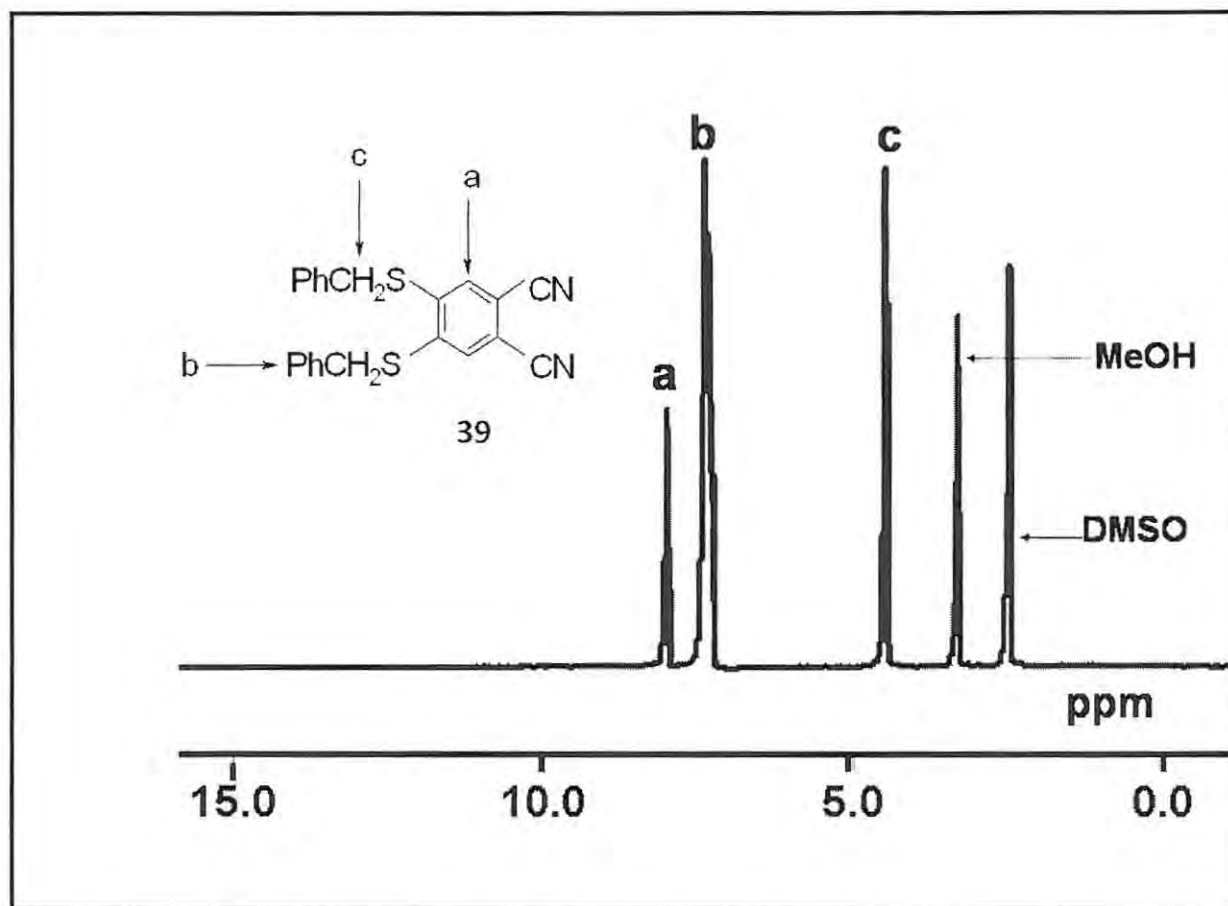
Fig. 3.2 NMR spectrum of complex **39**. Ph = phenyl group

The syntheses of FePc(SCH$_2$Ph)$_8$ (**9b**) and of CoPc(SCH$_2$Ph)$_8$ (**10b**) are outlined in Scheme 3.2.
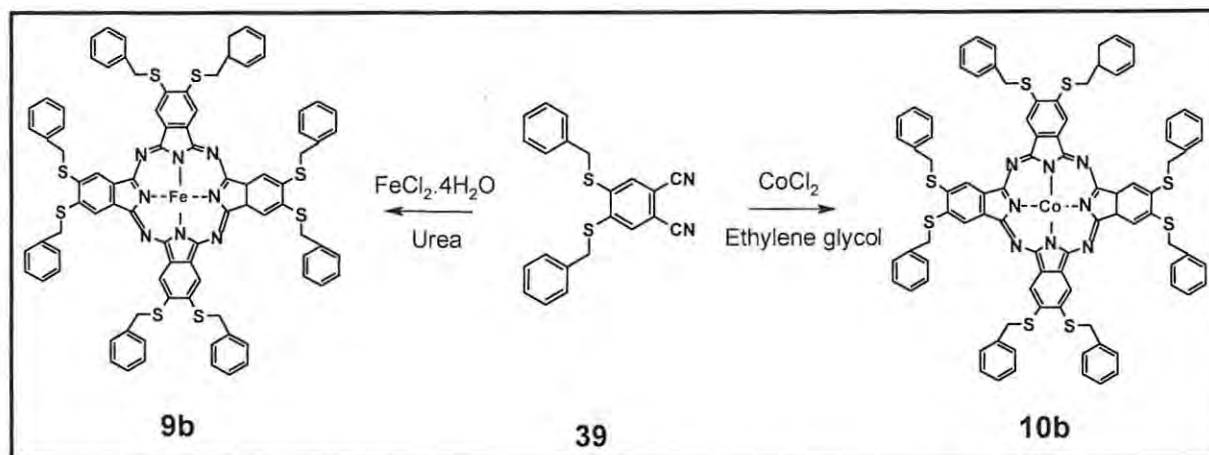
Scheme 3.2 Syntheses of FePc(SCH₂Ph)₈ (**9b**) and CoPc(SCH₂Ph)₈ (**10b**) from **39**

Complex **9b** gives best yields when synthesized using the urea method, as opposed to other methods [69]. Purification was performed by treating crude **9b** with hot alcohols.

Complex **10b** was synthesized according to the reported synthesis of octakis(alkylthio)-substituted phthalocyanines [457]. It was important to use the anhydrous form of the metal salt (CoCl₂) as this was found to give a purer product. Anhydrous CoCl₂ was obtained by heating commercially available CoCl₂.6H₂O to 140 °C resulting in the loss of the six water molecules. Complex **10b** was purified by rigorous washings with acetone and hexane. Complexes **9b** and **10b** are soluble in common organic solvents such as DMF, DMSO, and THF.

Table 3.1 lists the characterization data of the MPc complexes.

Chapter 3: Synthesis and characterization

Table 3.1 Characterization data of MPc complexes[a]

Complex	IR (KBr): ν, cm^{-1}	UV-visible: λ_{max}, nm[b]
5g	1625 (C=C)	657
6c	1382 (C=C), 1106 (Mn-OH), 681 (C-S-C)	764
6d	3062 (Ar-CH), 1569 (C=C), 915 (Mn-OH), 742 (C-S-C)	758
6e	3055 (Ar-CH), 1564 (C=C), 1330 (S=O), 1218 (S=O), 913 (Mn-OH), 765 (C-S-C)	741
7a	1633 (C=C)	675
8b	1382 (C=C), 832 (Mn-OH), 625 (C-S-C)	777
8d	3062 (Ar-CH), 1569 (C=C), 923 (Mn-OH), 742 (C-S-C)	730
8e	3053 (Ar-CH), 1569 (C=C), 1325 (S=O), 1236 (S=O), 924 (Mn-OH), 765 (C-S-C)	719
8f	1637 (C=C)	720
9b	3676 (Ar-CH), 1653 (C=C), 694 (C-S-C)	690
10a	1650 (C=C)	689
10b	3852 (Ar-CH), 1561 (C=C), 687 (C-S-C)	686

[a]**5g** = CoPc; **6c** = (OH)MnPc(SPh)$_4$; **6d** = α-(OH)MnTMPyPc; **6e** = α-Q-(OH)MnTMPyPc; **7a** = CoPc(COOH)$_4$; **8b** = (OH)MnPc(SCH$_2$Ph)$_4$; **8d** = β-(OH)MnTMPyPc; **8e** = β-Q-(OH)MnTMPyPc; **8f** = (Na)$_4$(OH)MnPc(SO$_3$)$_4$; **9b** = FePc(SCH$_2$Ph)$_8$; **10a** = CoPc(COOH)$_8$; **10b** = CoPc(SCH$_2$Ph)$_8$
[b]Recorded in DMF except **10b** which was recorded in THF

The absence of a prominent nitrile band at ~2200 cm^{-1} in the infrared spectra of complexes **9b** and **10b** (Table 3.1) confirms, to a certain extent, the presence of MPc and therefore successful conversion of **39** (displaying a nitrile peak in its infrared spectrum as stated in Chapter 2, Section 2.3.1.1.) into MPc. Nonetheless, supplementary characterization techniques are necessary to corroborate this conversion.

Chapter 3: Synthesis and characterization

Broad peaks in the ^{1}H NMR spectra of the Pc complexes studied in this work are due to aggregation occurring at the high concentrations used [458] and to the paramagnetic nature of the central metal ions. However, careful integration of the observed ^{1}H NMR peaks gave the expected number of protons. The Pc protons occurred as a broad singlet integrating for 8 at 8.00 ppm for complex **9b**. The phenyl protons, moreover, appeared downfield at 7.50 ppm as a broad multiplet integrating for 40 in the ^{1}H NMR spectrum of **9b**. The methylene protons of **9b** occurred up-field at 4.50 ppm, integrating for 16.

The Pc protons in the ^{1}H NMR spectrum of **10b** occurred as a broad singlet integrating for 8 at 8.20 ppm. The phenyl protons of **10b** occurred in the downfield ^{1}H NMR region at 7.20 ppm and integrated for 40. At 4.60 ppm, the protons pertaining to the methylene group of **10b** appeared as a multiplet integrating for 16 in the ^{1}H NMR spectrum.

UV-visible spectra of Pc complexes **9b** and **10b** in freshly distilled DMF or THF are shown in Fig. 3.3. Different solvents were employed because **10b** gave a better resolved Q band in THF as opposed to in DMF.
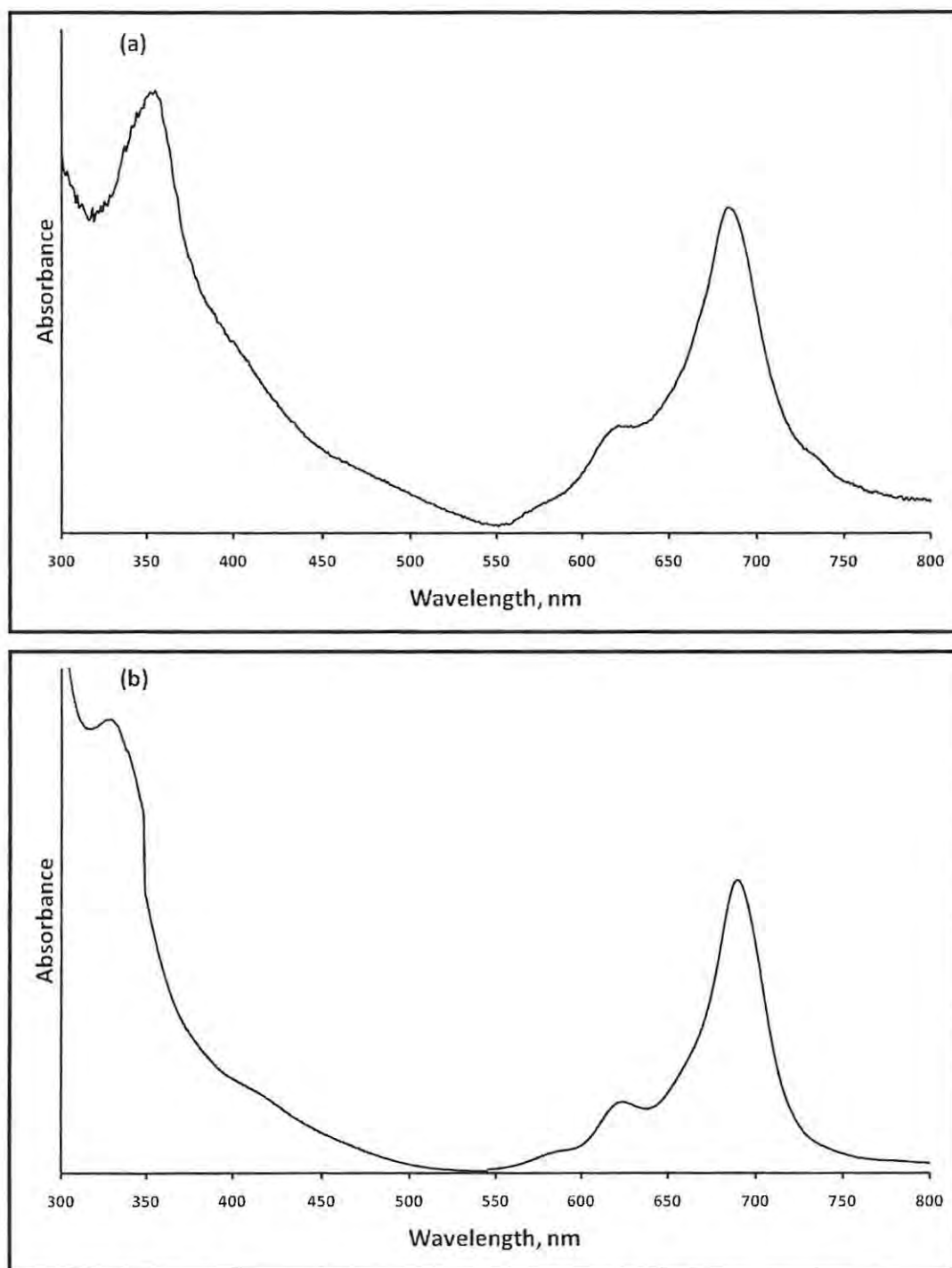
Fig. 3.3 UV-visible spectra of FePc(SCH$_2$Ph)$_8$ (**9b**) (a, in DMF) and CoPc(SCH$_2$Ph)$_8$ (**10b**) (b, in THF). Concentration $\approx$ 1 μM

Chapter 3: Synthesis and characterization

The Q bands occurred in the visible region at 690 nm (for complex **9b**) and 686 nm (for complex **10b**) in DMF and THF respectively. The characteristic B bands occur in the UV regions for complexes **9b** (at 359 nm) and **10b** (at 327 nm). The Q band wavelength values of complexes **9b** and **10b** are red-shifted relative to unsubstituted FePc or CoPc at ~670 nm [92,93,459] due to effects of the benzylthiol substituents. The electron-donating nature of the sulfur groups shifts the Q band to the red. The spectra of iron phthalocyanines have been the subject of several reports [460,461] and much controversy. The formation of μ-oxo Fe(II)Pc or Fe(III)Pc species has been reported for the same types of complexes, such as $Cl_{16}PcFe$ [460] hence it is important to determine the oxidation state of the central metal ion for each preparation of a FePc species, by using electrochemistry.

The mass spectra, by the MALDI-TOF technique, of the synthesized complexes **9b** and **10b** verified the anticipated structures. Molecular ions in **9b** and **10b** were identified at m/z: 1546.4 $[M + 1]^+$ and 1549.7 $[M + 1]^+$, respectively.

3.1.1.2. Electrochemical characterisation

The potentials for first reduction of complexes **9b** and **10b** are much less negative than those of other thio substituted CoPc and FePc complexes (Table 3.2), suggesting that the benzylthiol substituents confer ease of reduction on the CoPc and FePc species.

Fig. 3.4 shows the CV and SWV for complex **9b** in DMF.
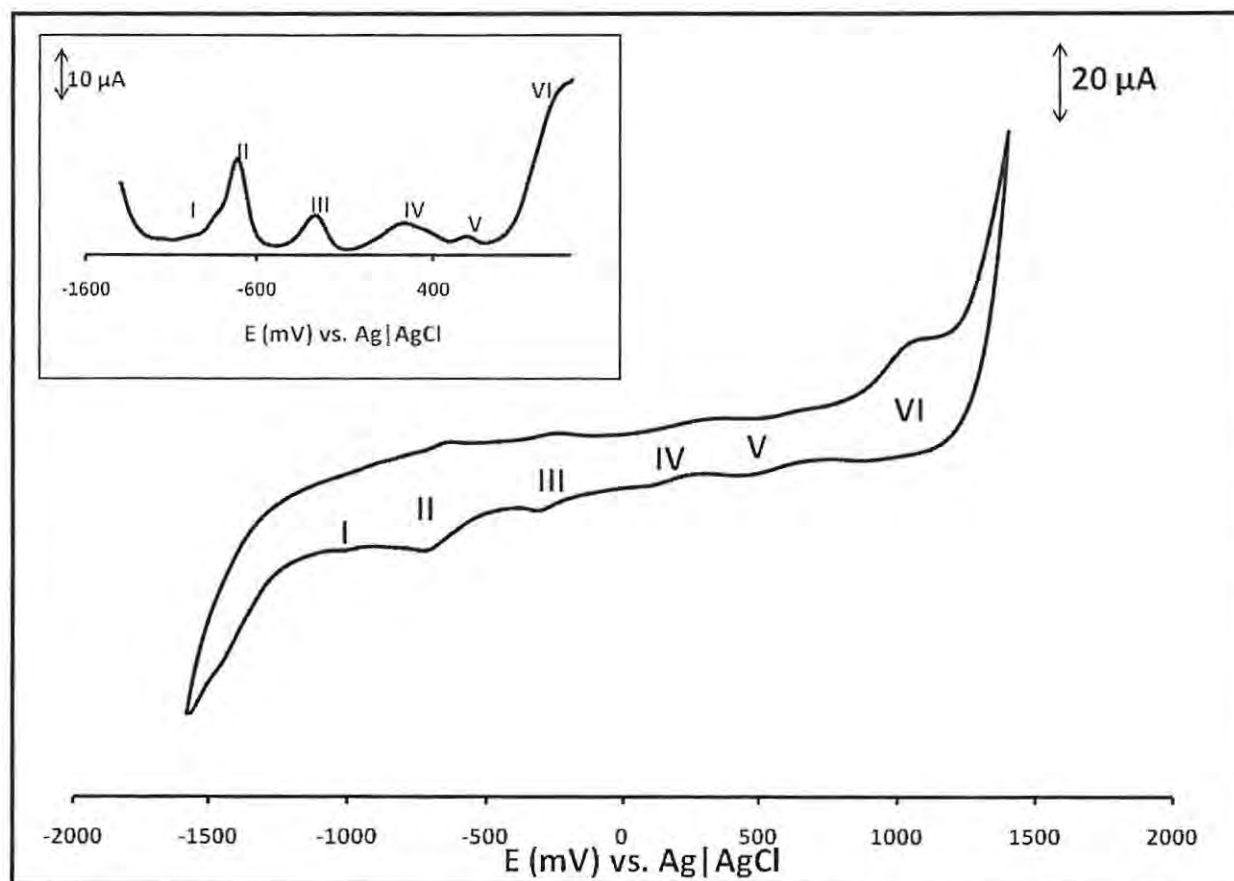
Fig. 3.4 Cyclic and square wave (insert) voltammograms on a GCE for FePc(SCH$_2$Ph)$_8$ (**9b**) in DMF containing 0.1 M TBAP. Scan rate = 100 mV.s^{-1}

In Fig. 3.4, six processes are observed. The couples exhibited reversible to quasi-reversible behaviour in that the ratio of the cathodic to anodic peak currents was not unity and ΔE values are larger than the 90 mV (observed for the ferrocenium/ferrocene standard) except for **II** and **III** which were reversible. Process **VI** was irreversible and the high currents suggest a contribution from substituents. A plot of peak current vs. square root of the scan rate is linear for all couples confirming diffusion control. Complex **9b** showed two Pc metal based processes (**III** and **IV**) and four Pc ring processes (**I, II, V, VI**), tentatively assigned thus in comparison with alkylthio Pcs, Table 3.2, but confirmed with spectroelectrochemistry (OTTLE) below. Cyclic (CV) and square wave (SWV) voltammetry of complexes **9b** and **10b** were performed in DMF containing 0.1 M TBAP; data are listed in Table 3.2.

Table 3.2 Redox potentials (V vs. Ag|AgCl) for complexes **9b** and **10b** measured in DMF containing 0.1 M TBAP[a,b]

Complex	$M^{III}Pc^0/$ $M^{III}Pc^{-1}$ (VI)	$M^{III}Pc^{-1}/$ $M^{III}Pc^{-2}$ (V)	$M^{III}Pc^{-2}/$ $M^{II}Pc^{-2}$ (IV)	$M^{II}Pc^{-2}/$ $M^{I}Pc^{-2}$ (III)	$M^{I}Pc^{-2}/$ $M^{I}Pc^{-3}$ (II)	$M^{I}Pc^{-3}/$ $M^{I}Pc^{-4}$ (I)
9b	1.14	0.60	0.25 (0.26)	-0.26 (-0.49)	-0.70	-1.3
10b		1.16	0.72 (0.72)	-0.096 (-0.38)	-0.58	-1.0

[a]**9b** = FePc(SCH₂Ph)₈; **10b** = CoPc(SCH₂Ph)₈

[b]Values in brackets are for Fe and Co octabutylthiometallophthalocyanine [23], for comparison

Spectroelectrochemistry for complex **9b**, at potentials of couple **III**, gave the spectral changes shown in Fig. 3.5.
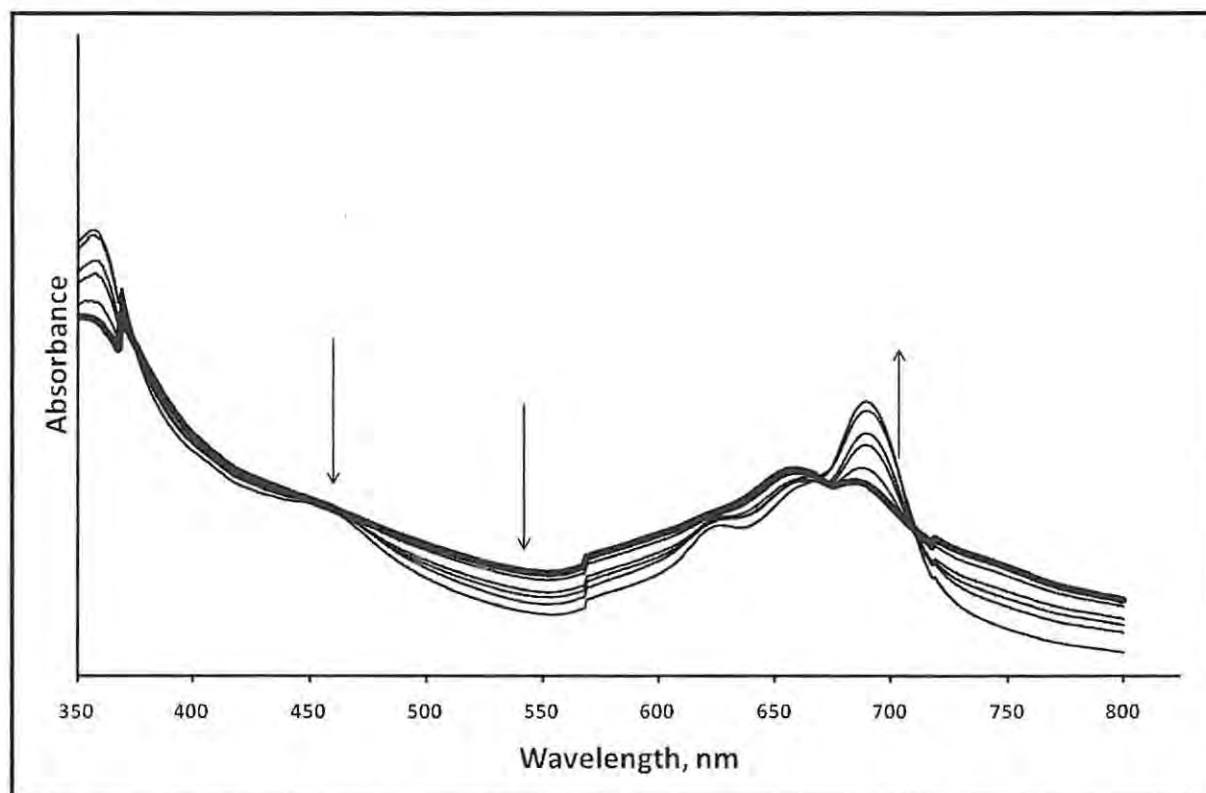
Fig. 3.5 UV-visible spectral changes observed using an OTTLE cell during the reduction of FePc(SCH$_2$Ph)$_8$ (**9b**) at -0.5 V in DMF containing TBAP

From Fig. 3.5, complex **9b** shows aggregation at the concentrations employed for the OTTLE cell, especially shown by the broad Q band before electrolysis. Upon reduction, the peak due to the monomer increased and shifted slightly to longer wavelengths, while the band at 450 nm, associated with charge transfer in axially ligated Fe(II)Pc complexes, increased at first then decreased in intensity. The disappearance of this band suggests a change in the oxidation state of the central Fe(II) ion. Generally, in phthalocyanine chemistry, the lack of disappearance of the Q band on reduction or oxidation suggests a metal-based process. Thus the spectral changes shown in Fig. 3.5 are typical of metal-based reduction, suggesting the formation of the Fe(I) species. The spectra of the Fe(I)Pc species are not well known. It has been reported [462] that the presence of Fe(I) disturbs the π-π* spectrum of the Pc resulting in a weak Q band and a pink solution. This work, however, shows that a strong Q band is still present following reduction of Fe(II)Pc to Fe(I)Pc, probably due to the influence of the ring substituents. The spectroelectrochemical studies hence confirm that couple **III** is due to Fe^{II}Pc^{-2}/Fe^{I}Pc^{-2}.

85

Chapter 3: Synthesis and characterization

Reduction of complex **9b** at the potentials of couple **II** resulted in a decrease in the Q band and the formation of bands in the 500 nm to 600 nm region, typical of ring reduction in MPc complexes and suggesting the formation of the Fe^IPc^{-3} species (Fig. not shown). Further reductions are expected to occur on the ring, and the assignments are listed in Table 3.2. Attempts to oxidize complex **9b** resulted in the formation of a broad Q band, probably due to the fact that the Fe(III)Pc species is characterized by a split Q band.

CV and SWV for complex **10b** are shown in Fig. 3.6.
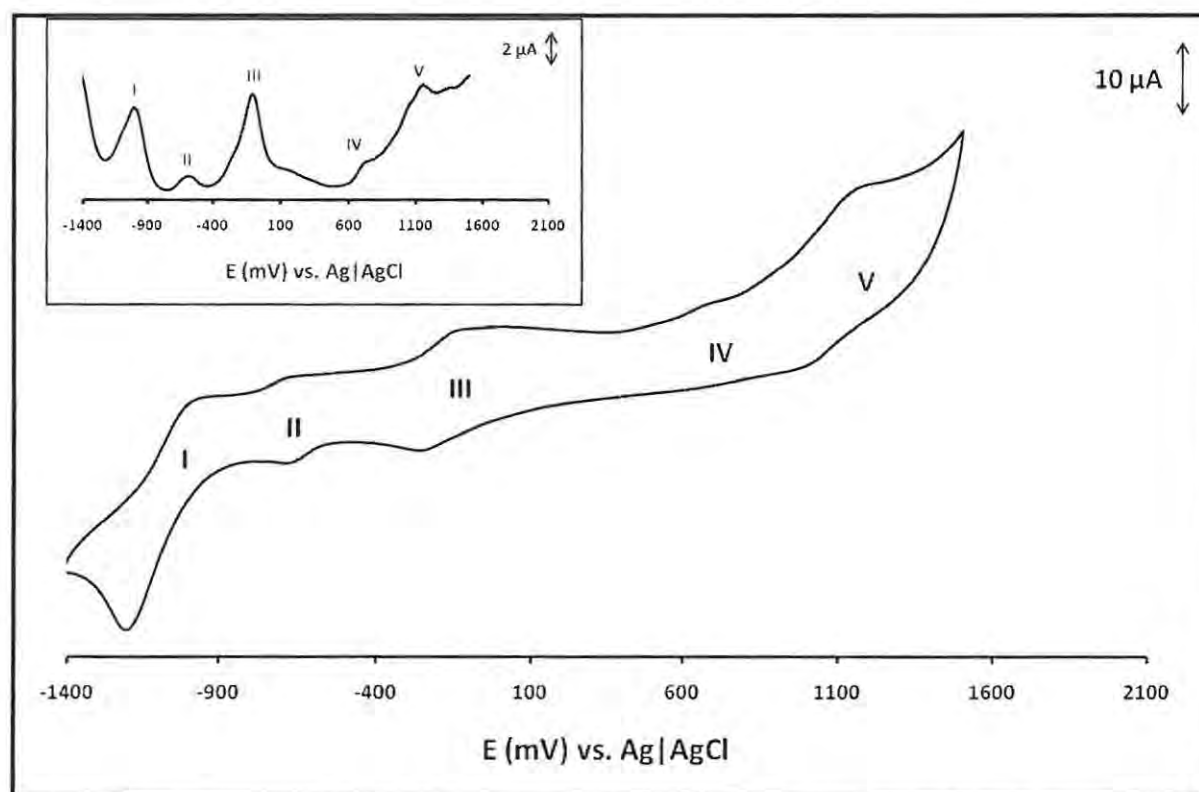
Fig. 3.6 Cyclic and square wave (insert) voltammograms on a GCE, for $CoPc(SCH_2Ph)_8$ (**10b**) in DMF containing TBAP. Scan rate = 100 mV.s^{-1}

From Fig. 3.6, the couples exhibited reversible to quasi-reversible behaviour in that the ratio of cathodic to anodic peak currents was not unity (e.g. processes **I**, **IV**, and **V**) and the anodic to cathodic peak potential separations (ΔE) were larger than 90 mV in some cases (ΔE = 90 mV was obtained for the ferrocenium/ferrocene internal standard). Lack of reversibility for the

86

thiosubstituted phthalocyanine complexes has been reported [36]. Couple **II** gave a ΔE of ~0 mV, suggesting adsorption behaviour of complex **10b**. Sharp peaks in the CV of alkylthio substituted MPc complexes have been observed [36], and such behaviour is attributed to the formation of adsorbed species. The plot of the peak current vs. square root of the scan rate was linear suggesting diffusion controlled behaviour for all couples except **II**, which showed adsorption behaviour.

Fig. 3.7 shows typical UV-visible spectral changes observed using an OTTLE cell during the reduction of complex **10b** and was employed to assign the CV couples of complex **10b**. The spectra were recorded continuously during the electrolysis and the first spectrum in Fig. 3.7(b) is the same as the last spectrum in Fig. 3.7(a).
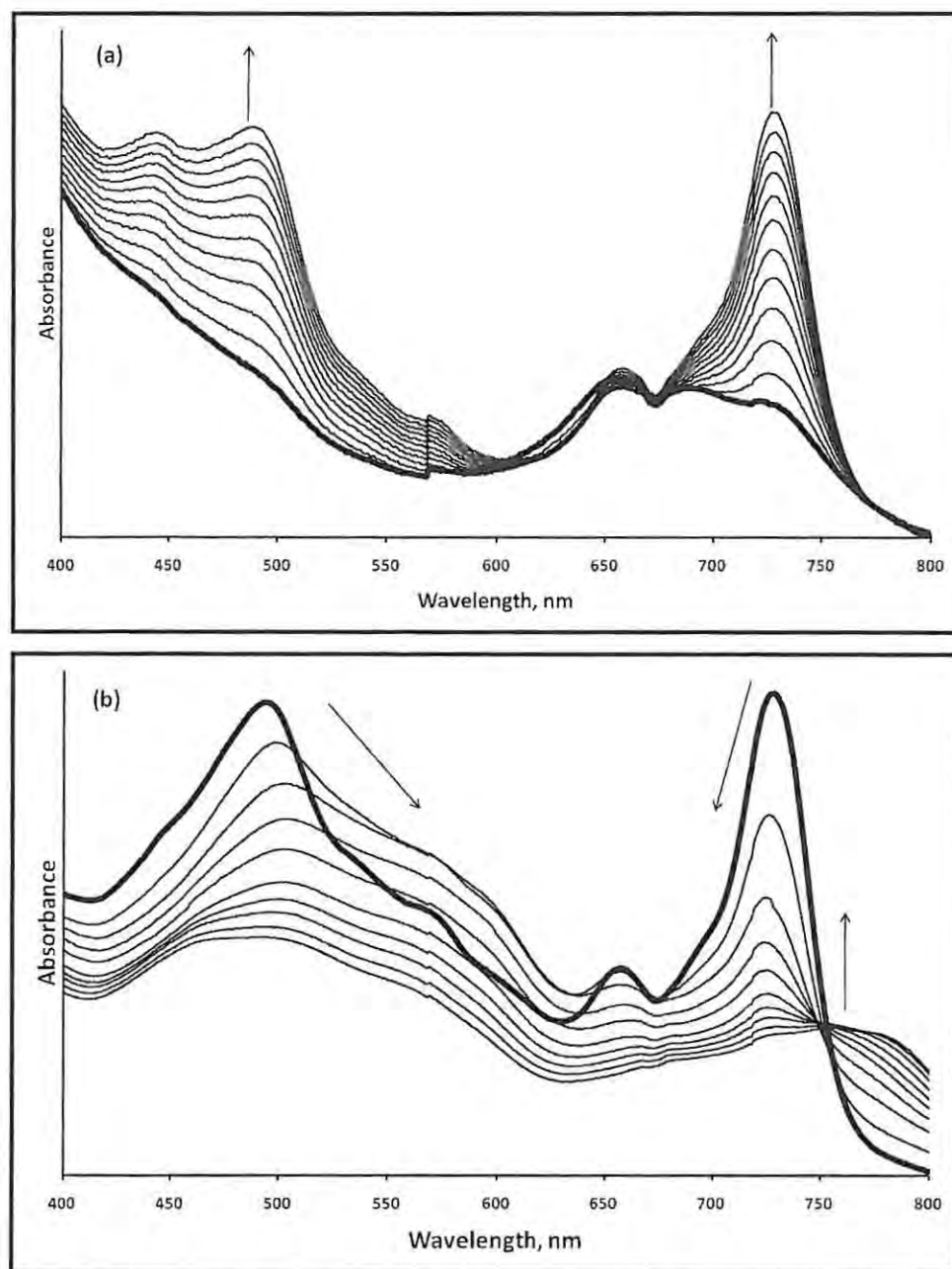
Fig. 3.7 UV-visible spectral changes observed using an OTTLE cell during the reduction of $CoPc(SCH_2Ph)_8$ (**10b**) at -0.5 V (a) and -1.0 V (b) in DMF containing TBAP

With respect to complex **10b**, reduction at potentials more negative than couple **III** (-0.5 V) resulted in the spectral changes shown in Fig. 3.7(a). At the high concentrations employed for the OTTLE studies, the complex is highly aggregated as seen in the first trace in Fig. 3.7(a), with the monomer peak at 680 nm and the peak due to aggregated species at 655 nm. Upon reduction, the

monomeric peak shifted from 680 nm to 726 nm and increased considerably in intensity. The spectral changes show that, upon reduction, the Pc molecules become disaggregated. New intense peaks between 400 nm and 500 nm are characteristic of Co^ICp species [459]. Also, the shift in the Q band, without decrease in intensity, is typical of metal based reduction in MPc complexes. Thus, the spectral changes shown in Fig. 3.7(a) clearly confirm that couple **III** is due to the reduction of $Co^{II}Pc$ to Co^IPc. The reduction was partly reversible in that applying zero volts resulted in the regeneration of the starting spectrum.

Further reduction of the species formed in Fig. 3.7(a), at potentials more negative than couple **II**, resulted in the spectral changes shown in Fig. 3.7(b), which consisted of a decrease in the Q band and the shifting of the band at 490 nm to longer wavelengths, followed by decrease in its intensity. New bands also formed in the 500 nm to 650 nm region. The decrease in the Q band is characteristic of ring-based processes. Bands in the 500 nm to 600 nm region are typical [463] of ring-based reduction and the formation of a Pc^{-3} species; thus, reduction at potentials of couple **II** results in the formation of Co^IPc^{-3} species. The zero volts value of the cathodic to anodic peak separation shows the reduction of Co^IPc^{-2} to Co^IPc^{-3} and results in adsorption of the latter on the electrode. Couple **I** is then due to the subsequent formation of the Co^IPc^{-4} species. Table 3.2 summarizes the assignments of the couples.

For complex **10b**, oxidation at potentials more positive than couple **IV** resulted in the spectral changes shown in Fig. 3.8, dominated by increase in the peak due to the monomer, which displayed a wavelength shift from 680 nm to 697 nm.
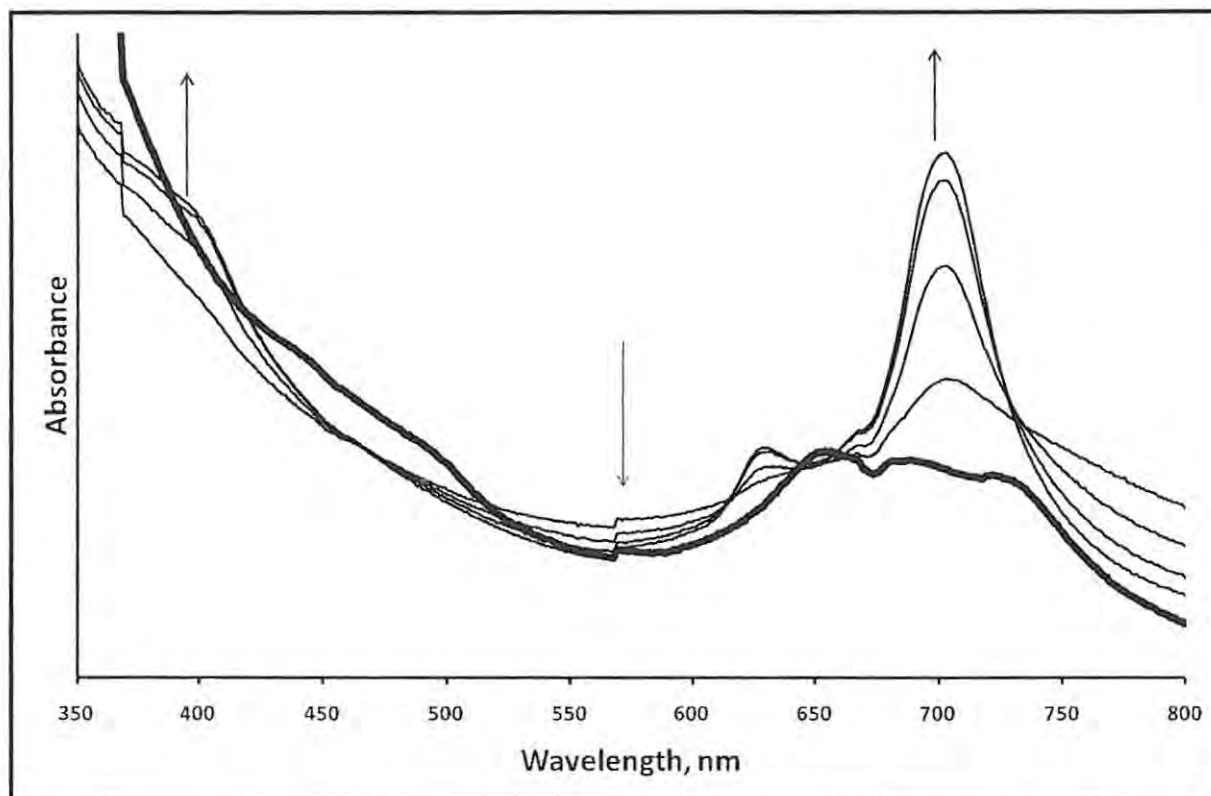
Fig. 3.8 UV-visible spectral changes observed using an OTTLE cell during the oxidation of CoPc(SCH$_2$Ph)$_8$ (**10b**) at +1.0 V in DMF containing TBAP

As with Fig. 3.7(a), the starting spectrum of Fig. 3.8 is typical of aggregated species, with one band associated with the monomer at lower energy and another band belonging to the aggregated species at higher energy, due to the high concentrations employed for the OTTLE cell. Because there was an increase in the Q band intensity, the spectral changes in Fig. 3.8 are due to the oxidation of Co(II) to Co(III) species. This shows that, at the potentials of couple **IV**, metal oxidation occurs, and that the couple is due to Co^{III}Pc^{-2}/Co^{II}Pc^{-2}. The subsequent oxidations are expected to be on the ring [121].

Chapter 3: Synthesis and characterization

3.1.2. Complexes: α-(OH)MnTMPyPc (6d), α-Q-(OH)MnTMPyPc (6e), β-(OH)MnTMPyPc (8d), β-Q-(OH)MnTMPyPc (8e)

These titled complexes of manganese, previously synthesised and characterized [31] as in Scheme 3.3, were available in the laboratory.
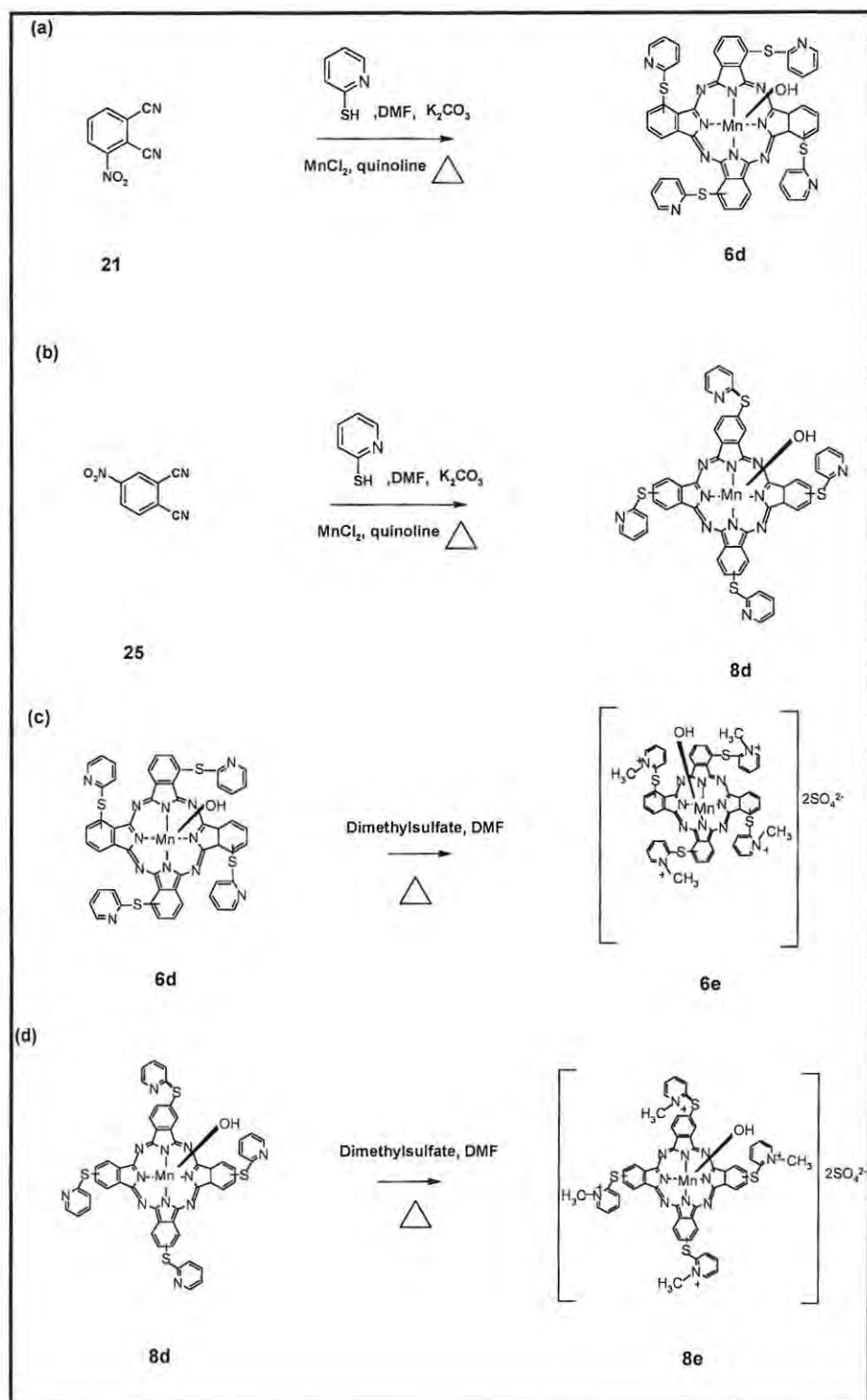
Scheme 3.3 Synthesis of α-(OH)MnTMPyPc (**6d**, a), α-Q-(OH)MnTMPyPc (**6e**, c), β-(OH)MnTMPyPc (**8d**, b), and β-Q-(OH)MnTMPyPc (**8e**, d)

Chapter 3: Synthesis and characterization

The quaternized MnPc derivatives **6e** and **8e** are water soluble. The quaternized complexes **6e** and **8e** are blue-shifted compared to the corresponding unquaternized derivatives (**6d** and **8d**), Fig. 3.9. This is due to the lowering of the electron-donating ability of the nitrogen groups on quaternization.
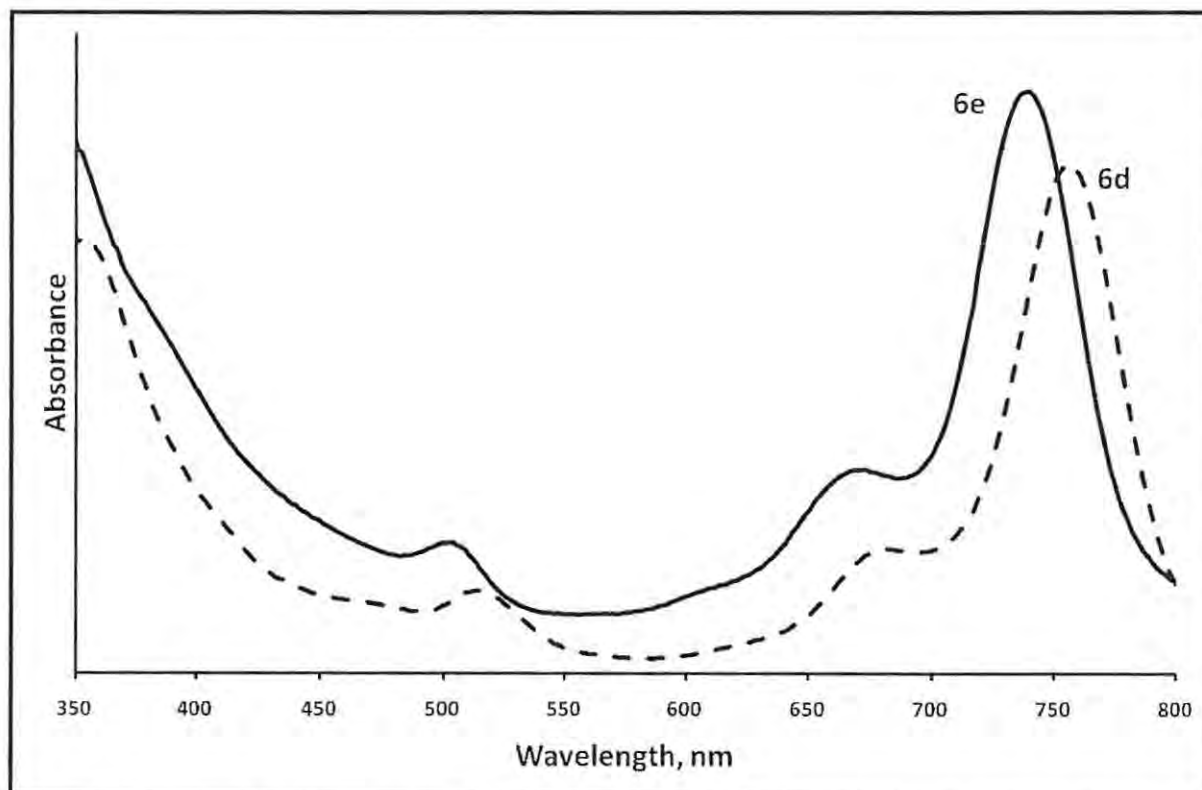
Fig. 3.9 UV-visible spectra of α-(OH)MnTMPyPc (**6d**) and α-Q-(OH)MnTMPyPc (**6e**) in DMF. Concentration ≈ 1 μM

UV-visible spectral data of **6d**, **6e**, **8d**, and **8e** (listed in Table 3.1) show red shifting compared to other complexes due to the influence of Mn and the presence of sulfur groups.

Mn complexes **6d**, **6e**, **8d**, and **8e** were employed in this work as self assembled monolayers and superoxide dismutase mimics hence their electrochemical characterization is reported. CV assignments using spectroelectrochemistry have been reported [31] but are also included in this work. The study of the electrochemistry of Mn macrocycles is important for their potential use as superoxide dismutase (SOD) mimics [389,419]. For this application it is important to understand the oxidation states of the central Mn ion in MnPc complexes.

Chapter 3: Synthesis and characterization

The first reduction in $Mn^{II}Pc^{-2}$ complexes has been a subject of some controversy, with some reports proposing ring reduction to the $Mn^{II}Pc^{-3}$ species, and others suggesting metal reduction to the $Mn^{I}Pc^{-2}$ species. The former species has been reported by our group and other authors [27,35,464] while the latter has rarely been observed [465]. This work reports the formation of a Mn(I)Pc species which depends on the nature of substituents on the MnTMPyPc complexes (quaternized or unquaternized).

The CVs and SWVs of complexes **6d** and **8e** were performed in DMF containing TBABF$_4$ as electrolyte, Fig. 3.10. Similar CVs were obtained for **6e** and **8d**.
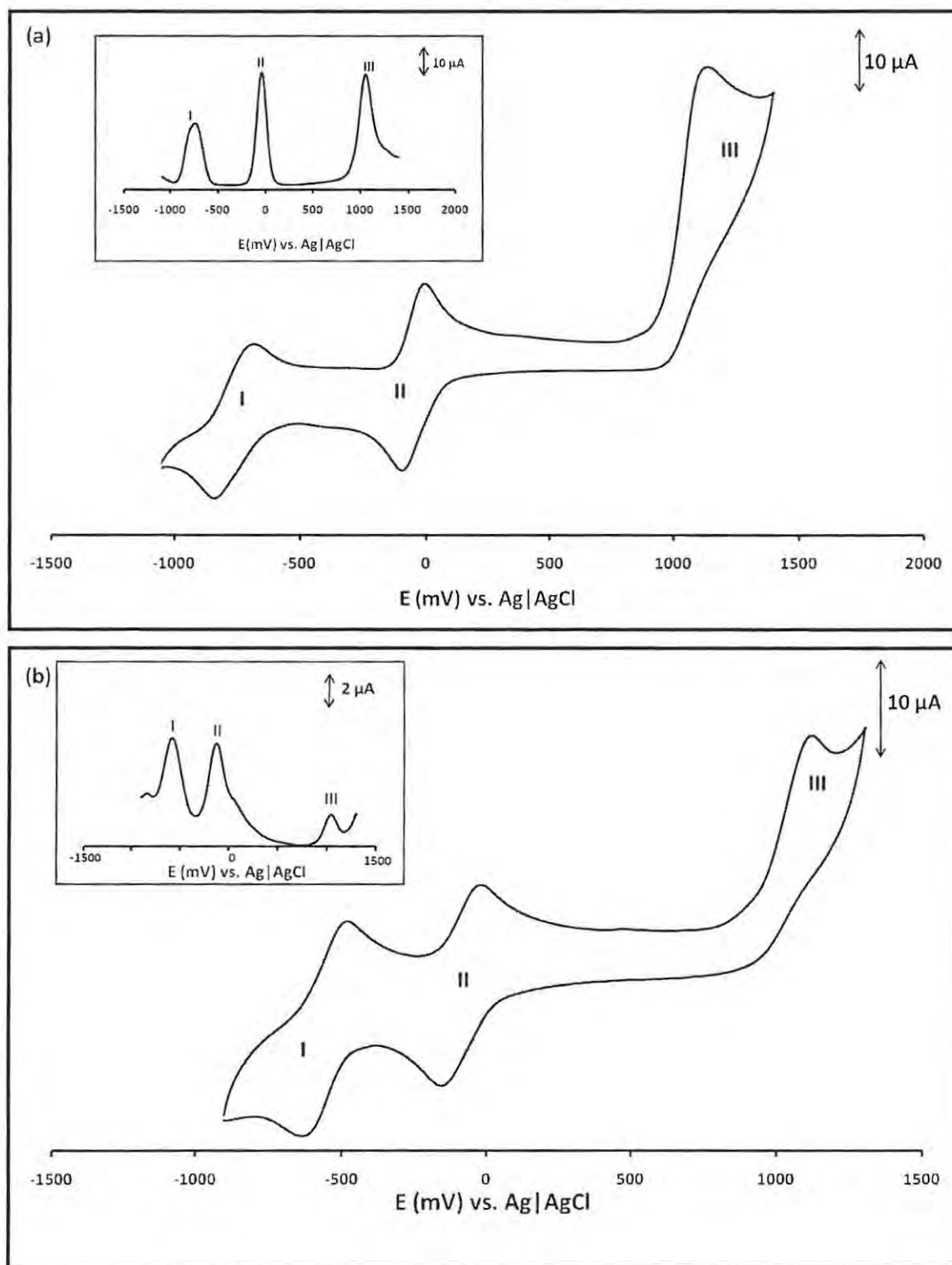
Fig. 3.10 Cyclic and square wave (insert) voltammograms of (a) α-(OH)MnTMPyPc (**6d**) and (b) β-Q-(OH)MnTMPyPc (**8e**) in DMF containing TBABF₄. Scan rate = 100 mV.s⁻¹

The half-wave potentials ($E_{1/2}$) for the MnPc complexes (**6d**, **6e**, **8d**, **8e**) are summarized in Table 3.3.

Table 3.3 Redox potentials (V vs. Ag|AgCl) for MnTMPyPc derivatives in DMF containing TBABF$_4$[a]

Complex	$Mn^{II}Pc^{-2}$ /$Mn^{II}Pc^{-3}$	$Mn^{II}Pc^{-2}$ /$Mn^{I}Pc^{-2}$	$Mn^{III}Pc^{-2}$ /$Mn^{II}Pc^{-2}$	Oxidation processes
6d	-0.76		-0.051	1.18
6e		-0.59	-0.056	1.10
8d	-0.71		-0.057	1.34
8e		-0.56	-0.063	1.13

[a]**6d** = α-(OH)MnTMPyPc; **6e** = α-Q-(OH)MnTMPyPc; **8d** = β-(OH)MnTMPyPc; **8e** = β-Q-(OH)MnTMPyPc

All complexes exhibited three reduction processes (labelled **I**, **II**, and **III**, e.g. for **6d** and **8e** in Fig. 3.10), Table 3.3. Couples **I** and **II** are quasi-reversible with peak separations larger than the expected 60 mV, suggesting slow electron transfer. The cathodic-to-anodic peak separation (ΔE) ranged from 100 to 130 mV and a value of 90 mV was obtained for ferrocene, at a scan rate of 100 mV.s^{-1}. The cathodic-to-anodic peak current ratio (I_{pa}/I_{pc}) were near unity for couples **I** and **II**. Process **III** was totally irreversible. Chronocoulometry showed that the ratios of the currents for processes **I** and **II** are equal and one-third those of process **III**. This is most probably due to the combination of Pc ring oxidation and the oxidation of aryl thio substituents. Single step (irreversible), multi-electron oxidation, accompanied by decomposition, has been reported in sulfur containing MPc complexes [36]. Plots of the square root of the scan rate vs. current were linear for all the processes **I** to **III**, confirming diffusion control. No new peaks (or changes in peak shape) were obtained upon changing the scan rate. Compared to other peripherally substituted thiol derivatives [419], complexes **6d** and **8d** are easier to reduce. The differences in the electron-donating or -withdrawing nature of the ring substituent will affect the ease of oxidation.

Peak assignments in Table 3.3 were confirmed by spectroelectrochemistry [31].

3.1.3. Complex (OH)MnPc(SPh)₄ (6c)

Synthesis of **6c** is outlined in Scheme 3.4.
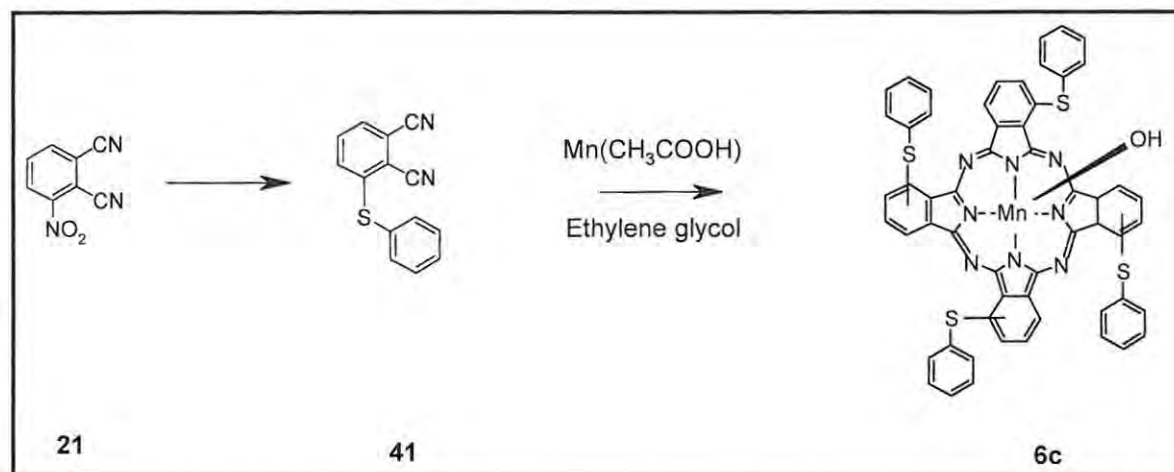
Scheme 3.4 Synthesis of (OH)MnPc(SPh)₄ (**6c**)

Complex **41**, available in the laboratory, were synthesised as described in Scheme 1.2. The disappearance of the sharp infrared nitrile (CN) band at 2226 cm^{-1} for **6c** confirmed the cyclotetramerization of the starting phthalonitrile **41**, Table 3.1. Complex **6c** was satisfactorily characterized using spectroscopic methods. Fig. 3.11 shows the UV-visible spectrum of complex **6c**. The Q band position is given Table 3.1.
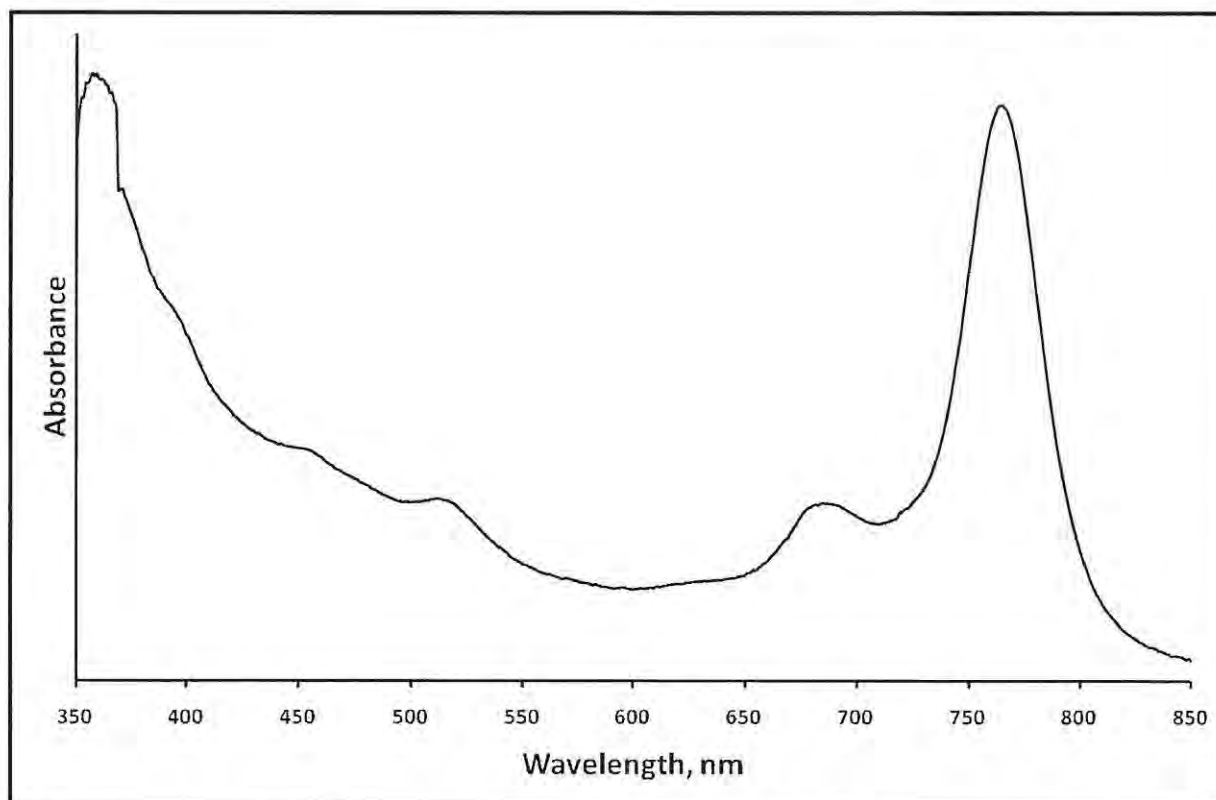
Fig. 3.11 UV-visible spectrum of (OH)MnPc(SPh)$_4$ (**6c**) in DMF. Concentration ≈ 1 µM

The UV-visible spectrum of **6c** in DMF displayed bands at 764, 681, 511, and 360 nm (Fig. 3.11). The UV-visible bands at 360 and 511 nm give **6c** its deep red colour [464]. The relatively large red-shift of the Q band (764 nm), typical of Mn^{III}Pc complexes [22,27,464,465] (Table 3.1), is enhanced by the electron-donating properties of sulfur. Table 3.1 shows that this complex is also more red-shifted than most other MnPcs due to nonperipheral substitution. Complex **6c** is soluble in a wide range of solvents ranging from less polar (e.g. DCM, CHCl$_3$) to more polar (e.g. DMSO, DMF).

Fig. 3.12 shows the cyclic and square wave (insert) voltammograms of complex **6c** in DMF.
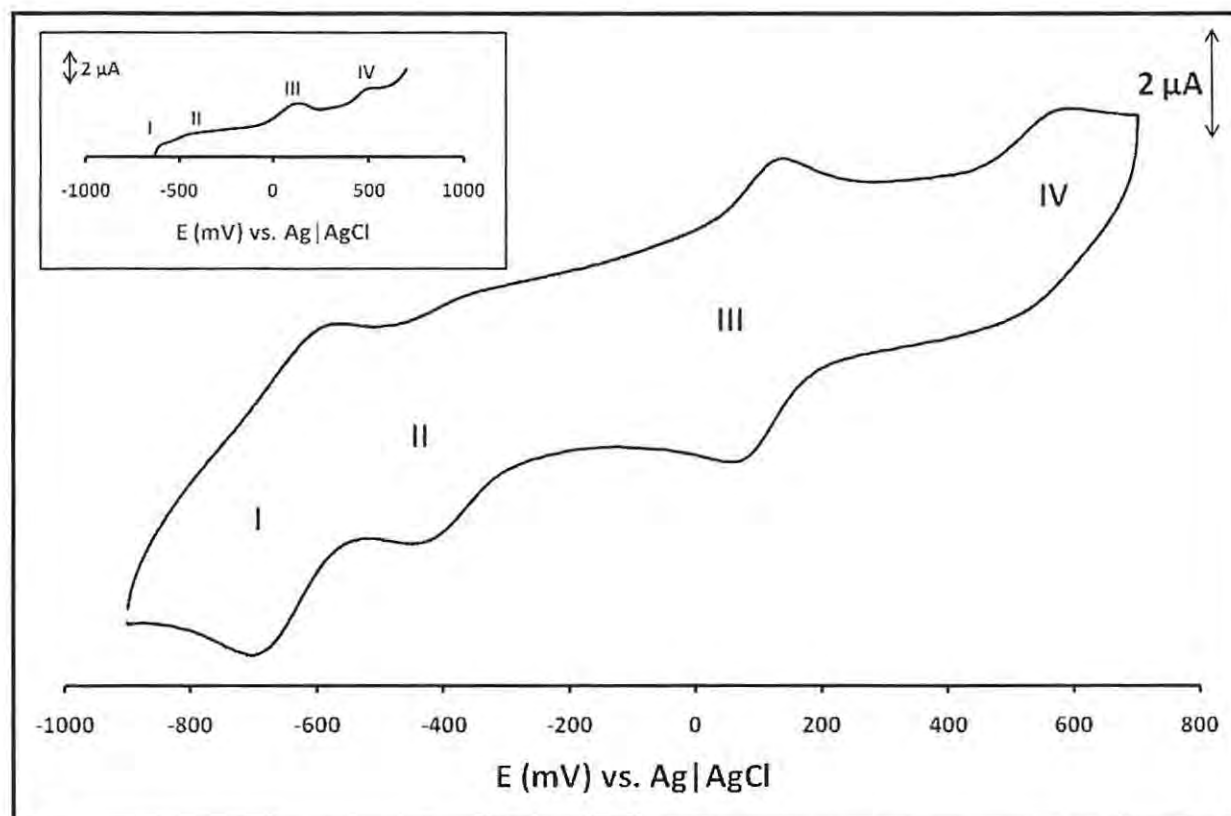
Fig. 3.12 Cyclic and square wave (insert) voltammograms of (OH)MnPc(SPh)$_4$ (**6c**) in DMF containing TBABF$_4$. Scan rate = 100 mV.s^{-1}

According to literature [27], the redox processes of **6c** are cautiously assigned as follows: **I**: Mn^{II}Pc^{-2}/Mn^{II}Pc^{-3}; **II**: Mn^{II}Pc^{-2}/Mn^{I}Pc^{-2}; **III**: Mn^{III}Pc^{-2}/Mn^{II}Pc^{-2}; **IV**: Mn^{III}Pc^{-1}/Mn^{III}Pc^{-2}. Processes **I** and **III** are relatively more reversible than processes **II** and **IV** (which exhibited quasi-reversible behaviour). No new peaks, other than those shown in Fig. 3.12, were obtained at different scan rates.

Chapter 3: Synthesis and characterization

3.1.4. Complex (OH)MnPc(SCH₂Ph)₄ (8b)

Synthesis of **8b** is outlined in Scheme 3.5.
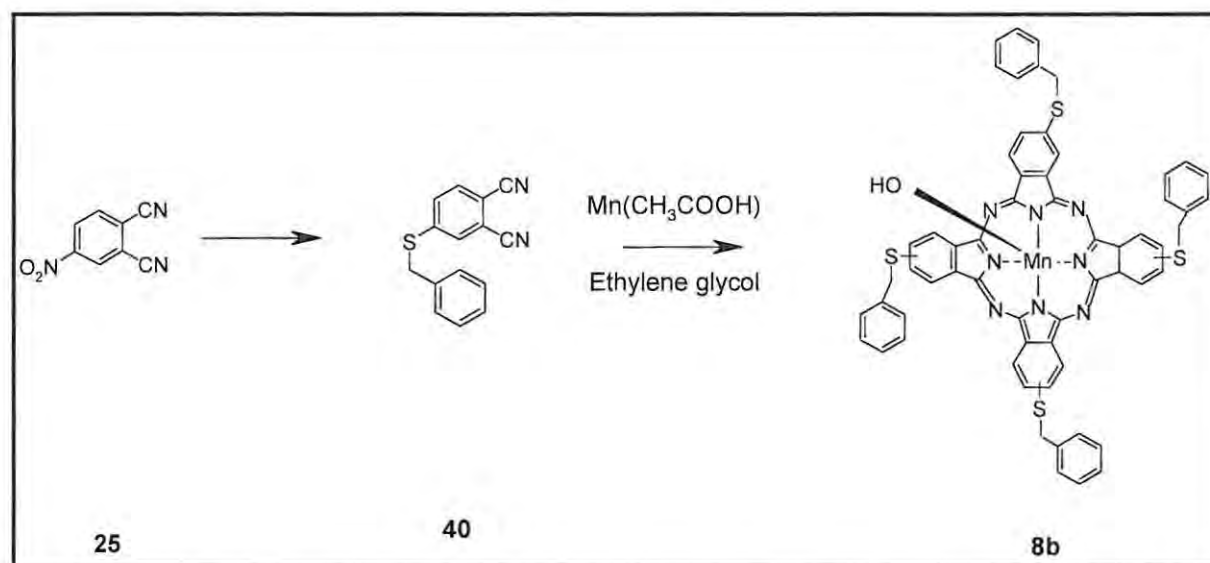
Scheme 3.5 Synthesis of (OH)MnPc(SCH₂Ph)₄ (**8b**)

Because the synthesis of **8b** has been reported [27] and was synthesized in this work specifically for SOD studies (Chapter 7), its characterization shall only be briefly discussed. Syntheses of complexes **25** and **40** was done according to Scheme 1.3 (both complexes were available in the laboratory).

As expected, no nitrile band (at ~2200 cm⁻¹) was observed in the infrared spectrum of **8b**, confirming, to some extent, the formation of the Pc, Table 3.1. C=C, Mn-OH, and C-S-C bands were observed in the infrared spectrum of **8b**.

Fig. 3.13 shows the UV-visible spectrum of **8b** in DMF, with λ_{max} at 777 nm (Table 3.1).
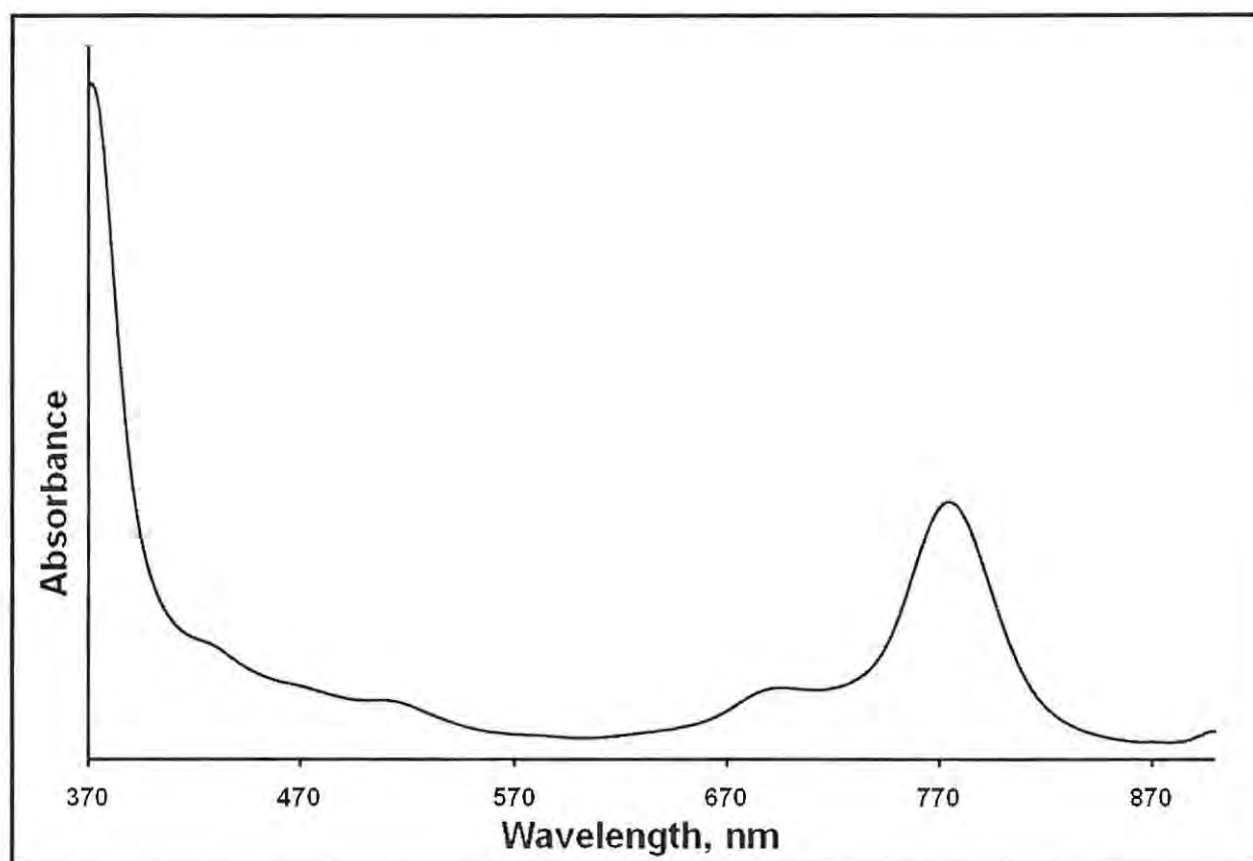
Fig. 3.13 UV-visible spectrum of **8b** in DMF. Concentration ≈ 1 μM

The UV-visible spectrum of **8b** in DMF displayed bands at 777, 692, 519, 434, and 373 nm, Fig. 3.13. As for complex **6c**, the significant red-shifting of the Q band (at 777 nm), especially in comparison with other MPcs of this work (Table 3.1), is due to the characteristic Mn metal and the sulfur electron-donating groups. Like **6c**, described above, complex **8b** is soluble in a wide range of solvents.

Fig. 3.14 shows the cyclic and square wave (insert) voltammograms of complex **8b** in THF.
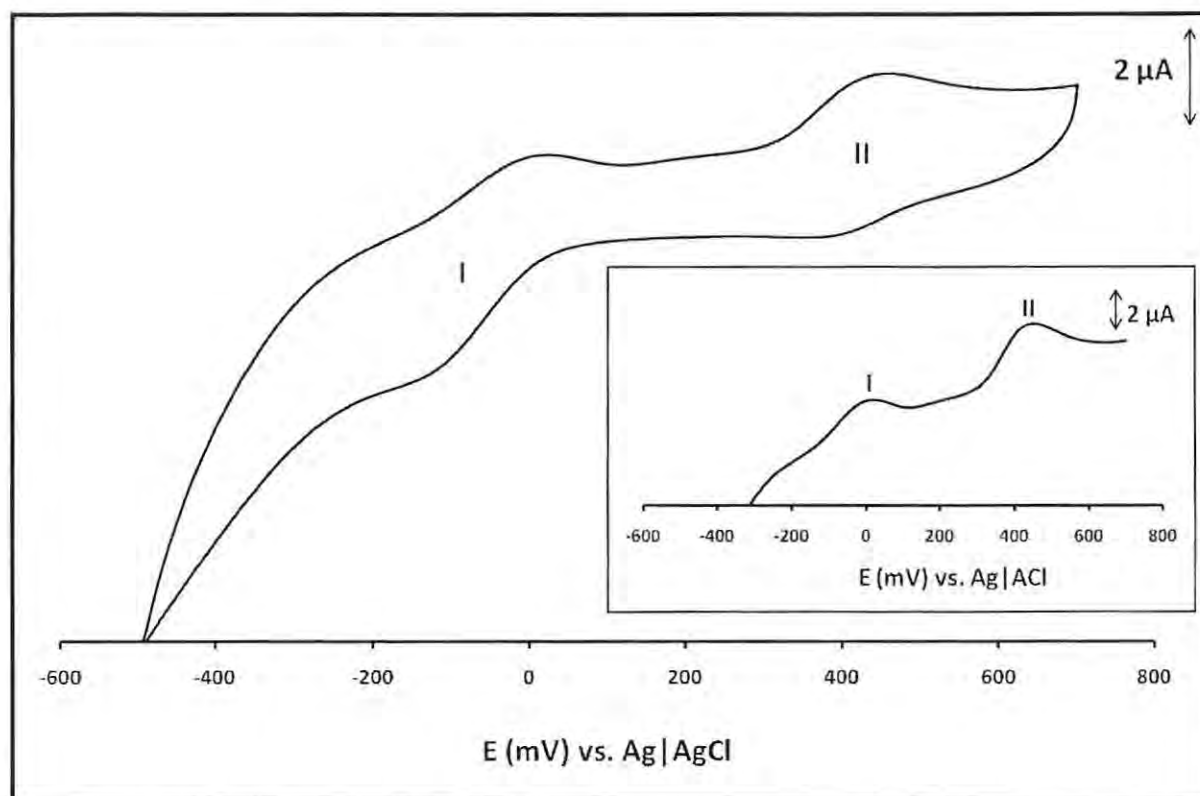
Fig. 3.14 Cyclic and square wave (insert) voltammograms of complex $(OH)MnPc(SCH_2Ph)_4$ (**8b**) in THF containing $TBABF_4$

From the literature [27], redox processes **I** and **II** of Fig. 3.14 correspond to $Mn^{III}Pc^{-2}/Mn^{II}Pc^{-2}$ and $Mn^{IV}Pc^{-2}/Mn^{III}Pc^{-2}$, respectively.

3.2. Cobalt carboxyl phthalocyanine complexes

Cobalt carboxyl complexes (**5g** (CoPc), **7a** $(CoPc(COOH)_4)$, and **10a** $(CoPc(COOH)_8))$ were synthesized and characterized according to the reported procedures [25,26,454]. Complexes **5g** and **7a** were available in the laboratory; but complex **10a** was synthesized for this work and hence its synthesis and characterization are described. Scheme 3.6 gives the synthetic outline of complex **10a**.
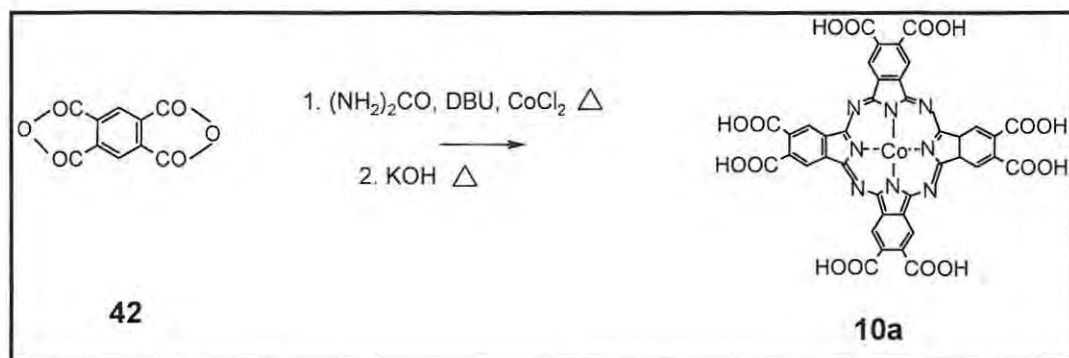
Scheme 3.6 Synthesis of CoPc(COOH)$_8$ (**10a**)

From Table 3.1, the C=C infrared bands of the CoPc complexes (**5g**, **7a**, and **10a**) occur at progressively higher wave numbers with increasing number of carboxy substituents. This suggests that the COOH groups do have some effect on the Pc properties. This observation is important for electrocatalytic studies as described in Chapter 5.

Fig. 3.15 shows the UV-visible spectra of **5g**, **7a**, and **10a** recorded in DMF. The Q band maxima of the CoPc complexes are listed in Table 3.1.
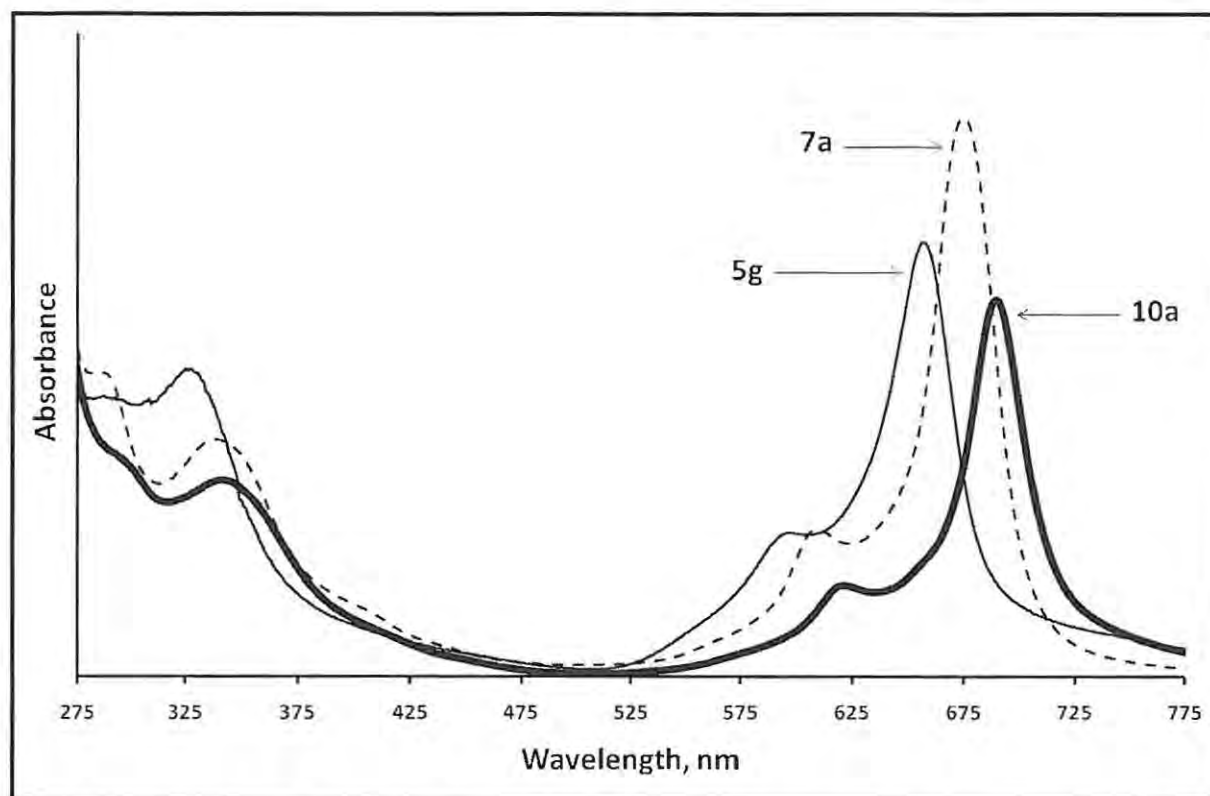
Fig. 3.15 UV-visible spectra of **5g** (CoPc), **7a** (CoPc(COOH)$_4$), and **10a** (CoPc(COOH)$_8$) recorded in DMF

From Fig. 3.15, there is an increase in the Q band maximum with increasing number of carboxyl substituents. Q band maxima are: CoPc = 657 nm, CoPc(COOH)$_4$ = 675 nm, CoPc(COOH)$_8$ = 689 nm. The number of carboxyl substituents thus exerts a significant effect on Pc spectral properties, supporting the argument that the substituent effect on the Pc electrocatalytic properties, described in Chapter 5, is an important study.

Since the complexes are known, no further characterization is provided but were as reported in literature [23,26]. The CV of adsorbed complexes will be provided in Chapter 5.

3.3. Complex (Na)$_4$(OH)MnPc(SO$_3$)$_4$ (8f)

Complex **8f** is well known and used in this work uniquely as a SOD mimic (Chapter 7). Its synthesis and characterization are only briefly described.

The microwave synthesis of **8f** is outlined in Scheme 3.7.

104
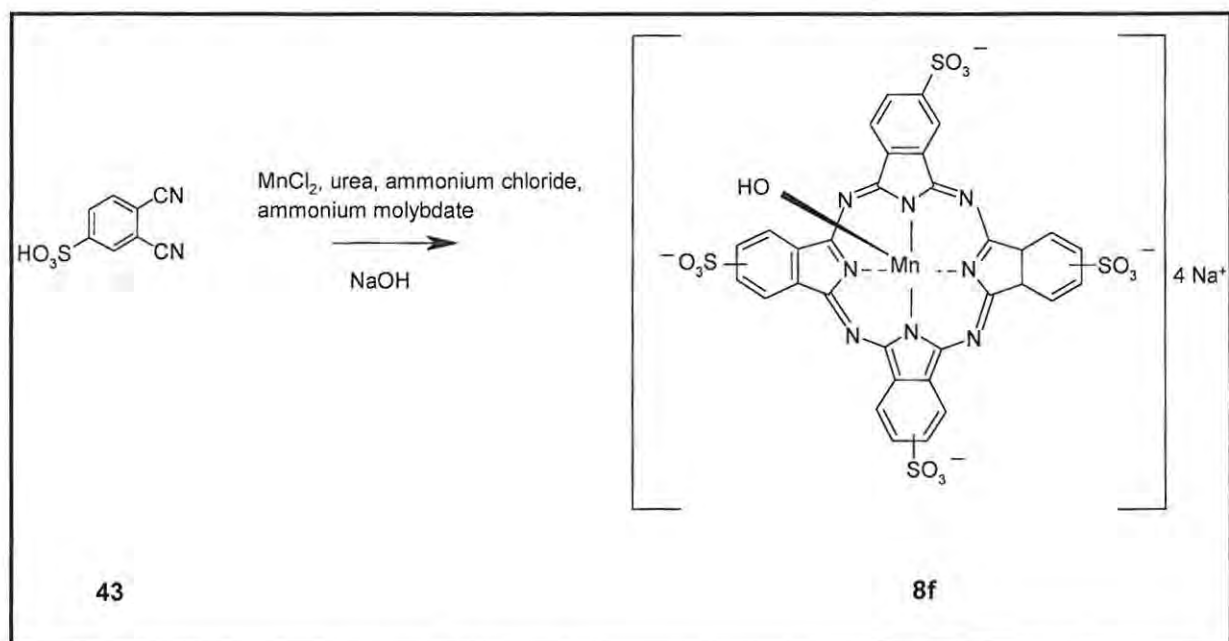
Scheme 3.7 Synthesis of $(Na)_4(OH)MnPc(SO_3)_4$ (**8f**)

The microwave synthesis of sulfonated Pcs, such as shown in Scheme 3.7, is a quick, convenient, and recently reported technique [28,466]. The infrared spectrum of **8f** showed the expected C=C band at 1637 cm^{-1}, Table 3.1. The UV-visible spectrum of **8f** is shown in Fig. 3.16.
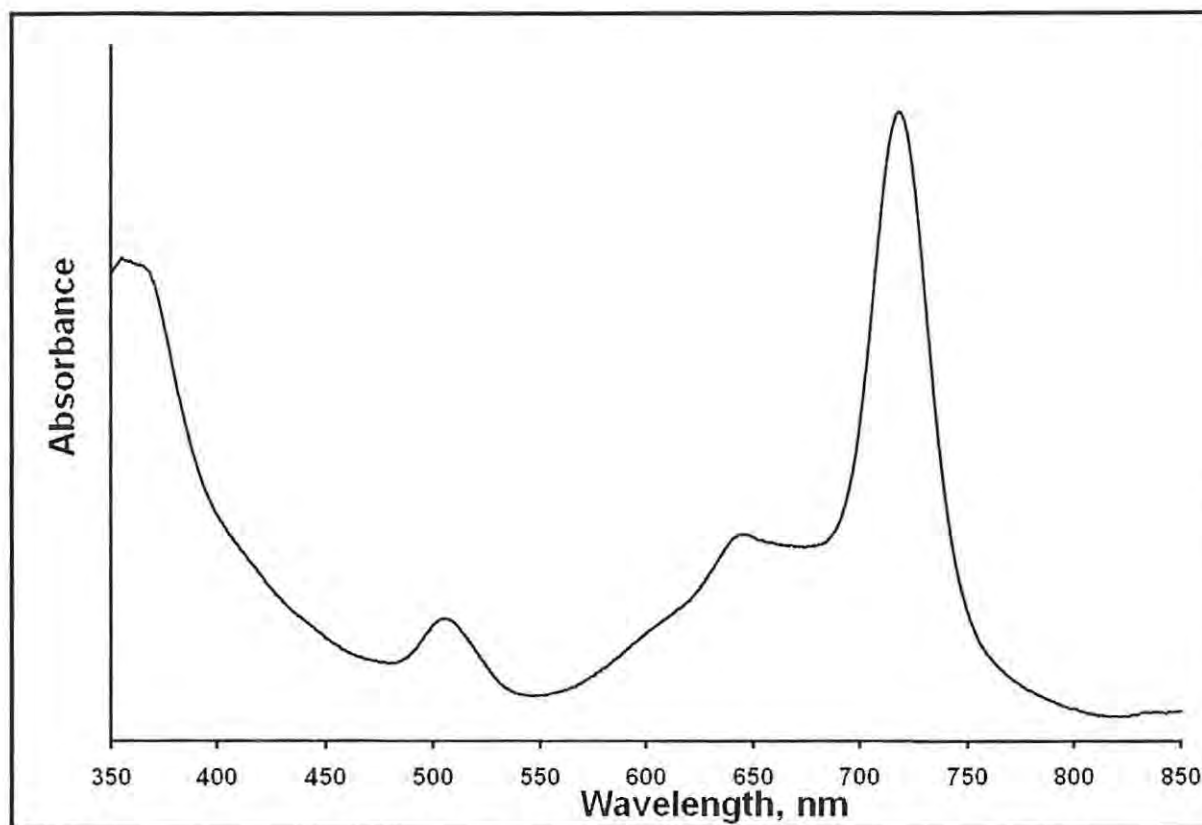
Fig. 3.16 UV-visible spectrum of $(Na)_4(OH)MnPc(SO_3)_4$ (**8f**) recorded in DMF. Concentration ≈ 1 μM

Complex **8f** displayed UV-visible spectral bands at 720, 650, 507, and 360 nm, Fig. 3.16. As expected for MnPc complexes, λ_{max} of **8f** (at 720 nm) shows a large red shift in comparison to the Fe and Co Pcs of this work (and like other MnPcs), Table 3.1. All other characterizations were as reported in the literature [28,466].

3.4. Conclusions

The syntheses of complexes **9b** and **10b** are reported for the first time. Complex **9b** gives best yields when synthesized using the urea method. Complex **10b** was synthesized according to the reported synthesis of octakis(alkylthio)-substituted phthalocyanines. It was important to use the anhydrous form of the metal salt ($CoCl_2$) because this gives a purer product.

All complexes of this work are soluble in common organic solvents (e.g. DMF), with the quaternized MnPc derivatives (**6e**, **8e**, and **8f**) also being water soluble. The infrared spectra of

all synthesized complexes displayed the expected characteristic bands. The UV-visible spectra of the complexes displayed wavelength maxima between 657 nm (for **5g**) and 777 nm (for **8b**) showing the effect of the central Pc metal and substituents on the absorption maximum. Furthermore, most synthesized complexes displayed absorption maxima that were mostly red-shifted relative to their unsubstituted counterparts, primarily due to the electron-donating nature of the sulfur groups. The quaternized complexes (**6e** and **8e**) are blue-shifted compared to the corresponding unquaternized derivatives (**6d** and **8d**) due to the lowering of the electron-donating ability of the nitrogen groups on quaternization. The infrared and UV-visible spectra of **5g**, **7a**, and **10a** suggest that the COOH groups do have an effect on the Pc properties.

Two metal-based redox processes ($M^{III}Pc^{-2}/M^{II}Pc^{-2}$ and $M^{II}Pc^{-2}/M^{I}Pc^{-2}$) were observed for **9b** and **10b**. Complex **9b** displayed four ring redox processes, whilst three such processes were observed for complex **10b**. The potentials for the first reduction of complexes **9b** and **10b** are much less negative than those of other thio-substituted CoPc and FePc complexes. This suggests that the phenylthiol substituents confer ease of reduction on the CoPc and FePc species. The MnPc complexes **6d**, **6e**, **8d**, and **8e** each displayed three redox processes, two of which are metal based. This work reports the formation of Mn(I)Pc species from the first reduction step of $Mn^{II}Pc^{-2}$, which depends on the nature of the substituents for the MnTMPyPc complexes.

CHAPTER 4: ELECTRODE MODIFICATION BY GRAFTING

This work presents the first report of the coordination of a metallophthalocyanine (MPc) to an electrode pre-modified with aryl radicals. MPc complexes (especially CoPc derivatives) are excellent electrocatalysts for many analytes. The most effective methods of electrode modification using MPc complexes include electropolymerization and the formation of self-assembled monolayers. Both of these require synthesis of derivatised MPc species, which is time consuming. The method presented in this work provides a new way of forming a stable electrode with the readily available MPc complex, $CoPc(COOH)_4$ (**7a**), without the need for complicated and lengthy syntheses.

4.1. Characterization

Scheme 4.1 represents the modification of a glassy carbon electrode (GCE) by grafting employed in this work.

Chapter 4: Electrode modification by grafting
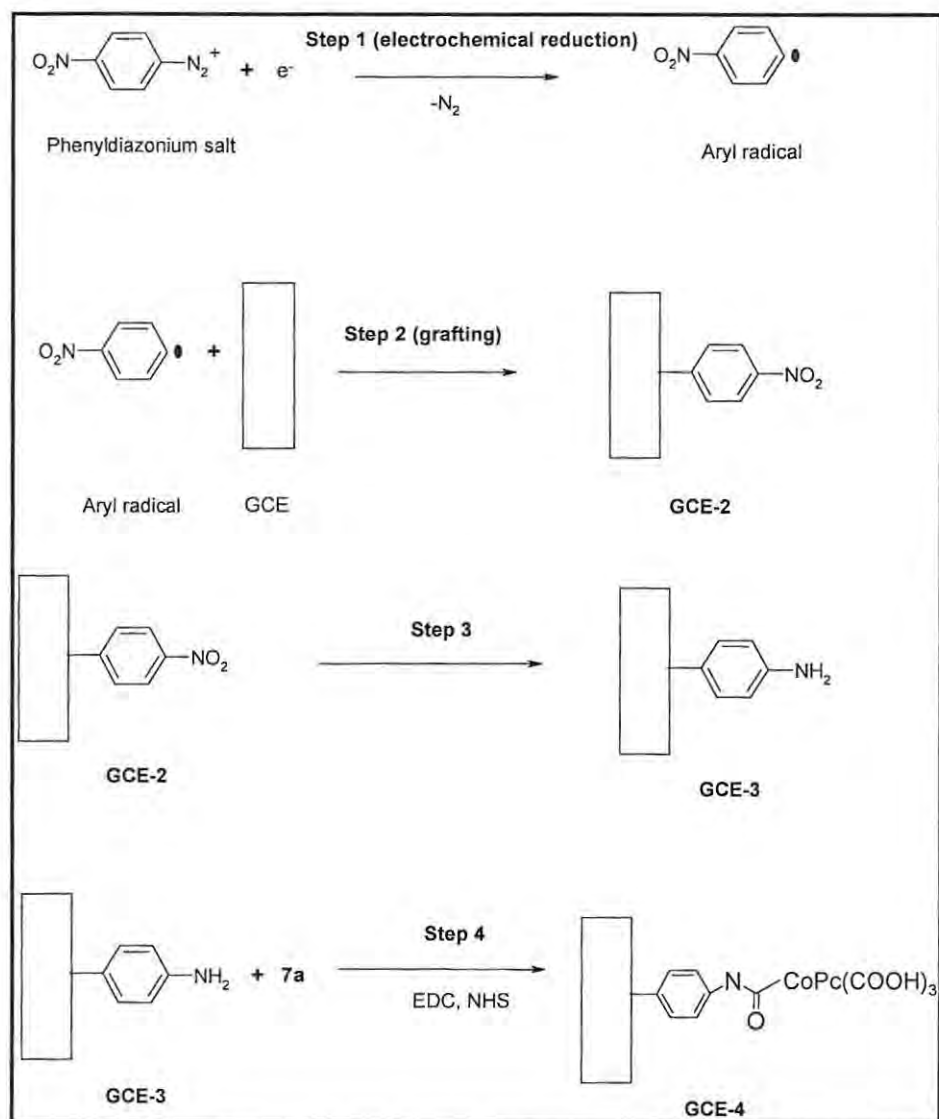
Scheme 4.1 Aryl radical modification of a GCE

Step 1 involves the electrochemical reduction of a phenyldiazonium salt to an aryl radical, Scheme 4.1. Step 2 involves the grafting of the aryl radical to a GCE [189] to form **GCE-2**. This is followed by the electrochemical reduction of the NO_2 group (of **GCE-2**) to NH_2 forming **GCE-3**, Step 3 (Scheme 4.1). $CoPc(COOH)_4$ (**7a**) is then attached to the NH_2 group (of **GCE-3**) using a combination of 1-ethyl-3-(3-dimethylaminopropyl)-carbodiimide (EDC) and N-hydroxysuccinimide (NHS) as coupling agents, Step 4 (Scheme 4.1), forming the amide bond functionalized **GCE-4**. Scheme 4.2 exemplifies this amide bond formation (Step 4, Scheme 4.1) using EDC and NHS.

Chapter 4: Electrode modification by grafting
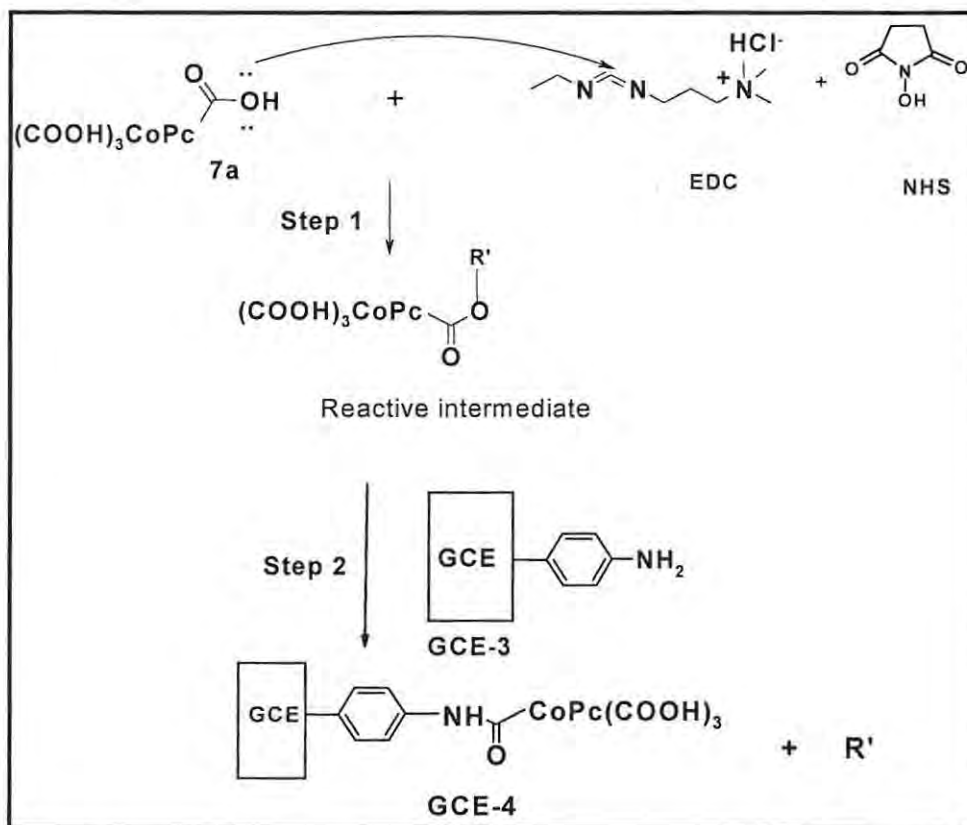
Scheme 4.2 Formation of **GCE-4**

EDC is an agent used extensively to couple carboxyl groups to amines, e.g. in peptide synthesis, to form amide bonds. EDC alone is, however, not efficient in forming amide bonds because failure to react quickly with an amine results in hydrolysis and regeneration of the carboxyl. NHS is thus used in conjunction with EDC to enhance the efficiency of EDC coupling [467-470]; NHS, used in conjunction with EDC, converts carboxyl groups to more stable intermediates.

Jiang *et al* [471] have estimated that, using the mixture of EDC and NHS, about 60 % of carboxylic acid groups are NHS activated, 30 % EDC activated, leaving only 10 % not activated. Scheme 4.2 shows the mechanistic activation of a carboxylic acid group of $CoPc(COOH)_4$ by EDC and NHS forming a reactive intermediate. This is followed by the reaction of this intermediate with an amine on **GCE-3** and the formation of an amide bond [472]. This last reaction forms **GCE-4**. Several coupling times (4, 8, 12, and 24 hours) were studied but the best

110

results, especially with respect to surface coverage, were obtained after a 24 hour coupling time. Characterization of these electrodes in a $K_3Fe(CN)_6$ (Fe^{III}/Fe^{II} couple) solution revealed that maximum surface coverage and the smallest background currents were obtained after a 24 hour coupling time.

The initial part in the modification of glassy carbon electrodes of this work involves aryl radicals being generated from the electrochemical reduction of 4-nitrobenzenediazonium tetrafluoroborate (phenyldiazonium salt, Scheme 4.1) [22]. Such aryl radicals are unstable and react immediately with the electrode surface. This leads to the formation of strong covalent carbon-carbon bonds between the carbon of the GCE and the nitrophenyl group (Step 2, Scheme 4.1). Fig. 4.1 shows the cyclic voltammograms for scan numbers 1, 2, and 50 (labeled with arrows) of a GCE recorded in a fresh solution of 0.01 M phenyldiazonium salt, in acetonitrile containing 0.1 M TBABF$_4$.
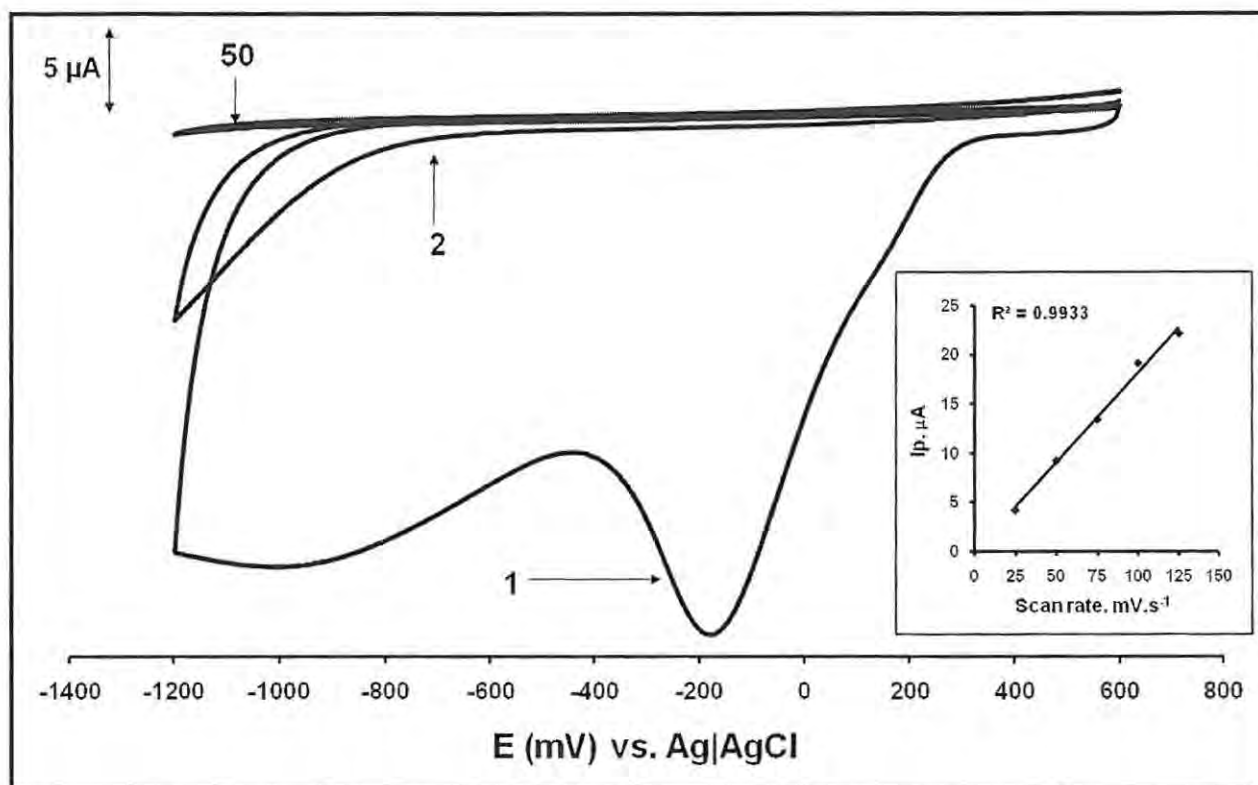
Fig. 4.1 Cyclic voltammograms of a GCE recorded in 0.01 M of phenyldiazonium salt. Scan rate = 200 mV.s^{-1}. Insert: peak current (I$_p$) vs. scan rate plot for scan 1

The broad peak, at approximately -1.0 V (Fig. 4.1, scan 1), corresponds to the one electron reduction of phenyldiazonium salt, step 1 (Scheme 4.1), Eq. 4.1 [188]:

$$(NO_2)ArN_2^+ + e^- \rightarrow (NO_2)Ar^\bullet + N_2 \qquad\qquad 4.1$$
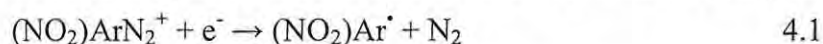
where Ar represents the aryl group (C$_6$H$_4$) and Ar$^\bullet$ the aryl radical.

The irreversible peak of scan 1 (Fig. 4.1), at approximately -0.2 V, is due to adsorbed species of phenyldiazonium salt, as has been reported previously [188]. This fact was confirmed by a plot of peak current (I$_p$) vs. scan rate for this peak (Fig. 4.1, insert). The straight line obtained proved that the peak (at -0.20 V) is due to a surface reaction. For the adsorbed state of phenyldiazonium salt, the activation energy for reduction (which is related to the applied overpotential) is much smaller than the activation energy of unadsorbed species (a broad reduction wave around -1.0 V). In Fig. 4.1, there is a clear difference (i.e. inhibition of redox processes) between scan number 1 and scan number 2. This observed inhibition is due to the layer of GCE bound nitrophenyls

blocking any electron transfer and thus explains the absence of redox peaks in scan number 2 [188].

The cyclic voltammogram of **GCE-2**, after derivatization by cyclic voltammetry multi-scanning in a solution of 0.01 M phenyldiazonium salt in acetonitrile containing 0.1 M TBABF$_4$ (for 50 scans) and then rinsing thoroughly with acetone, was recorded in a blank solution of 0.1 M TBABF$_4$ in acetonitrile. The result is shown in Fig. 4.2.
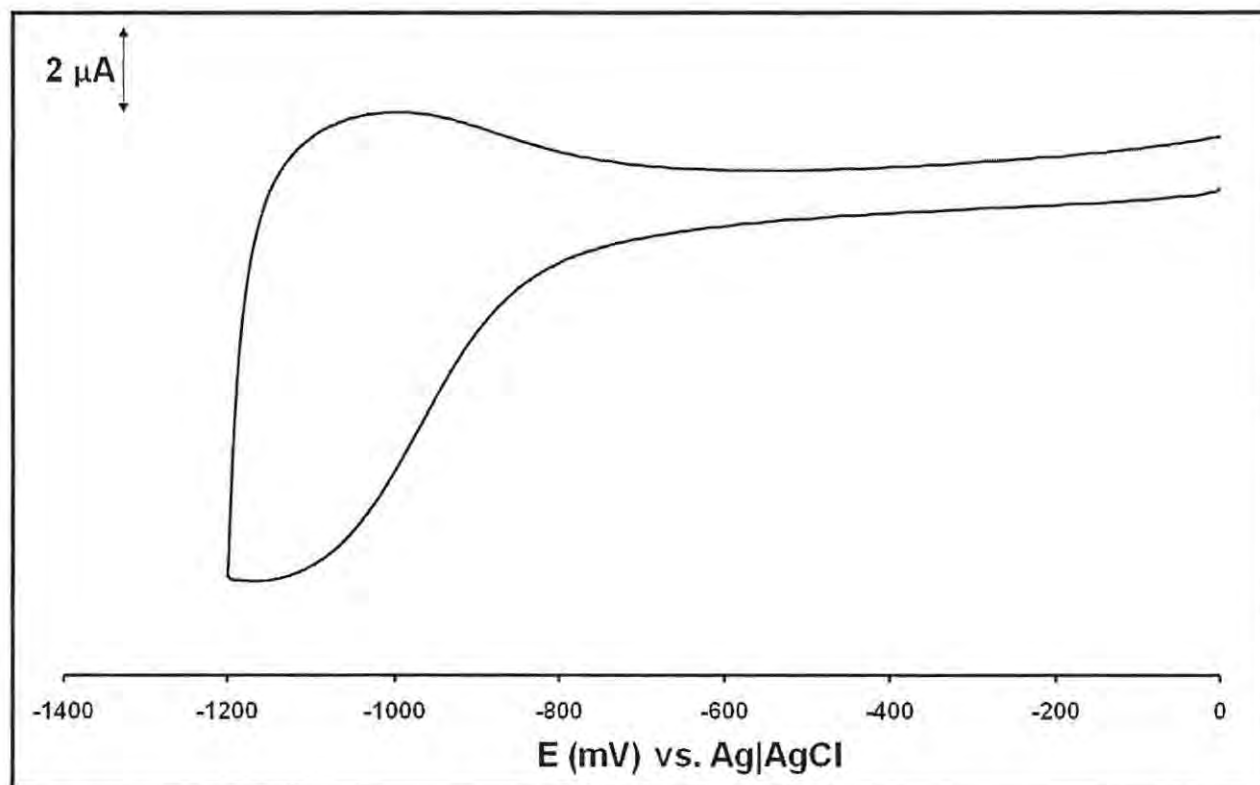
Fig. 4.2 Cyclic voltammogram of **GCE-2**, after derivatization, recorded in 0.1 M TBABF$_4$ in acetonitrile. Scan rate = 200 mV.s^{-1}

The quasi-reversible cyclic voltammetric peak around -1.1 V in Fig. 4.2 is due to the 4-nitrophenyl group redox process, Eq. 4.2 [188]:

$$GCE\text{-}ArNO_2 + e^- \leftrightarrow GCE\text{-}ArNO_2^{\bullet-} \qquad\qquad 4.2$$

where GCE = GCE surface and Ar = C$_6$H$_4$.

The redox process in Fig. 4.2 occurs near the potential of nitrobenzene itself [188] and was observed even after several scans. The electrochemical reduction of the NO$_2$ to NH$_2$ to form the

113

aryl amino functionalized **GCE-3** (Step 3, Scheme 4.1) [190] was carried out as follows. **GCE-2** was thoroughly rinsed with acetone to remove any unadsorbed species, then transferred to a solution of 0.1 M KCl in EtOH:H$_2$O (1:9, v:v). The cyclic voltammetric results of **GCE-2** in this solution are shown in Fig. 4.3.
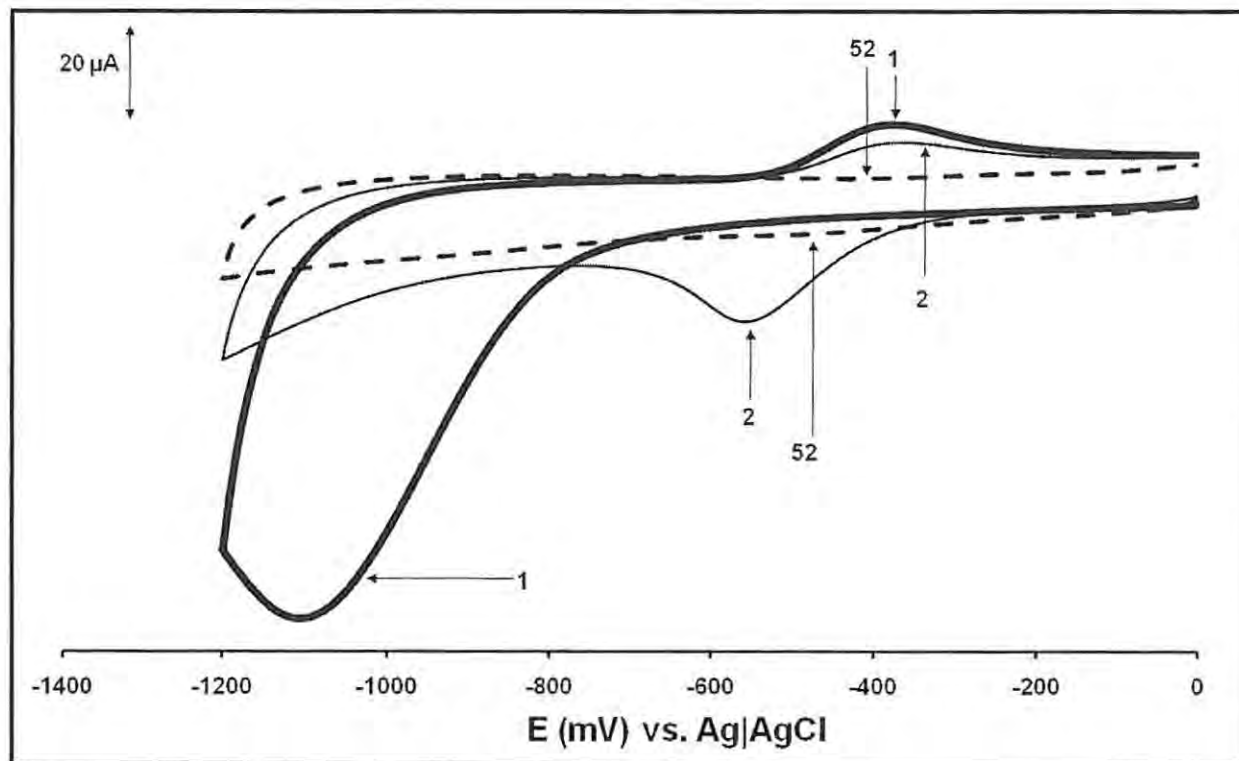
Fig. 4.3 Cyclic voltammogram of **GCE-2** recorded in 0.1 M KCl in EtOH:H$_2$O (1:9, v:v). Scan rate = 200 mV.s^{-1}

Scan number 1 of Fig. 4.3 has a broad reduction peak at -1.15 V and an anode peak at E$_p$ ≈ -0.4 V. The peak at -1.15 V is related to the six-electron reduction of nitrophenyl to phenylhydroxylamine [192,473]. Then, upon reversal of the scan direction, some of the phenylhydroxylamine formed is oxidized at -0.4 V to nitrosobenzene. The formation of ArNH$_2$ from the reduction of the nitrosobenzene corresponds to the reduction peak at -0.55 V during the second scan [192,473]. With each scan, more phenylhydroxylamine is converted into ArNH$_2$ and the peak currents decrease with scan number from 2 to 52 (due to inhibition by the layers of NH$_2$) and finally disappear when the conversion is complete (scan number 52, Fig. 4.3). The

114

overall transformation of $ArNO_2$ to $ArNH_2$ may be represented by the following equation [473-475]:

$$GCE\text{-}ArNO_2 + 6e^- + 6H^+ \rightarrow GCE\text{-}ArNH_2 + 2H_2O \qquad 4.3$$

where $Ar = C_6H_4$.

The fact that no reductive peak at -0.55 V was observed in the first scan can be explained by the absence of nitrosobenzene, which is formed for the first time at the end of scan number 1.

Fig. 4.4 shows the cyclic voltammograms of **GCE-4** recorded in a blank (1 M $HClO_4$) solution showing the dependence of peak current on scan rate. The insert of Fig. 4.4 shows the linear dependence of peak current on scan rate of **GCE-4** in a blank (1 M $HClO_4$) solution, which is typical of adsorbed species.
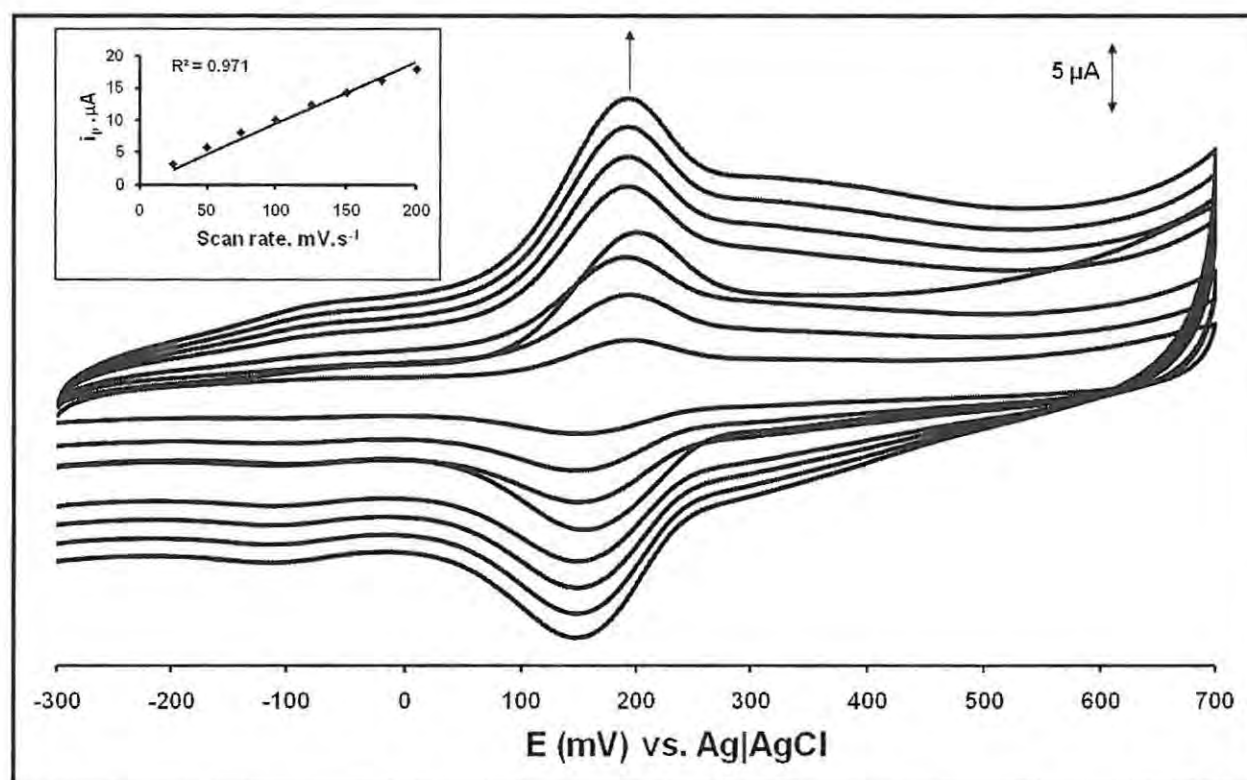
Fig. 4.4 Cyclic voltammograms of **GCE-4** recorded in 1 M $HClO_4$ (25 - 200 mV.s^{-1}). Insert: scan rate study of **GCE-4** in 1 M $HClO_4$

The peak couple at approximately 150 mV in Fig. 4.4 is assigned to $Co^{III}Pc^{-2}/Co^{II}Pc^{-2}$.

Surface coverage (Γ) may be calculated using [106]:

$$i_p = \frac{n^2 F^2 A \Gamma (v)}{4RT} \qquad\qquad 4.4$$

where i_p is the peak current (amps), n is the number of electrons, F is the Faraday constant (F = 96485 C.mol^{-1}), A is the electrode surface area (cm^2), v is the scan rate (V.s^{-1}), R is the gas constant (R = 8.314 J.K^{-1}.mol^{-1}), and T is the temperature in Kelvin. The Γ value of **GCE-4** was estimated from the background corrected peak current (i_p) under the [Co^{III}Pc^{-2}/Co^{II}Pc^{-2}] couple (Fig. 4.4) and its value of 4.2×10^{-9} mol.cm^{-2} is forty times higher than the 1×10^{-10} mol.cm^{-2} range reported for metallophthalocyanines lying flat on the surface [476-478]. This supports the expected perpendicular orientation of CoPc(COOH)$_4$ in **GCE-4**.

4.2. Electroanalysis

4.2.1. Electrocatalytic activity of GCE-4 towards thiocyanate

GCE-4 cannot detect other analytes of this work (melatonin, nitrite, and L-cysteine) hence only the electrocatalytic activity of this electrode towards thiocyanate is reported.

Fig. 4.5 shows the cyclic voltammogramms of **GCE-4** recorded in the absence (1) and presence (2) of thiocyanate in pH 4 buffer.
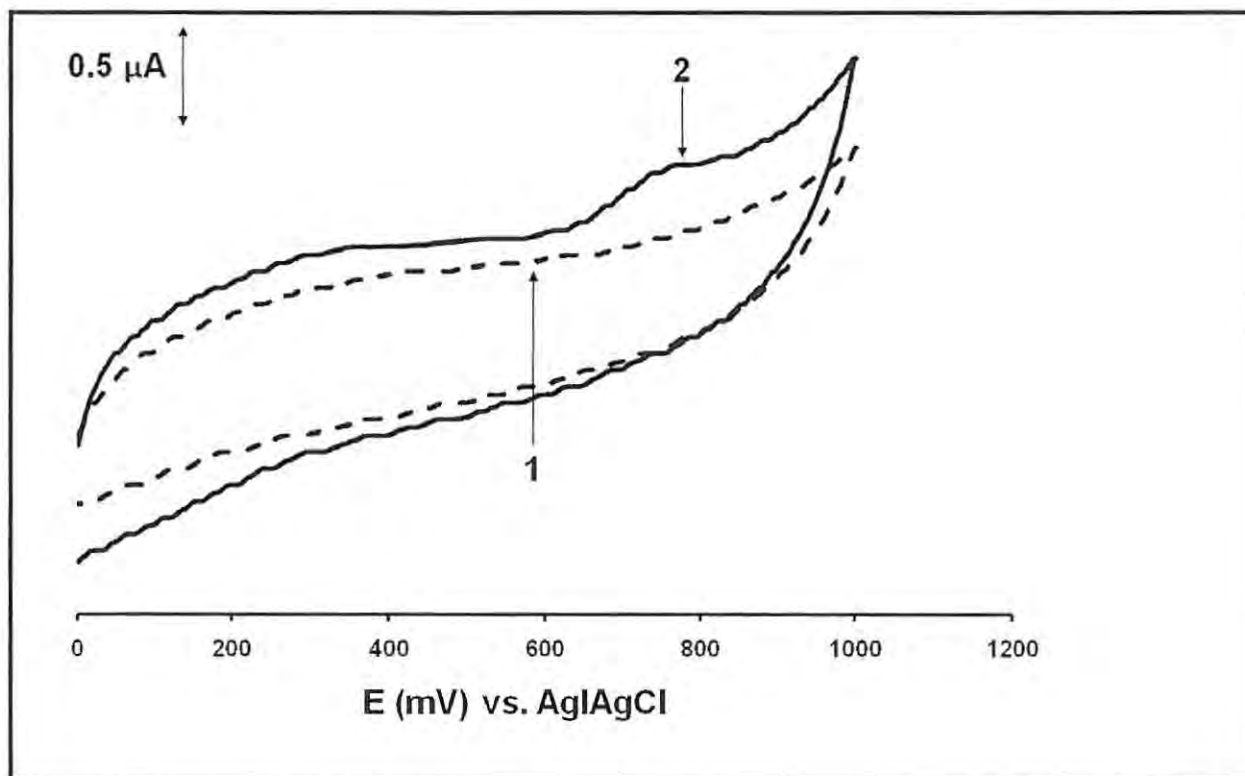
Fig. 4.5 Cyclic voltammograms of **GCE-4** recorded in pH 4 buffer (1) and 7.2 × 10^{-4} M thiocyanate (2). Scan rate = 200 mV.s^{-1}

When **GCE-4** is immersed in a pH 4 buffer the $Co^{III}Pc^{-2}/Co^{II}Pc^{-2}$ Pc peak shown in Fig. 4.4 is no longer observed in Fig. 4.5. This may be tentatively suggested as being due to the catalytic process of this peak working on the thiocyanate (mechanism below) and hence it would not be as clear as in a blank solution (Fig. 4.4).

No peaks were observed on un-modified GCE, **GCE-2**, or **GCE-3** recorded in thiocyanate in pH 4 buffer (curves not shown). But on **GCE-4** an oxidation peak was clearly observed at $E_p \approx 0.75$ V (Fig. 4.5, curve 2). The observation of the peak proves electrocatalytic activity of **GCE-4** towards the oxidation of thiocyanate. Previous studies [23] showed that the peak for the electrocatalyzed oxidation of thiocyanate occurred at similar potentials to those reported in this work, Table 4.1.

Table 4.1 Electrochemical parameters of thiocyanate determination[a]

MPc	Electrode	E_p (V) vs. Ag|AgCl	LOD (M)	Ref.
CoPc(COOH)$_4$	**GCE-4**	0.75	6.5×10^{-6}	This work
CoOBTPc	Au SAM	0.78	1.1×10^{-7}	23
CoOHETPc	Au SAM	0.75	9.1×10^{-6}	23
CoPc	PVC membrane	Not stated	5.0×10^{-7}	321
FeOBTPc	Au SAM	0.76	1.0×10^{-7}	23
FeOHETPc	Au SAM	0.74	9.1×10^{-6}	23

[a]OBTPc = octabutylthiometallophthalocyanine; OHETPc = octa(hydroxyethylthio) phthalocyanine; Au SAM = self assembled monolayer on gold electrode; PVC = polyvinyl chloride

The Tafel slope was determined by using the standard equation (Eq. 4.5) for a totally irreversible process [455]:

$$E_p = \frac{2.3RT}{2(1-\alpha)nF}\log\upsilon + K \qquad\qquad 4.5$$

where α is the transfer coefficient, υ the scan rate, n the number of electrons involved in the rate determining step and K is the intercept. A plot of E_p vs. log v for **GCE-4** in thiocyanate in pH 4 buffer solution (Fig. 4.6) gave a linear relationship.
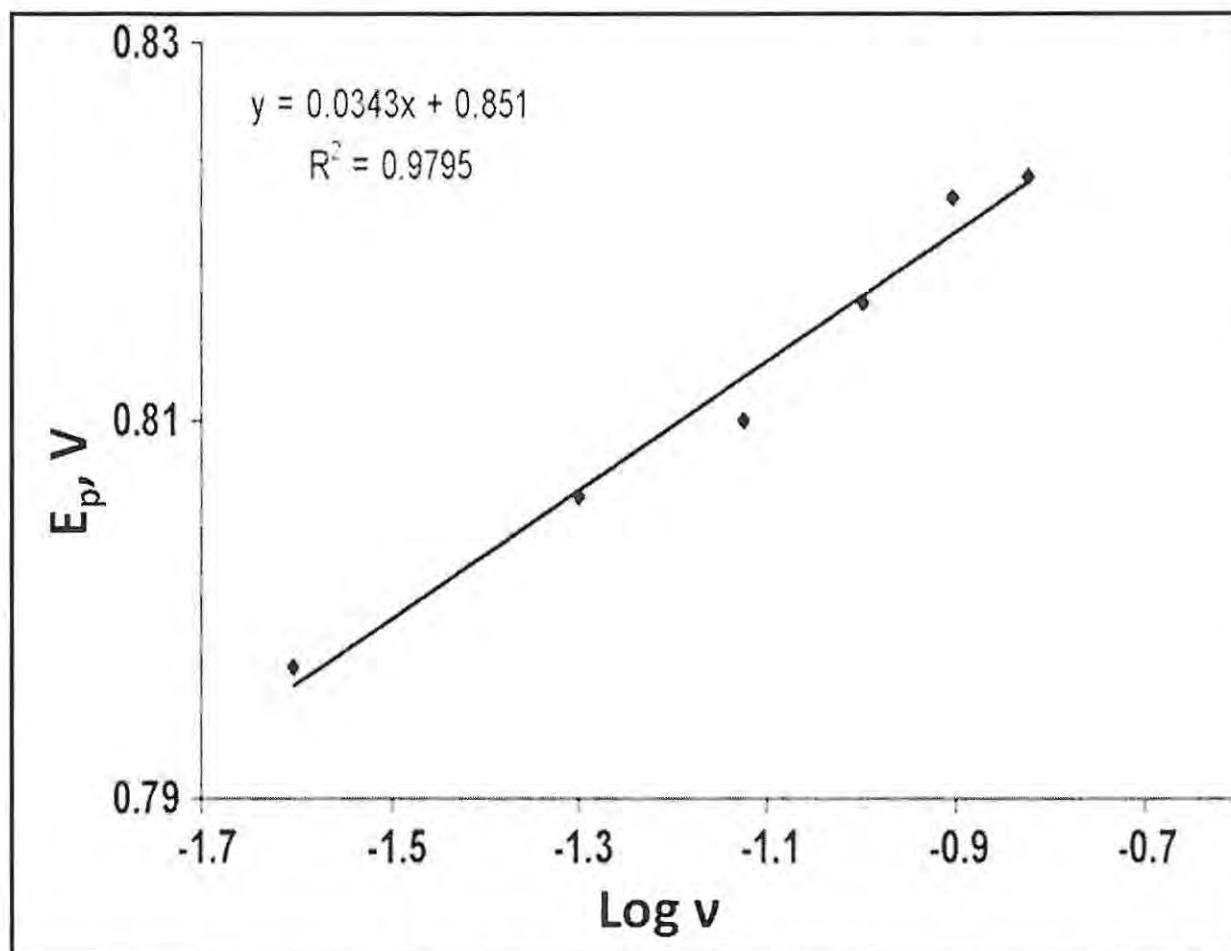
Fig. 4.6 Plot of E_p vs. log v for **GCE-4** in 7.2×10^{-4} M thiocyanate in pH 4 buffer solution

A Tafel slope (calculated using Eq. 4.5) of 68 mV.decade^{-1} indicates that a fast one-electron transfer is followed by a slow chemical step. The calculated α value of approximately 0.5 (α = 0.6) suggests that there is an almost equal probability of forming either products or reactants from the reaction transition state. The total number of electrons (n_t) involved in the electrocatalytic oxidation of thiocyanate was calculated using Eq. 4.6, valid for a totally irreversible electrode process [455]:

$$i_p = 2.99x10^5 n_t \left[(1-\alpha)n\right]^{\frac{1}{2}} AC_o D^{\frac{1}{2}} v^{\frac{1}{2}} \qquad 4.6$$

where A is the area of the electrode (cm^2), C_o the concentration of the electroactive reactant (mol.cm^{-3}), and D is the diffusion coefficient of thiocyanate (D = 2.15×10^{-5} cm^2.s^{-1} [479]). The total number of electrons transferred, calculated using Eq. 4.6, was calculated as one (n_t = 1.3).

Fig. 4.7 shows the linear relationship ($R^2 = 0.990$) between the peak current and the thiocyanate ion concentration (mM range) for **GCE-4**.
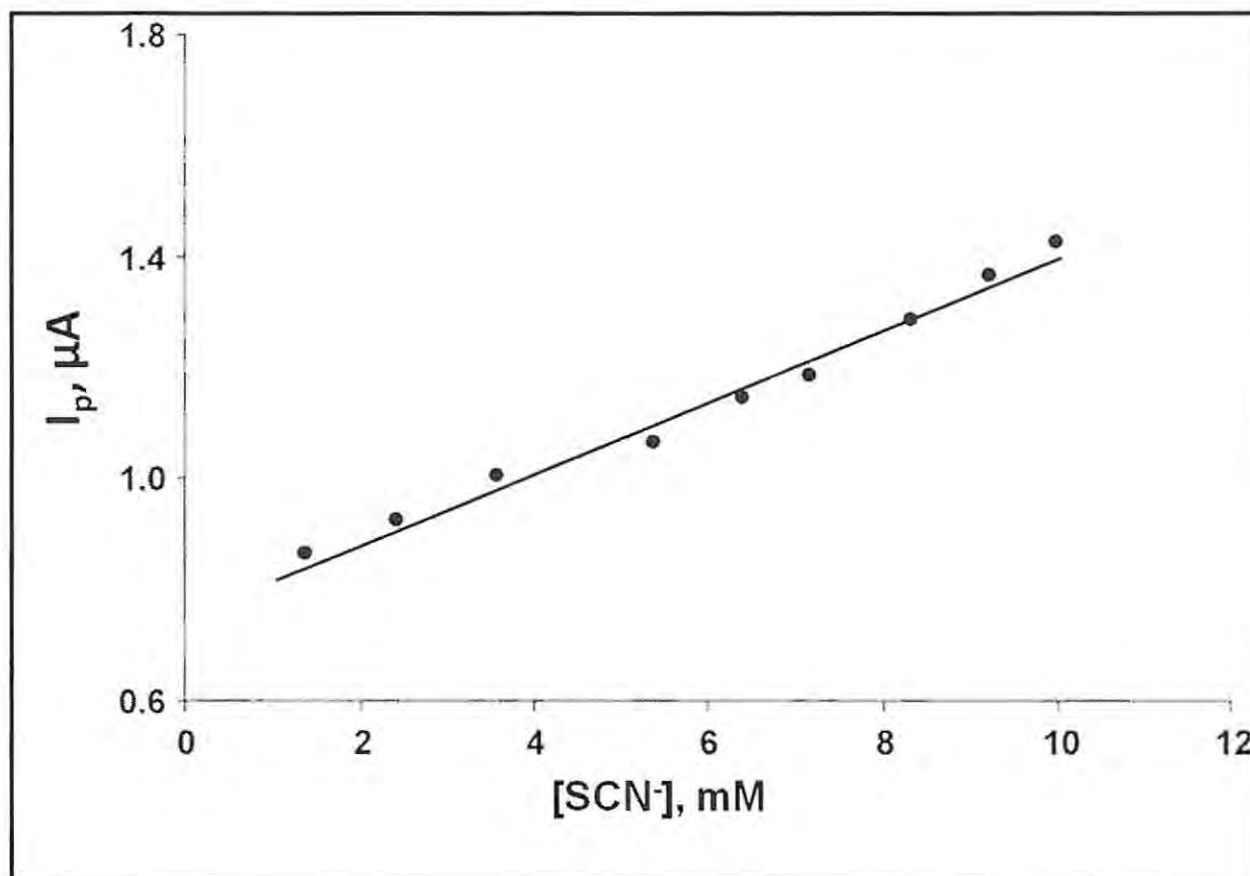
Fig. 4.7 Plot of peak current vs. thiocyanate (SCN⁻) concentration

The linear range was 0.001 - 0.01 M and a sensitivity of 67 $\mu A.M^{-1}$ was obtained. **GCE-4** is useful for analyses of thiocyanate concentrations up to 0.01 M (beyond which the linear relationship is lost). Due to the linear relationship of Fig. 4.7, the graph may be used as an analytical tool for determining the concentration of thiocyanate in solution in this range. The detection limit is 6.5 × 10^{-6} M (3σ criteria), a value which is comparable to other types of thiocyanate selective electrodes [23,323,480,481], Table 4.1.

4.2.2. Possible mechanisms

Fig. 4.8 shows the UV-visible spectra of $CoPc(COOH)_4$ (1) and $CoPc(COOH)_4$ + SCN⁻ (2) recorded in DMF.
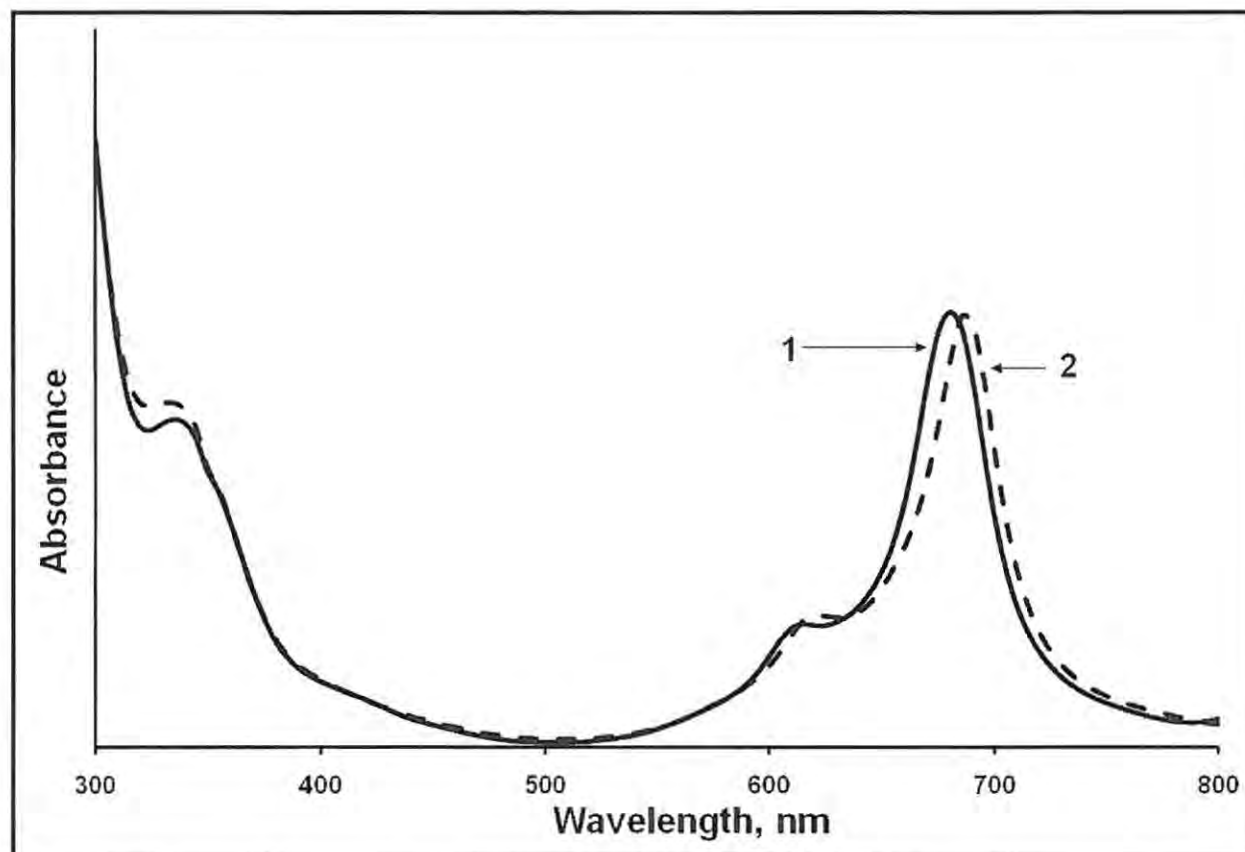
Fig. 4.8 UV-visible spectra of $CoPc(COOH)_4$ (1) and $CoPc(COOH)_4$ + SCN⁻ (2) recorded in DMF. Concentration of $CoPc(COOH)_4 \approx 1$ μM

The 5 nm shift in the Q band between $CoPc(COOH)_4$ ($\lambda_{max} = 680$ nm) and $CoPc(COOH)_4$ + SCN⁻ ($\lambda_{max} = 685$ nm) confirms a coordination of SCN⁻ to $CoPc(COOH)_4$. Shifts in the Q band are typical of axial ligation in MPc complexes [459]. Based on the above observations, the following mechanism is proposed for the catalytic oxidation of SCN⁻:

$$Co^{II}Pc + SCN^- \rightarrow [(SCN^-)Co^{II}Pc]^- \qquad\qquad 4.7$$

$$[(SCN^-)Co^{II}Pc]^- \rightarrow [(SCN^-)Co^{III}Pc] + e^- \qquad\qquad 4.8$$

$$[(SCN^-)Co^{III}Pc] \xrightarrow{\ Acid\ } Co^{II}Pc + HSCN \qquad\qquad 4.9$$

121
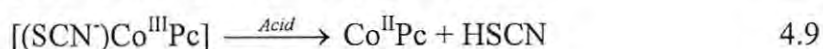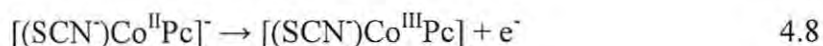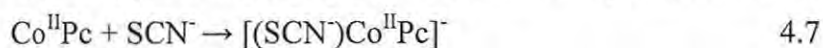
Eq. 4.7 is proposed because shifts in spectra typical of axial ligand exchange were observed on addition of SCN⁻ to solutions of CoPc(COOH)$_4$ (Fig. 4.8). Eq. 4.8 is proposed because oxidation of thiocyanate occurs at potentials following the formation of the Co^{III}Pc. The total number of electrons involved was found to be unity, hence suggesting the formation of HSCN in acid media rather than the more common (SCN)$_2$. However, the reported [23] reduction peak due to HSCN was not observed in this work.

4.3. Conclusions

This work represents the first report of the coordination of a metallophthalocyanine (**7a**) to an electrode pre-modified with aryl radicals. The electrode is named **GCE-4**. The modification technique is advantageous in that a stable electrode is formed with a readily available MPc complex, CoPc(COOH)$_4$ in this study, without the need for a complicated and lengthy syntheses typical of most self assembled monolayer studies. Furthermore, a variety of functional groups may be ultimately attached to the electrode to enhance its properties. **GCE-4** cannot detect the other analytes of this work (melatonin, nitrite, and L-cysteine) but can detect thiocyanate at a potential and limit of detection comparable to those of published reports. **GCE-4** can also reliably detect thiocyanate in the mM range and can hence be used as a sensor in this range. A mechanism for the interaction of thiocyanate with the CoPc(COOH)$_4$ of **GCE-4** has been proposed based on UV-visible observations, kinetics, and electrochemical behaviour.

CoPc(COOH)$_4$ grafted onto a GCE, as described in this chapter, detects thiocyanate. But CoPc(COOH)$_4$ adsorbed onto a GCE, described in Chapter 5, does not detect thiocyanate. This may be tentatively suggested as being due to the fact that, in the case of the grafted GCE, the organic layer between CoPc(COOH)$_4$ and the GCE facilitates the difficult electrochemical oxidation of thiocyanate (there is such no such organic layer when CoPc(COOH)$_4$ is adsorbed onto a GCE).

CHAPTER 5: ELECTRODE MODIFICATION BY ADSORPTION

The catalytic activity of CoPc complexes is highly dependent on the substituent [283]. This work compares the catalytic activity of the well-known cobalt phthalocyanine (CoPc, **5g**) with those of cobalt tetracarboxy phthalocyanine (CoPc(COOH)$_4$, **7a**) and cobalt octacarboxy phthalocyanine (CoPc(COOH)$_8$, **10a**) [25,26,454] when adsorbed onto glassy carbon electrodes, for the electrocatalytical detection of nitrite, L-cysteine, and melatonin. The electrodes cannot detect thiocyanate.

5.1. Characterization of modified electrodes

5.1.1. Electrochemistry

Fig. 5.1 shows the cyclic voltammograms of a glassy carbon electrode (GCE) modified with CoPc (as an example) recorded in pH 4 buffer at different scan rates.
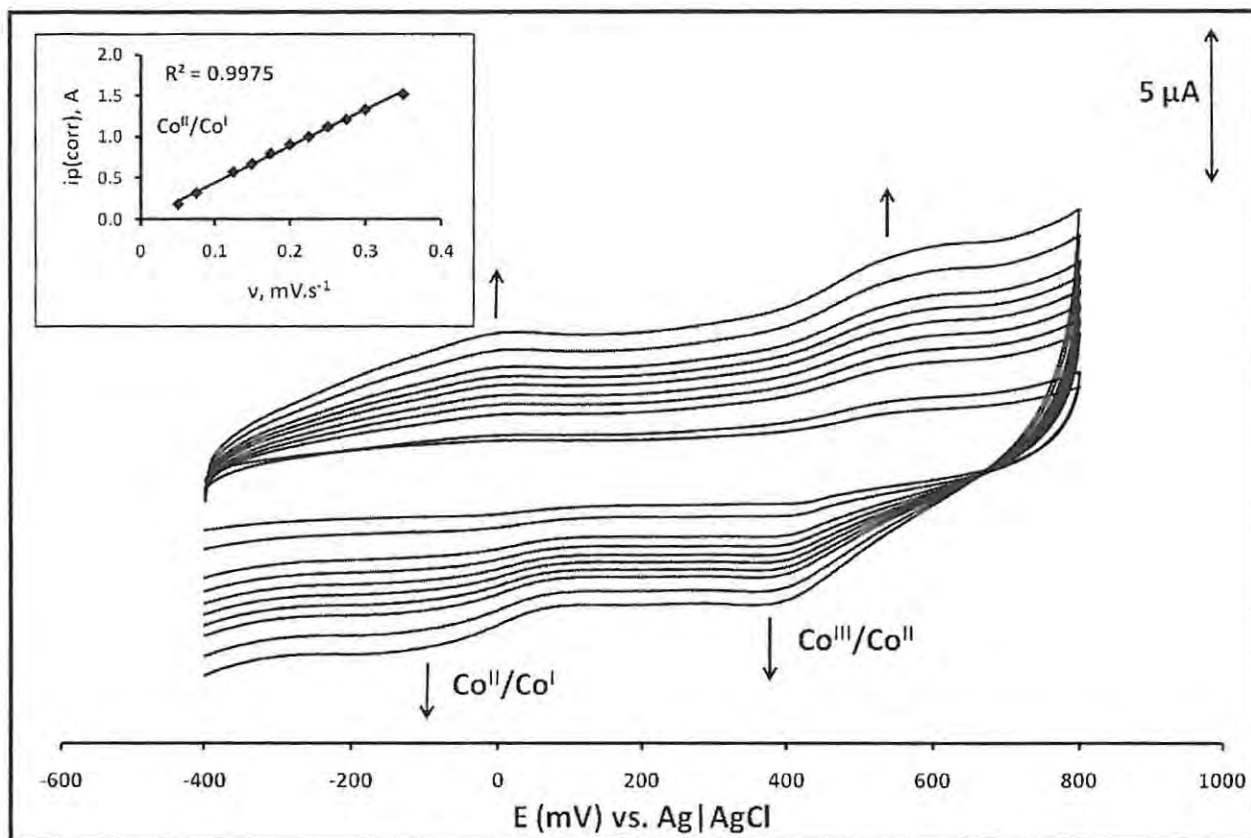
Fig. 5.1 Cyclic voltammograms of CoPc GCE recorded in pH 4 buffer solution. Insert: Scan rate study of the CoPc GCE recorded in pH 4 buffer solution

Two processes are observed for all GCE modified electrodes attributed to the Co^{II}/Co^{I} redox process (at $E_{1/2}$ (V) vs. Ag|AgCl: -0.10 V, -0.15 V, and -0.30 V for CoPc, CoPc(COOH)$_4$, and CoPc(COOH)$_8$ modified electrodes, respectively) and the Co^{III}/Co^{II} redox process (at $E_{1/2}$ (V) vs. Ag|AgCl: 0.45 V, 0.35 V, and 0.30 V for CoPc, CoPc(COOH)$_4$, and CoPc(COOH)$_8$ modified electrodes, respectively), see Table 5.1.

124

Chapter 5: Electrode modification by adsorption

Table 5.1 Characterization and analyte peak potentials of adsorbed CoPc complexes

Complex	$E_{1/2}$ (V vs. Ag|AgCl)		E_p (V vs. Ag|AgCl)			Γ (mol.cm^{-2})
	Co^{III}/Co^{II}	Co^{II}/Co^{I}	Nitrite (pH 7.4)	L-Cysteine (pH 4)	Melatonin (pH 7.4)	
CoPc	0.45	-0.10	0.80	0.50	0.65	6.07×10^{-11}
CoPc(COOH)$_4$	0.35	-0.15	0.80	0.63	0.60	6.50×10^{-10}
CoPc(COOH)$_8$	0.30	-0.30	0.85	0.65	0.60	4.74×10^{-11}

Thus, as the number of carboxy ring substituents increases, the CoPc derivatives become more difficult to reduce and easier to oxidize, as expected. These values are in accordance with the literature [121] for CoPc derivatives, the differences being due to the differing phthalocyanine substituents. The current for all redox peaks increased linearly with increasing scan rate, Fig. 5.1 insert. The behaviour is typical for a species chemically adsorbed on a surface [455]. The slope of the straight line in Fig. 5.1 (insert) can be used to calculate the surface coverage (Γ) according to Eq. 5.1:

$$i_p = \frac{n^2 F^2 A \Gamma(\upsilon)}{4RT} \qquad\qquad 5.1$$

where i_p is the peak current (amps), n is the number of electrons, A is the geometrical area of the electrode (cm^2), ν is the scan rate (V.s^{-1}) and the other symbols have their usual meanings given in the List of Symbols. Γ values for CoPc and CoPc(COOH)$_8$ modified electrodes are slightly less than 1×10^{-10} mol.cm^{-2} and slightly more for CoPc(COOH)$_4$, Table 5.1, than expected for a monolayer coverage for MPc molecule lying flat on a surface [221]. However, the Γ values are within the same order of magnitude for the three electrodes, allowing for comparison of their catalytic activity.

Fig. 5.2 shows the cyclic voltammograms of un-modified GCE (curve 1), CoPc GCE (curve 2), CoPc(COOH)$_4$ GCE (curve 3), and CoPc(COOH)$_8$ GCE (curve 4) recorded in 1 mM potassium ferricyanide.
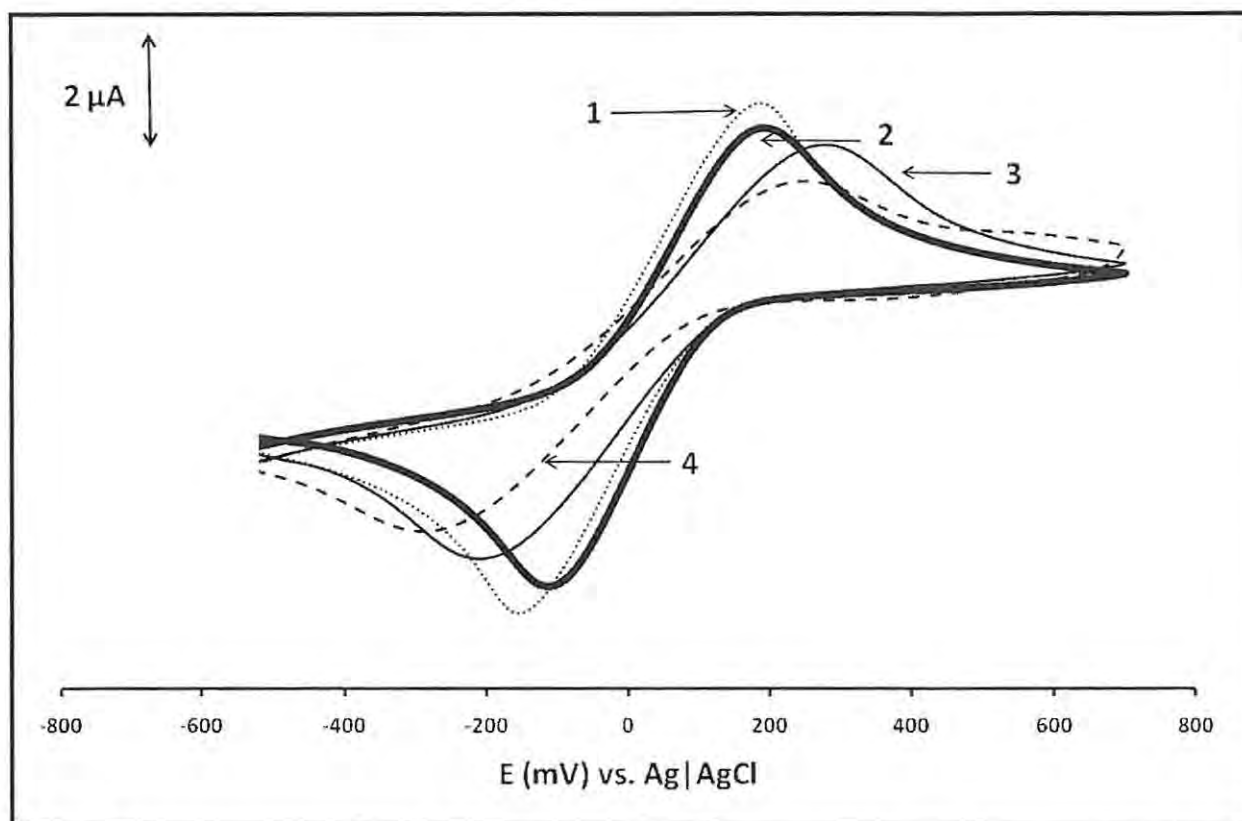
Fig. 5.2 Cyclic voltammograms of GCE (1), CoPc GCE (2), CoPc(COOH)$_4$ GCE (3), and CoPc(COOH)$_8$ GCE (4) recorded in 1 mM potassium ferricyanide. Scan rate = 100 mV.s^{-1}

The blocking ability of MPc for the ferricyanide couple becomes more inhibited with increasing number of substituents, as evidenced by the increase in anodic-to-cathodic peak separation (ΔE), with the exception of CoPc, where ΔE decreases slightly. The increase in ΔE for the [Fe(CN)$_6$$^{3-}$]/[Fe(CN)$_6$$^{4-}$] couple, for GCE modified with CoPc(COOH)$_4$ and CoPc(COOH)$_8$, suggests a decrease in electron transfer rate at the electrode surface. However, the peaks due to ferricyaninde are still present, showing that the modified electrodes do not completely inhibit the process. For CoPc there was actually an improvement in the ΔE value as stated above. The lack of inhibition of the [Fe(CN)$_6$$^{3-}$] /[Fe(CN)$_6$$^{4-}$] redox couple has been reported previously, using adsorbed cobalt tetra-aminophthalocyanine films on vitreous carbon electrodes [167]. Both modified and un-modified electrodes were reported to show the same redox potential and almost equal peak current intensities for the [Fe(CN)$_6$$^{3-}$] /[Fe(CN)$_6$$^{4-}$] redox reaction, and the modified electrodes acted as electronic conductors which allowed rapid electron transfer to the solution

126

species [167]. Thus the lack of inhibition of the $[Fe(CN)_6^{3-}]$ /$[Fe(CN)_6^{4-}]$ in Fig. 5.2 is not surprising.

5.1.2. Impedance

The impedance data may be represented b y plotting $-Z''$ (the maginary component of the impedance) against Z' (the real component of the impedance) and such a plot is commonly called a Nyquist plot. Fig. 5.3(a) shows the Nyquist plots for all of the electrodes of this work, recorded in 0.1 M potassium ferricyanide.
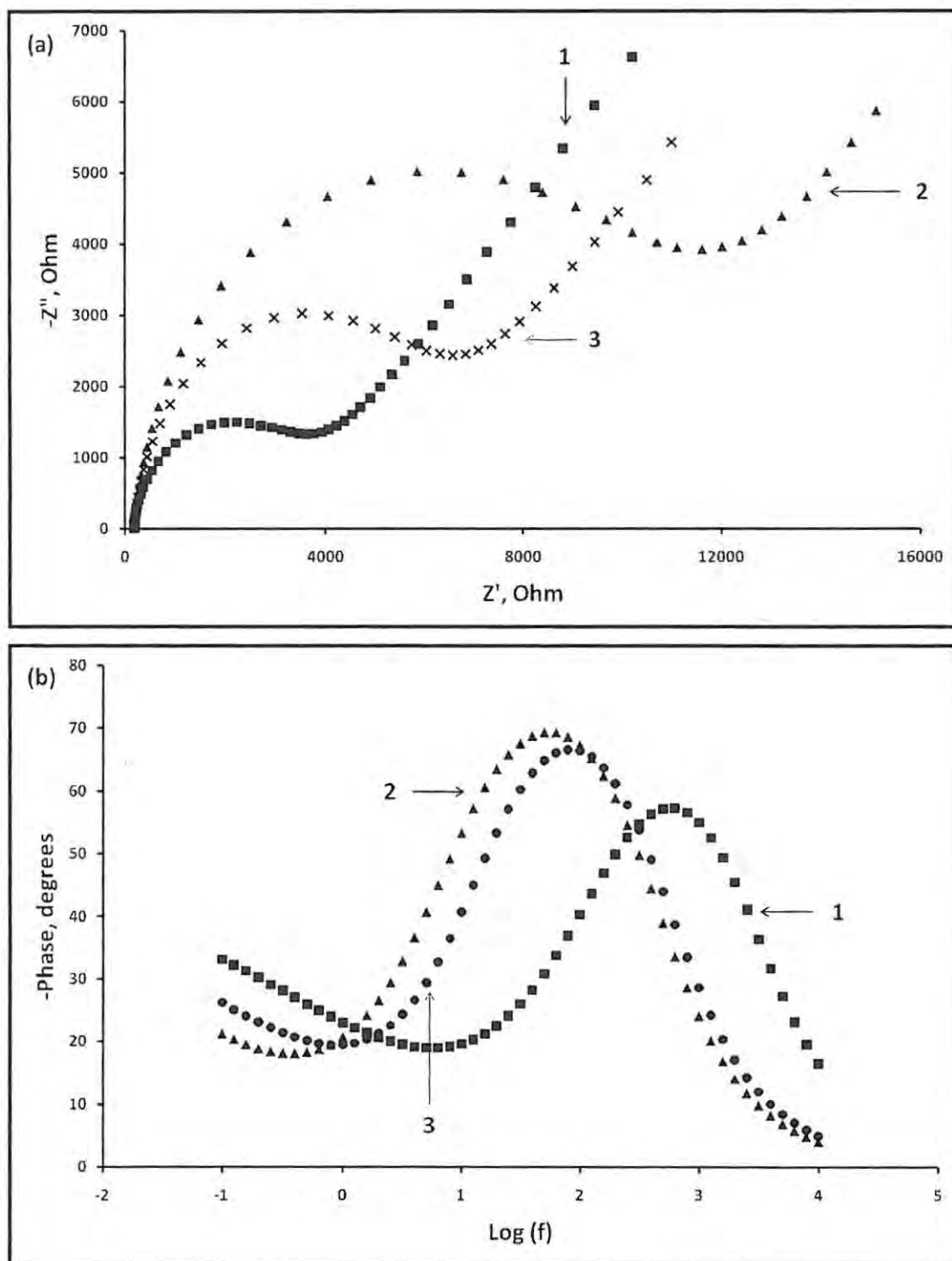
Fig. 5.3 Nyquist (a) and Bode (b) plots of electrodes modified with CoPc (1), CoPc(COOH)$_4$ (2), and CoPc(COOH)$_8$ (3), recorded in 0.1 M potassium ferricyanide. Potential of impedance measurements = 100 mV

Chapter 5: Electrode modification by adsorption

As shown in Fig. 5.3(a), all the modified electrodes exhibit semicircular plots, as expected. The larger the arc diameter of the Nyquist plot and the resistance to charge transfer value (R_{ct}), the greater the impedance. The impedances of the electrodes used in this work increased in the following order:

CoPc (4.24×10^3 Ω) < CoPc(COOH)$_8$ (7.33×10^3 Ω) < CoPc(COOH)$_4$ (1.29×10^4 Ω)

CoPc(COOH)$_4$ had the highest surface coverage (Table 5.1) and, expectedly, it has the largest R_{ct}. This suggests a more effective electrode modification by CoPc(COOH)$_4$ than for the other complexes.

The Bode plots (plots of -phase-shift (-θ) vs. log frequency (log (f)) are shown in Fig. 5.3(b) for the electrodes of this work, recorded in 0.1 M potassium ferricyanide. A phase angle greater or equal to 90° signifies that the modified electrode behaves like an ideal capacitor [482]. This means that the modified electrode is an effective insulating film and that there is no current leakage at defect sites. If the phase angle is less than 90° then the modified electrode is permeable to ions from the solution. Fig. 5.3(b) shows that the GCE electrodes, modified by the different CoPc derivatives, have phase angles of less than 90°, confirming that the electrodes are permeable to ions from the $[Fe(CN)_6]^{3-}/[Fe(CN)_6]^{4-}$ solution and do not behave like ideal capacitors. CoPc(COOH)$_4$ formed the most effective film on the GCE because it displayed the highest phase angle (closest to 90°). The opposite is true for CoPc, Fig. 5.3(b). These trends are confirmed by the Nyquist plots of Fig. 5.3(a) and the R_{ct} values given above.

5.2. Effects of substituents on analytes

5.2.1. Electrocatalysis of nitrite

Electrocatalysis by a modified electrode is characterized by an increase in the current and a shift of the potential to lower values with respect to an un-modified electrode. Fig. 5.4 shows the cyclic voltammograms of GCEs modified by the different CoPc derivatives recorded in 1 mM nitrite (in pH 7.4 buffer solution).
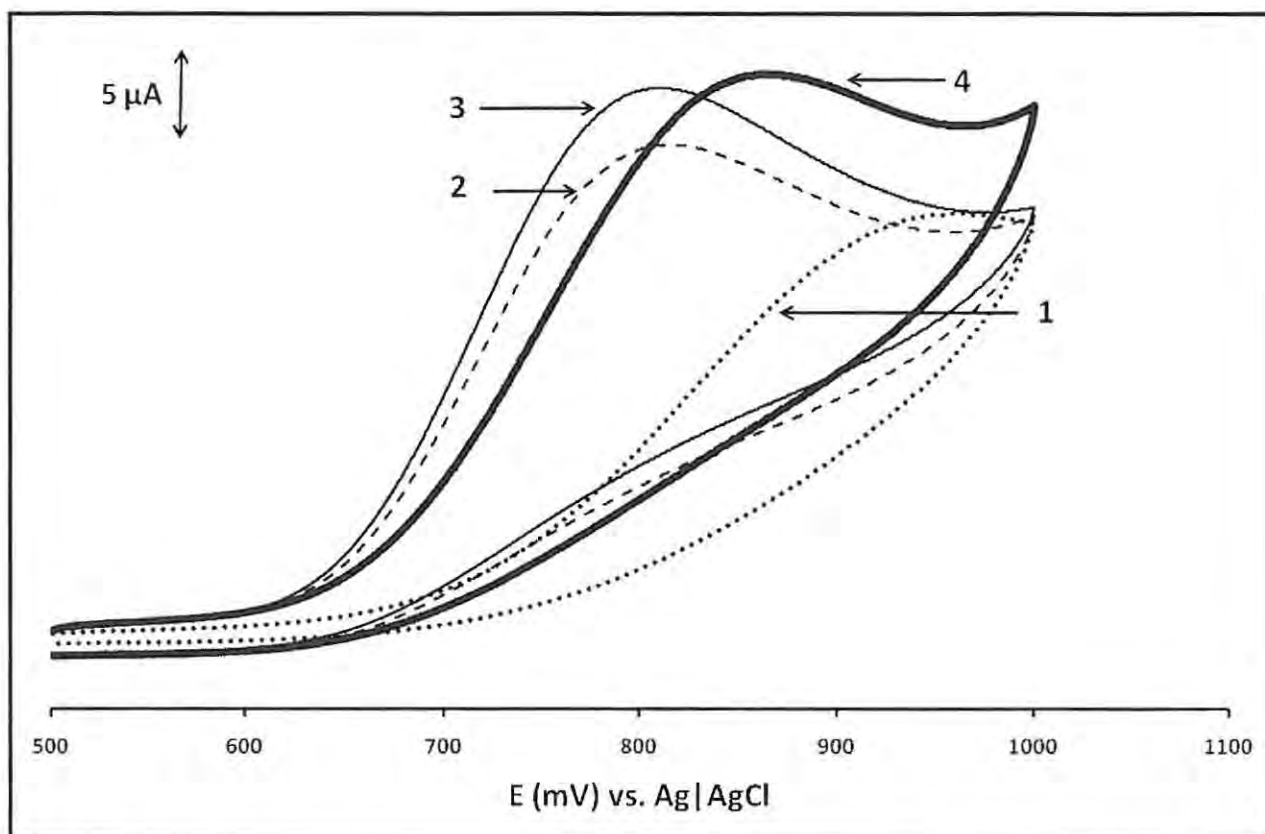
Fig. 5.4 Cyclic voltammograms of un-modified (1), CoPc (2), CoPc(COOH)$_4$ (3), and CoPc(COOH)$_8$ (4) modified GCEs recorded in 1 mM nitrite. Scan rate = 100 mV.s^{-1}

At pH 7.4, used in this work, the disproportionation of nitrite to nitric oxide (NO) is insignificant, thus the observed responses are a result of the oxidation of nitrite, not NO. At pH 4 (used below for cysteine oxidation) NO predominates, hence pH 7.4 was used for nitrite detection rather than the pH 4 used below.

The un-modified glassy carbon electrode (1) displayed an undefined nitrite oxidation peak at ~950 mV vs. Ag|AgCl, Fig. 5.4, as has been reported [483,484]. Electrodes modified with CoPc derivatives showed nitrite oxidation peaks at much lower oxidation potentials and with more clearly defined peaks, Fig. 5.4, curves 2-4 (Table 5.1). Electrodes modified with CoPc and CoPc(COOH)$_4$ displayed nitrite oxidation at lowest potentials (0.80 V vs. Ag|AgCl), but CoPc(COOH)$_8$ gave a slightly higher current response, although with a slightly more positive peak potential, Fig. 5.4 (and Table 5.1). CoPc(COOH)$_4$ had a higher surface coverage but did not show larger currents. The number of ring substituents thus does affect the potential of nitrite

oxidation to a small extent. There is a linear relationship between the peak current and the square root of the scan rate, which indicates a diffusion-controlled electrocatalytic oxidation of nitrite on the modified electrodes, Fig. 5.5(a) (using $CoPc(COOH)_8$ as an example). The plot of sweep-rate normalized current density ($I_p.v^{-1/2}$) vs. scan rate (Fig. 5.5(b)) confirms a catalytic process [484]. Fig. 5.5(c) shows a plot of E_p (V) vs. log v (V.s^{-1}) for the $CoPc(COOH)_8$ modified electrode (as an example) recorded in 1 mM nitrite in pH 7.4 buffer solution.
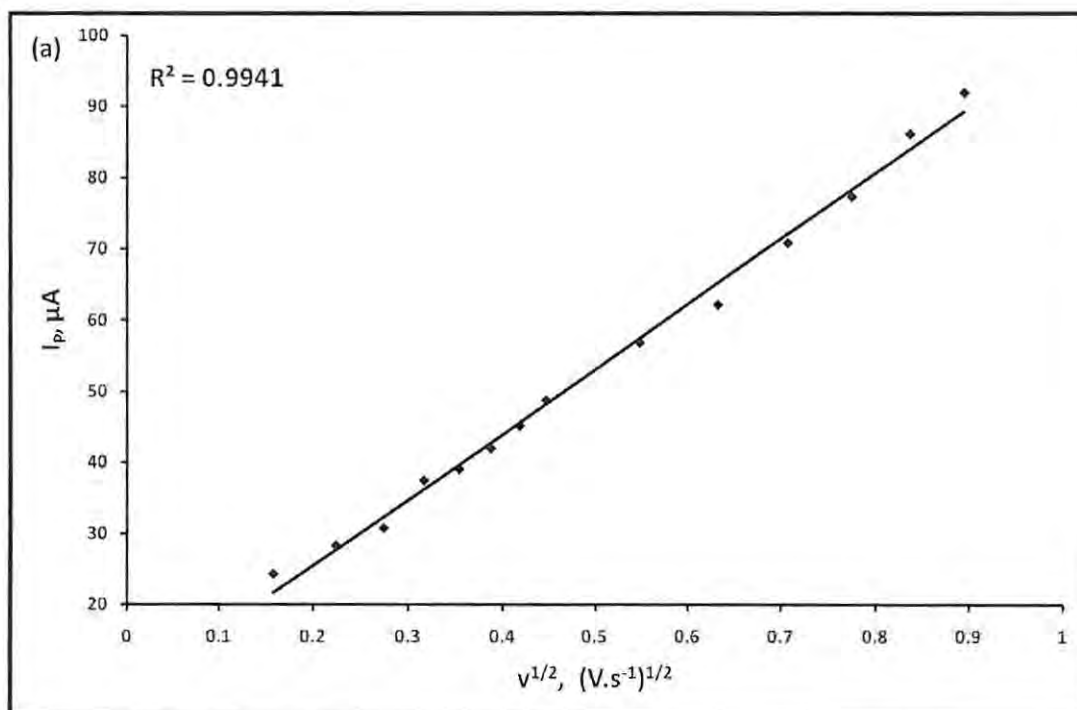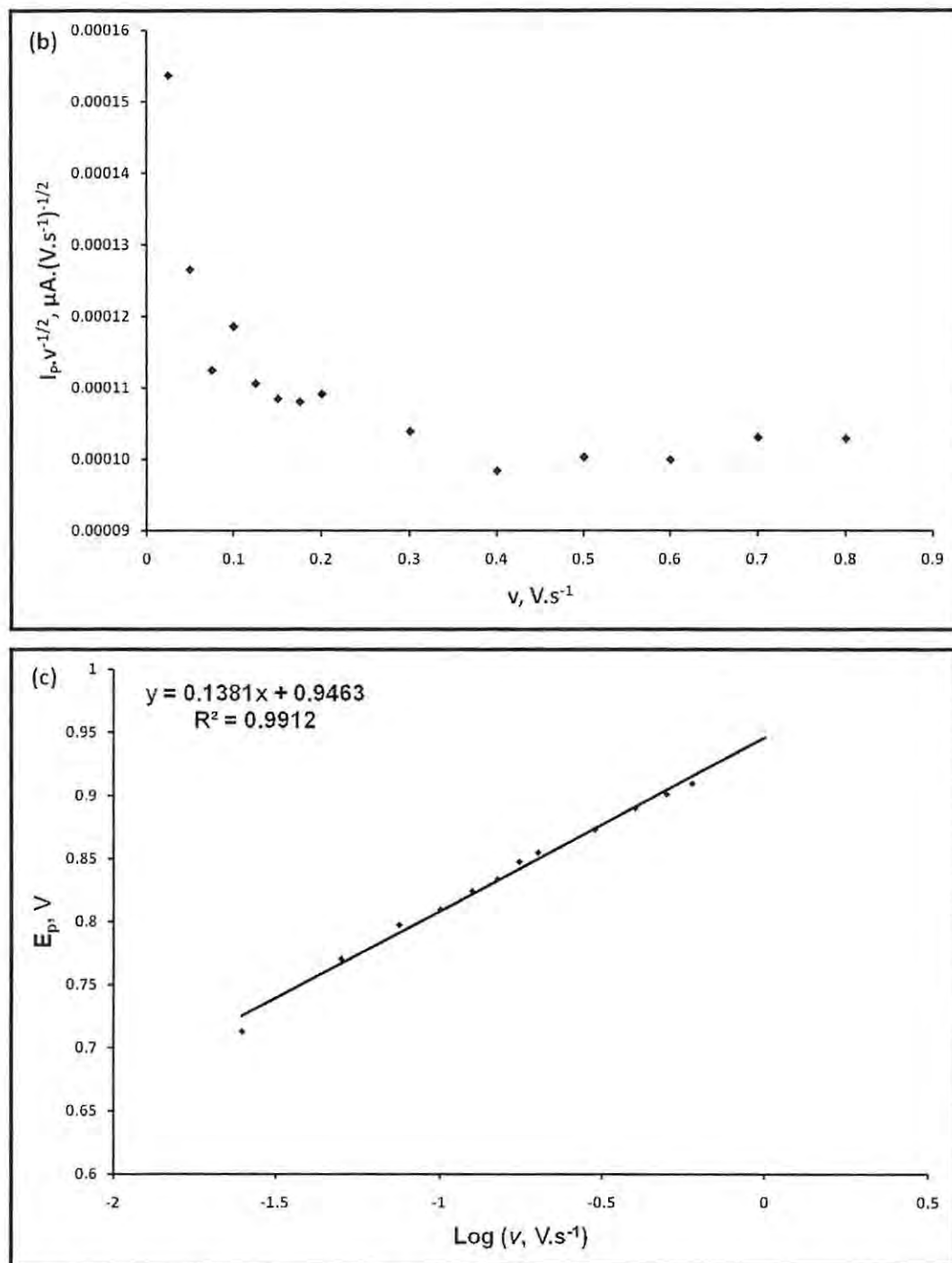
Fig. 5.5 (a) Plot of I_p vs. $v^{1/2}$, (b) plot $I_p.v^{-1/2}$ vs. v, and (c) plot of E_p vs. log v for 1 mM nitrite. Electrode: $CoPc(COOH)_8$ adsorbed onto GCE

Electrodes modified with CoPc and $CoPc(COOH)_4$ displayed similar behaviour in their detection of nitrite to that shown in Fig. 5.5(a) to (c). A linear relationship between E_p (V) and log v, Fig.

Chapter 5: Electrode modification by adsorption

5.5(c), confirms kinetic irreversibility [319]. The Tafel slope was determined using Eq. 5.2 [455]:

$$E_p = \frac{2.3RT}{2(1-\alpha)nF}\log \upsilon + K \qquad\qquad 5.2$$

where α is the transfer coefficient, υ is the scan rate, n is the number of electrons involved in the rate determining step, and K is the intercept. Tafel slopes, calculated from E_p vs. log υ for nitrite detection, are shown in Table 5.2.

Table 5.2 Kinetic parameters for nitrite, L-cysteine, and melatonin determination[a]

Analyte	CoPc			CoPc(COOH)$_4$			CoPc(COOH)$_8$		
	α	Tafel slope (mV.dec^{-1})	n_t	α	Tafel slope (mV.dec^{-1})	n_t	α	Tafel slope (mV.dec^{-1})	n_t
Nitrite	0.79	288	2	0.79	276	2	0.79	276	2
L-cysteine	0.67	180	1	0.68	185	1	0.81	315	1
Melatonin	0.51	120	2	0.53	125	2	0.64	165	2

[a]α = transfer coefficient; mV.dec^{-1} = mV.decade^{-1}; n_t = total number of electrons involved

Large Tafel slopes (>120 mV.decade^{-1}), such as obtained in this work (Table 5.2), indicate either chemical reactions coupled to electrochemical steps, or strong substrate-catalyst interactions in a reaction intermediate [319,480,485]. Such high slopes make the calculation of α, the transfer coefficient, unreliable. However these values are included in Table 5.2.

The total number of electrons (n_t) involved in the electrocatalytic oxidation of nitrite was calculated using Eq. 5.3 [455]:

$$i_p = 2.99x10^5 n_t \left[(1-\alpha)n\right]^{\frac{1}{2}} AC_o D^{\frac{1}{2}} \upsilon^{\frac{1}{2}} \qquad\qquad 5.3$$

where A is the area of the electrode (cm^2), C$_o$ is the concentration of the electroactive reactant (mol.cm^{-3}) and D is the diffusion coefficient of nitrite (D = 2.1 × 10^{-5} cm^2.s^{-1} [481]). The total number of electrons transferred is two, Table 5.2, a value which agrees with the literature [32].

Fig. 5.6 shows the linear variation of peak current vs. the nitrite concentration for CoPc(COOH)$_4$ adsorbed onto a GCE as an example.
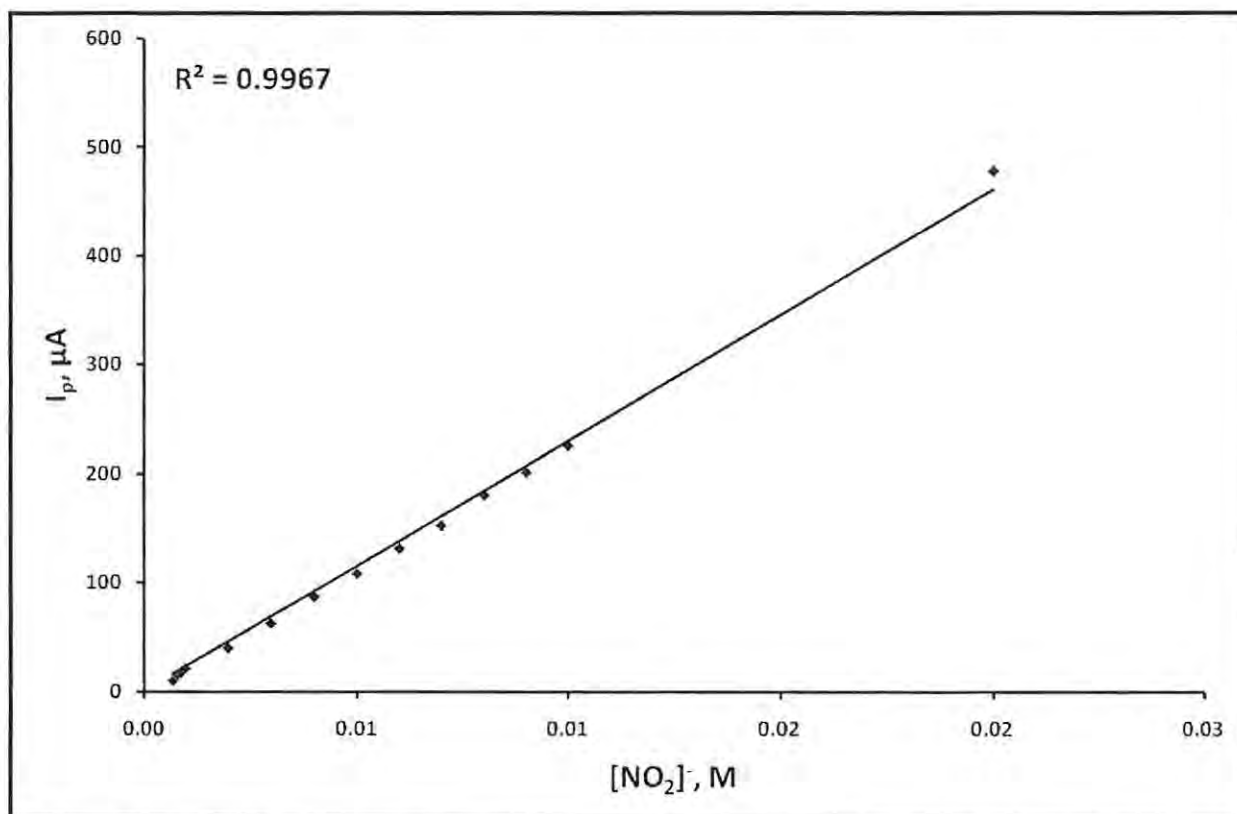
Fig. 5.6 Plot of I_p vs. the nitrite ion concentration for CoPc(COOH)$_4$ adsorbed onto a GCE

Linear plots were also observed for the electrodes modified with CoPc and CoPc(COOH)$_8$, for concentrations in the 10^{-4} to 10^{-2} M region. Good nitrite limits of detection (10^{-7} M region, 3σ criteria) were obtained, Table 5.3.

134

Chapter 5: Electrode modification by adsorption

Table 5.3 Analytical parameters for the determination of nitrite, L-cysteine, and melatonin[a]

Analyte	CoPc			CoPc(COOH)$_4$			CoPc(COOH)$_8$		
	LOD (μM)	Sensitivity (A.M^{-1})	% decay	LOD (μM)	Sensitivity (A.M^{-1})	% decay	LOD (μM)	Sensitivity (A.M^{-1})	% decay
Nitrite	0.142	0.021	13	0.139	0.022	17	0.117	0.026	4
L-cysteine	0.884	0.002	13	0.111	0.027	16	0.507	0.005	17
Melatonin	1.70	0.014	16	0.119	0.015	17	0.144	0.012	10

[a]LOD = limit of detection; % decay over 35 continuous scans

CoPc(COOH)$_4$ has a higher surface coverage and detection limit for nitrite than CoPc(COOH)$_8$, Tables 5.1 and 5.3. UV-visible spectroscopy was used to investigate the mode of interaction between nitrite and the CoPc derivatives as was the case for SCN$^-$ in Chapter 4. Even though these studies were done in solution, whereas the CoPc derivatives are adsorbed onto electrodes for the catalytic oxidation of nitrite, the UV-visible studies do give an indication of the possible interaction between CoPc derivatives and nitrite. For CoPc (in non-aqueous media) and CoPc(COOH)$_8$ (in pH 7.4 buffer), addition of nitrite resulted only in a 5 nm shift in the Q band of the complexes. Such small shifts are associated with axial ligation in MPc complexes [459], but for CoPc(COOH)$_4$ there was evidence of aggregation, Fig. 5.7.
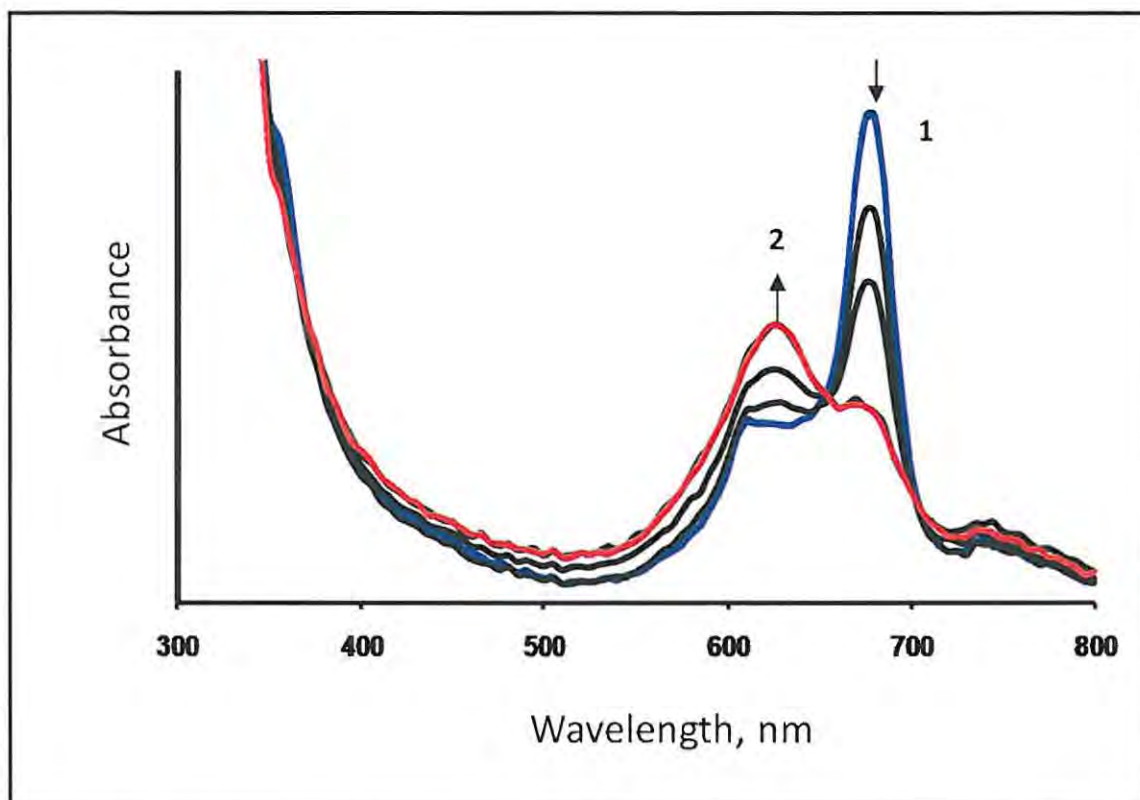
Fig. 5.7 Electronic absorption spectrum of $CoPc(COOH)_4$ before (1) and after (2) addition of nitrite in pH 7.4 buffer

Aggregation in MPc complexes is usually depicted as a coplanar association of rings and it is dependent on the concentration, the nature of the solvent, the ions in solution, the nature of the substituents, and the complexed metal ions. $MPc(COOH)_8$ complexes are generally monomeric in solution [486], while $MPc(COOH)_4$ complexes are aggregated due to the plurality of substituents. In the presence of nitrite, $CoPc(COOH)_4$ shows aggregation which is not observed for the other analytes. Thus the higher limit of detection observed for $CoPc(COOH)_4$ compared to $CoPc(COOH)_8$, even though the former has a larger surface coverage, may be a result of the mode of interaction of nitrite with adsorbed $CoPc(COOH)_4$,monomer which results in a decrease in the current and an unfavourable limit of detection. The sensitivities of all the modified electrodes for nitrite detection are similar, Table 5.3. In terms of short term stability (Table 5.3, as % decay), $CoPc(COOH)_8$ modified glassy carbon electrode was the most stable as proven by

Chapter 5: Electrode modification by adsorption

35 continuous cyclic voltammogram recordings in 1 mM nitrite solution (in pH 7.4 buffer) with practically no loss in current.

Table 5.4 lists the electrochemical parameters of nitrite determination for electrodes of this work with literature [32,319,320,487].

Table 5.4 The properties of modified electrodes as electrochemical sensors for nitrite[a]

MPc	Electrode	E_p (V) vs. Ag|AgCl	LOD (M)	Ref.
CoPc	GCE	0.80	1.42×10^{-7}	This work
CoPc(COOH)$_4$	GCE	0.80	1.39×10^{-7}	This work
CoPc(COOH)$_8$	GCE	0.85	1.17×10^{-7}	This work
CoPc	VCE	0.87	Not reported	319
CoTDMPc	Au SAM	0.77	Not reported	32
MnTDMPc	Au SAM	0.79	Not reported	32
NiTAMPc	GCE	0.86	Not reported	487
NiTBMPc	Poly-Au	0.83	Not reported	320
NiTDMPc	Poly-Au	0.80	Not reported	320

[a]TD = tetrakis (dodecylmercapto); TA = tetraamino; TB = tetrakis (benzylmercapto); GCE = glassy carbon electrode; VCE = vitreous carbon electrode; Au SAM = self assembled monolayer on gold electrode; Poly-Au = polymerization on gold electrode; LOD = limit of detection

From Table 5.4, the electrodes of this work were able to detect nitrite at potentials comparable to those of other works. The limits of nitrite detection by modified electrodes of this work are desirably low in the 10^{-7} M region (these limits are often not specified in the literature).

The proposed mechanism for catalysis of nitrite oxidation using CoPc derivatives (CoPc and CoPc(COOH)$_8$) is shown by Eqs. 5.4 - 5.6:

$$Co^{II}Pc + NO_2^- \rightarrow [Co^{II}Pc(NO_2^-)]^- \qquad 5.4$$

$$[Co^{II}Pc(NO_2^-)]^- \rightarrow Co^{III}Pc(NO_2^-) + e^- \qquad 5.5$$

$$Co^{III}Pc(NO_2^-) + H_2O \rightarrow Co^{II}Pc + NO_3^- + 2H^+ + e^- \qquad 5.6$$
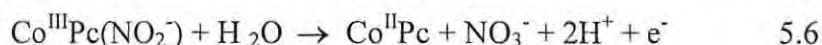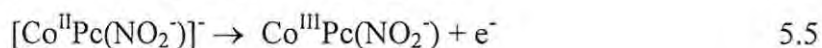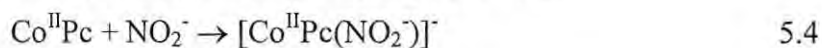
Eq. 5.4 is suggested because the coordination of nitrite to $M^{II}Pc$ was confirmed by UV-visible studies for CoPc and CoPc(COOH)$_8$. Eq. 5.5 involves the oxidation of $Co^{II}Pc$ to $Co^{III}Pc$ because

nitrite oxidation occurs where $Co^{III}Pc$ species exist, Fig. 5.1. Nitrate is the most common oxidation product of nitrite and the total number of electrons involved is two, therefore Eq. 5.6 is proposed.

5.2.2. Electrocatalysis of L-cysteine

Fig. 5.8 shows the cyclic voltammograms of all of the electrodes of this work recorded in 1 mM L-cysteine in pH 4 buffer.
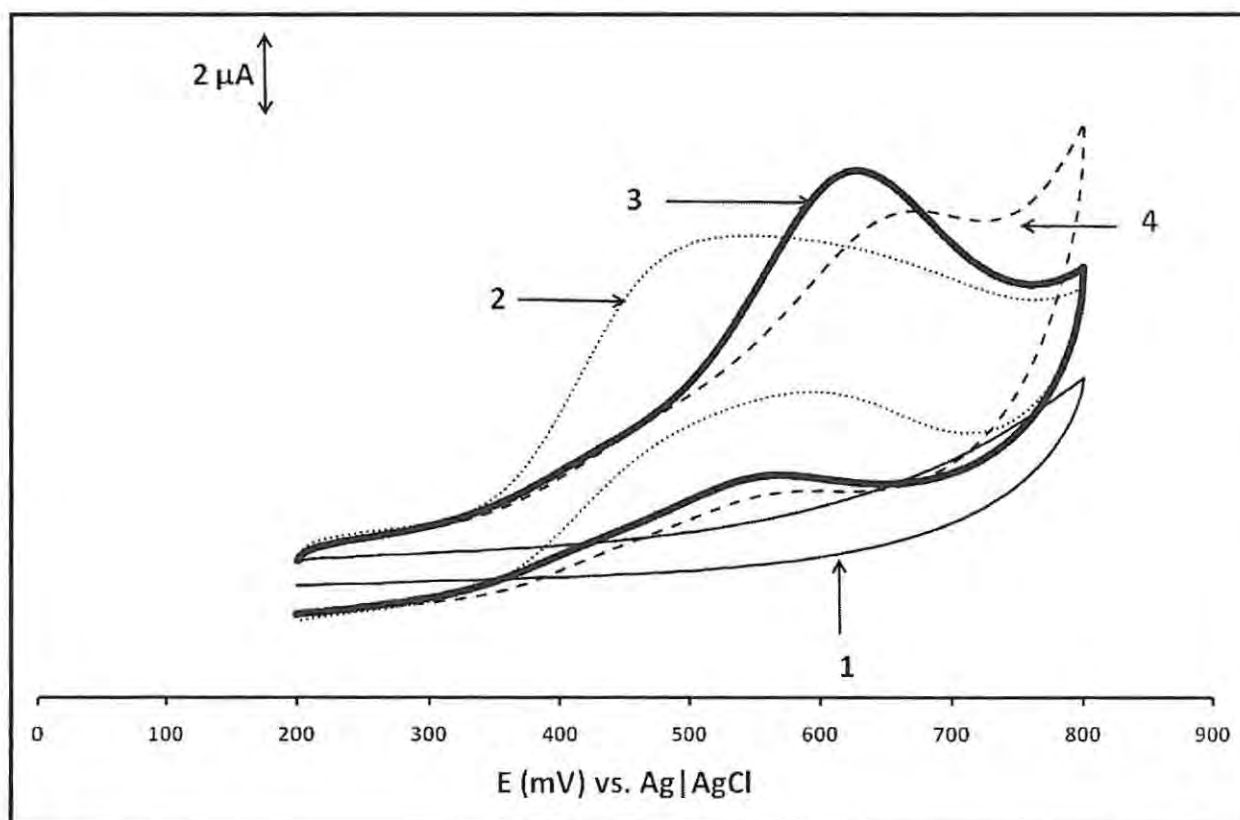
Fig. 5.8 Cyclic voltammograms of un-modified (1), CoPc (2), CoPc(COOH)$_4$ (3), and CoPc(COOH)$_8$ (4) modified GCEs recorded in 1 mM L-cysteine. Scan rate = 100 mV.s^{-1}

At pH 4 used for L-cysteine detection, the Co^{III}/Co^{II} species is involved, rather than the Co^{II}/Co^{I} involved at pH 7.4 [283].

For consistency, the Co^{III}/Co^{II} couple is used for catalyses of all analytes discussed in this work. The un-modified glassy carbon electrode (1, Fig. 5.8) could not detect L-cysteine as evidenced

Chapter 5: Electrode modification by adsorption

by the absence of any peak [283,299]. The CoPc derivatives showed peaks due to the oxidation of L-cysteine (curves 2-4, Fig. 5.8). CoPc modified electrode (curve 2) displayed an L-cysteine oxidation peak at the lowest potential (~0.5 V vs. Ag|AgCl), but electrodes modified with $CoPc(COOH)_4$ (curve 3) and $CoPc(COOH)_8$ (curve 4), have L-cysteine detection peaks at 0.63 and 0.65 V vs. Ag|AgCl respectively and displayed higher peak current responses. The highest current response was obtained for $CoPc(COOH)_4$, but at a more positive potential compared to CoPc. The high current response for $CoPc(COOH)_4$ could be due to the high surface coverage for this complex, Table 5.1. Spectroscopic studies showed only axial ligation and not the aggregation observed above for nitrite. Plots of I_p (A) vs. $v^{1/2}$ ($(V.s^{-1})^{1/2}$), $I_p.v^{-1/2}$ vs. v ($V.s^{-1}$), and E_p (V) vs. log v ($V.s^{-1}$) were similar to those observed above for nitrite oxidation (Fig. 5.5) confirming a diffusion-controlled catalytic process and kinetic irreversibility.

Tafel slopes in the range of 180 to 315 $mV.decade^{-1}$ were obtained for all the modified electrodes of this work recorded in L-cysteine, Table 5.2. The total number of electrons (n_t) involved in the electrocatalytic oxidation of L-cysteine by the modified electrodes, calculated using Eq. 5.3, is one (Table 5.2).

Linear plots of peak current vs. L-cysteine concentration (10^{-4} - 10^{-2} M) were obtained for all the CoPc derivatives. Fig. 5.9 gives an example using CoPc adsorbed onto a GCE.
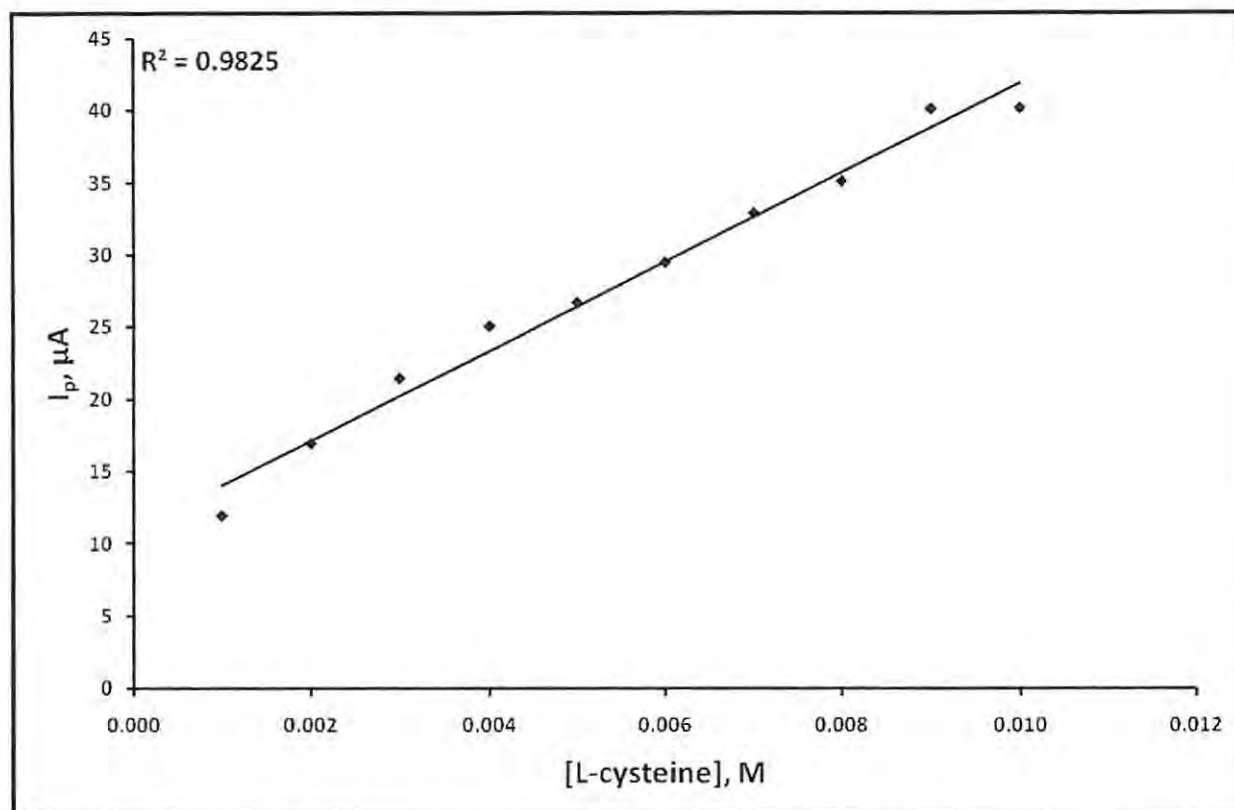
Fig. 5.9 Plot of I_p vs. L-cysteine concentration for CoPc adsorbed onto a GCE

The limits of detection (3σ criteria) were in the 10^{-7} M region, Table 5.3. The CoPc(COOH)$_4$ GCE showed the lowest limit of detection (Table 5.3), also proven by its high current response in Fig. 5.8. Moreover, the sensitivity of CoPc(COOH)$_4$ was the highest of all electrodes studied, Table 5.3.

The MPc modified electrodes displayed reasonable stability over 35 continuous cyclic voltammetry recordings, Table 5.3. The passivation of the electrode surface is due to the known adsorptive coordination of cysteine oxidation products (cystine) on the electrode. The stability also decreases with the increasing number of substituents on the CoPc (Table 5.3), although the difference between CoPc(COOH)$_4$ and CoPc(COOH)$_8$ is minimal. The bulkiness of the substituents appears to disturb the stability.

Table 5.5 lists the electrochemical parameters for L-cysteine determination using electrodes of this work and others [23,33,34,205,347,488].

Chapter 5: Electrode modification by adsorption

Table 5.5 The properties of modified electrodes as electrochemical sensors for L-cysteine[a]

MPc	Electrode	LOD (M)	E_p (V) vs. Ag|AgCl	Ref.
CoPc	GCE	8.84×10^{-7}	0.50	This work
CoPc(COOH)$_4$	GCE	1.11×10^{-7}	0.63	This work
CoPc(COOH)$_8$	GCE	5.07×10^{-7}	0.65	This work
CoPc	Carbon paste	3.1×10^{-8}	0.4	488
CoPc(SC$_4$H$_9$)$_8$	Au SAM	3.1×10^{-7}	0.42	34
CoPc(COCl)$_4$	2-ME-Au	5×10^{-7}	0.36,0.63	205
CoPc(SC$_2$H$_4$OH)$_8$	Au SAM	5.2×10^{-7}	0.50	23
FePc	4-MPy-Au	2×10^{-6}	0.14	347
FePc(SC$_4$H$_9$)$_8$	Au SAM	3.0×10^{-7}	0.33	33
FePc(SC$_2$H$_4$OH)$_8$	Au SAM	5.2×10^{-7}	0.38	23

[a]GCE = glassy carbon electrode; Au SAM = self assembled monolayer on gold electrode; 2-ME-Au = pre-formed SAM on gold using 2-mercaptoethanol, 4-MPy-Au = pre-formed SAM on gold using 4-mercaptopyridine; LOD = limit of detection

Even though the electrodes employed detected L-cysteine at higher potentials with respect to some of the literature, these potentials are still quite low, Table 5.5. The limits of L-cysteine detection by electrodes of this work are comparable to those obtained from the literature.

On CoPc modified electrodes, the oxidation of cysteine in acidic media has been reported to occur in steps consisting of the oxidation of Co^{II}Pc to Co^{III}Pc, followed by the oxidation of cysteine, and the regeneration of Co^{II}Pc according to Eqs. 5.7 - 5.10 [283]:

$$Co^{II}Pc \rightarrow Co^{III}Pc + e^- \qquad 5.7$$

$$RSH + Co^{III}Pc \rightarrow RS^+\text{-}Co^{II}Pc \qquad 5.8$$

$$RS^+\text{-}Co^{II}Pc \rightarrow Co^{II}Pc + RS^+ \qquad 5.9$$

$$2RS^+ \rightarrow RSSR \qquad 5.10$$

where RSH = cysteine and RSSR = cystine.

5.2.3. Electrocatalysis of melatonin

Fig. 5.10 shows the cyclic voltammograms of an un-modified GCE (1) and CoPc derivative modified GCEs (2 - 4) recorded in melatonin (in PBS, pH 7.4) - this pH was chosen because it is a biological pH).
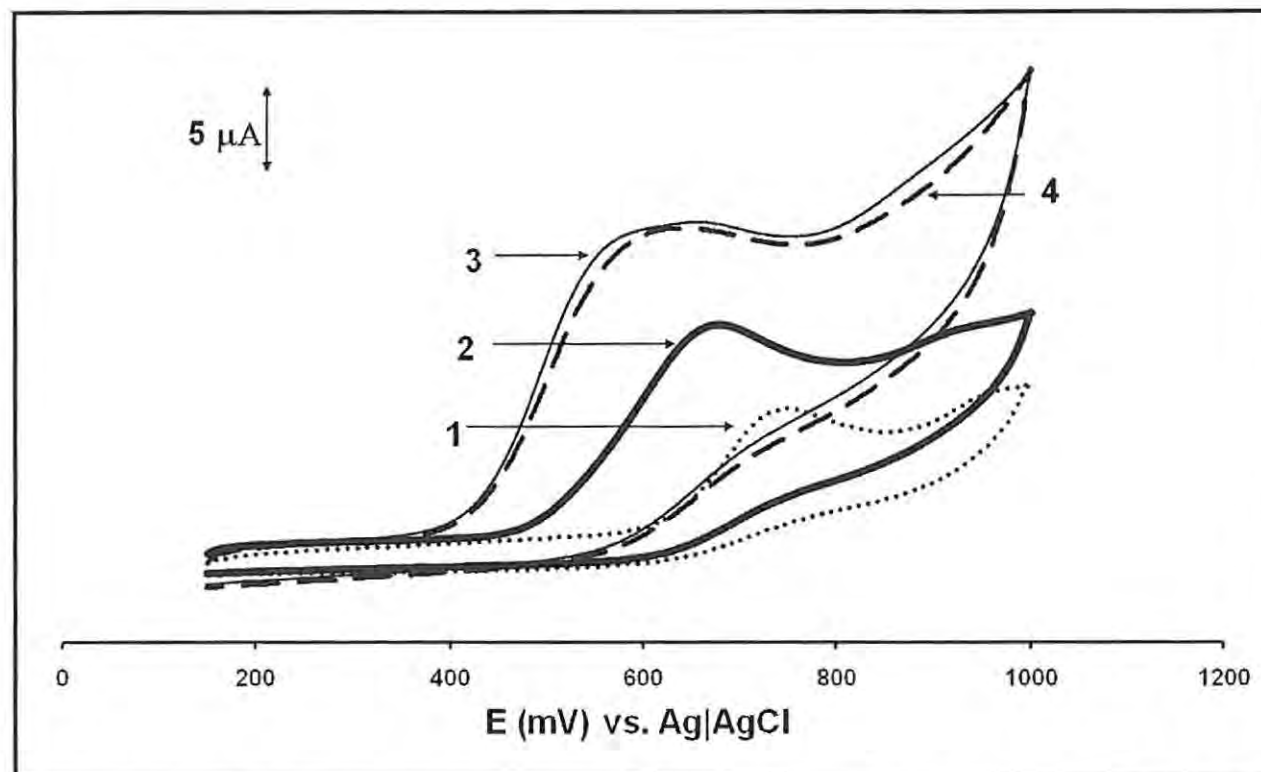
Fig. 5.10 Cyclic voltammograms of GCE (1), CoPc GCE (2), CoPc(COOH)$_4$ GCE (3), and CoPc(COOH)$_8$ GCE (4) recorded in 1 mM melatonin (in PBS, pH 7.4). Scan rate = 50 mV.s^{-1}

All electrodes showed oxidation of melatonin. The observation of melatonin peaks on carbon electrodes has been reported [311,489]. CoPc GCE (curve 2, Fig. 5.10), displays a higher peak current response and shift to lower melatonin oxidation potential (at 0.65 V vs. Ag|AgCl) compared to the un-modified electrode (0.75 V vs. Ag|AgCl), hence showing catalytic activity. CoPc(COOH)$_4$ GCE (curve 3) and CoPc(COOH)$_8$ GCE (curve 4) display even better catalytic abilities towards melatonin oxidation as judged by the significant increase in current and shift to much lower oxidation potentials (at E$_p$ ~0.60 V vs. Ag|AgCl) relative to the un-modified GCE

Chapter 5: Electrode modification by adsorption

(and CoPc GCE), Fig. 5.10. Linear plots of the peak current vs. the square root of the scan rate were obtained confirming diffusion controlled oxidation of melatonin for all the electrodes.

Using Eq. 5.2, Tafel slopes ranging from 120 to 165 mV.decade^{-1} were obtained for melatonin oxidation, Table 5.2, showing that the first one electron transfer is rate determining. The transfer coefficient (α) values, reported in Table 5.2, ranged from 0.51 to 0.64. The total number of electrons involved in the catalytic oxidation of melatonin, for all electrodes employed in this work, was calculated to be two (Table 5.2) using Eq. 5.3 and a diffusion coefficient of melatonin of 5.28×10^{-6} cm^2.s^{-1} [489]. Even though the detection of melatonin on MPc modified electrodes has not been studied as extensively as in this work, the kinetic properties presented here do agree with published work on un-modified glassy carbon electrodes [311,312].

All CoPc modified electrodes reliably detected melatonin in the 10^{-4} to 10^{-2} M range and therefore can be used for analysis of melatonin concentrations in this range. Fig. 5.11 gives an example using CoPc(COOH)$_4$ adsorbed onto GCE.
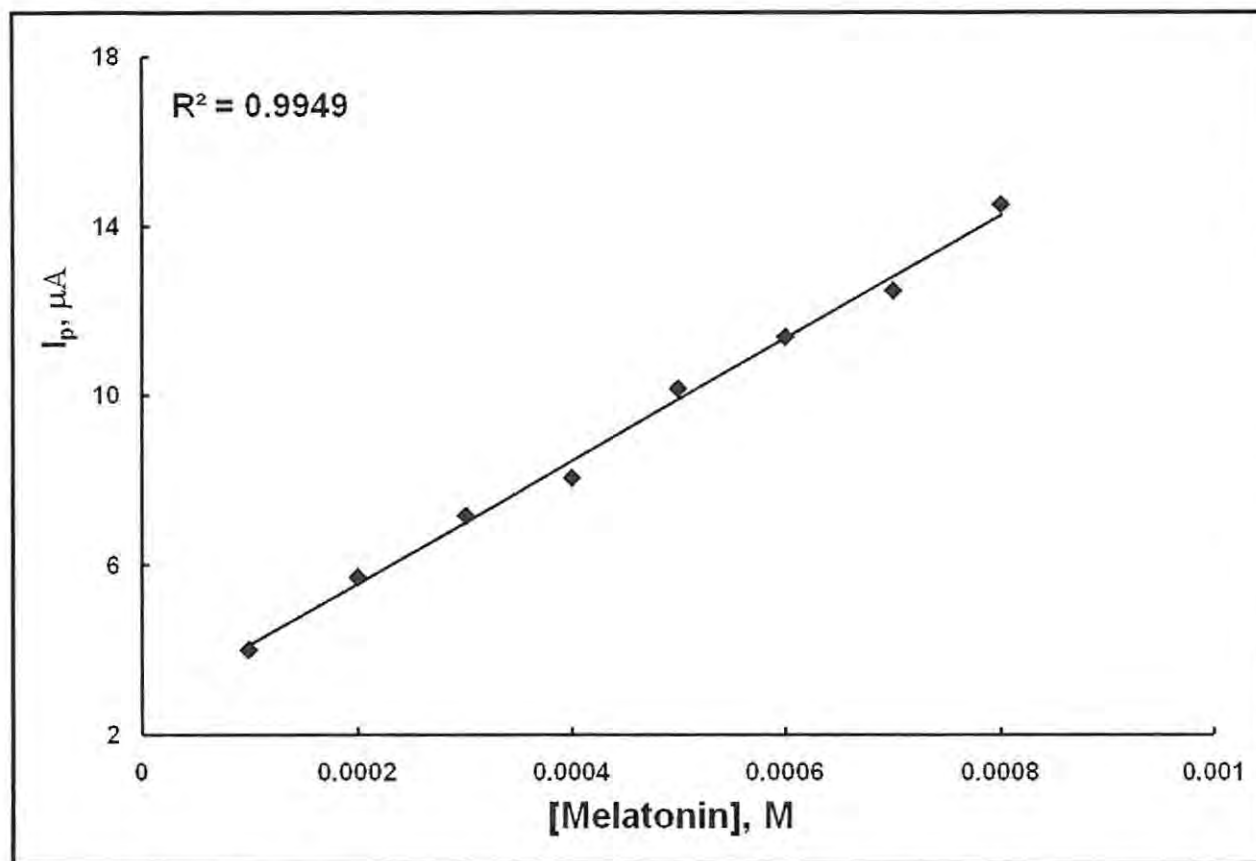
Fig. 5.11 Plot of I_p vs. the melatonin concentration for $CoPc(COOH)_4$ adsorbed onto GCE

The limits of detection for all electrodes (for melatonin in PBS, pH 7.4), calculated using the 3σ criterion, lay in the 10^{-7} to 10^{-6} M region (Table 5.3).

The stabilities of the electrodes were studied by monitoring the decreases in current with scan number. Fig. 5.12 shows, as an example, a plot of the peak current vs. the scan number recorded in melatonin (in PBS, pH 7.4) for $CoPc(COOH)_4$ GCE.
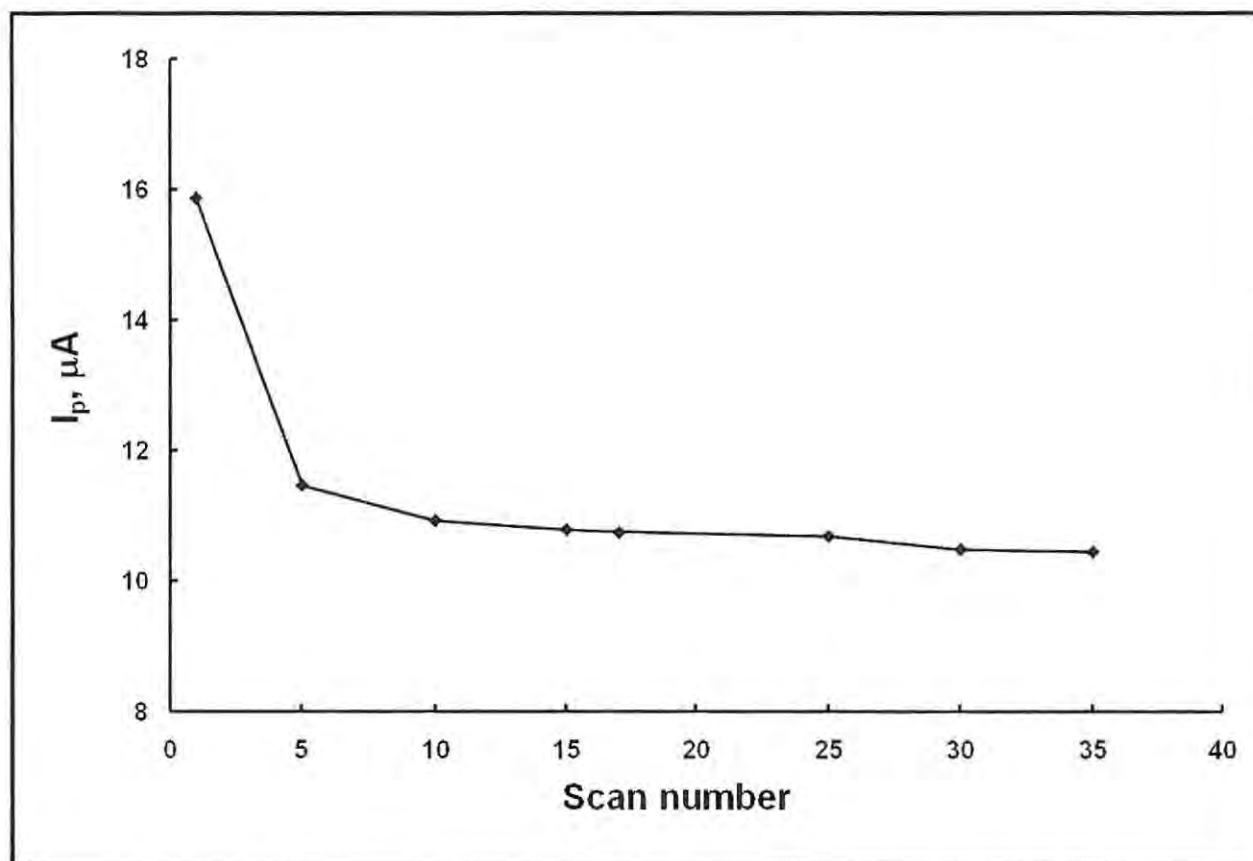
Fig. 5.12 Plot of I_p vs. cyclic voltammetry scan number for CoPc(COOH)$_4$ GCE recorded in 1 mM melatonin

There were decreases of 10 - 17% (Table 5.3) in the oxidation peak current after the fifteenth scan for all electrodes. This indicates that there was some passivation on the electrode, surface perhaps due to adsorption of product(s) of melatonin oxidation on the electrode [312]. Thereafter, the peak currents stabilized, showing no significant differences between subsequent scans (Fig. 5.12) and thus high resistance to passivation. The largest loss in current after 35 scans was obtained for an un-modified GCE (40 % decrease) and the best stability was obtained with the CoPc(COOH)$_8$ modified electrode (10% decrease). This shows that electrode modification with a specific CoPc derivative improves the long-term stability of the glassy carbon electrode.

Table 5.6 lists the electrochemical parameters for melatonin determination for the modified electrodes.

Table 5.6 The properties of modified electrodes as electrochemical sensors for melatonin[a]

MPc	Electrode	LOD (M)	E_p (V) vs. Ag|AgCl	Ref.
CoPc	GCE	1.70×10^{-6}	0.65	This work
CoPc(COOH)$_4$	GCE	1.19×10^{-7}	0.60	This work
CoPc(COOH)$_8$	GCE	1.44×10^{-7}	0.60	This work
-	Carbon paste	2.3×10^{-6}	Not stated	312

[a]GCE = glassy carbon electrode; LOD = limit of detection

The electrochemical detection of melatonin has not been extensively studied and this work, to the best knowledge of the author, presents for the first time the electrochemical detection of melatonin using electrodes with adsorbed MPcs. Furthermore, these electrodes displayed better limits of melatonin detection than those reported in the literature, Table 5.6.

To investigate the interaction of melatonin with CoPc derivatives, the changes in UV-visible spectra of solutions of CoPc, CoPc(COOH)$_4$, and CoPc(COOH)$_8$, were recorded before and after addition of melatonin. Small shifts (~5 nm) in Q band maxima were observed. Such small shifts in spectra are typical of axial ligation in MPc complexes [459]. Even though these studies were done in solution they may give an idea of the behaviour in the adsorbed state.

The most likely mechanism for the oxidation of melatonin (Eqs. 5.11 - 5.14) takes into account that the first one electron transfer is rate determining (from Tafel slopes) and that the total number of electrons transferred is two.

$$Co^{II}Pc + RNH \rightarrow (RNH)Co^{II}Pc \qquad 5.11$$

$$(RNH)Co^{II}Pc \rightarrow [(RNH)Co^{III}Pc]^+ + e^- \qquad 5.12$$

$$[(RNH)Co^{III}Pc]^+ \rightarrow [(RN^•)Co^{III}Pc]^+ + e^- + H^+ \qquad 5.13$$

$$[(RN^•)Co^{III}Pc] \rightarrow Co^{II}Pc + \text{oxidation products} \qquad 5.14$$
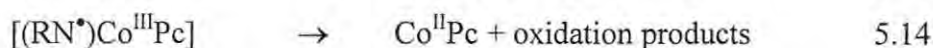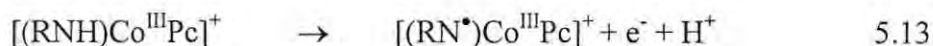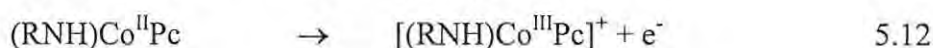
where RNH represents melatonin and the oxidation products include the dimer shown in Fig. 5.13.
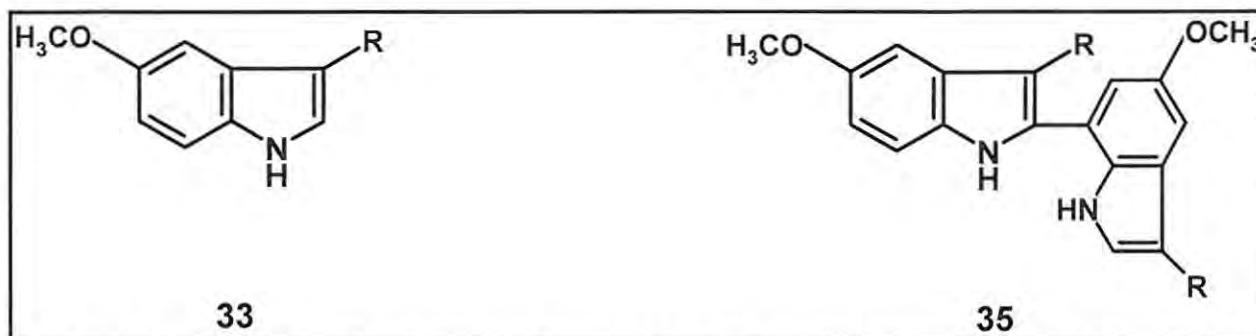
Fig. 5.13 The molecular structure of melatonin (**33**) and its possible oxidation product (**35**). R = CH$_2$CH$_2$NHCOCH$_3$

Two electrons are involved hence Eqs. 5.12 and 5.13 are proposed. Eq. 5.11 is proposed on the basis of coordination of melatonin to CoPc, CoPc(COOH)$_4$, and CoPc(COOH)$_8$. Eq. 5.12 is also proposed because the catalytic oxidation of melatonin is within the range of Co$^{III/II}$ (Fig. 5.1) and is catalyzed by this couple.

One important factor in biological sensing is the ability of the electrode to differentiate between interfering species present in the system. The ability of the GCE modified by CoPc derivatives to differentiate common species, which may be present when analyzing melatonin, was studied using square wave voltammetry (SWV), Figs. 5.14 and 5.15.
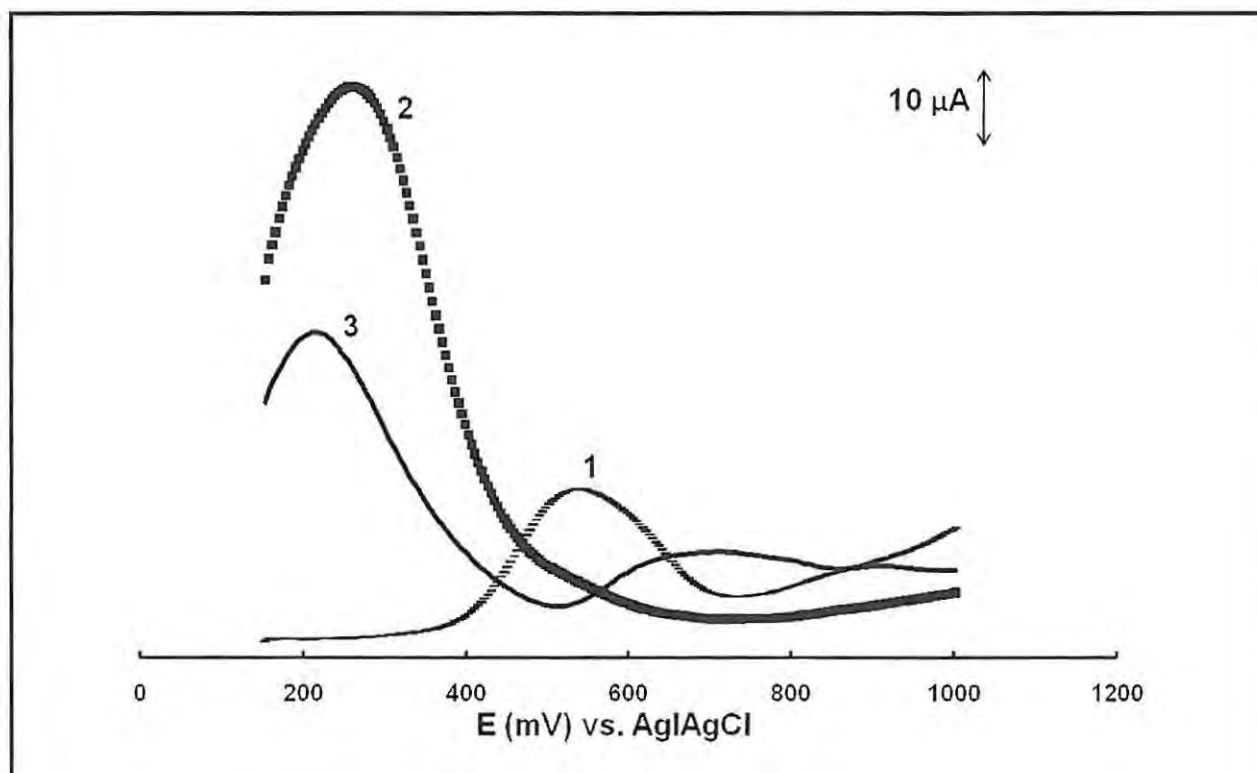
Fig. 5.14 Square wave voltammograms of CoPc(COOH)$_4$ GCE in (1) melatonin (ME), (2) ascorbic acid (AA), and (3) a mixture of ME and AA acid. [AA] = 1 × 10^{-2} M; [ME] = 1 × 10^{-3} M
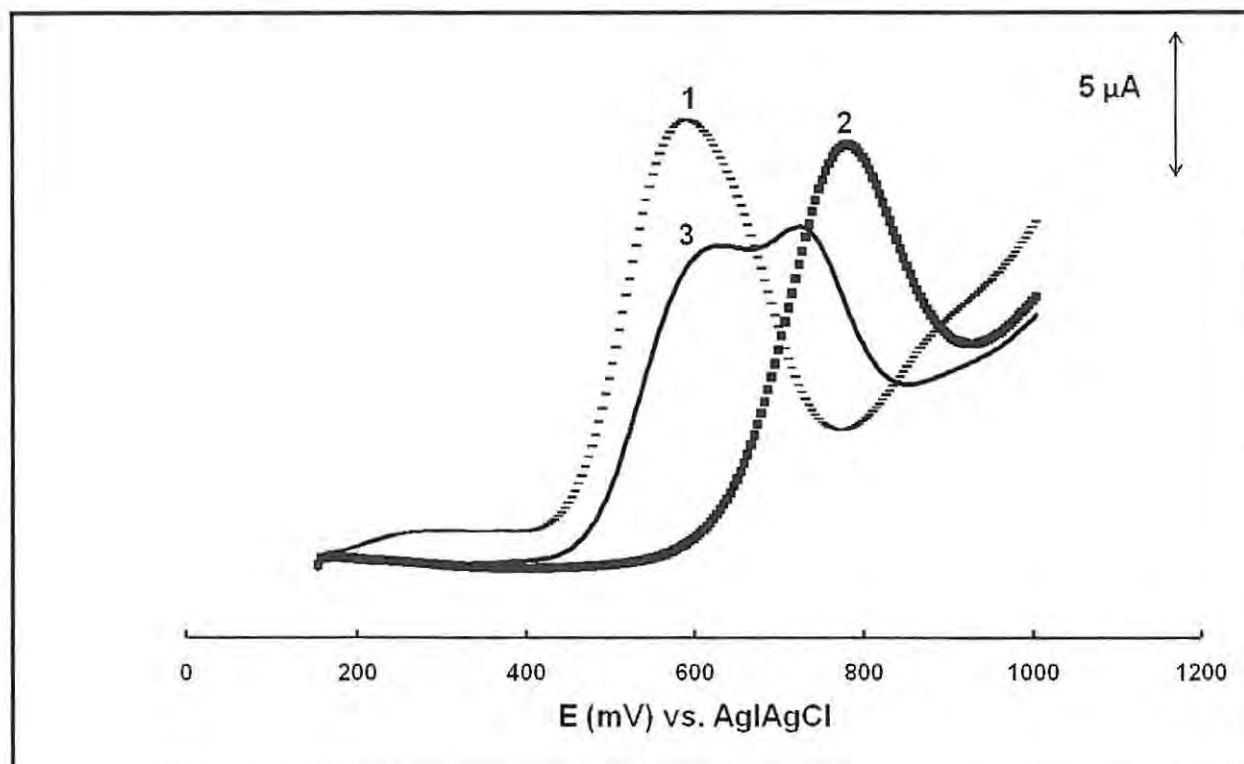
Fig. 5.15 Square wave voltammograms of CoPc(COOH)$_4$ GCE in (1) melatonin (ME), (2) tryptophan (Tryp), and (3) a mixture of ME and Tryp. [Tryp] = [ME] = 1 × 10^{-3} M

The interferents chosen were ascorbic acid (concentration ten times that of melatonin) and tryptophan (concentration the same as melatonin). The concentrations were chosen to mimic, to some extent, those in biological systems. The detection of melatonin in the presence of ascorbic acid is shown in Fig. 5.14 on CoPc(COOH)$_4$ GCE. This electrode was chosen because it showed the best overall catalytic behaviour for the detection of melatonin, compared to the other CoPc derivatives, in terms of low potential (compared to CoPc) and better sensitivity (compared to CoPc and CoPc(COOH)$_8$), Tables 5.1 and 5.3. Using SWV on the CoPc(COOH)$_4$ GCE, melatonin shows a broad peak, Fig. 5.14 (curve 1), but the peaks of melatonin and ascorbic acid in the mixture (curve 3) are quite separated from each other so that simultaneous analyses of both species are possible. The peak of melatonin is smaller and shifted in the presence of ascorbic acid whilst the peak of ascorbic acid decreases in the presence of melatonin, Fig. 5.14. This is most likely due to both species (melatonin and ascorbic acid) interfering with each other in the detection process. Nevertheless, as stated above, melatonin and ascorbic acid could be

149

simultaneously detected clearly. For tryptophan, peak distinctions in the mixture (curve 3) are still discernible but overlapped, Fig. 5.15. The peaks of tryptophan and melatonin decrease when both species are present in the solution, Fig. 5.15, due to the reason given above.

Fig. 5.16 shows SWV of a mixture containing melatonin, tryptophan, and ascorbic acid on CoPc modified electrodes.
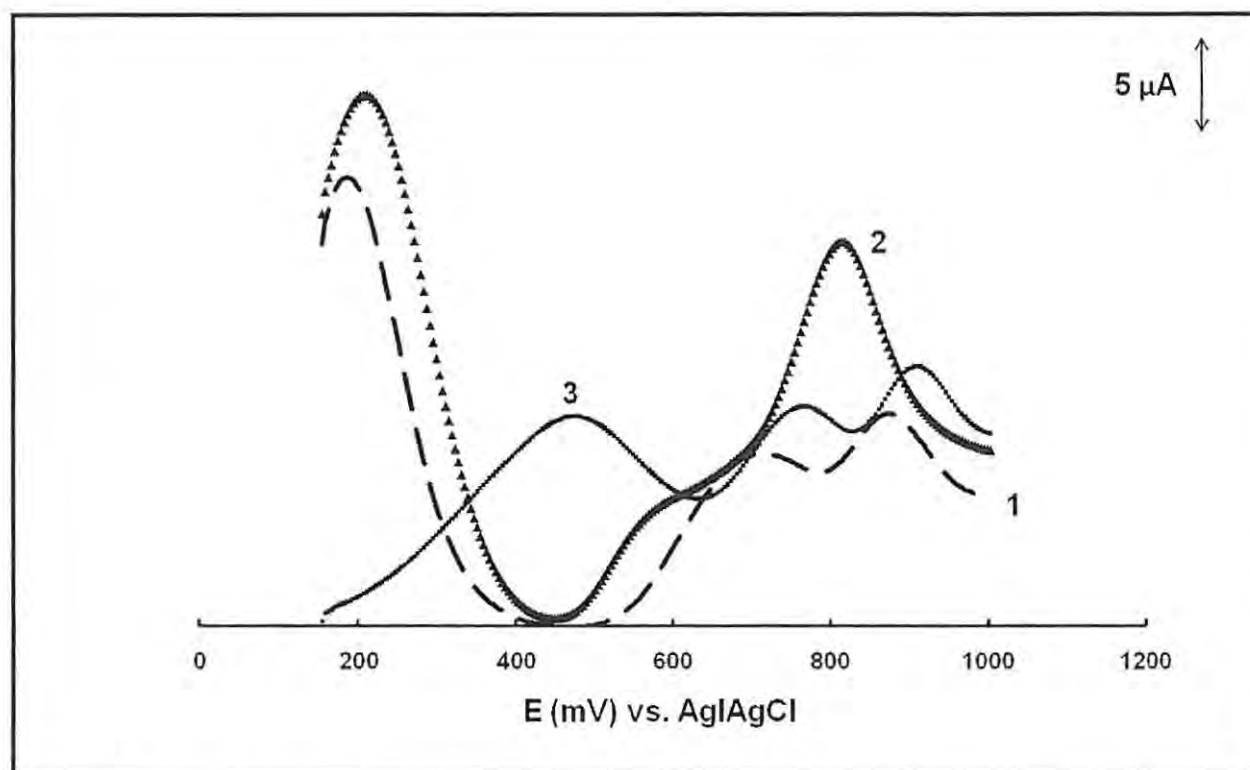
Fig. 5.16 Square wave voltammograms of CoPc GCE (1), CoPc(COOH)$_4$ GCE (2), and CoPc(COOH)$_8$ GCE (3) recorded in a mixture of 1×10^{-2} M AA, 1×10^{-3} M Tryp, and 1×10^{-3} M ME

The best separation of the peaks was obtained on CoPc GCE (curve 1) and CoPc(COOH)$_8$ GCE (curve 3). The worst separation was for un-modified GCE (not shown). CoPc(COOH)$_8$ gave a broad melatonin detection peak but well defined ascorbic acid and tryptophan peaks, Fig. 5.16. All three analytes (melatonin, tryptophan, and ascorbic acid) can thus be detected simultaneously on the CoPc modified electrode and tryptophan and ascorbic acid do not interfere with the detection of melatonin when all are present in a mixture.

Chapter 5: Electrode modification by adsorption

The content of melatonin in capsules, each containing 3 mg melatonin, was determined in PBS (pH 7.4) using cyclic voltammetry standard addition methods. All electrodes gave melatonin concentrations of 3 mg per capsule as specified by the supplier. The values are: CoPc GCE = 3.17 mg/capsule, $CoPc(COOH)_4$ GCE = 2.99 mg/capsule, and $CoPc(COOH)_8$ GCE = 3.19 mg/capsule.

5.3. Conclusions

The catalytic activity of CoPc complexes is highly dependent on the substituent, hence this work compares the catalytic activity of cobalt phthalocyanine (CoPc, **5g**) with those of cobalt tetracarboxy phthalocyanine ($CoPc(COOH)_4$, **7a**) and cobalt octacarboxy phthalocyanine ($CoPc(COOH)_8$, **10a**), when adsorbed onto glassy carbon electrodes, for the electrocatalytical detection of nitrite, L-cysteine, and melatonin (the electrodes cannot detect thiocyanate). Characterization of the modified electrodes proved that as the number of carboxy ring substituents increases, the CoPc derivative becomes more difficult to reduce and easier to oxidize. The resistance to charge transfer value is highest for $CoPc(COOH)_4$ which suggests a more effective electrode modification than for the other two complexes - this may be due to the higher surface coverage by $CoPc(COOH)_4$ on the GCE. Impedance measurements also showed that the GCE electrodes modified by the CoPc derivatives do not behave like ideal capacitors in $[Fe(CN)_6]^{3-}/[Fe(CN)_6]^{4-}$ solution.

Electrodes modified with CoPc derivatives showed larger nitrite oxidation peaks at much lower oxidation potentials than an un-modified GCE. CoPc and $CoPc(COOH)_4$ modified electrodes displayed nitrite oxidation at lowest potentials, but $CoPc(COOH)_8$ gave a slightly higher current response. $CoPc(COOH)_4$ had a higher surface coverage but does not show larger nitrite oxidation currents. This shows that the number of ring substituents does affect the potential of nitrite oxidation. Good limits of detection for nitrite (10^{-7} M region) were obtained for all modified electrodes. From UV-visible spectral studies, addition of nitrite to CoPc and $CoPc(COOH)_8$ showed axial ligation of the MPc complexes. But for $CoPc(COOH)_4$ there was evidence of aggregation which may explain the unfavourable limits of detection obtained for the $CoPc(COOH)_4$ GCE. A mechanism for the catalysis of nitrite oxidation using CoPc and $CoPc(COOH)_8$ has been proposed.

Chapter 5: Electrode modification by adsorption

All modified electrodes of this work could detect L-cysteine, whereas an un-modified electrode could not. The limits of L-cysteine detection by the modified electrodes are in the 10^{-7} M region. The stabilities of the electrodes in detecting L-cysteine decreased with increasing number of substituents on the CoPc which indicates that the bulkiness of the substituents disturbs the stability. A mechanism for catalysis of L-cysteine oxidation using CoPc and $CoPc(COOH)_8$ has been proposed.

The modified electrodes detected melatonin at higher peak currents and lower peak potentials than an un-modified gold electrode. The limits of melatonin detection of the modified electrodes lay in the 10^{-7} to 10^{-6} M region. Electrode modification with a specific CoPc was shown to improve the long-term stability of the GCE for the detection of melatonin. A mechanism for the oxidation of melatonin by the CoPc derivatives was proposed in which: axial ligation of the MPc complexes to melatonin occurs; the first one electron transfer reaction is rate determining; and the total number of electrons transferred is two. The modified electrodes accurately measured the contents of capsule melatonin concentrations as specified by the supplier. With respect to biological sensing, all of the modified electrodes could differentiate between melatonin, tryptophan, and ascorbic acid in a mixture.

All of the modified electrodes of this work can reliably detect nitrite, L-cysteine, and melatonin in the 10^{-4} to 10^{-2} M region.

CHAPTER 6: SELF ASSEMBLED MONOLAYERS

MPc complexes substituted with thio groups ((OH)MnPc(SPh)$_4$ (**6c**), α-(OH)MnTMPyPc (**6d**), α-Q-(OH)MnTMPyPc (**6e**), β-(OH)MnTMPyPc (**8d**), β-Q-(OH)MnTMPyPc (**8e**), FePc(SCH$_2$Ph)$_8$ (**9b**), CoPc(SCH$_2$Ph)$_8$ (**10b**)) were used to form self assembled monolayers (SAMs). SAM studies with complex **8b** were not done because they have been reported [32]. Alkyl or arylthio MPcs are known to form SAMs without cleavage of the aryl or alkyl group [23]. The SAMs were characterized using the following techniques: voltammetry, impedance measurements, atomic force microscopy (AFM), and scanning electrochemical microscopy (SECM). The SAMs were used as electrochemical sensors of nitrite and L-cysteine. These studies are detailed in this section. Thiocyanate (Chapter 4) and melatonin (Chapter 5) cannot be detected by these electrodes.

6.1. Characterization

6.1.1. Cyclic voltammetry

Voltammetry techniques for the characterization of SAMs are based on the principal that SAMs block a number of Faradic processes [23].

Fig. 6.1 shows the first scan voltammograms of the SAMs in pH 4 buffer, which confirm that the responses are not due to polymerized species because polymers form only on continuous scanning. Raman spectroscopy was used to confirm the formation of the SAMs (i.e. Au-S bond): a weak pe ak for the Au-S vibration was observed at ~310 cm^{-1} [490] . SAM formation is dependent on the central metal and involves distinct metal redox processes [27,320].
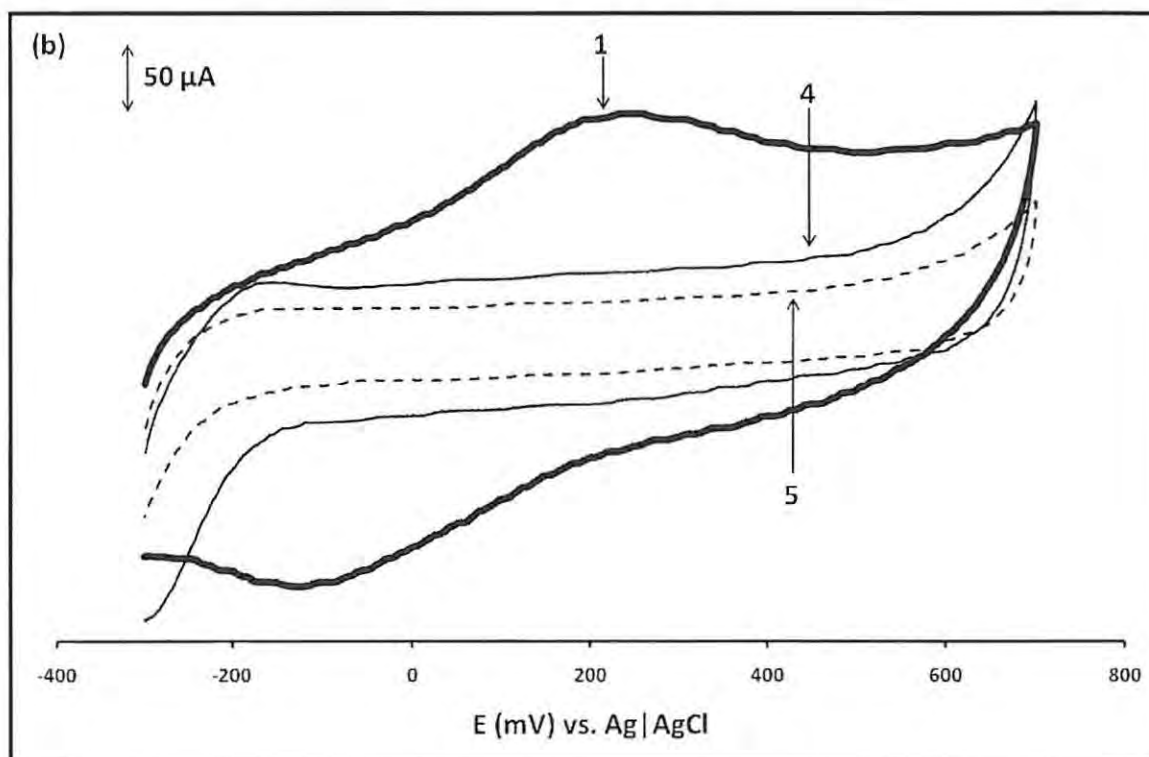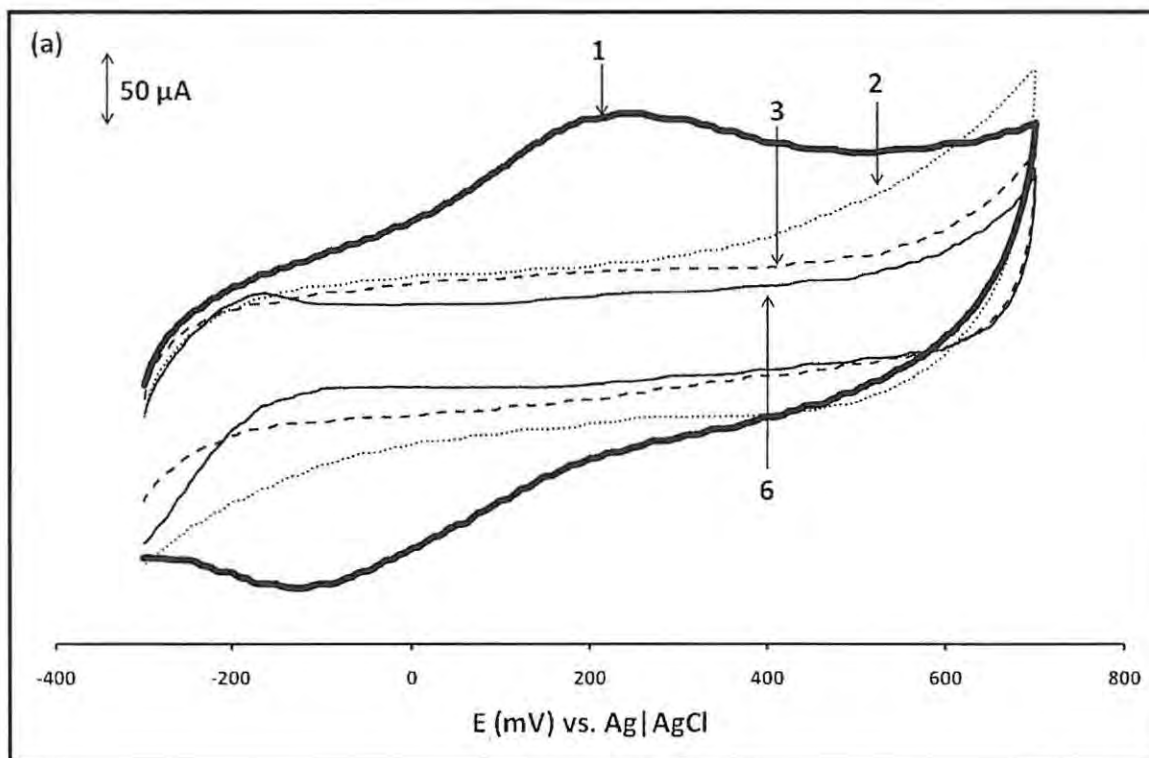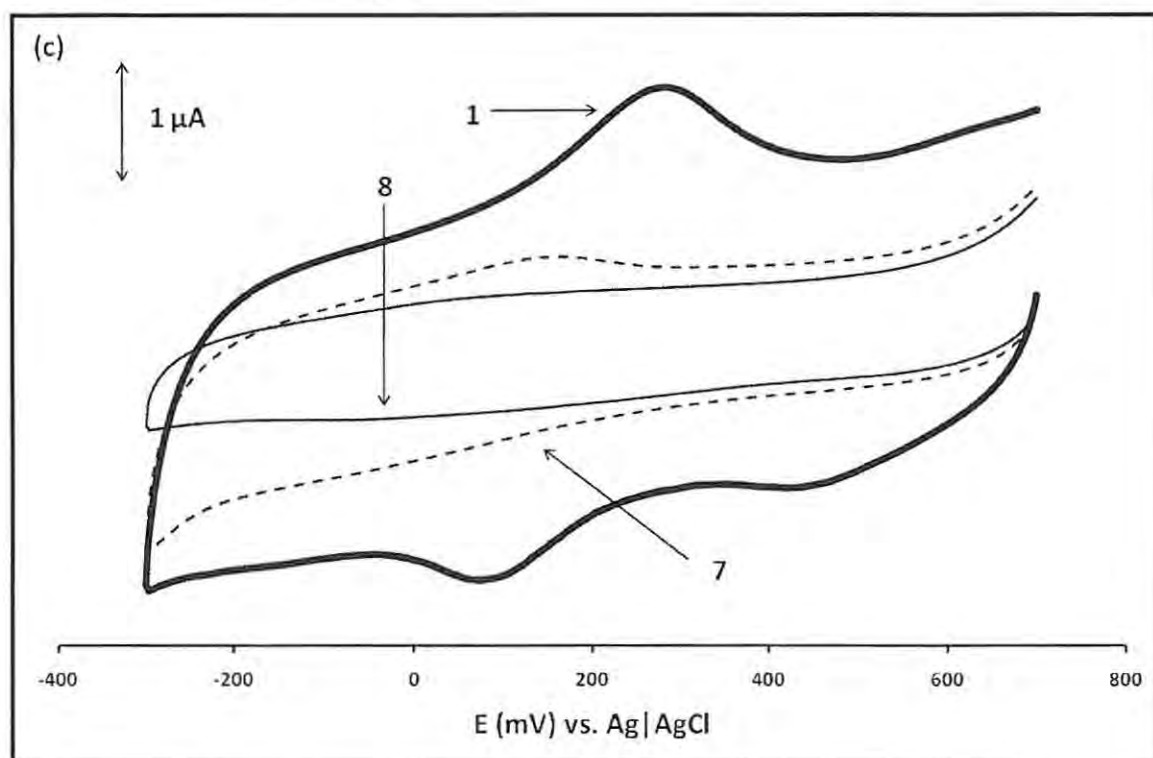
Fig. 6.1 (a) - (c) Cyclic voltammograms of an un-modified gold electrode (1) and of SAM gold electrodes modified with $(OH)MnPc(SPh)_4$ (**6c**, 2), α-$(OH)MnTMPyPc$ (**6d**, 3), α-Q-$(OH)MnTMPyPc$ (**6e**, 4), β-$(OH)MnTMPyPc$ (**8d**, 5), β-Q-$(OH)MnTMPyPc$ (**8e**, 6), $FePc(SCH_2Ph)_8$ (**9b**, 7), and $CoPc(SCH_2Ph)_8$ (**10b**, 8) recorded in 1 M Na_2SO_4 at 100 $mV.s^{-1}$

6.1.1.1. Ion barrier factor (Γ_{ibf})

The ion barrier factor (Γ_{ibf}) is obtained by comparison of the total charge under the gold redox peak of a SAM modified electrode (Q_{SAM}) with that of an un-modified electrode (Q_{Bare}), Eq. 6.1, as Eq. 1.5:

$$\Gamma_{ibf} = 1 - \frac{Q_{SAM}}{Q_{Bare}} \qquad\qquad 6.1$$

An ion barrier factor of one indicates that there are no pinholes in the SAM and that it is an ideal barrier to ion and solvent permeability [132,218].

Fig. 6.1 (a) - (c) shows the cyclic voltammograms for an un-modified gold electrode (curve 1) and for SAM modified gold electrodes (curves 2 - 8) recorded in 1 M Na_2SO_4 in pH 4 buffer solution. The peaks observed on the un-modified gold electrode (curve 1) are due to the gold

155

oxide redox reaction. Upon modification, the peaks disappear completely for all of the complexes (curves 2 - 8). From Fig. 6.1, ion barrier factors between 0.9814 (for complex **9b**) and 0.9998 (for complex **8d**) were obtained (using Eq. 6.1) for all of the SAM complexes, Table 6.1. This shows that only 1 - 2 % of the gold surface is not covered by the complex SAMs and that the SAMs are compact and virtually defect free. For MnPc derivatives, ion barrier factors were closer to 1 (Table 6.1) showing that the Mn complexes (**6c**, **6d**, **6e**, **8d**, **8e**) form better SAMs than the FePc (**9b**) or CoPc (**10b**) derivatives in this work. The peaks near -200 mV for the MnPc SAM modified electrodes are due to MnPc based processes. These results confirm that all of the SAMs are well packed, have a strong passivating aptitude, and act as efficient barriers to ion permeability.

Table 6.1 Characterization parameters of MnPc SAM complexes[a]

Parameter	6c	6d	6e	8d	8e	9b	10b
Ion barrier factor, Γ_{ibf}	1	0.9997	0.9994	0.9998	0.9996	0.9814	0.9938
Interfacial capacitance, C_s (μF.cm^{-2})	308	452	539	303	302	~800	500
Surface coverage, Γ (mol.cm^{-2})	1.06×10^{-10}	1.73×10^{-10}	2.77×10^{-10}	2.80×10^{-10}	2.67×10^{-10}	4.24×10^{-10}	1.55×10^{-10}

[a]**6c** = (OH)MnPc(SPh)$_4$; **6d** = α-(OH)MnTMPyPc; **6e** = α-Q-(OH)MnTMPyPc; **8d** = β-(OH)MnTMPyPc; **8e** = β-Q-(OH)MnTMPyPc; **9b** = FePc(SCH$_2$Ph)$_8$; **10b** = CoPc(SCH$_2$Ph)$_8$

6.1.1.2. Interfacial capacitance (C_s)

A defined potential window of a cyclic voltammogram, in which no peaks are observed for both un-modified and SAM modified gold electrodes, will have a charging current (i_{ch}), whose value may be used to calculate the interfacial capacitance (C_s) using Eq. 6.2, as Eq. 1.6:

$$C_s = \frac{i_{ch}}{vA} \qquad \qquad 6.2$$

where v is the scan rate (V.s^{-1}) and A is the electrode surface area (cm^2).

Chapter 6: Self assembled monolayers

The lower the C_s value, the fewer are the defects present in the SAM and so the less permeable is the electrode surface to electrolyte ions [132,219]. A SAM modified gold electrode should therefore display a lower C_s value than an un-modified gold electrode.

Fig. 6.1 was used to estimate the C_s values in the potential window of -0.3 to -0.1 V. The C_s values ranged from 302 (β-Q-(OH)MnTMPyPc, **8e**) to 800 (FePc(SCH$_2$Ph)$_8$, **9b**) μF.cm^{-2} for all of the SAMs of this work, Table 6.1. The C_s values are lower than for an un-modified gold electrode (C_s = 1500 μF.cm^{-2}). Values of C_s for un-modified gold electrodes have been reported to be ~20 mF.cm^{-2} [491]. The value reported in this work is also within the mF.cm^{-2} range. The decrease in C_s on formation of SAMs is attributed to a closely packed, relatively defect free coverage for all of the SAMs. The highest C_s value, for a FePc(SCH$_2$Ph)$_8$ SAM modified electrode (C_s ≈ 800 μF.cm^{-2}) is nevertheless significantly lower than the C_s value of the un-modified gold electrode (C_s = 1500 μF.cm^{-2}). The lowest C_s values are for the MnPc derivatives, especially **6c**, **8d**, and **8e**, which are tetrasubstituted. Thus the MnPcs also form better SAMs. For the octasubstituted Pcs, containing similar substituents, the higher C_s value of FePc(SCH$_2$Ph)$_8$ SAM (**9b**) relative to CoPc(SCH$_2$Ph)$_8$ SAM (**10b**), shows that the former contains more defects than the latter. This is illustrated in Fig. 6.1(c) where the cyclic voltammogram of the SAM of CoPc(SCH$_2$Ph)$_8$ (curve 8) shows lower currents than of FePc(SCH$_2$Ph)$_8$ SAM (curve 7).

As mentioned, the tetrasubstituted Pcs form better SAMs. Octopus orientated MPcs, assumed for octasubstituted Pcs, are reported [221] to form poorly organized SAMs especially because the Pc rings are tilted on the gold surface. This explains why the MnPc tetrasubstituted Pcs form better SAMs. FePc(SCH$_2$Ph)$_8$ SAM may show more tilting than CoPc(SCH$_2$Ph)$_8$ SAM, hence the differences in their C_s values. Although true comparison is difficult, the C_s values obtained in this work are higher than those obtained in the literature [33]. The substituents of the Pcs studied in this work possess bulky phenolic groups which may lower the compactness hence increasing the C_s values to a large extent.

6.1.1.3. Underpotential deposition (UPD) of copper

Fig. 6.2 shows how the SAMs of all the complexes inhibit the Faradic process of Cu metal deposition onto a gold electrode relative to an un-modified gold electrode (curve 1).
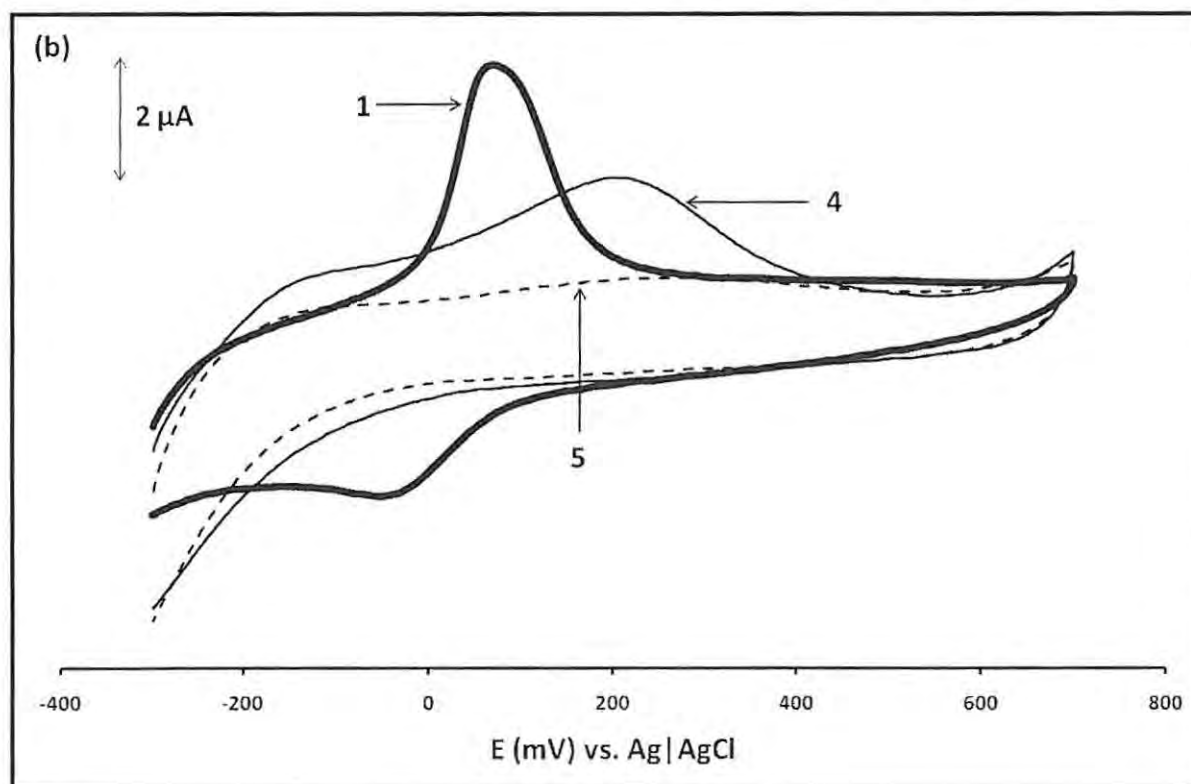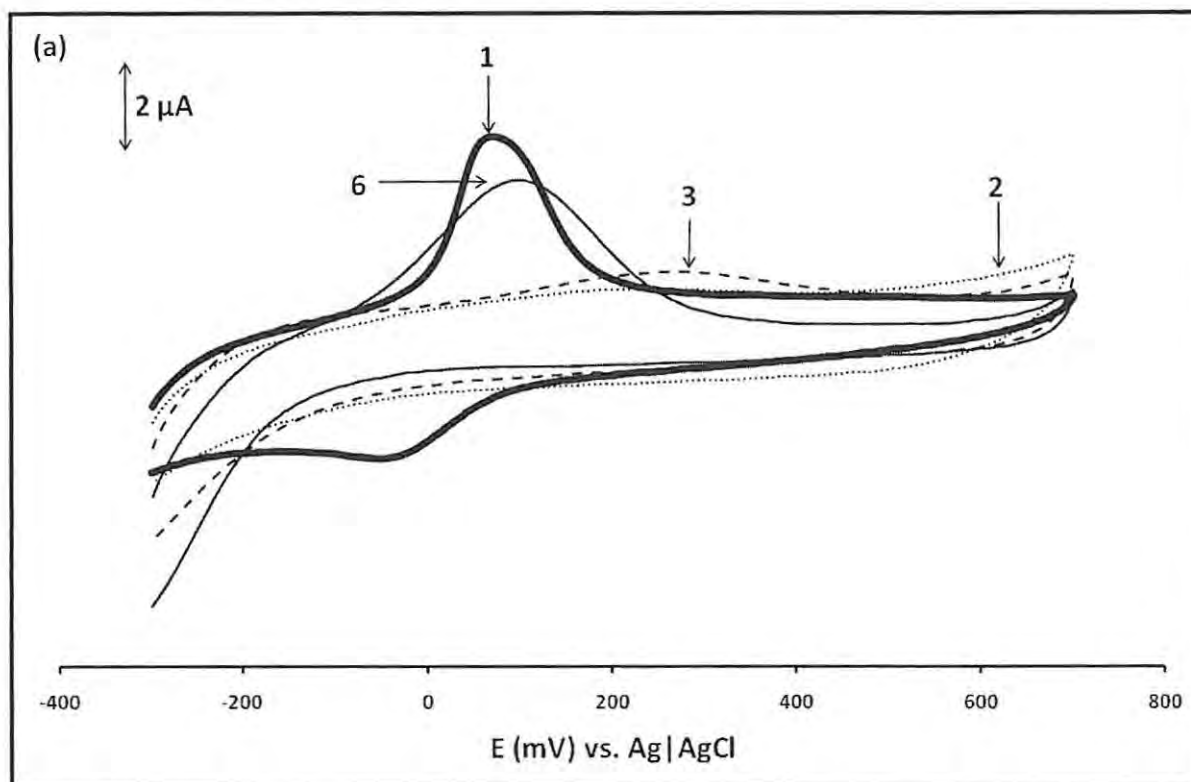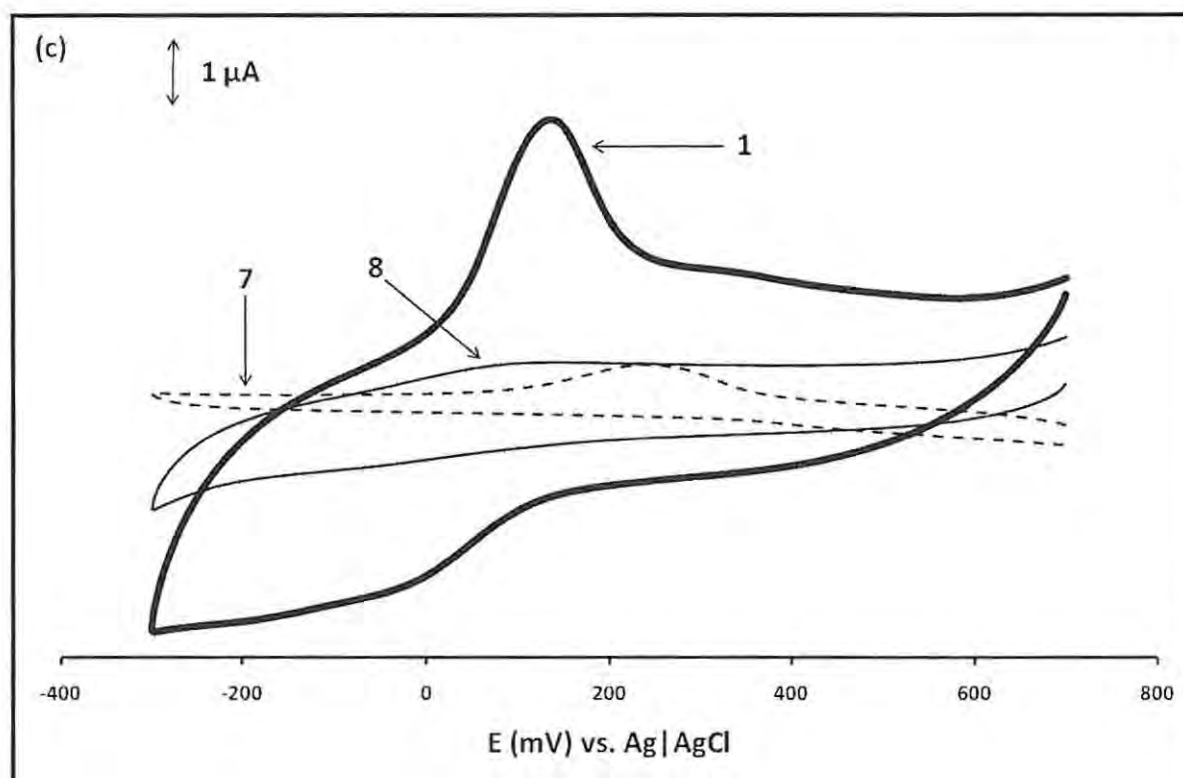
Fig. 6.2 (a) - (c) Cyclic voltammograms of an un-modified gold electrode (1) and of SAM gold electrodes modified with $(OH)MnPc(SPh)_4$ (**6c,** 2), α-$(OH)MnTMPyPc$ (**6d,** 3), α-Q-$(OH)MnTMPyPc$ (**6e,** 4), β-$(OH)MnTMPyPc$ (**8d,** 5), β-Q-$(OH)MnTMPyPc$ (**8e,** 6), $FePc(SCH_2Ph)_8$ (**9b,** 7), and $CoPc(SCH_2Ph)_8$ (**10b,** 8) recorded in 1 mM $CuSO_4$ at 100 mV.s^{-1}

The bulk deposition of copper began at approximately +0.1 V vs. Ag|AgCl during the negative going scan of the un-modified gold electrode, Fig. 6.2. A large underpotential deposition (UPD) stripping peak for the Cu metal is observed between 0 and 0.15 V on the return scan (Fig. 6.2, curve 1). This peak has a characteristic shape and occurs in a similar potential window to that previously published [211,492]. Negligible current responses are observed on the cyclic voltammograms of SAMs of **6c** (curve 2), **8d** (curve 5), **9b** (curve 7), and **10b** (curve 8), relative to that of the un-modified gold electrode (curve 1), Fig. 6.2. Low intensity peaks upon return were observed for complexes **6e** (curve 4) and **8e** (curve 6), Fig. 6.2. For complex **6e** (curve 4), the peak at 0.20 V is associated with the Mn^{IV}/Mn^{III} couple in agreement with the literature [27,35]. For complex **8e** (curve 6), the peak at 0.1 V is also associated with the Mn^{IV}/Mn^{III} couple because there was no Cu deposition peak on the forward scan so that this peak cannot be

159

due to Cu stripping. Therefore, from Fig. 6.2, all SAMs cover the gold surface well because the gold surface is no longer accessible to the Cu solution and hence no redox reaction is clearly observed.

6.1.1.4. Inhibition of Fe^{III}/Fe^{II} redox processes

Fig. 6.3 shows the cyclic voltammograms of $[Fe(H_2O)_6]^{3+}/[Fe(H_2O)_6]^{2+}$ in 1 M $HClO_4$ solution on an un-modified gold electrode (curve 1) and on SAM modified gold electrodes (curves 2 to 8).
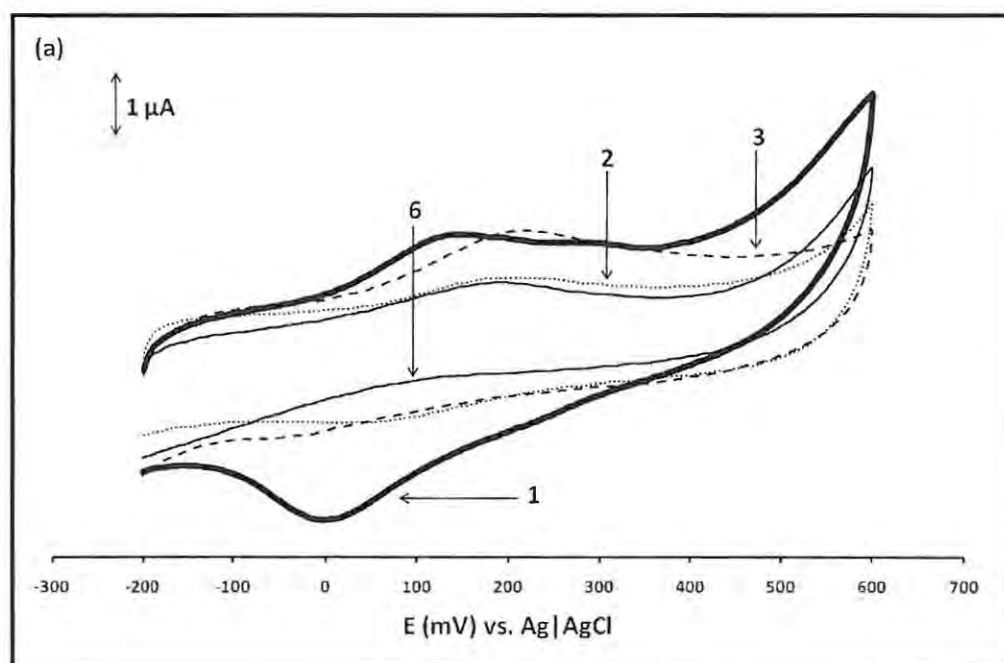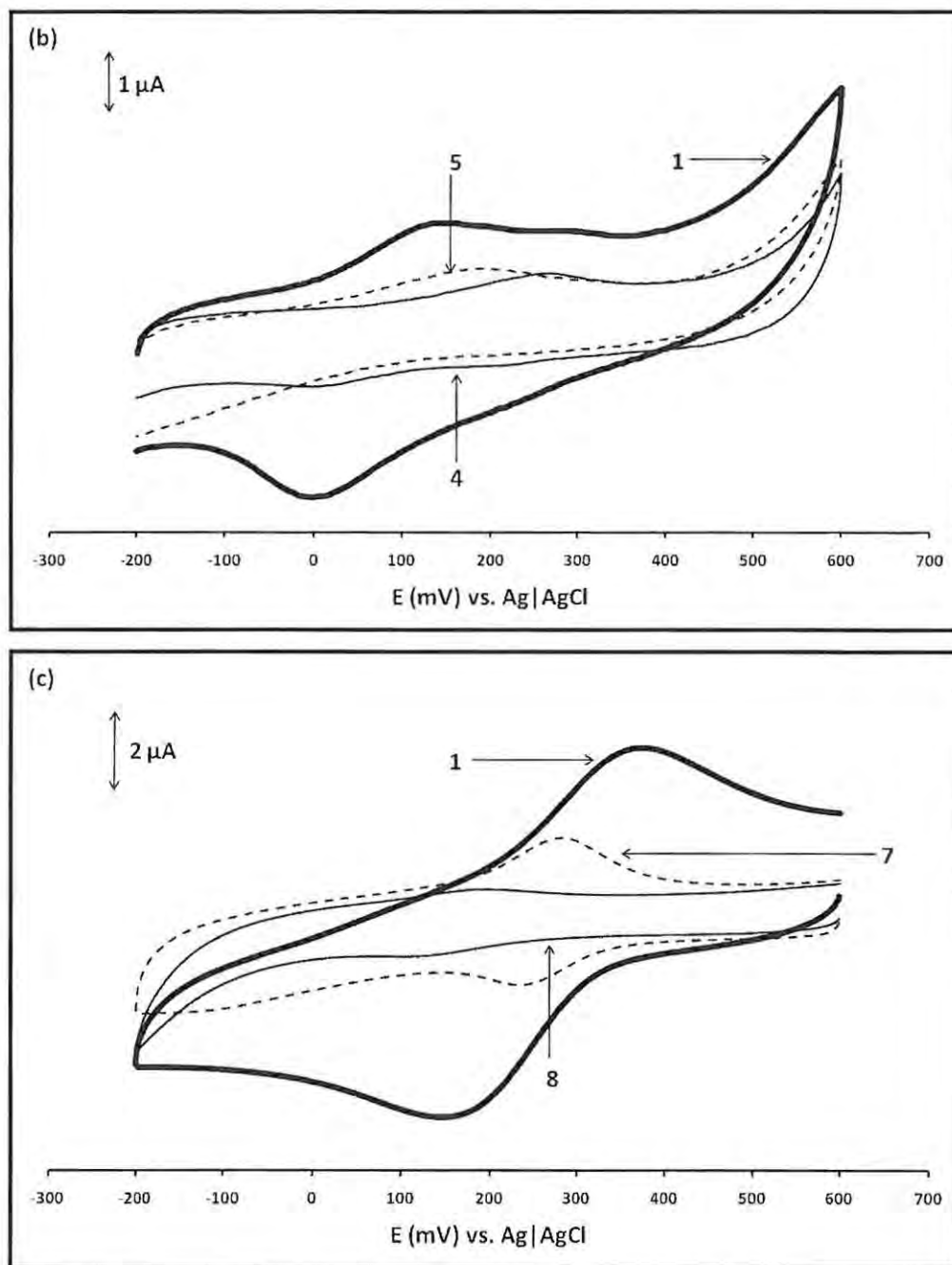
Fig. 6.3 (a) - (c) Cyclic voltammograms of an un-modified gold electrode (1) and of SAM gold electrodes modified with $(OH)MnPc(SPh)_4$ (**6c,** 2), α-$(OH)MnTMPyPc$ (**6d**, 3), α-Q-$(OH)MnTMPyPc$ (**6e**, 4), β-$(OH)MnTMPyPc$ (**8d**, 5), β-Q-$(OH)MnTMPyPc$ (**8e,** 6), $FePc(SCH_2Ph)_8$ (**9b**, 7), and $CoPc(SCH_2Ph)_8$ (**10b**, 8) recorded in 1 mM $Fe(NH_4)SO_4$ 1 M $HClO_4$ solution at 100 $mV.s^{-1}$

Chapter 6: Self assembled monolayers

$Fe(NH_4)SO_4$ in $HClO_4$ was used as the analyzing electrolyte because its redox couple $[Fe(H_2O)_6]^{3+}/[Fe(H_2O)_6]^{2+}$ has a lower electron transfer rate constant than $[Fe(CN)_6]^{3-}/[Fe(CN)_6]^{4-}$ and hence mass transport does not determine the reaction rate, even at small overpotentials [493]. The Faradic couple $[Fe(H_2O)_6]^{3+}/[Fe(H_2O)_6]^{2+}$ occurring in Fig. 6.3 in the +0.1 to +0.4 V region on the un-modified gold electrode (curve 1) is largely inhibited for all of the SAM modified gold electrodes. Complexes **8e** (curve 6) and **10b** (curve 8) SAM show the best inhibition of the redox processes showing that these films are more compact and act as better barriers to the transport of $[Fe(H_2O)_6]^{3+}/[Fe(H_2O)_6]^{2+}$ ions.

6.1.1.5. Surface coverage (Γ)

Fig. 6.4 shows the cyclic voltammograms of SAM complexes of **6d** (a), **9b** (b), and **10b** (c), as examples, recorded in 1 M $HClO_4$.
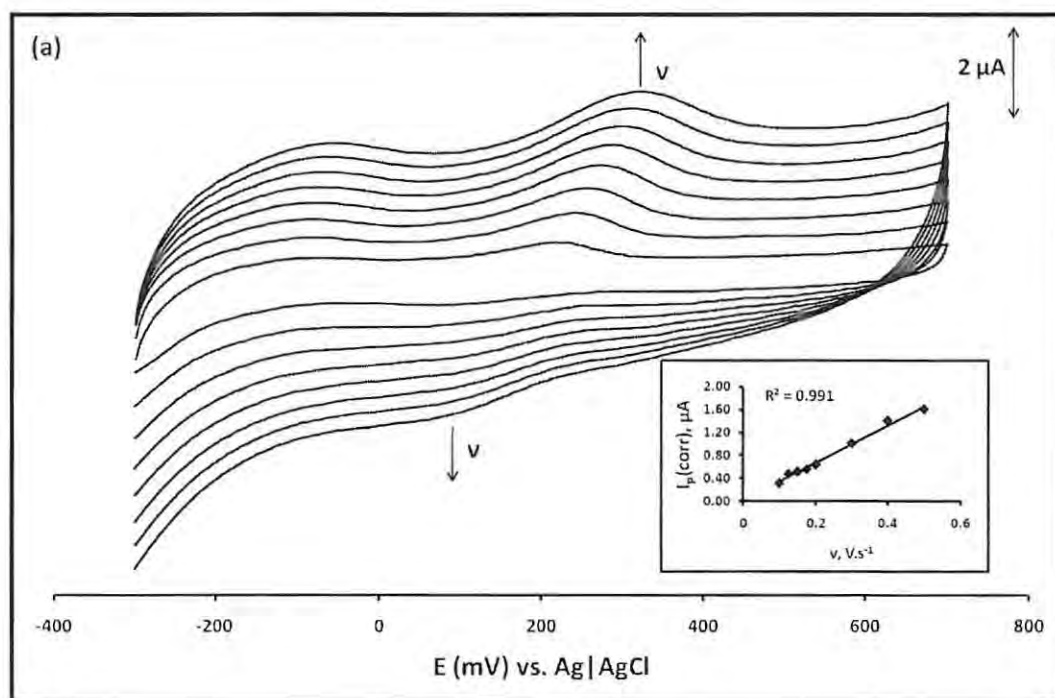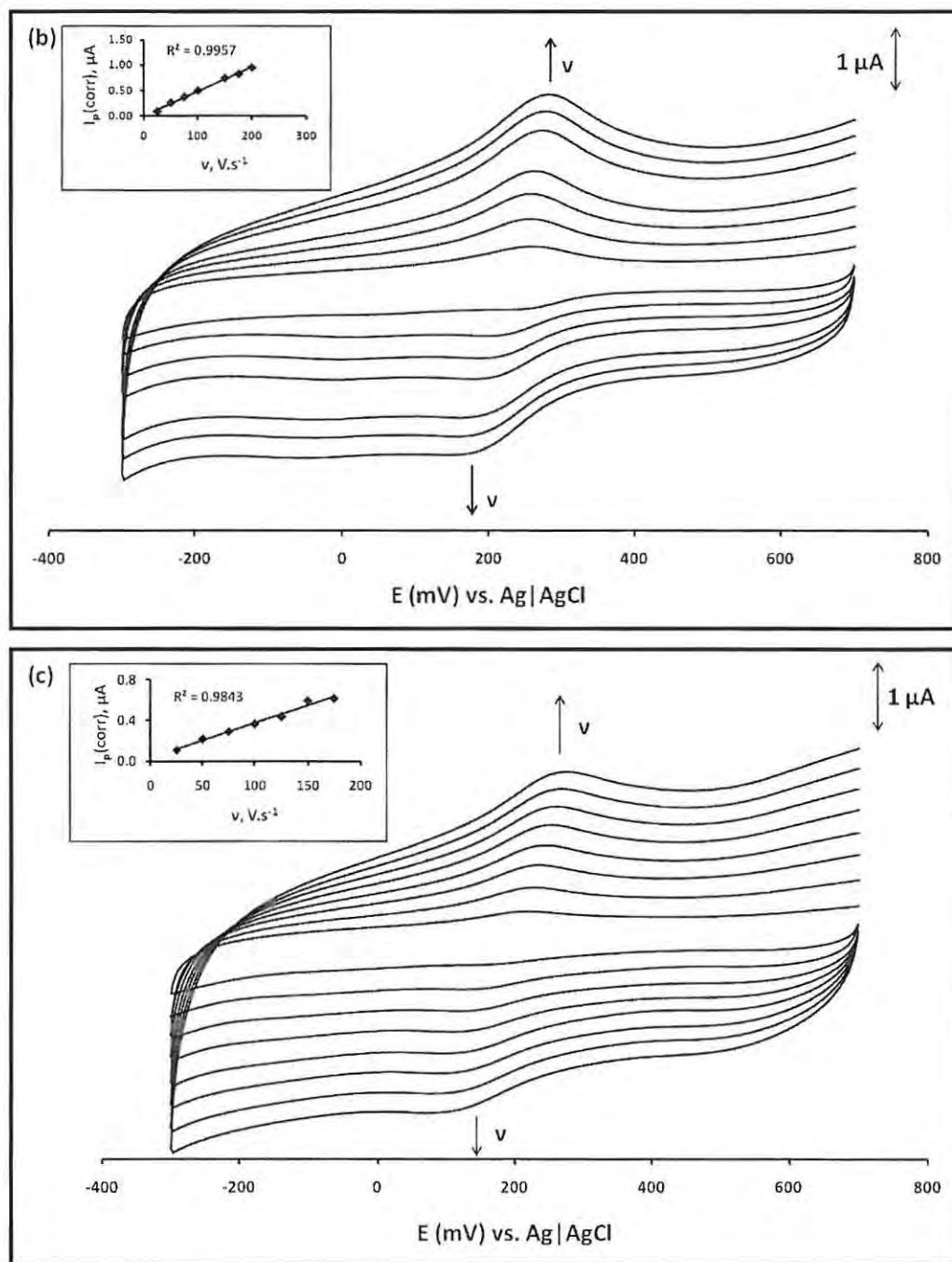
Fig. 6.4 Cyclic voltammograms of SAM gold electrodes modified with α-(OH)MnTMPyPc (**6d**, a), FePc(SCH$_2$Ph)$_8$ (**9b**, b), and CoPc(SCH$_2$Ph)$_8$ (**10b**, c) in 1 M HClO$_4$ solution (25-200 mV.s^{-1}). Insert: plot of I$_p$(corr) vs. ν of the respective voltammograms

From Fig. 6.4(a), the peak at ~200 mV vs. Ag|AgCl is assigned to the Mn^{IV}Pc^{-2}/Mn^{III}Pc^{-2} processes in agreement with the literature [27,35]. This peak was not evident in solution, Fig.

163

3.10 (Chapter 3), which is not surprising because some MPc complexes, e.g. NiPc, show metal based processes only when adsorbed [299]. The Fe^{III}/Fe^{II} couple was observed at 0.25 V vs. Ag|AgCl in agreement with the literature [494], Fig. 6.4(b). This Fe^{III}/Fe^{II} couple is evident in Fig. 6.3 and in a less defined manner in Figs. 6.1 and 6.2. The couple at ~200 mV in Fig. 6.4(c) for the complex **10b** SAM is assigned to Co^{III}/Co^{II} in agreement with the literature for SAMs of CoPc complexes [494]. This Co^{III}/Co^{II} couple was less defined, except at high scan rates in Fig. 6.4(c) and was unclear in Figs. 6.1 - 6.3. From Fig. 6.4, the peak separation (ΔE) of the Fe^{III}/Fe^{II} (b) and Co^{III}/Co^{II} (c) couples were 100 mV and 180 mV, respectively, at $v = 200$ mV.s^{-1}, higher than the expected 0 V for adsorbed species. This indicates slow electron transfer processes ($\Delta E = 0$ was observed at low scan rates for the Fe^{III}/Fe^{II} couple, Fig. 6.4(b)). The inserts of Fig. 6.4 show linear increases of the peak corrected current vs. the scan rate. The slopes of the straight lines can be used to calculate the surface coverages (Γ) using Eq. 6.3, which is similar to Eq. 1.7:

$$i_p = \frac{n^2 F^2 A \Gamma (v)}{4RT} \qquad\qquad 6.3$$

where i_p is the peak current (amps), n is the number of electrons, F is the Faraday constant (F = 96485 C.mol^{-1}), A is the electrode geometrical surface area (cm^2), v is the scan rate (V.s^{-1}), R is the gas constant (R = 8.314 J.K^{-1}.mol^{-1}), and T is the temperature in Kelvin. The Γ values were estimated from the background corrected current (i_{corr}) under the metal redox peaks (Fig. 6.4). Values of i_{corr} increased linearly as a function of the scan rate as shown in Fig. 6.4 (inserts), as expected for adsorbed species. The Γ values of all of the MnPc SAMs, Table 6.1, were in the range 1.06×10^{-10} to 2.80×10^{-10} mol.cm^{-2}. For octasubstituted FePc (SCH$_2$Ph)$_8$ SAM and CoPc(SCH$_2$Ph)$_8$ SAM, the Γ values were 4.24×10^{-10} and 1.55×10^{-10} mol.cm^{-2}, respectively. All these values are within the range (10^{-10} mol.cm^{-2}) reported for other metallophthalocyanine macrocycles adsorbed as monolayers [476-478,492].

6.1.2. Impedance

The impedance data were plotted as Nyquist plots (-Z" the imaginary component of the impedance against Z' the real component of the impedance). Fig. 6.5(a) shows the Nyquist plots of the un-modified gold electrode (insert), CoPc(SCH$_2$Ph)$_8$ SAM (curve 1) and FePc(SCH$_2$Ph)$_8$ SAM (curve 2) recorded in 0.1 M potassium ferricyanide.
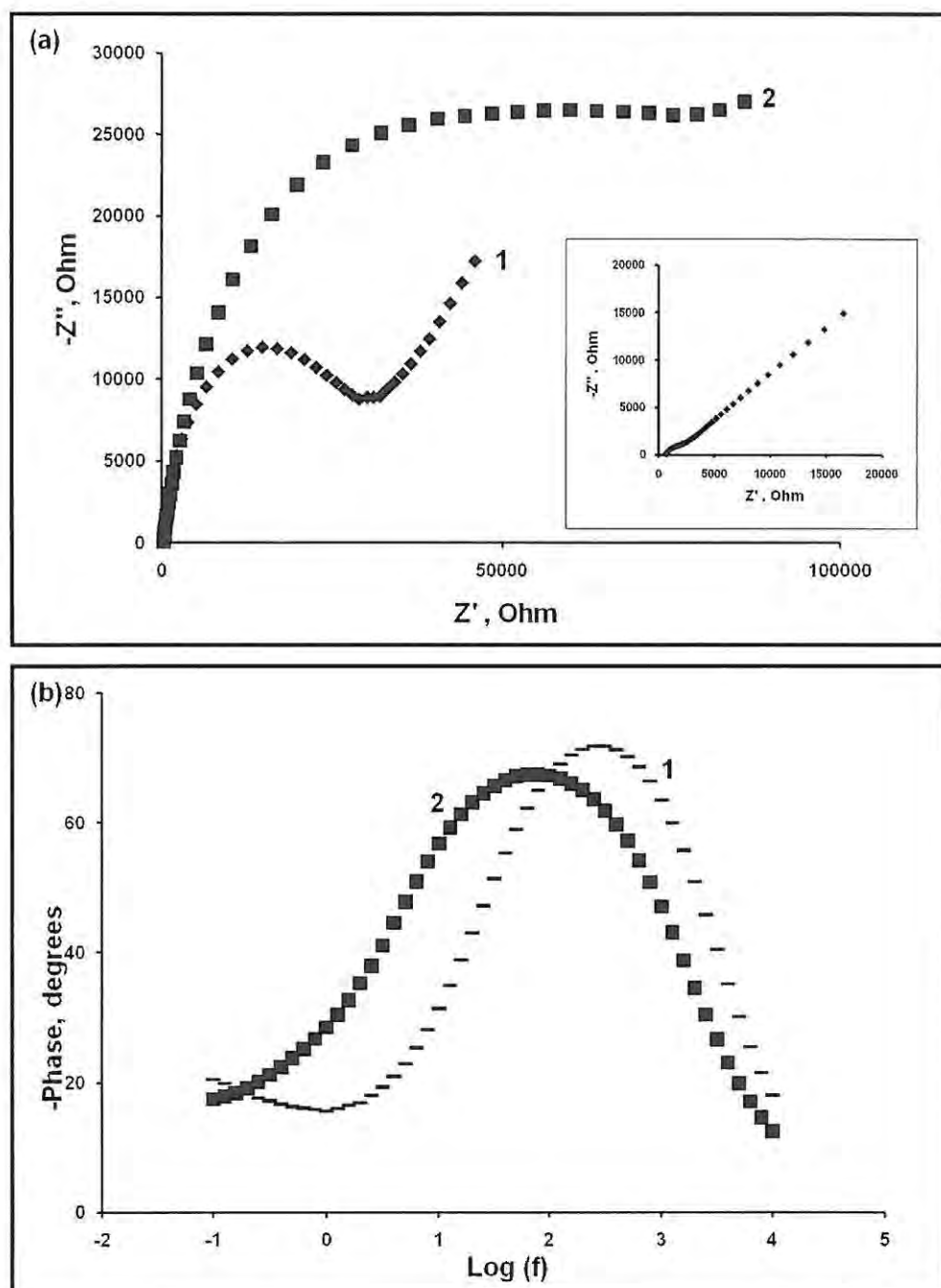
Fig. 6.5 (a) Nyquist plots of the un-modified gold electrode (insert), CoPc(SCH$_2$Ph)$_8$ SAM (1), and FePc(SCH$_2$Ph)$_8$ SAM (2). (b) Bode plots of CoPc(SCH$_2$Ph)$_8$ SAM (1) and FePc(SCH$_2$Ph)$_8$ SAM (2). Solution: 0.1 M potassium ferricyanide. Potential of impedance measurements = 100 mV

Chapter 6: Self assembled monolayers

The un-modified gold electrode (Fig. 6.5(a), insert) gave a characteristic straight line. Octasubstituted $FePc(SCH_2Ph)_8$ SAM (curve 2) had a greater impedance than $CoPc(SCH_2Ph)_8$ SAM (curve 1) as evidenced by its greater arc radius and larger resistance to charge transfer (R_{ct}) (R_{ct} values are: $CoPc(SCH_2Ph)_8$ SAM = $3.29 \times 10^4\ \Omega$; $FePc(SCH_2Ph)_8$ SAM = $6.72 \times 10^4\ \Omega$). This shows a degree of selectivity of $CoPc(SCH_2Ph)_8$ SAM because, in solutions studies, the ion barrier factor (Γ_{ibf}) and the interfacial capacitance (C_s) showed that the $CoPc(SCH_2Ph)_8$ SAM was more inhibiting to electrochemical solution processes (Table 6.1).

The resistance to charge transfer values (R_{ct}) of the MnPc SAM modified electrodes vary as follows, Table 6.2: **6e** ($R_{ct} = 1.60 \times 10^2\ \Omega$) < **8e** ($R_{ct} = 1.91 \times 10^2\ \Omega$) < **6d** ($R_{ct} = 2.09 \times 10^2\ \Omega$) < **8d** ($R_{ct} = 2.97 \times 10^2\ \Omega$) < **6c** ($R_{ct} = 8.39 \times 10^3\ \Omega$).

The MnPc derivatives have much lower R_{ct} values than the $FePc(SCH_2Ph)_8$ and $CoPc(SCH_2Ph)_8$ derivatives suggesting a more conducting nature for the MnPc derivatives. This again demonstrates the selectivity of the SAM modified electrodes. In the solutions used for cyclic voltammetry studies above, the MnPc complexes were less conducting (i.e. formed better SAMs) than the FePc and CoPc SAMs. But, in potassium ferricyanide solution, the MnPcs are more conducting due to their lower R_{ct} values, Table 6.2. Furthermore, complexes **6d**, **6e**, **8d**, and **8e** displayed similar R_{ct} values as expected due to their similar structures.

Fig. 6.5(b) shows the Bode plots (plots of -phase angle vs. log frequency) for $CoPc(SCH_2Ph)_8$ SAM (curve 1) and $FePc(SCH_2Ph)_8$ SAM (curve 2) recorded in 0.1 M potassium ferricyanide. For Bode plots, a phase angle greater or equal to 90° signifies that the modified electrode behaves like an ideal capacitor [482]. This means that the modified electrode is an effective insulating film and that there is no current leakage at defect sites. If the phase angle is less than 90° then the modified electrode is permeable to ions from the solution. Fig. 6.5(b) shows that, for $CoPc(SCH_2Ph)_8$ SAM (curve 1) and $FePc(SCH_2Ph)_8$ SAM (curve 2), the phase angle was less than 90° confirming that the modified electrodes are permeable to ions from the $[Fe(CN)_6]^{3-}$ /$[Fe(CN)_6]^{4-}$ solution. Similar results were obtained for the MnPc derivatives **6c**, **6d**, **6e**, **8d**, and **8e**.

Chapter 6: Self assembled monolayers

Table 6.2 Values of the resistance to charge transfer (R_{ct}) for MPc SAMs[a]

Complex SAM	R_{ct} (Ω)
6c	8.39×10^3
6d	2.09×10^2
6e	1.60×10^2
8d	2.97×10^2
8e	1.91×10^2
9b	6.72×10^4
10b	3.29×10^4

[a]**6c** = $(OH)MnPc(SPh)_4$; **6d** = α-$(OH)MnTMPyPc$; **6e** = α-Q-$(OH)MnTMPyPc$; **8d** = β-$(OH)MnTMPyPc$; **8e** = β-Q-$(OH)MnTMPyPc$; **9b** = $FePc(SCH_2Ph)_8$; **10b** = $CoPc(SCH_2Ph)_8$

6.1.3. Atomic force microscopy

Fig. 6.6 shows the atomic force microscopy (AFM) image of a gold surface before (a) and after (b) modification with complex **6c** SAM, as an example.

167

(a) Roughness: 1.257 nm
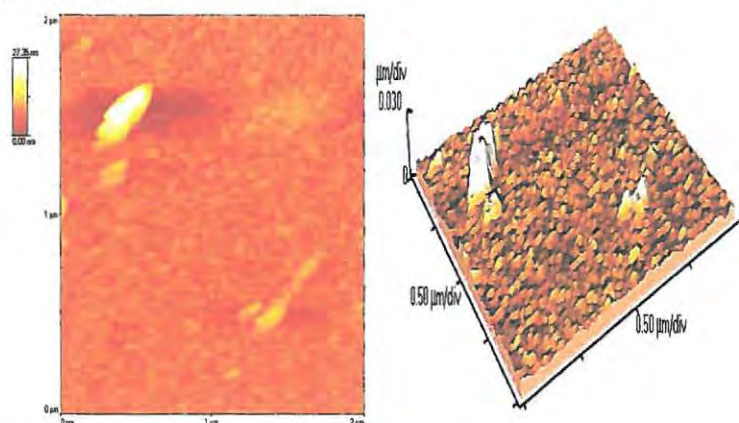
(b) Roughness: 1.017 nm
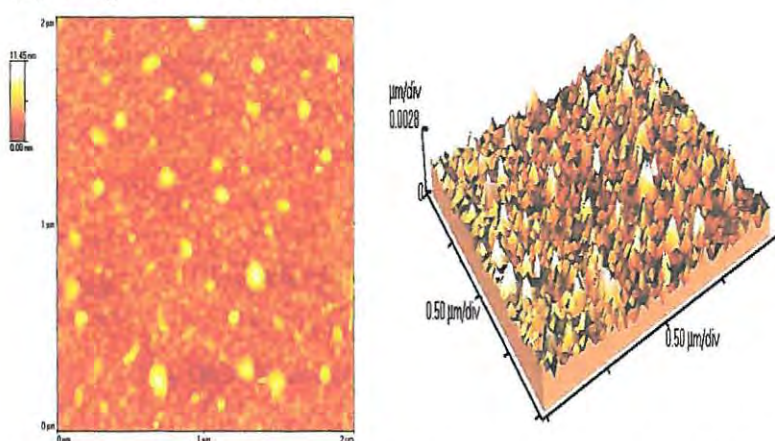
Fig. 6.6 AFM image of a gold surface before (a) and after (b) modification with complex **6c** SAM

There is a clear difference in the morphology of the un-modified gold electrode and its complex **6c** SAM counterpart, Fig. 6.6. The AFM images show that the un-modified gold electrode has a rougher surface (mean roughness = 1.257 nm) than complex **6c** SAM (mean roughness = 1.017 nm). This possibly indicates that **6c** fills depressions in the gold electrode forming a smoother and relatively uniform layer. The brighter areas on the un-modified gold sample are most likely due to imperfections since they disappear on modification.

168

Chapter 6: Self assembled monolayers

6.1.4. Scanning electrochemical microscopy

For the first time, scanning electrochemical microscopy (SECM) was used for the characterization of **6c**, **9b**, and **10b** SAMs.

The SECM scanning probe technique is based on Faradic current changes at an ultramicroelectrode tip that is moved across the surface of a sample (a square shaped gold electrode in this work). The images obtained depend on the sample topography and surface conductivity. Distinct differences were observed between SECM images of un-modified gold surfaces and gold surfaces modified with $(OH)MnPc(SPh)_4$ (**6c**) SAM, $FePc(SCH_2Ph)_8$ (**9b**) SAM, and $CoPc(SCH_2Ph)_8$ (**10b**) SAM recorded using a 25 μm Pt microelectrode in phosphate buffer solution containing 5 mM ferrocyanide as redox mediator, Fig. 6.7.
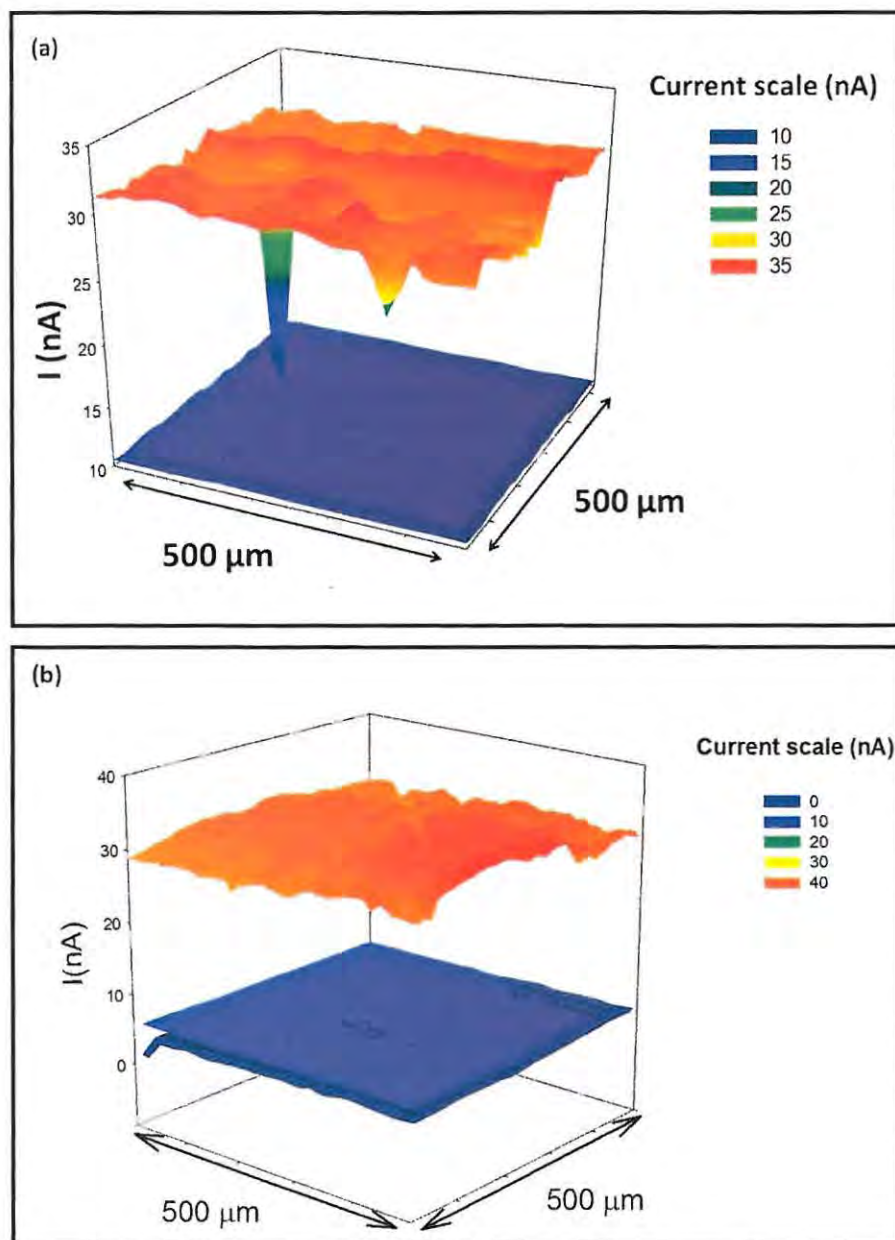
Fig. 6.7 SECM surface images of (a) an un-modified gold electrode (top) and a gold electrode modified with (OH)MnPc(SPh)$_4$ (**6c**, bottom) (b) an un-modified gold electrode (top) and gold electrodes modified with FePc(SCH$_2$Ph)$_8$ (**9b**, middle) and CoPc(SCH$_2$Ph)$_8$ (**10b**, bottom and meshed)

The differences observed in Fig. 6.7 are primarily due to variations in surface conductivity and topography. The relatively high current of the un-modified gold surface indicates, as expected,

its highly conductive nature. Smaller tip currents at the SAM modified gold surfaces indicate that the rate of $[Fe(CN)_6]^{3-}$ regeneration at the SAM area is slower than that at the un-modified gold due to the presence of the blocking SAM layer slowering the electron transfer rate. The dense and compact layer of the SAMs on the gold surface resulted in a very smooth topography, Fig. 6.7. Although information obtained from SECM should not be over-emphasized, it still provides clear evidence for electrode functionalization by the complexes as SAMs with smaller electron exchange rates. This data shows, on a microscopic scale, the possibility of imaging zones of the electrode surface having different physico-chemical properties. For **9b** and **10b** the SAM modified gold surface SECM images are predictably similar (Fig. 6.7(b)) mostly due to the structural similarities of the MPcs (**9b** and **10b**).

6.2. Analyses

Nitrite and L-cysteine could be analyzed by all of the SAMs. Thiocyanate and melatonin cannot be detected by any of the SAMs.

6.2.1. Nitrite

6.2.1.1. Iron and cobalt octaphenylthiophthalocyanine

Fig. 6.8(a) shows the cyclic voltammograms of $FePc(SCH_2Ph)_8$ (**9b**) SAM recorded in nitrite in pH 7.4 buffer solution showing the dependence of peak currents on scan rates. The disproportionation of nitrite to NO is insignificant at the pH used, thus the observed responses are for the oxidation of nitrite, not nitric oxide.
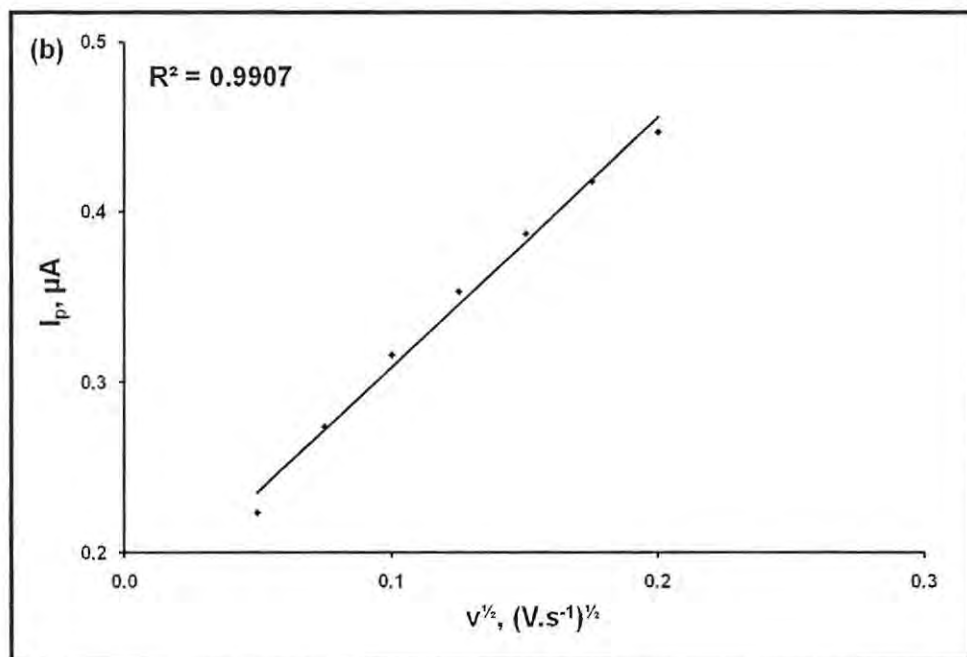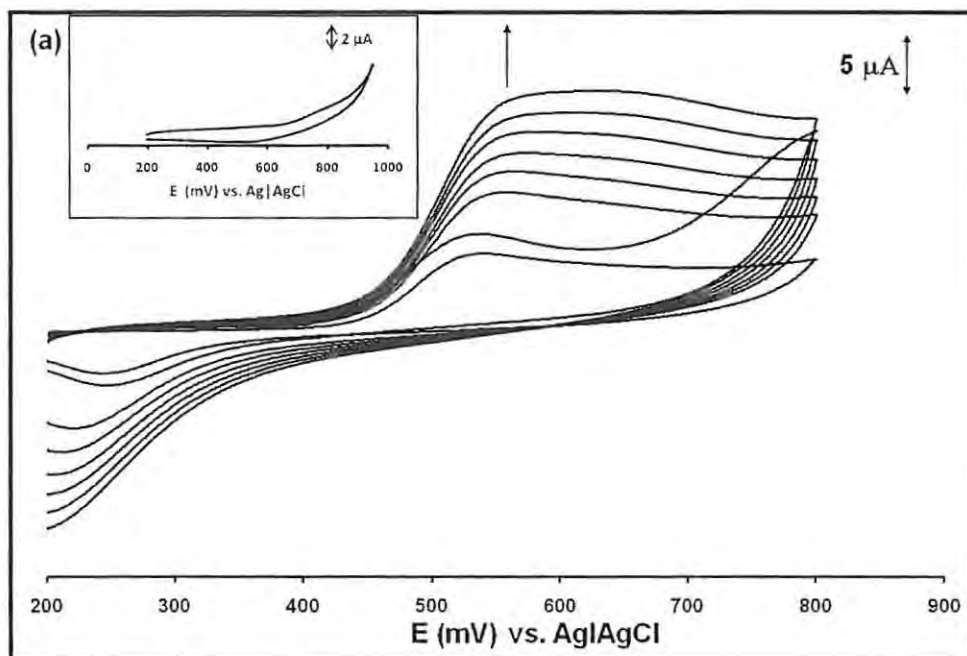
Chapter 6: Self assembled monolayers
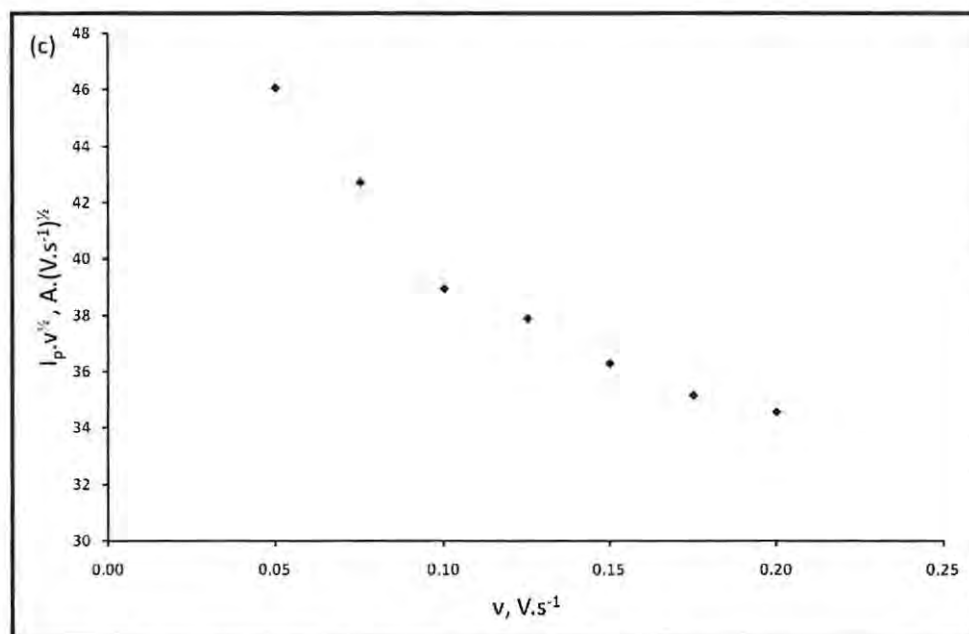
Fig. 6.8 (a) Cyclic voltammograms (50 - 200 mV.s^{-1}) and the cyclic voltammogram (100 mV.s^{-1}) of nitrite on an un-modified gold electrode as insert. (b) Plot of I_p vs. $v^{1/2}$. (c) Plot of $I_p.v^{-1/2}$ vs. v in 1 mM nitrite. Electrode: FePc(SCH$_2$Ph)$_8$ (**9b**) SAM

On the un-modified gold electrode the nitrite oxidation is observed at a more positive potential (0.77 V) than on FePc(SCH$_2$Ph)$_8$ SAM (0.55 V), Fig. 6.8(a). Furthermore, a huge increase in the current was obtained for FePc(SCH$_2$Ph)$_8$ SAM in comparison to the un-modified gold electrode. The electrocatalytic oxidation of nitrite by FePc(SCH$_2$Ph)$_8$ SAM occured at a potential of ~550 mV which is significantly lower than reported in the literature [299,495,496]. The values for all of the SAMs are shown in Table 6.3.

Table 6.3 Electrochemical parameters for determination of nitrite on SAM gold electrodes[a,b]

MPc	E_p (V) vs. Ag|AgCl	LOD (M)	Ref.
6c	0.69	2.94×10^{-7}	This work
6d	0.72	2.69×10^{-7}	This work
6e	0.74	2.72×10^{-7}	This work
8d	0.74	3.02×10^{-7}	This work
8e	0.76	1.78×10^{-7}	This work
9b	0.55	9×10^{-4}	This work
10b	0.72	3×10^{-4}	This work
FeTBMPc	0.66	Not reported	32
FeTDMPc	0.71	Not reported	32
CoTBMPc	0.75	Not reported	32
MnTBMPc	0.76	Not reported	32
CoTDMPc	0.77	Not reported	32
MnTDMPc	0.79	Not reported	32

[a]**6c** = (OH)MnPc(SPh)$_4$; **6d** = α-(OH)MnTMPyPc; **6e** = α-Q-(OH)MnTMPyPc; **8d** = β-(OH)MnTMPyPc; **8e** = β-Q-(OH)MnTMPyPc; **9b** = FePc(SCH$_2$Ph)$_8$; **10b** = CoPc(SCH$_2$Ph)$_8$
[b]TB = tetrakis (benzylmercapto); TD = tetrakis (dodecylmercapto); LOD = limit of detection

For CoPc(SCH$_2$Ph)$_8$ (**10b**) SAM there is an increase in the anodic current and a shift to smaller overpotentials with an increase in scan rate (Fig. not shown). For FePc(SCH$_2$Ph)$_8$ (**9b**) SAM an increase in the anodic current with scan rate was observed, as for CoPc(SCH$_2$Ph)$_8$ SAM, but with a shift to larger overpotentials, Fig. 6.8(a). Fig. 6.8(b) shows a linear relationship between the peak current and the square root of scan rate, which indicates a diffusion controlled electrocatalytic oxidation of nitrite. The plot of scan rate normalized current density ($I_p.v^{-\frac{1}{2}}$) vs. the scan rate (Fig. 6.8(c)) exhibited a shape indicative of a catalytic process.

The Tafel slopes were determined using the standard equation (Eq. 6.4) for a totally irreversible process [455]:

$$E_p = \frac{2.3RT}{2(1-\alpha)nF}\log \upsilon + K \qquad\qquad 6.4$$

where α is the transfer coefficient, v is the scan rate, n is the number of electrons involved in the rate determining step, and K is the intercept.

Plots of E_p vs. log v for FePc(SCH$_2$Ph)$_8$ SAM and CoPc(SCH$_2$Ph)$_8$ SAM for nitrite in pH 7.4 buffer solution, e.g. Fig. 6.9 for FePc(SCH$_2$Ph)$_8$ SAM, gave linear relationships.
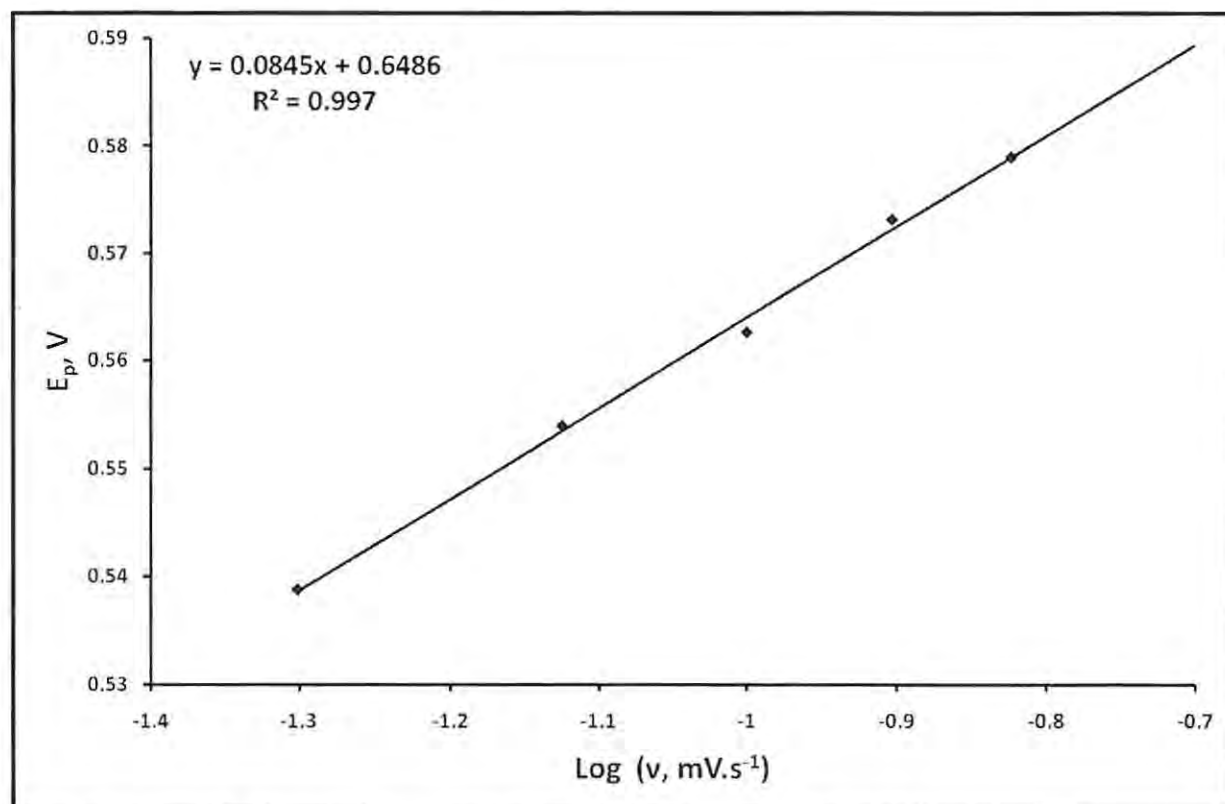
Fig. 6.9 Plot of E_p vs. log v for 1 mM nitrite on FePc(SCH$_2$Ph)$_8$ SAM

Table 6.4 shows the electrocatalytic properties of the cobalt and iron octaphenylthiophthalocyanine SAMs for nitrite oxidation.

Table 6.4 Electrochemical parameters for determination of nitrite for the MPc complexes of this work[a,b]

Parameter	6c	6d	6e	8d	8e	9b	10b
Tafel slope $(mV.decade^{-1})$	132	157	167	152	94	170	100
α	0.81	0.62	0.65	0.61	0.37	0.68	0.73
n_t	2.30	2.06	1.99	2.01	2.00	0.82	0.83
Sensitivity $(A.M^{-1})$	0.0068	0.0065	0.0097	0.0057	0.0078	0.0063	0.0083
LOD (M)	2.94×10^{-7}	2.69×10^{-7}	1.78×10^{-7}	3.02×10^{-7}	2.72×10^{-7}	9.04×10^{-4}	3.32×10^{-4}
Stability as % decay[c]	10	3	1	4	1	1	12

[a]**6c** = $(OH)MnPc(SPh)_4$; **6d** = α-$(OH)MnTMPyPc$; **6e** = α-Q-$(OH)MnTMPyPc$; **8d** = β-$(OH)MnTMPyPc$; **8e** = β-Q-$(OH)MnTMPyPc$; **9b** = $FePc(SCH_2Ph)_8$; **10b** = $CoPc(SCH_2Ph)_8$

[b]α = transfer coefficient; n_t = total number of electrons involved; LOD = limit of detection

[c]Over 35 continuous scans

For $FePc(SCH_2Ph)_8$ (**9b**) SAM, a high Tafel slope of 170 mV.decade^{-1} was obtained. Tafel slopes larger than the normal 30 - 120 mV.decade^{-1} are known and have been related either to chemical reactions coupled to electrochemical steps or to substrate-catalyst interactions in a reaction intermediate [319,480,485,497]. Thus, supported by the spectroscopic studies below, interaction of the substrate (nitrite) and the catalyst (MPc) may be the main cause of the large Tafel slope. A Tafel slope of 100 mV.decade^{-1} was obtained for $CoPc(SCH_2Ph)_8$ SAM suggesting the involvement of one electron in the rate determining step. An α value higher than 0.5, obtained for both SAMs (α = 0.68 and 0.73, Table 6.4, for $FePc(SCH_2Ph)_8$ SAM and $CoPc(SCH_2Ph)_8$ SAM respectively), suggests that there is a greater probability that the reaction transition state will form the product. The α value for the $FePc(SCH_2Ph)_8$ (**9b**) SAM is tentative because the Tafel slope is large and does not fall within the normal 30 to 120 mV.decade^{-1} region.

The total number of electrons (n_t) involved in the electrocatalytic oxidation of nitrite by the SAMs was calculated using Eq. 6.5, valid for a totally irreversible electrode process [455]:

$$i_p = 2.99x10^5 n_t \left[(1-\alpha)n\right]^{\frac{1}{2}} AC_o D^{\frac{1}{2}} \upsilon^{\frac{1}{2}} \qquad\qquad 6.5$$

where A is the area of the electrode (cm^2), C_o is the concentration of cysteine ($mol.cm^{-3}$), and D is the diffusion coefficient of nitrite (D = 2.1 × 10^{-5} $cm^2.s^{-1}$) [481,496]. The total number of electrons transferred was calculated to be 0.8 (i.e. near unity) for both FePc(SCH$_2$Ph)$_8$ (9b) SAM and CoPc(SCH$_2$Ph)$_8$ (10b) SAM, Table 6.4.

Fig. 6.10 shows the linear relationship between the peak current and the nitrite ion concentration (mM range) for FePc(SCH$_2$Ph)$_8$ SAM (a) and CoPc(SCH$_2$Ph)$_8$ SAM (b).
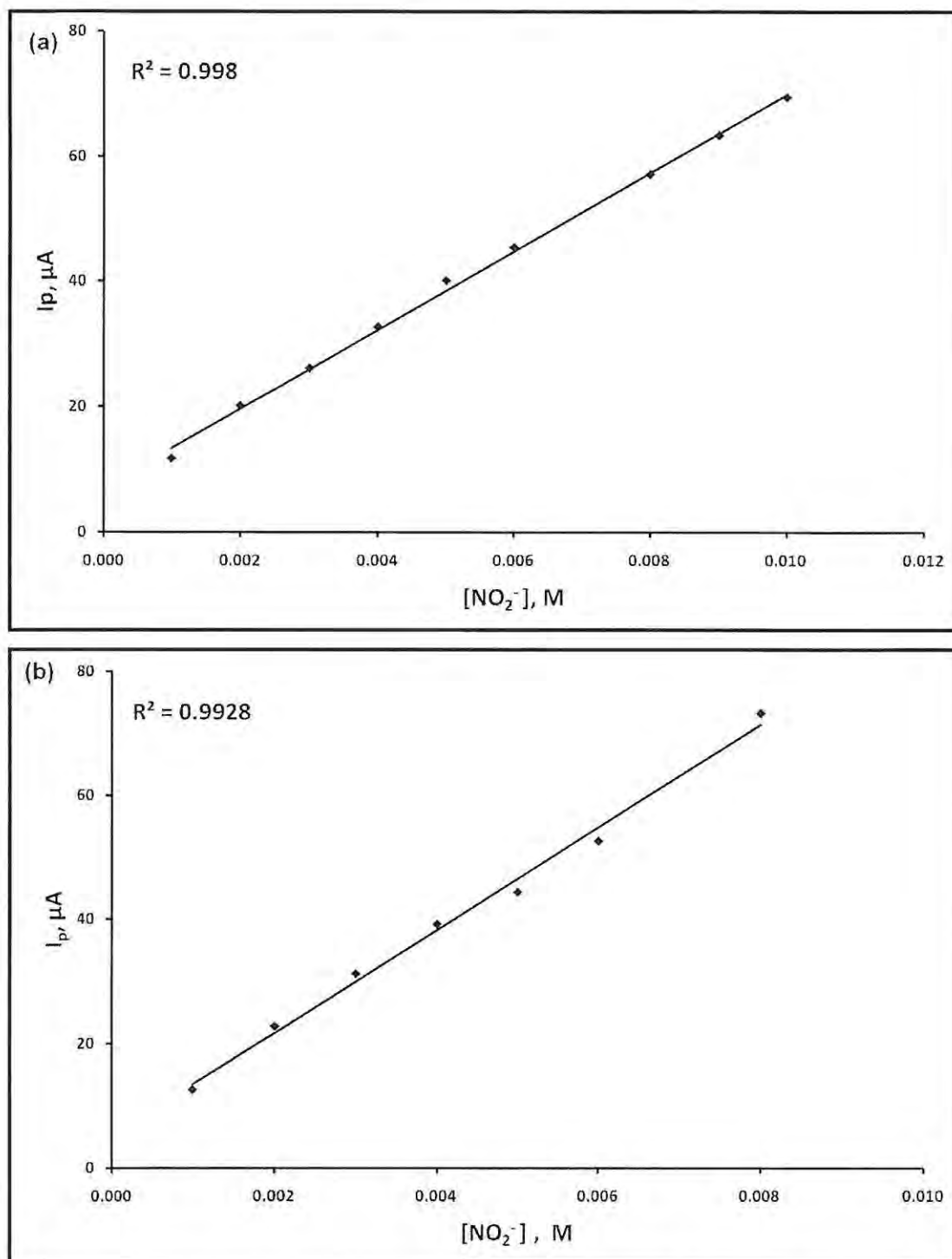
Fig. 6.10 Plots of I_p vs. nitrite ion concentration for $FePc(SCH_2Ph)_8$ (**9b**) SAM (a) and $CoPc(SCH_2Ph)_8$ (**10b**) SAM (b)

Chapter 6: Self assembled monolayers

Fig. 6.10(a) shows that there is a linear relationship between the peak current and the nitrite ion concentration (mM range) for the $FePc(SCH_2Ph)_8$ SAM making the electrode useful for analyses of nitrite concentrations up to 1×10^{-2} M, with a detection limit of 9.04×10^{-4} M (3σ criterion), Table 6.4. This detection limit is higher than previously reported [495] and for the $CoPc(SCH_2Ph)_8$ SAM below.

The $CoPc(SCH_2Ph)_8$ SAM modified electrode is useful for analyses of nitrite concentrations up to 8.0×10^{-3} M (beyond which the linear relationship, Fig. 6.10(b), is lost). For $CoPc(SCH_2Ph)_8$ SAM, the detection limit was found to be 3.32×10^{-4} M (3σ criterion), Table 6.4, a value which is higher than reported for nitrite detection on porphyrin complexes [299]. The sensitivity of $CoPc(SCH_2Ph)_8$ SAM (0.083 A.M^{-1}) is larger than that of $FePc(SCH_2Ph)_8$ SAM (0.063 A.M^{-1}), although both values are within the ranges obtained for the MnPc SAMs, Table 6.4.

Fig. 6.11 shows the UV-visible spectra of $Fe^{II}Pc(SCH_2Ph)_8$ in the absence (1) and presence (2) of NO_2^- recorded in DMSO. This work was done in order to study the mechanism. Even though in solution, such studies do give an indication of interactive behaviour.
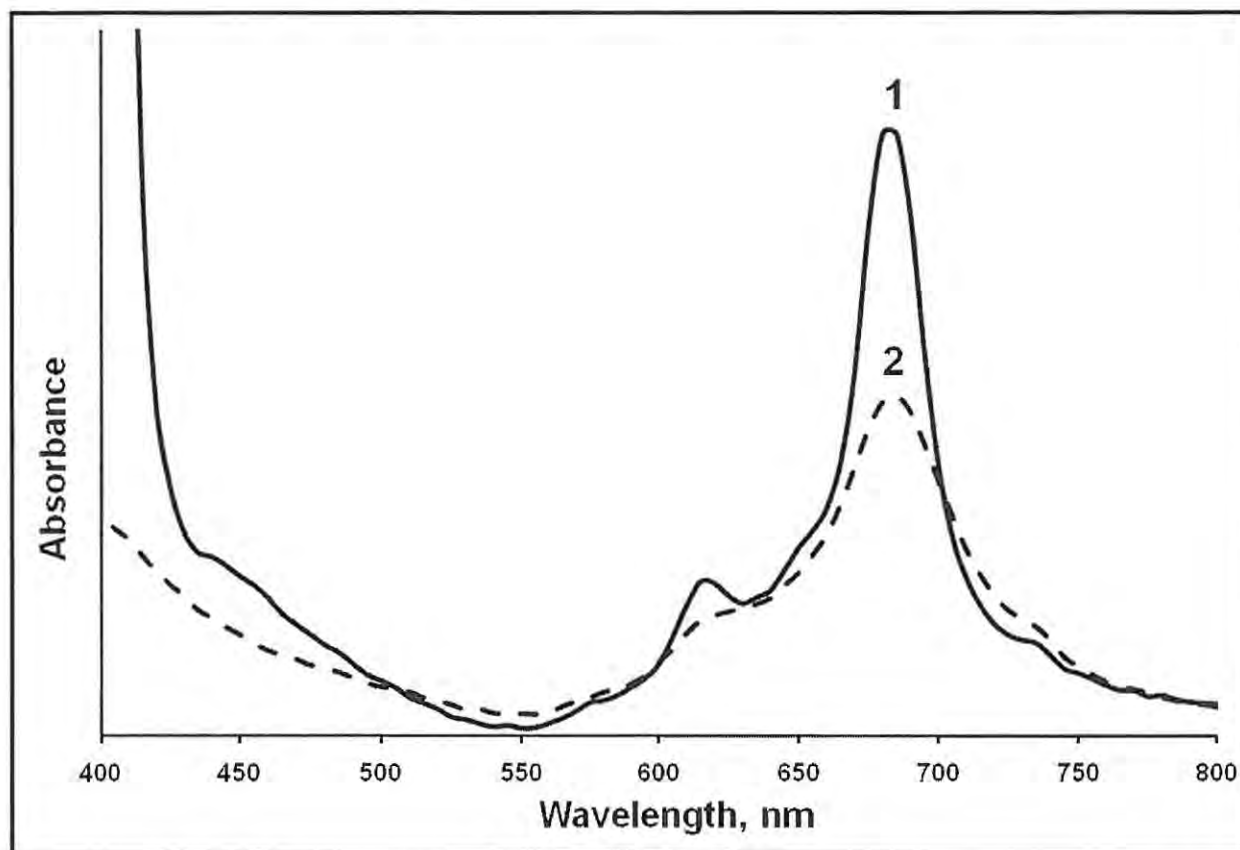
Fig. 6.11 UV-visible spectra of $Fe^{II}Pc(SCH_2Ph)_8$ in the absence (1) and presence (2) of nitrite recorded in DMSO. Concentration ≈ 1 µM

From Fig. 6.11, the 5 nm shift in the Q band of $Fe^{II}Pc(SCH_2Ph)_8$ from $\lambda_{max} = 685$ nm (in the absence of nitrite) to $\lambda_{max} = 680$ nm (in the presence of nitrite) confirms an axial ligation coordination of NO_2^- to the $Fe^{II}Pc(SCH_2Ph)_8$ complex [459]. Similar spectral changes were observed for $Co^{II}Pc(SCH_2Ph)_8$.

Based on the above discussion, the mechanism for the catalytic oxidation of nitrite using the $FePc(SCH_2Ph)_8$ SAM and $CoPc(SCH_2Ph)_8$ SAM may be represented by Eqs. 6.6 - 6.8:

$$M^{II}Pc + NO_2^- \rightarrow (NO_2^-)M^{II}Pc \qquad \qquad 6.6$$

$$(NO_2^-)M^{II}Pc \rightarrow (NO_2^-)M^{III}Pc + e^- \qquad \qquad 6.7$$

$$(NO_2^-)M^{III}Pc \rightarrow M^{II}Pc + NO_2 \qquad \qquad 6.8$$
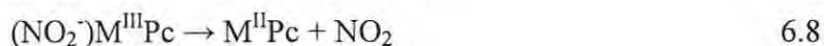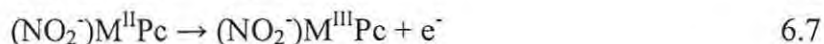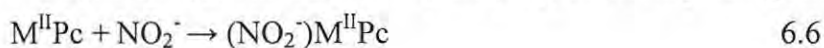
And the NO_2 species may then disproportionate to give nitrite and nitrate as follows:

$$2NO_2 + H_2O \rightarrow NO_2^- + NO_3^- + 2H^+ \qquad \qquad 6.9$$
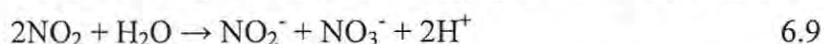
where MPc represents $FePc(SCH_2Ph)_8$ or $CoPc(SCH_2Ph)_8$.

180

Eq. 6.6 is proposed on the basis of the coordination of nitrite to complexes **9b** and **10b**. This was proven spectroscopically by the addition of nitrite to solutions of $FePc(SCH_2Ph)_8$ or $CoPc(SCH_2Ph)_8$ (e.g. Fig. 6.11). Eq. 6.7 is proposed because the catalytic oxidation of nitrite is within the range where $Fe^{III}Pc$ or $Co^{III}Pc$ exist, Fig. 6.4(b) and (c), and is catalyzed by this couple. The Tafel plots also showed that the first one-electron transfer is the rate limiting step (Eq. 6.7). To account for a total of one electron transferred, the most likely product is NO_2, Eq. 6.8.

The peak currents, recorded in 1 mM nitrite in pH 7.4 buffer solution, in a potential window of +200 to +800 mV vs. Ag|AgCl, were virtually unchanged for $FePc(SCH_2Ph)_8$ SAM and decreased by 12% for $CoPc(SCH_2Ph)_8$ SAM over 35 cyclic voltammetry scans, Table 6.4. This shows high stability (especially of the former electrode) for nitrite oxidation.

6.2.1.2. Manganese phthalocyanine derivatives

Fig. 6.12 shows the cyclic voltammograms of SAMs of complexes **6d** (1), **6e** (2), **8d** (3), **8e** (4), and **6c** (5) recorded in 1 mM nitrite (in pH 7 buffer solution).
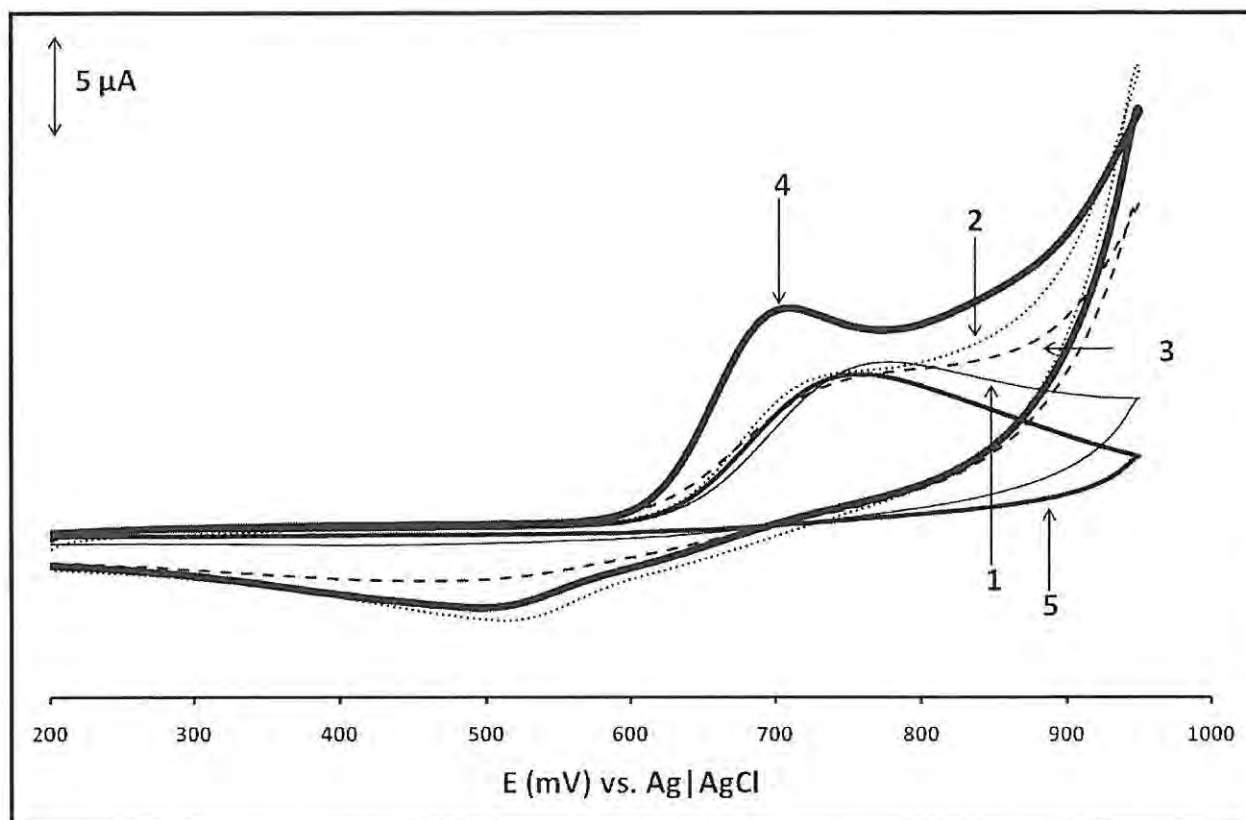
Fig. 6.12 Cyclic voltammograms of SAMs of α-(OH)MnTMPyPc (**6d**, 1), α-Q-(OH)MnTMPyPc (**6e**, 2), β-(OH)MnTMPyPc (**8d**, 3), β-Q-(OH)MnTMPyPc (**8e**, 4), and (OH)MnPc(SPh)$_4$ (**6c**, 5) recorded in 1 mM nitrite at 50 mV.s^{-1}

As mentioned, a weak peak was observed for nitrite on an un-modified gold electrode (Fig. 6.8(a) insert). Nitrite oxidation peaks were observed between 0.72 V and 0.76 V vs. Ag|AgCl for SAMs of the MnPc complexes, compared to ~0.55 V vs. Ag|AgCl for the FePc(SCH$_2$Ph)$_8$ and 0.72 V vs. Ag|AgCl for the CoPc(SCH$_2$Ph)$_8$ SAMs, Table 6.3. Nitrite oxidation occurs on the un-modified gold electrode at approximately 0.77 V vs. Ag|AgCl, but the peak current is enhanced (and the overpotential decreased) on modification with all of the SAMs. The values of the nitrite detection potentials for the MnPc SAMs compare well with the SAM literature, Table 6.3, but are worse than for the FePc(SCH$_2$Ph)$_8$ SAM.

Linear relationships between the peak current and the square root of the scan rate were obtained, which indicates diffusion controlled electrocatalytic oxidation of nitrite by the SAMs of the MnPc complexes. Plots of scan rate normalized current density (I$_p$.v$^{-1/2}$) vs. scan rate showed

182

Chapter 6: Self assembled monolayers

shapes indicative of catalytic processes when recorded in nitrite solution (Figs. not shown, but similar to Fig. 6.8).

Tafel slopes for the Mn complexes are in the range of the $FePc(SCH_2Ph)_8$ and $CoPc(SCH_2Ph)_8$ complexes, except for **8e**, Table 6.4. High Tafel slopes for complexes **6d**, **6e**, and **8d** SAMs indicate extensive interaction between nitrite and catalyst [319,480,485,497]. Complex **6c** SAM displayed a Tafel slope closer to 120 mV.decade^{-1}, Table 6.3, suggesting that the first one electron transfer is rate determining. Complex **8e** SAM had an even lower Tafel slope of ~90 mV.decade^{-1}. Low Tafel slopes indicate high electrocatalytic activity [498] and hence, based on this observation, complexes **6c**, **8e**, and **10b** show better catalytic activity for nitrite oxidation than complexes **6d**, **6e**, **8d**, and **9b**.

There is a greater probability of forming products in the reaction transition state for all SAMs (α > 0.5), except for complex **8e** which gave an α value less than 0.5, Table 6.4. Again, since most of the Tafel slopes are large and do not fall within the usual 30 to 120 mV.decade^{-1} region, the α values are tentative. Two electrons are involved in the electro-oxidation of nitrite (using diffusion coefficient = 2.1×10^{-5} cm^2.s^{-1} [481,496]) by the MnPc SAMs (calculated using Eq. 6.5), Table 6.4. This value contrasts with complexes **9b** and **10b** SAMs which showed the involvement of only one electron and is possibly related to the redox processes involved. The $M^{III}Pc/M^{II}Pc$ process is involved for complexes **9b** and **10b**, whilst the $M^{IV}Pc/M^{III}Pc$ process is involved for the MnPcs (Eqs. 6.10 - 6.12 below). Further studies are needed to verify this.

Complexes **6e** and **8e** SAMs were the most stable because there was only a 1 % decay in the peak current output over 35 continuous scans when recorded in 1 mM nitrite solution, Table 6.4. The rest of the SAMs (for complexes **6c**, **6d**, and **8d**) also showed good stability, Table 6.4.

Nitrite sensitivities of all SAMs of this work ranged between 0.0057 and 0.0097 A.M^{-1}, with the complex **6e** SAM having the highest value, Table 6.4. All of the MnPc SAMs displayed linear relationships between the peak current and the nitrite concentration (10^{-4} - 10^{-2} M range), Fig. 6.13, and therefore can be used dependably for the determination of nitrite in this concentration range.
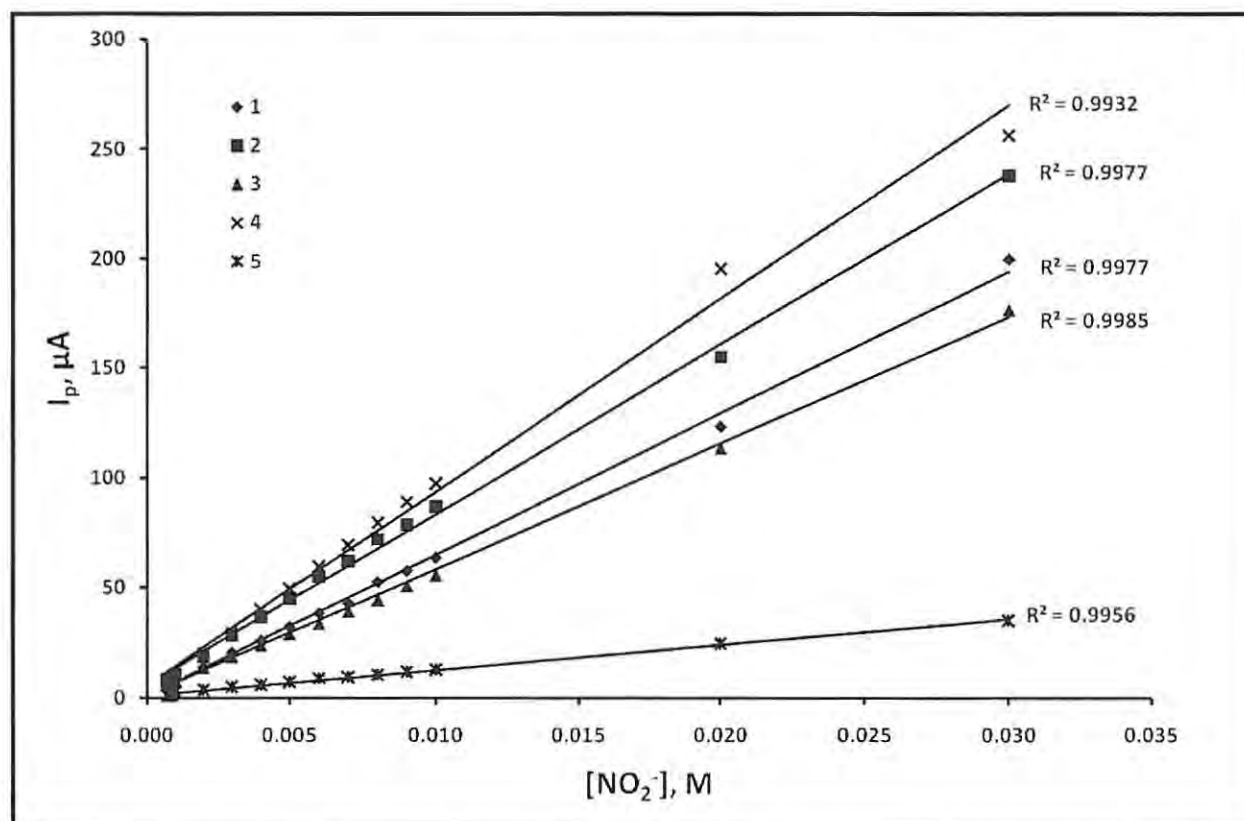
Fig. 6.13 Plot of I_p vs. nitrite ion concentration for SAMs of α-(OH)MnTMPyPc (**6d**, 1), α-Q-(OH)MnTMPyPc (**6e**, 2), β-(OH)MnTMPyPc (**8d**, 3), β-Q-(OH)MnTMPyPc (**8e**, 4), and (OH)MnPc(SPh)₄ (**6c**, 5)

Nitrite detection limits (3σ criterion) for all SAMs of this work are in the 10^{-7} M region with complex **8e** SAM showing the best value of 1.78×10^{-7} M, Table 6.4.

Comparing the FePc(SCH₂Ph)₈ and CoPc(SCH₂Ph)₈ complexes with the MnPc complexes shows that the MnPc complexes have much better detection limits. This could be because octasubstituted complexes may take on an octopus orientation (Fig. 1.17, Chapter 1) which is known to form poorly organised SAMs [221]. There are also two electrons involved in the interaction of the MnPc complexes with nitrite, Table 6.4; this value differs with FePc(SCH₂Ph)₈ and CoPc(SCH₂Ph)₈ due to the reason discussed above.

To investigate the mechanism for nitrite oxidation by the MnPc derivatives, UV-visible spectral studies were done. UV-visible spectra of the MnPc complexes displayed shifts in the Q band

184

maximum after addition of nitrite, which indicates some interaction of MPc with nitrite (Figs. not shown).

Based on the above discussion, the mechanism for the catalytic oxidation of nitrite, using the MnPc SAMs, may be represented as Eqs. 6.10 - 6.12:

$$Mn^{III}Pc + NO_2^- \rightarrow [(NO_2^-)Mn^{III}Pc]^- \qquad 6.10$$

$$[(NO_2^-)Mn^{III}Pc]^- \rightarrow (NO_2^-)Mn^{IV}Pc + e^- \qquad 6.11$$

$$(NO_2^-)Mn^{IV}Pc + H_2O \rightarrow Mn^{III}Pc + NO_3^- + 2H^+ + e^- \qquad 6.12$$
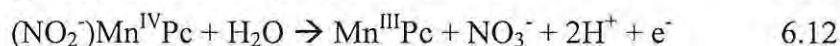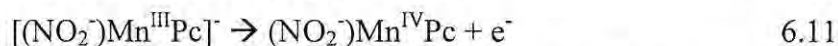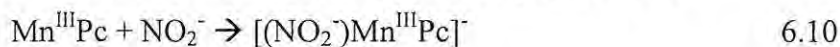
Eq. 6.10 is proposed on the basis of the coordination of nitrite to complexes **6c**, **6d**, **6e**, **8d**, and **8e** which was proven spectroscopically. Eq. 6.11 is proposed because the catalytic oxidation of nitrite is within the range where Mn^{IV}/Mn^{III} exists [31] and is catalyzed by this couple. To account for a total of 2 electrons transferred, the most likely product is NO_3^-, Eq. 6.12.

6.2.2. Cysteine

6.2.2.1. Iron and cobalt octaphenylthiophthalocyanine

No L-cysteine peak was observed on an un-modified gold electrode under the conditions used in this work (Fig. not shown). L-cysteine has been known to form SAMs on un-modified gold electrodes [499], but the SAMs were formed at more positive values than used in this work [500]. On the SAMs of this work, L-cysteine peaks were observed in the potential windows shown in Fig. 6.14, as an example.
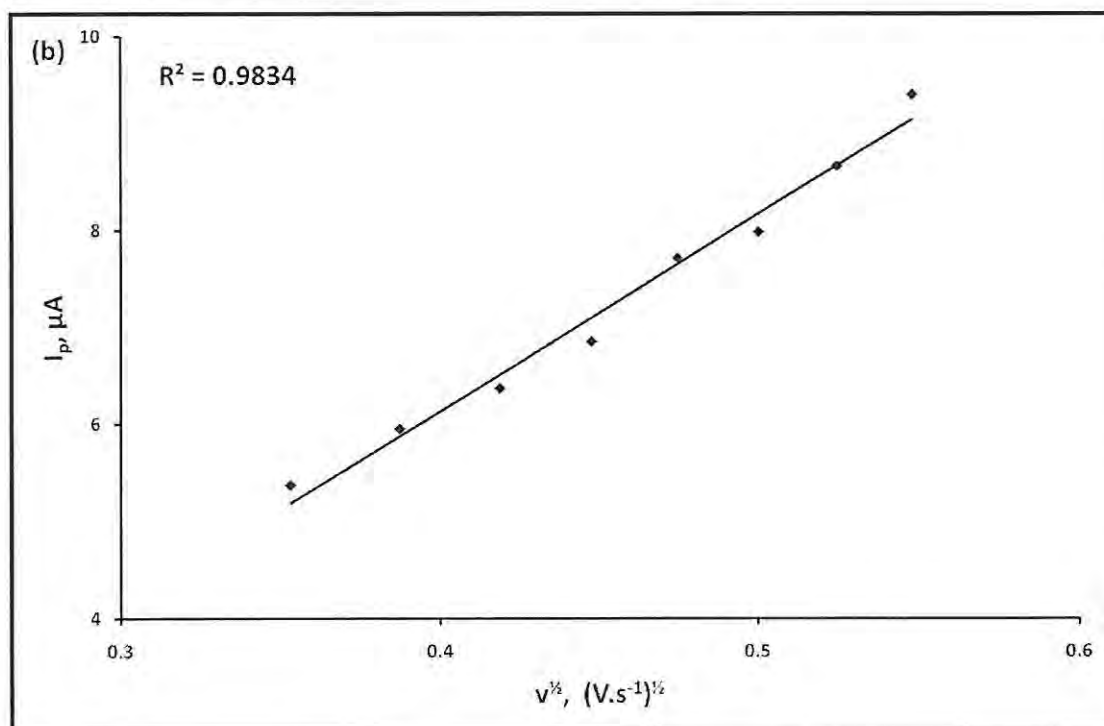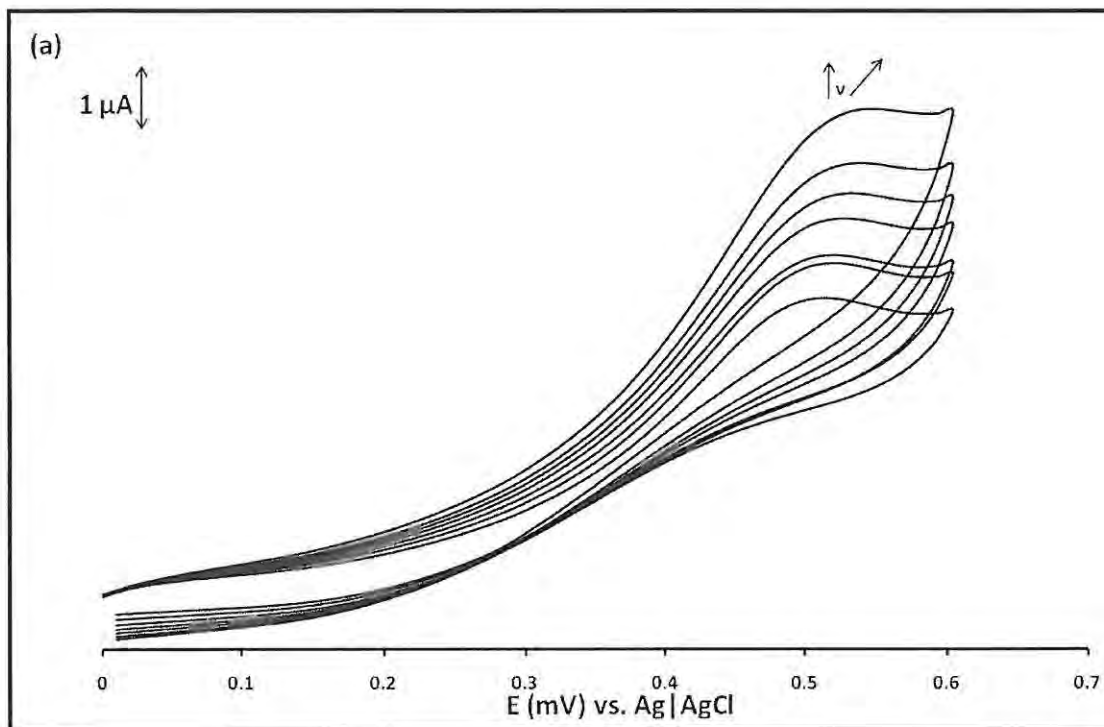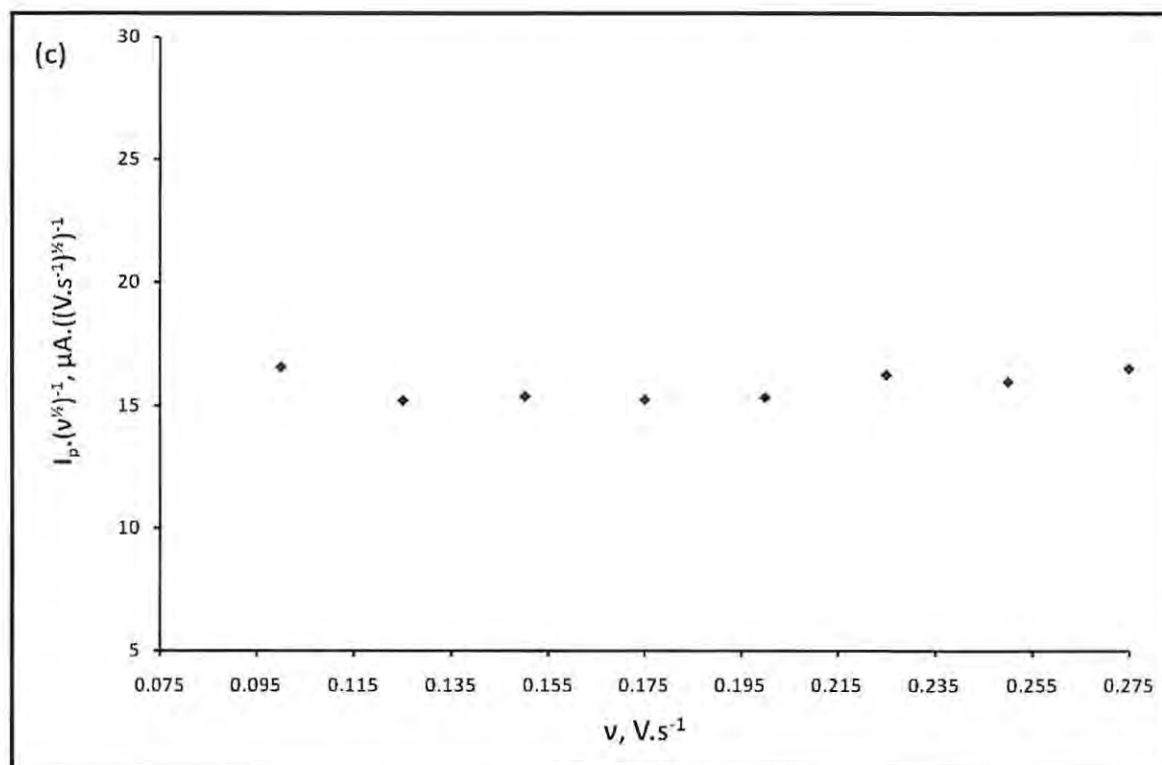
Fig. 6.14 (a) Cyclic voltammograms of CoPc(SCH₂Ph)₈ SAM modified electrode recorded in 1 mM L-cysteine (50 - 300 mV.s⁻¹). (b) Plot of I_p vs. $v^{1/2}$. (c) Plot of $I_p.v^{-1/2}$ vs. v in 1 mM L-cysteine. Electrode: CoPc(SCH₂Ph)₈ SAM

The cyclic voltammograms in Fig. 6.14(a) of the CoPc(SCH₂Ph)₈ SAM modified electrode recorded in 1 mM L-cysteine show the dependence of the peak currents on the scan rates. Similar peaks were obtained for the FePc(SCH₂Ph)₈ SAM modified electrode (Figs. not shown). The properties of MPc SAM modified electrodes as electrochemical sensors for L-cysteine of this work and from the literature [23,33,34,205,347,488] are compared in Table 6.5.

Table 6.5 The properties of MPc SAM modified electrodes as electrochemical sensors for L-cysteine [a,b]

MPc	Electrode	LOD (M)	E_p (V) vs. Ag|AgCl	Ref.
6c	Au	2.89×10^{-7}	0.68	This work
6d	Au	3.10×10^{-7}	0.69	This work
6e	Au	2.88×10^{-7}	0.75	This work
8d	Au	3.14×10^{-7}	0.73	This work
8e	Au	2.83×10^{-7}	0.75	This work
9b	Au	3.85×10^{-7}	0.50	This work
10b	Au	4.44×10^{-7}	0.70	This work
FePc	4-MPy-Au	2×10^{-6}	0.14	347
$FePc(SC_4H_9)_8$	Au	3.0×10^{-7}	0.33	33
$FePc(SC_2H_4OH)_8$	Au	5.2×10^{-7}	0.38	23
CoPc	Carbon paste	3.1×10^{-8}	0.4	488
$CoPc(SC_4H_9)_8$	Au	3.1×10^{-7}	0.42	34
$CoPc(COCl)_4$	2-ME-Au	5×10^{-7}	0.36,0.63	205
$CoPc(SC_2H_4OH)_8$	Au	5.2×10^{-7}	0.50	23

[a] **6c** = $(OH)MnPc(SPh)_4$; **6d** = α-$(OH)MnTMPyPc$; **6e** = α-Q-$(OH)MnTMPyPc$; **8d** = β-$(OH)MnTMPyPc$; **8e** = β-Q-$(OH)MnTMPyPc$; **9b** = $FePc(SCH_2Ph)_8$; **10b** = $CoPc(SCH_2Ph)_8$
[b] LOD = limit of detection; 4-MPy-Au = pre-formed SAM on gold using 4-mercaptopyridine; 2-ME-Au = pre-formed SAM on gold using 2-mercaptoethanol

The electrocatalytic oxidation of L-cysteine by $FePc(SCH_2Ph)_8$ and $CoPc(SCH_2Ph)_8$ SAMs occurs at potentials of 700 and 500 mV vs. Ag|AgCl, respectively, Table 6.5. From Fig. 6.14(a), there is an increase in the anodic current and a shift to larger overpotentials with an increase in scan rate. Fig. 6.14(b) shows a linear relationship between the peak current and the square root of the scan rate, which indicates a diffusion-controlled electrocatalytic oxidation of L-cysteine by $CoPc(SCH_2Ph)_8$ SAM. The plot of the scan rate normalized current density ($I_p.v^{-1/2}$) vs. the scan rate, Fig. 6.14(c), exhibits a shape typical of a catalytic process.

Plots of E_p vs. log v for CoPc(SCH$_2$Ph)$_8$ SAM and FePc(SCH$_2$Ph)$_8$ SAM for L-cysteine in pH 4 buffer solution show linear relationships as shown in Fig. 6.15 for FePc(SCH$_2$Ph)$_8$ SAM.
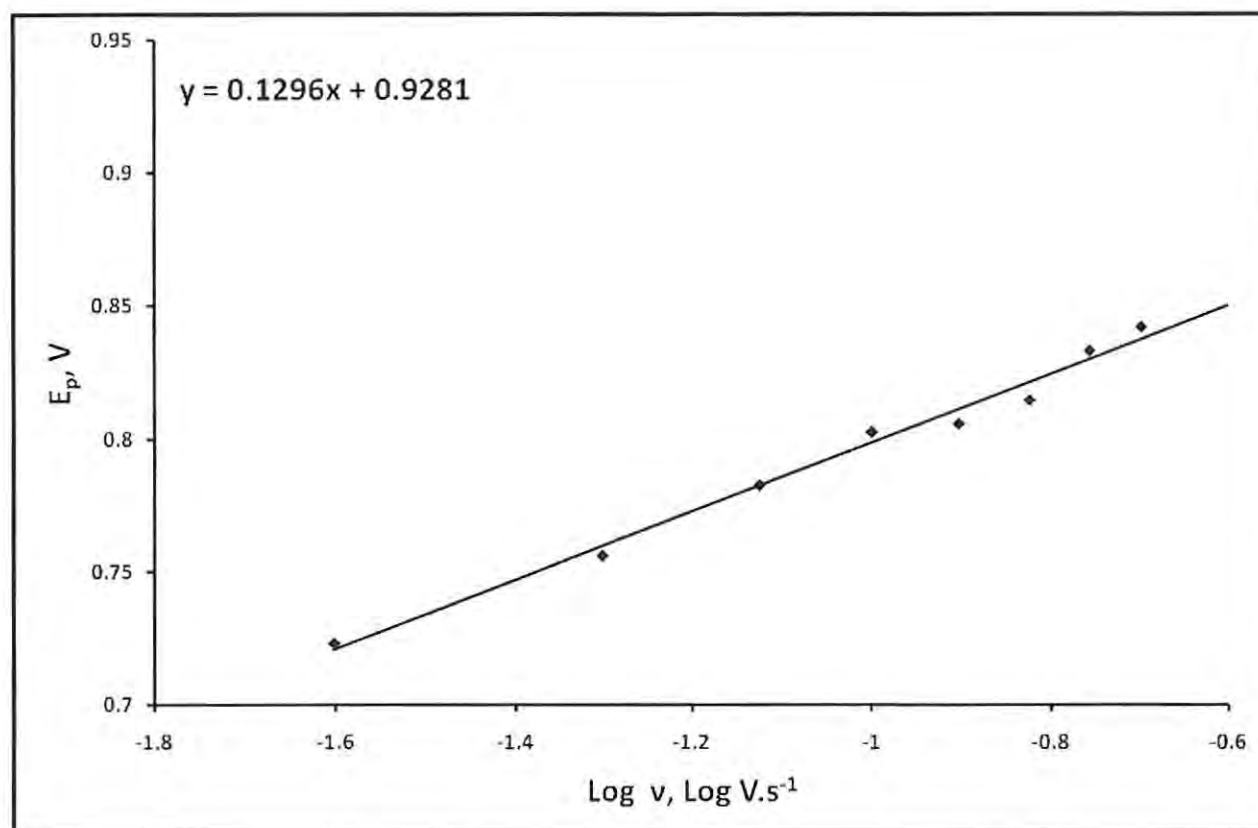
Fig. 6.15 Plot of E_p vs. log v for 1 mM L-cysteine on FePc(SCH$_2$Ph)$_8$ SAM

Tafel slopes of 259 and 178 mV.decade^{-1} were calculated, using Eq. 6.4, for FePc(SCH$_2$Ph)$_8$ and CoPc(SCH$_2$Ph)$_8$ SAMs, respectively, Table 6.6.

Chapter 6: Self assembled monolayers

Table 6.6 Electrochemical parameters for L-cysteine determination using the MPc complexes of this work[a,b]

Parameter	6c	6d	6e	8d	8e	9b	10b
Tafel slope (mV.decade^{-1})	234	191	132	148	106	259	178
α	0.75	0.69	0.56	0.60	0.45	0.77	0.67
n_t	1.00	1.13	1.30	1.05	1.16	1.32	1.16
Sensitivity (A.M^{-1})	0.0024	0.0062	0.0061	0.0055	0.0065	0.0045	0.0038
LOD (M)	2.89 × 10^{-7}	3.10 × 10^{-7}	2.83 × 10^{-7}	3.14 × 10^{-7}	2.88 × 10^{-7}	3.85 × 10^{-7}	4.44 × 10^{-7}
Stability as % decay[c]	6	3	3	6	4	17	6

[a] **6c** = $(OH)MnPc(SPh)_4$; **6d** = α-(OH)MnTMPyPc; **6e** = α-Q-(OH)MnTMPyPc; **8d** = β-(OH)MnTMPyPc; **8e** = β-Q-(OH)MnTMPyPc; **9b** = $FePc(SCH_2Ph)_8$; **10b** = $CoPc(SCH_2Ph)_8$

[b] α = transfer coefficient; n_t = total number of electrons involved; LOD = limit of detection

[c] Over 35 continuous scans

Fig. 6.16 shows the UV-visible spectra of $FePc(SCH_2Ph)_8$ before (1) and after (2) the addition of L-cysteine.
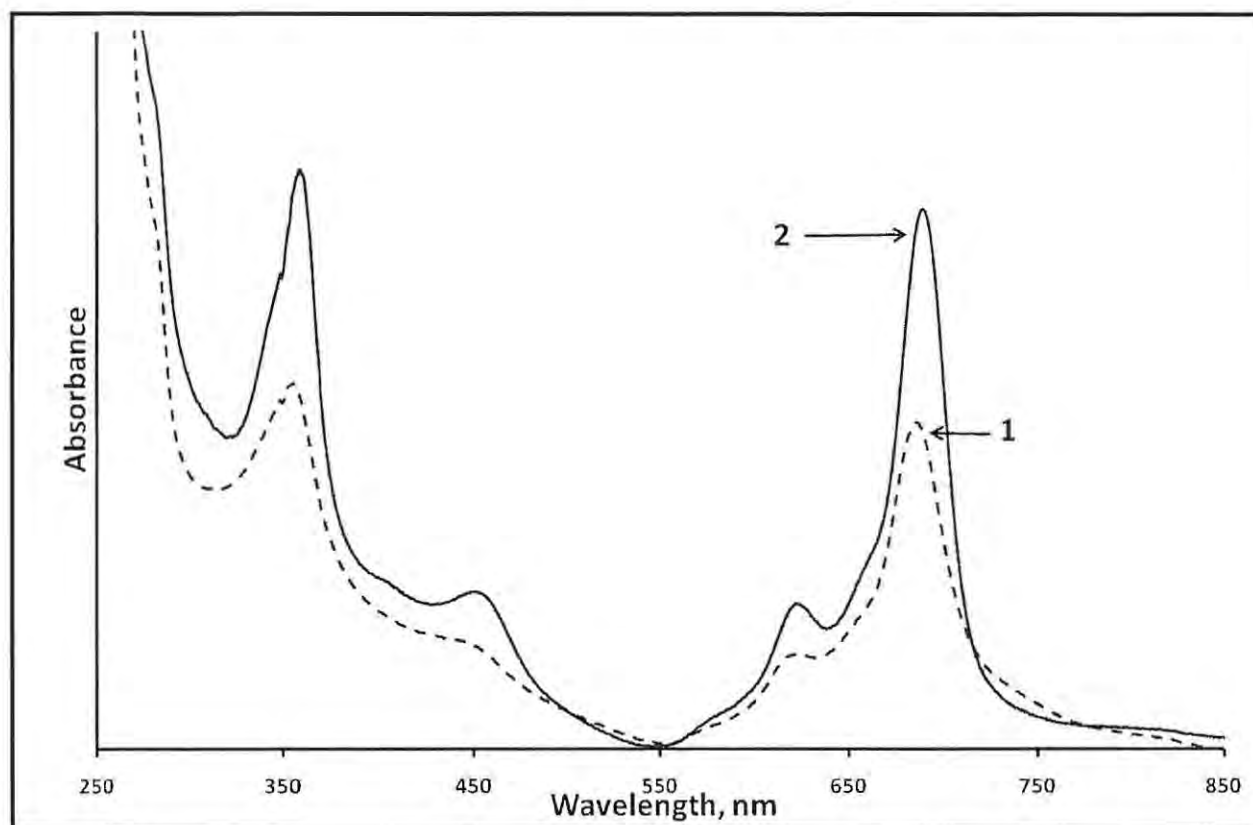
Fig. 6.16 UV-visible spectra of FePc(SCH$_2$Ph)$_8$ before (1) and after (2) addition of L-cysteine. FePc(SCH$_2$Ph)$_8$ concentration $\approx$ 1 μM

Small shifts in the Q-band maximum, as obtained for complexes **9b** (Fig. 6.16) and **10b** (spectrum not shown) are typical of axial ligation in MPcs [459]. These studies therefore prove, to some extent, that the MPcs of this work do interact with L-cysteine.

The interaction between the substrate (L-cysteine) and the catalyst (MPc) may be the main cause of the large Tafel slopes [319,480,485,497], Table 6.6. Values of α above 0.5, obtained for both SAMs (α = 0.77 and 0.67 for FePc(SCH$_2$Ph)$_8$ SAM and CoPc(SCH$_2$Ph)$_8$ SAM, respectively, Table 6.6) suggest that there is a greater probability that the reaction transition state will form the product. But these values of α are tentative because of the unusually large Tafel slopes.

The total number of electrons (n$_t$) involved in the electrocatalytic oxidation of L-cysteine, calculated using Eq. 6.5 (where D for L-cysteine = 4.8 × 10^{-5} cm^2.s^{-1} [34]), is one for FePc(SCH$_2$Ph)$_8$ and CoPc(SCH$_2$Ph)$_8$ SAMs, Table 6.6.

Chapter 6: Self assembled monolayers

Fig. 6.17 shows the linear relationship between the peak current and the L-cysteine concentration (10^{-4} - 10^{-2} M range) for the FePc(SCH$_2$Ph)$_8$ SAM.
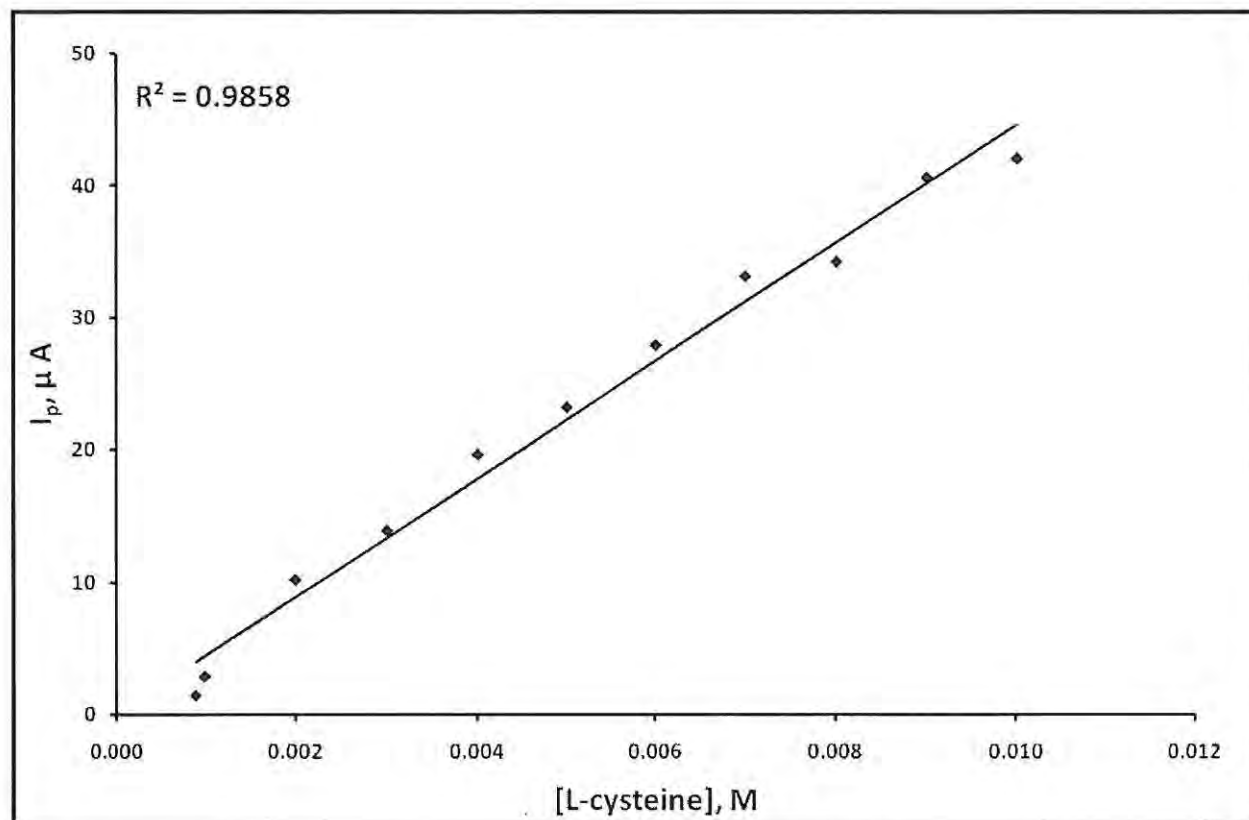
Fig. 6.17 Plot of I_p vs. L-cysteine concentration for FePc(SCH$_2$Ph)$_8$ SAM

The linear relationship of Fig. 6.17 shows that the modified electrode may be used for the determination of L-cysteine in the concentration range shown. The detection limit of the FePc(SCH$_2$Ph)$_8$ (**9b**) SAM is 3.85 × 10^{-7} M (3σ criterion), a value which is better than or comparable to that reported in literature, Table 6.5. Similar results were obtained for CoPc(SCH$_2$Ph)$_8$ (**10b**) SAM (Fig. not shown) and results are listed in Tables 6.5 and 6.6. The limit of detection of FePc(SCH$_2$Ph)$_8$ SAM is lower than its Co counterpart and FePc(SCH$_2$Ph)$_8$ SAM had a higher sensitivity, Table 6.6, due to the higher catalytic currents.

Based on the above discussion and literature reports [23,283], the mechanism for the catalytic oxidation of L-cysteine, using the SAMs of this work, may be represented by Eqs. 6.13 - 6.16:

$$M^{II}Pc \rightarrow M^{III}Pc + e^- \qquad 6.13$$

$$RSH + M^{III}Pc \rightarrow RS^+\text{-}M^{II}Pc \qquad\qquad 6.14$$

$$RS^+\text{-}M^{II}Pc \rightarrow M^{II}Pc + RS^+ \qquad\qquad 6.15$$

$$2RS^+ \rightarrow RSSR \qquad\qquad 6.16$$

where MPc = $CoPc(SCH_2Ph)_8$ or $FePc(SCH_2Ph)_8$, RSH = cysteine, and RSSR = cystine (the oxidation product of cysteine).

Eq. 6.13 is proposed because the oxidation of L-cysteine occurs within the potential range of the $M^{III/II}Pc$ couples [23]. Eq. 6.14 is proposed on the basis of coordination of L-cysteine to complexes **9b** and **10b** which was proved spectroscopically (e.g. Fig. 6.16). The RS^+ moiety then dissociates from the $M^{II}Pc$ complex and forms a bond with another RS^+ moiety to give cystine, the most common oxidation product of cysteine.

All of the SAM modified electrodes of this work are quite stable, as proven by 35 continuous cyclic voltammetry scans recorded in 1 mM L-cysteine. The $FePc(SCH_2Ph)_8$ SAM modified electrode gave a 17% decrease in peak current output after 35 scans, whereas the $CoPc(SCH_2Ph)_8$ SAM modified electrode was more stable showing only a 6% decrease in peak current output over the same scan range, Table 6.6.

6.2.2.2. Manganese phthalocyanine derivatives

Fig. 6.18 shows the cyclic voltammograms of the SAMs of complexes **6d** (1), **6e** (2), **8d** (3), **8e** (4), and **6c** (5) recorded in L-cysteine in pH 4.
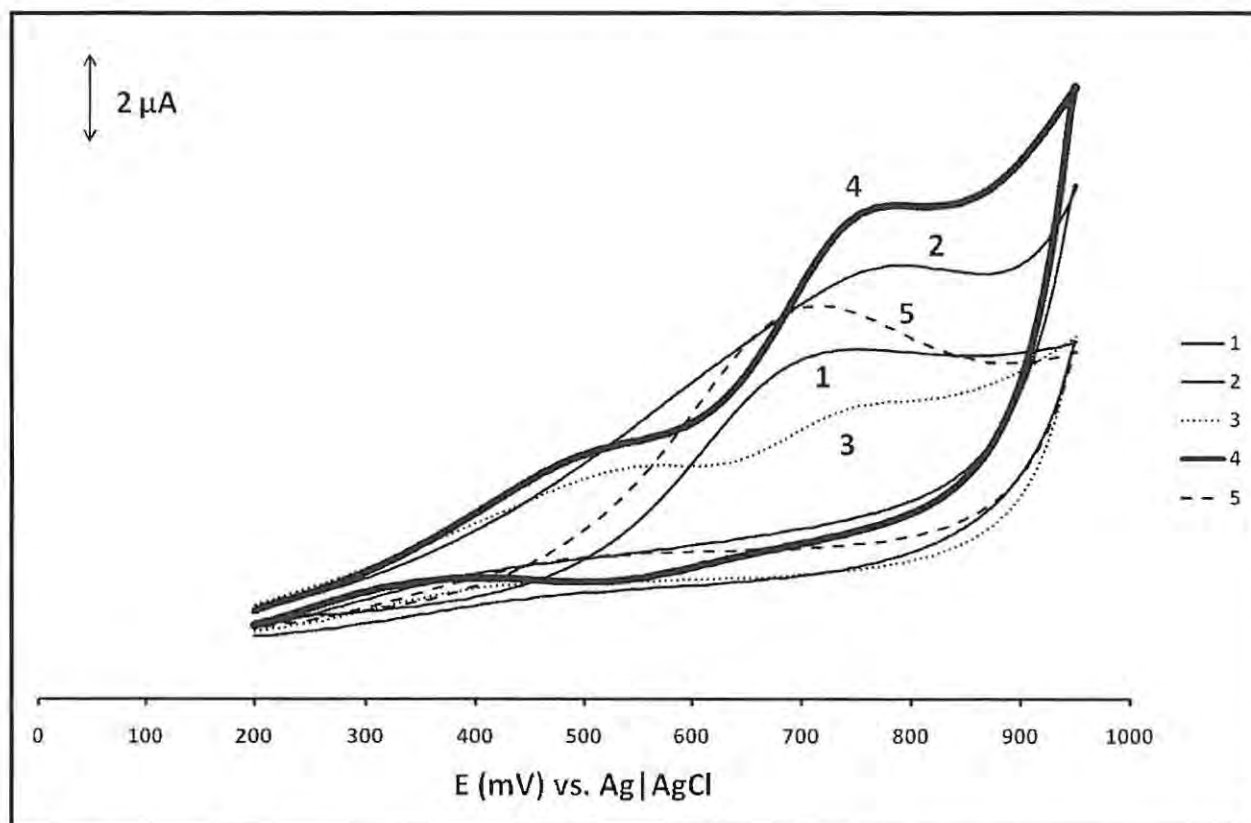
Fig. 6.18 Cyclic voltammograms of SAMs of α-(OH)MnTMPyPc (**6d**, 1), α-Q-(OH)MnTMPyPc (**6e**, 2), β-(OH)MnTMPyPc (**8d**, 3), β-Q-(OH)MnTMPyPc (**8e**, 4), and (OH)MnPc(SPh)$_4$ (**6c**, 5) recorded in L-cysteine at 50 mV.s^{-1}

No peaks were observed for the un-modified gold electrode recorded in L-cysteine (in pH 4 buffer) solution (Fig. not shown), but L-cysteine oxidation peaks were observed between 0.68 V and 0.75 V vs. Ag|AgCl for the MnPc SAMs, Table 6.5. The peaks near 0.45 V (observed for complexes **6e**, **8d**, and **8e**) are due to MnPc [27,320], and are slightly shifted compared to Fig. 6.4(a) due to differences in the media.

Fig. 6.19(a) shows a linear relationship between the peak current and the square root of the scan rate which indicates a diffusion-controlled electrocatalytic oxidation of L-cysteine by complex **6d** SAM, as an example.

194

$$y = 0.0958x + 0.8355$$
$$R^2 = 0.9928$$
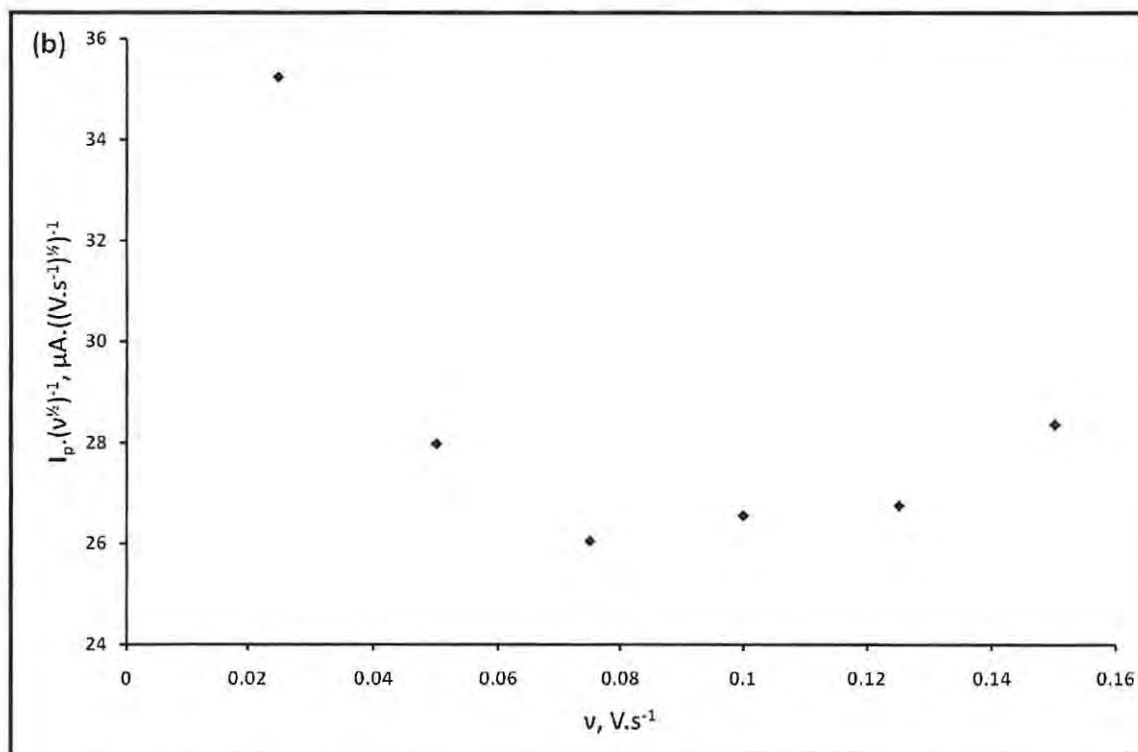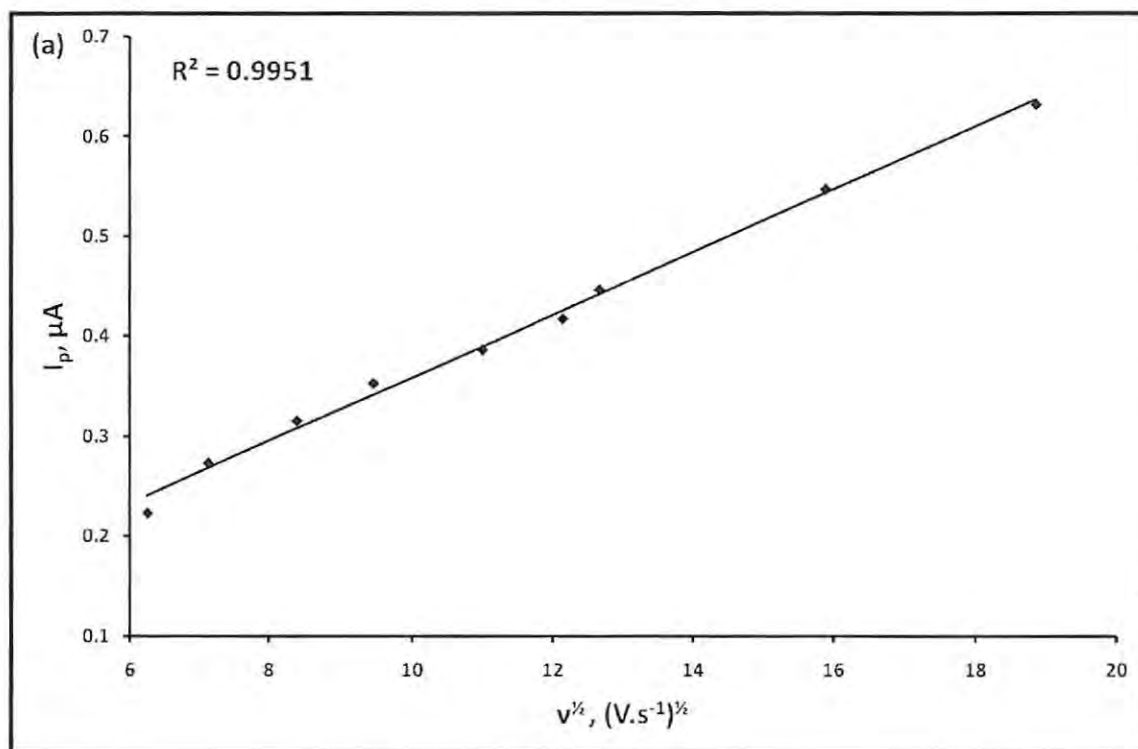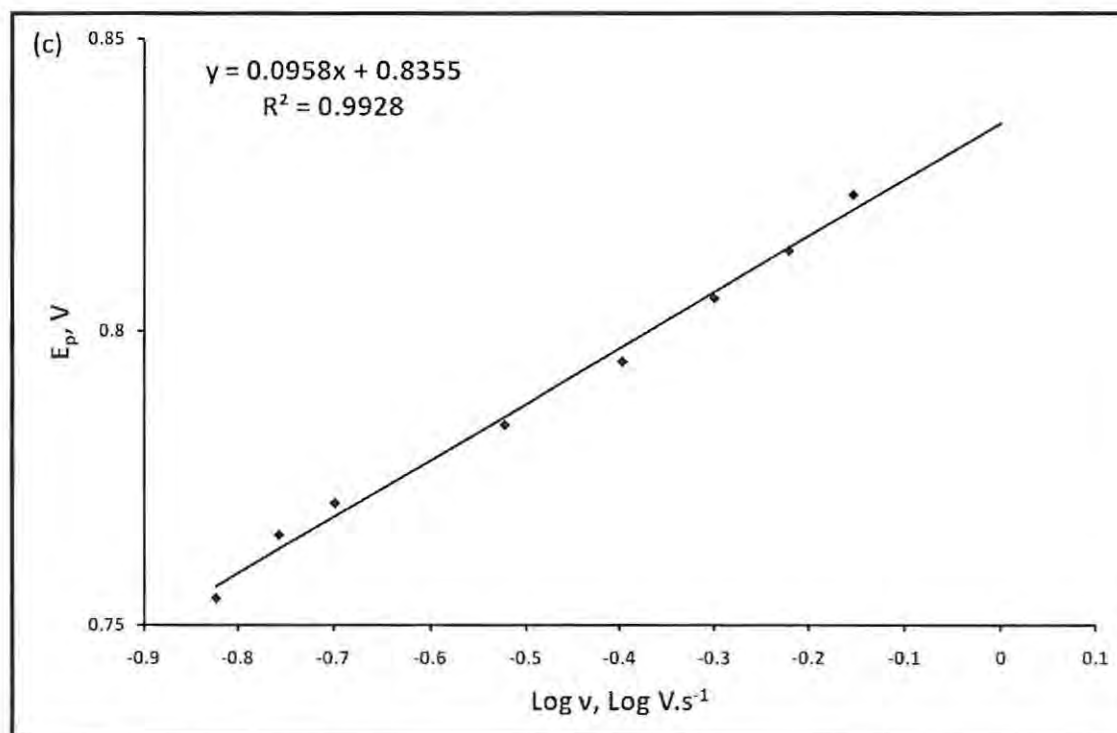
Fig. 6.19 (a) Plot of I_p vs. $v^{\frac{1}{2}}$. (b) Plot of $I_p.v^{-\frac{1}{2}}$ vs. v. (c) Plot of E_p vs. log v for 1 mM L-cysteine. Electrode: $(OH)MnPc(SPh)_4$ (**6c**) SAM

The plot of the scan rate normalized current density ($I_p.v^{-\frac{1}{2}}$) vs. the scan rate, Fig. 6.19(b), exhibits a shape typical of a catalytic process. Similar results were obtained for SAM complexes **6c, 6e, 8d,** and **8e** (Figs. not shown).

A plot of E_p vs. log v for all of the MnPc SAMs, recorded in L-cysteine solution, gave a linear relationship. An example using complex **6d** is shown in Fig. 6.19(c). Tafel slopes, calculated using Eq. 6.4, in the region of 106 - 234 mV.decade^{-1} were obtained for all of the MnPc SAM modified electrodes, Table 6.6. Tafel slope values are in some cases as high as for the $FePc(SCH_2Ph)_8$ and $CoPc(SCH_2Ph)_8$ complexes. Thus, as for the $FePc(SCH_2Ph)_8$ and $CoPc(SCH_2Ph)_8$ complexes, interactions between the substrate (L-cysteine) and the catalyst (MPc) [283] may be the main cause of the large Tafel slopes. Values of α above 0.5, obtained for the SAMs of **6c, 6d, 6e,** and **8d** (Table 6.6), suggest greater probabilities of forming products than reforming reactants from the transition state. The α values for complexes **6c, 6d, 6e,** and **8d** are tentative because the Tafel slopes are large and do not fall within the normal 30 to 120 mV.decade^{-1} region, as was also found for the $FePc(SCH_2Ph)_8$ complex.

196

Chapter 6: Self assembled monolayers

The total number of electrons (n_t) involved in the electro-oxidation of L-cysteine, calculated using Eq. 6.5 (where D for L-cysteine = 4.8×10^{-5} $cm^2.s^{-1}$ [34]), is one ($n_t \sim 1$, Table 6.6) for all of the MnPc SAMs of this work, as found for the FePc(SCH$_2$Ph)$_8$ and CoPc(SCH$_2$Ph)$_8$ complexes. All of the MnPc SAMs displayed good stability as there was only less than 10 % decay in the peak current output over 35 continuous scans recorded in 1 mM L-cysteine solution, Table 6.6. The sensitivities of all MnPc SAM complexes lay in the 0.0024 - 0.0065 $A.M^{-1}$ region (Table 6.6), with complex **8e** SAM displaying the highest value. The sensitivity in most cases is better than for the FePc(SCH$_2$Ph)$_8$ and CoPc(SCH$_2$Ph)$_8$ complexes. Fig. 6.20 shows the linear relationships between the peak current and the L-cysteine concentration (10^{-4} - 10^{-2} M range) for all of the MnPc SAMs, showing that they may be used reliably for the determination of L-cysteine in this concentration range.
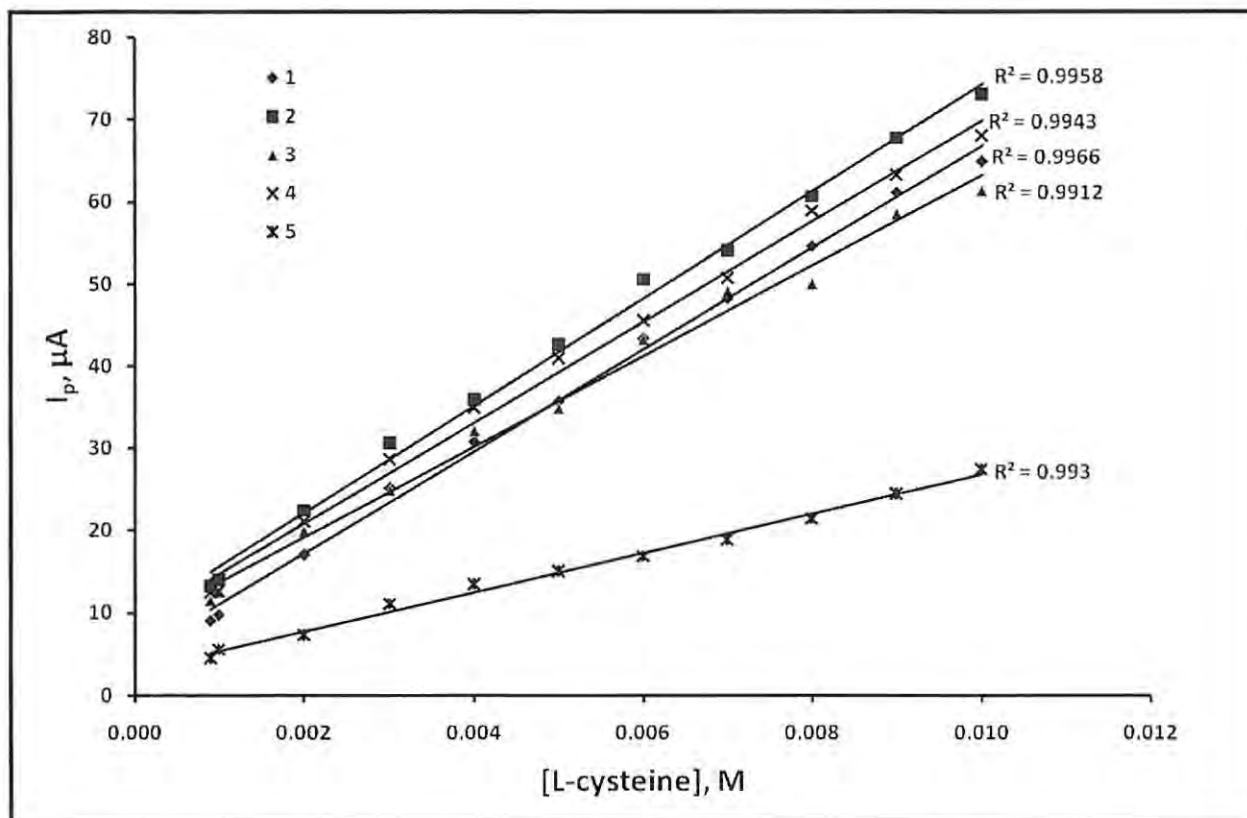
Fig. 6.20 Plot of I_p vs. L-cysteine concentration for SAMs of α-(OH)MnTMPyPc (**6d**, 1), α-Q-(OH)MnTMPyPc (**6e**, 2), β-(OH)MnTMPyPc (**8d**, 3), β-Q-(OH)MnTMPyPc (**8e**, 4), and (OH)MnPc(SPh)$_4$ (**6c**, 5)

The L-cysteine limits of detection (3σ criterion) for all of the SAMs are in the 10^{-7} M region, with complex **6e** SAM having the best value of 2.83×10^{-7} M, Tables 6.5 and 6.6. These values are compared with the literature values in Table 6.5. All of the SAMs had comparable, or better, L-cysteine limits of detection than the literature values on gold electrodes. The differences in detection limits could be a result of the extent of orbital overlap of metal orbitals with the analyte orbitals during the electron transfer. In terms of lowering of overpotential, however, better values have been reported in the literature for CoPc and FePc derivatives, Table 6.5.

From the above study, the mechanism for electrocatalysis of L-cysteine by the MnPc complexes is proposed as Eqs. 6.17 - 6.20:

$$Mn^{III}Pc \rightarrow Mn^{IV}Pc + e^- \qquad 6.17$$

$$RSH + Mn^{IV}Pc \rightarrow RS^+\text{-}Mn^{III}Pc \qquad 6.18$$

$RS^+-Mn^{III}Pc \rightarrow Mn^{III}Pc + RS^+$ 6.19

$2RS^+ \rightarrow RSSR$ 6.20
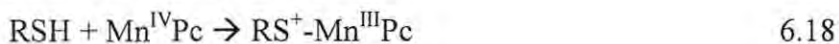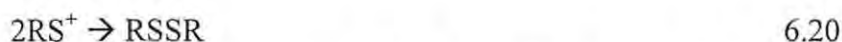
where MnPc = complexes **6c**, **6d**, **6e**, **8d**, and **8e**, RSH = cysteine, and RSSR = cystine.

Eq. 6.17 is proposed because the oxidation of L-cysteine occurs within the potential range of the Mn^{IV}/Mn^{III} couple [31]. Eq. 6.18 is proposed on the basis of coordination of L-cysteine to the MnPc complexes, which was proven spectroscopically. The RS^+ moiety then dissociates from the $Mn^{III}Pc$ complex, Eq. 6.19, and forms a bond with anther RS^+ moiety to give cystine, the most common oxidation product of cysteine, Eq. 6.20.

6.3. Conclusions

MPc complexes substituted with thio groups ($(OH)MnPc(SPh)_4$ (**6c**), α-$(OH)MnTMPyPc$ (**6d**), α-Q-$(OH)MnTMPyPc$ (**6e**), β-$(OH)MnTMPyPc$ (**8d**), β-Q-$(OH)MnTMPyPc$ (**8e**), $FePc(SCH_2Ph)_8$ (**9b**), and $CoPc(SCH_2Ph)_8$ (**10b**)) were used to form self assembled monolayers (SAMs). Voltammetry, impedance measurements, atomic force microscopy, and scanning electrochemical microscopy proved that all of the SAMs are well packed, and are strongly passivating, acting as selective and efficient barriers to ion permeability. Furthermore, surface coverage studies confirmed that the MPc macrocycles adsorb onto the gold electrode as monolayers. All of the MPc SAMs were successfully used as electrochemical sensors of nitrite and L-cysteine (thiocyanate and melatonin cannot be detected by these electrodes). The MPc SAMs showed larger nitrite oxidation peaks at much lower oxidation potentials than with an un-modified gold electrode. All of the MPc SAMs gave linear relationships between the peak current and the nitrite concentration, with the MnPcs doing so over a wider range than the $FePc(SCH_2Ph)_8$ and $CoPc(SCH_2Ph)_8$ SAMs. Nitrite sensitivities of all of the SAMs of this work are in the mA.M^{-1} range, with complex **6e** SAM having the highest value. The MnPc SAMs gave much better limits of detection of nitrite than the $FePc(SCH_2Ph)_8$ and $CoPc(SCH_2Ph)_8$ SAMs. All of the SAMs of this work showed good stability in analyzing nitrite solutions. Two electrons are involved in the electro-oxidation of nitrite by the MnPc SAMs. This value contrasts with that for the $FePc(SCH_2Ph)_8$ and $CoPc(SCH_2Ph)_8$ SAMs (which showed the involvement of one electron) and is possibly explained by the redox processes involved. The $M^{III}Pc/M^{II}Pc$ process is involved for $FePc(SCH_2Ph)_8$ and $CoPc(SCH_2Ph)_8$ SAMs, but the $M^{IV}Pc/M^{III}Pc$ process is involved for the

199

Chapter 6: Self assembled monolayers

MnPcs. Further studies are needed to verify this. A mechanism for the interaction of nitrite with the MPc SAMs is proposed, based on UV-visible spectral observations, kinetics, and electrochemical behaviour.

All of the SAM modified electrodes in this work can detect L-cysteine, whereas an un-modified electrode cannot. Linear relationships between the peak current and the L-cysteine concentration (10^{-4} - 10^{-2} M range) were obtained for all of the MPc SAMs. L-cysteine sensitivities for all of the SAMs of this work are in the mA.M^{-1} range, with complex **8e** SAM having the highest value. The MnPc SAMs gave better limits of detection of L-cysteine than the FePc(SCH$_2$Ph)$_8$ and CoPc(SCH$_2$Ph)$_8$ SAMs. All of the SAMs of this work showed good stability in analyzing L-cysteine solutions, with the MnPc SAMs being the most stable. UV-visible spectral observations, kinetics, and electrochemical studies enabled a mechanism for the interaction of the MPcs with L-cysteine to be proposed.

CHAPTER 7: SUPEROXIDE DISMUTASE STUDIES

This chapter describes the use of manganese phthalocyanines (**6c** (MnPc(SPh)$_4$), **6d** (α-(OH)MnTMPyPc), **6e** (α-Q-(OH)MnTMPyPc), **8b** ((OH)MnPc(SCH$_2$Ph)$_4$), **8d** (β-(OH)MnTMPyPc), **8e** (β-Q-(OH)MnTMPyPc), **8f** ((Na)$_4$(OH)MnPc(SO$_3$)$_4$)) as superoxide dismutase (SOD) mimics. Manganese (III) tetrakis (1-methyl-4-pyridyl)porphyrin (**38**), a commercially available SOD mimic, was also used in this work.

7.1. Mn^{III}/Mn^{II} redox potentials

Several correlations between the redox potential and the SOD-like activity have been reported in the literature [27,31,361,410,413,418,419,427]. The action of the complexes as SOD mimics is based on the catalysis of the superoxide dismutation reaction which involves the Mn^{III}/Mn^{II} redox process. To make this redox catalysis efficient, the redox potential of the Mn^{III}/Mn^{II} couples should be between the potential where O$_2$$^{\bullet-}$ is reduced (0.87 V vs. NHE (normal hydrogen electrode) in aqueous solution (pH = 7) or >1.2 V vs. NHE in an aprotic solution such as DMF or DMSO) and oxidized (-0.16 V vs. NHE in an aqueous solution (pH = 7) or -0.59 V vs. NHE in an aprotic solution) [421,501,502]. All of the complexes examined met these criteria, as shown in Table 7.1 (axial ligands for the MnPc complexes have been left out of the table for simplicity).

Chapter 7: Superoxide dismutase studies

Table 7.1 The redox potentials of the Mn^{III}/Mn^{II} couple for complexes used as SOD mimics (see list of abbreviations as a foot-note to this table)

Complex	Identification of the complex	$E_{1/2}$ (V) vs. NHE Mn^{III}/Mn^{II}	Ref.
Manganese (III) 2,(3)-tetraphenylthiophthalocyanine: (OH)MnPc(SPh)$_4$	6c	-0.26[a]	This work
Manganese (III) 1,(4)-tetra-(2-mercaptopyridine)phthalocyanine: α-(OH)MnTMPyPc	6d	0.14[a]	[31]
Manganese (III) quaternized 1,(4)-tetra-(2-mercaptopyridine)phthalocyanine: α-Q-(OH)MnTMPyPc	6e	0.14[a] 0.26[c]	[31] This work
Manganese (III) tetrakis (benzyl-mercapto) phthalocyanine: (OH)MnPc(SCH$_2$Ph)$_4$	8b	-0.11[a]	This work
Manganese (III) tetrakis (1-methyl-4-pyridyl)porphyrin	8d	0.13[a]	[31]
Quaternized manganese (III) 2,(3)-tetra-(2-mercaptopyridine)phthalocyanine: β-Q-(OH)MnTMPyPc	8e	0.13[a] 0.22[c]	[31] This work
Manganese (III) tetrasulfonatedphthalocyanine: (Na)$_4$(OH)MnPc(SO$_3$)$_4$	8f	Not determined*	This work
Manganese (III) tetrakis (1-methyl-4-pyridyl) porphyrin: [Mn^{III}TMPyP]$^{5+}$	38	0.06[b]	[361]
[Mn(III)TE-2-PyP(OH$_2$)]$^{5+}$		0.23[b]	[361]

Table 7.1 continues

Table 7.1 continues			
Mn(III)TrM-2-PyP^{4+}		0.12[b]	[361]
Mn(III)TM-3-PyP^{5+}		0.05[b]	[361]
Mn(III)Br$_8$TCPP		0.128[e]	[501]
[Mn(III)BM-2-PyP]$^{3+}$		0.05[b]	[361]
[Mn^{III}T-2,3-PyPz]$^{+}$		0.09[f]	[419]
[Mn(III)T(TFTMA)P]$^{5+}$		0.06[b]	[361]
[Mn(III)T(2,6-Cl$_2$-3-SO$_3$-P)P]$^{3-}$		0.09[b]	[361]
[Mn(III)Pc]$^{+}$		-0.03[g]	[419]
[Mn(III)T(2,6-F$_2$-3-SO$_3$-P)P]$^{3-}$		-0.01[b]	[361]
[Mn(III)T(TMA)P]$^{5+}$		-0.10[b]	[361]
[Mn(III)T(PFP)P]$^{+}$		-0.12[h]	[419]
[Mn(III)TPP]$^{+}$		-0.27[h]	[419]
[Mn(III)TCPP]$^{3-}$		-0.19[b]	[361]
[Mn(III)T-4-PyP]$^{+}$		-0.20[h]	[419]
[Mn(III)T-2-PyP]$^{+}$		-0.28[h]	[419]

[a] $E_{1/2}$ values were determined in dimethylformamide (DMF) containing tetrabutylammonium tetrafluoroborate (TBABF$_4$)

[b] $E_{1/2}$ values were determined in 0.05 M phosphate buffer, pH 7.8, 0.1 M NaCl

[c] $E_{1/2}$ values were determined in PBS (pH 7.4)

[d] E_{pc}: redox potential for the cathodic peak (Mn^{III}/Mn^{II} redox process is irreversible)

[e] Specific metal couple not given i.e. only stated as 'metal-centered redox potential'

[f] $E_{1/2}$ values were determined in 9/1 (v/v) DMF + aqueous solutions 0.05 M tris buffer, pH 7.9, 0.1 M NaCl and extrapolated to aqueous medium values

[g] $E_{1/2}$ values were determined in 8.5/0.5/1 (v/v/v) methanol + aqueous + pyridine solution, 0.05 M tris buffer, pH 7.9, 0.1 M NaCl. Pyridine was used to increase the solubility of the phthalocyanine

[h] $E_{1/2}$ values were determined in 9/1 (v/v) methanol + aqueous solutions, 0.05 M tris buffer, pH 7.9, 0.1 M NaCl

Chapter 7: Superoxide dismutase studies

*Not determined: no clear voltammetric peaks were observed to assess a metal-centered redox process

List of abbreviations:

$[Mn(III)TE-2-PyP(OH)_2]^{5+}$: manganese (III) 5,10,15,20-tetrakis(N-ethylpyridinium-2-yl)porphyrin

$[Mn(III)TrM-2-PyP]^{4+}$: manganese (III) 5-(2-pryridyl)-10,15,20-tris(N-methylpyridinium-2-yl)porphyrin

$[Mn(III)TM-3-PyP]^{5+}$: manganese(III) tetrakis (1-methyl-3-pyridyl) porphyrin

$Mn(III)Br_8TBAP$: manganese (III) β-octabromo-*meso*-tetrakis(4-carboxyphenyl)porphyrin

$[Mn(III)BM-2-PyP]^{3+}$: manganese (III) 5,10,15,20-bis(2-pyridyl)-bis(N-methylpyridinium-2-yl)porphyrin

$[Mn^{III}T-2,3-PyPz]^{+}$: manganese (III) tetrakis (2,3-pyridino)porphyrazine

$[Mn(III)T(TFTMA)P]^{5+}$: manganese (III) 5,10,15,20-tetrakis(2,3,56-tetrafluoro-N,N,N-trimethylanilinium-4-yl)porphyrin

$[Mn(III)T(2,6-Cl_2-3-SO_3-P)P]^{3-}$: manganese (III) 5,10,15,20-tetrakis(2,6-dichloro-3-sulfonatophenyl)porphyrin

$[Mn(III)Pc]^{+}$: manganese (III) phthalocyanine

$[Mn(III)T(2,6-F_2-3-SO_3-P)P]^{3-}$: manganese (III) 5,10,15,20-tetrakis(2,6-difluoro-3-sulfonatophenyl)porphyrin

$[Mn(III)T(TMA)P]^{5+}$: manganese (III) 5,10,15,20-tetrakis(N,N,N-trimethylamilinium-4-yl)porphyrin

$[Mn(III)T(PFP)P]^{+}$: manganese (III) 5,10,15,20-tetrakis(pentflurophenyl)porphyrin

$[Mn(III)TPP]^{+}$: manganese (III) 5,10,15,20-tetrakis(phenyl)porphyrin

$[Mn(III)TCPP]^{3-}$: manganese (III) 5,10,15,20-tetrakis(4-carboxylatophenyl)porphyrin

$[Mn(III)T-4-PyP]^{+}$: manganese (III) tetra(4-pyridyl)porphyrin

$[Mn(III)T-2-PyP]^{+}$: manganese (III) tetra(2-pyridyl)porphyrin

MnSOD: manganese superoxide dismutase

$[Mn^{III}Cl_4TE-2-PyP]^{5+}$: manganese (III) β-tetrachloro[34]-5,10,15,20-tetrakis(N-ethylpyridinium-2-yl)porphyrin

$[Mn^{III}TrM-2-PyP]^{4+}$: manganese 5-(2-pyridyl)-10,15,20-tris(N-methylpyridinium-2-yl)porphyrin

Chapter 7: Superoxide dismutase studies

The results shown in Table 7.1 clearly indicate the possibility of tuning the Mn^{III}/Mn^{II} redox potential of the complexes by controlling either the geometry or the electronic density around the Mn centre by varying the substituents in this class of complexes [325]. As far as the water-soluble complexes are concerned, based solely on the redox potential value of the Mn-centred process, complexes **6e** and **8e** might be expected to behave as SOD mimics. Complexes **6e** and **8e** are soluble in both water and DMF. Thus, in DMF, these complexes, as well as the DMF soluble complexes **6d** and **8d**, are expected to behave similarly towards the dismutation of superoxide. The potential values obtained might allow further examination of the possibility of using these complexes as SOD mimics if the metal-centered redox potential is considered as a major factor affecting SOD-like activity *in vitro*. The impact of electrostatics should also be considered for both *in vitro* and *in vivo* testing although this point is now being largely revisited in recently reported studies [421].

7.2. Superoxide production using the xanthine-xanthine oxidase reaction: urate assay

The first step involves determining whether or not the putative SOD mimic interferes with the xanthine-xanthine oxidase reaction. The MnPc complex should only dismutate the produced superoxide radical, without interfering with the reaction. The evaluation of such behaviour is done by monitoring the rate of urate production, followed at 290 nm, produced by the xanthine-xanthine oxidase reaction. Fig. 7.1 shows the absorbance against time graphs of the xanthine-xanthine oxidase reaction, without (1) and with (2) a supposed SOD mimic (complex **8b** in this case).

Fig. 7.1 Plots of absorbance against time for xanthine (35 μM) + xanthine oxidase (0.01 U.mL^{-1}) without (1) and with (2) (OH)MnPc(SCH$_2$Ph)$_4$ (**8b**, 0.2 μM)

The slopes of the plots are very similar proving that complex **8b** does not inhibit production of superoxide by xanthine oxidase. Note that the shift (at time zero) in the absorbance at 290 nm in the presence of complex **8b** is due to the absorbance of this complex itself in this region. All of the examined MnPcs do not interfere with the xanthine-xanthine oxidase reaction, as shown by similar studies. It was confirmed that DMSO, used to dissolve some of the SOD mimics, also does not interfere (data not shown).

7.3. Superoxide production using the xanthine-xanthine oxidase reaction: McCord-Fridovich assay

The McCord-Fridovich assay is among the most developed tests for the monitoring of superoxide [361,409,410,413,418,419,421] although it is not consensual and it measures overall kinetics for a given set of conditions. This assay is based on the kinetic competition for

Chapter 7: Superoxide dismutase studies

superoxide reduction between the SOD mimic and cytochrome c [369,430]. The xanthine-xanthine oxidase reaction is used to produce the superoxide which then reduces cytochrome c to ferrocytochrome c. The latter is measured using UV-visible spectrophotometry at 550 nm. If SOD is added, the superoxide produced by the xanthine-xanthine oxidase reacts with SOD and does not reduce ferricytochrome c, and hence there is less ferrocytochrome c as evidenced by the decrease in absorbance at 550 nm compared to that in the absence of SOD (data not shown).

As suggested by Durot *et al.* [389], k_{cat}, the apparent catalytic rate constant for the dismutation of superoxide can be obtained from the IC50, which is the concentration of the putative SOD mimic that induces a 50 % inhibition of the reduction of cytochrome c, using Eq. 7.1:

$$k_{cat} = \frac{k_{Cytc}[cytc]}{IC50} \qquad\qquad 7.1$$

where [cyt*c*] is the concentration of cytochrome c and k_{Cytc} is the known rate constant of the bimolecular reaction between the superoxide radical and cytochrome c: k_{Cytc} (pH = 7.8 and at 21°C) = 2.6×10^5 $M^{-1}.s^{-1}$ [431]. Values of k_{cat} allow SOD activities obtained by the McCord-Fridovich assay with different concentrations of cytochrome c (or markers other than cytochrome c) to be compared. All of the measurements were made for the same time duration and it was confirmed that there was no slowly developing influence by the complexes on xanthine oxidase activity for longer times.

McCord-Fridovich assays were done on all of the manganese phthalocyanines of this work. Fig. 7.2, which is representative of all of the manganese phthalocyanines studied, shows the typical evolution of the absorbance at 550 nm with time and its decrease in the presence of the complex, for a given concentration of complex **8b**.
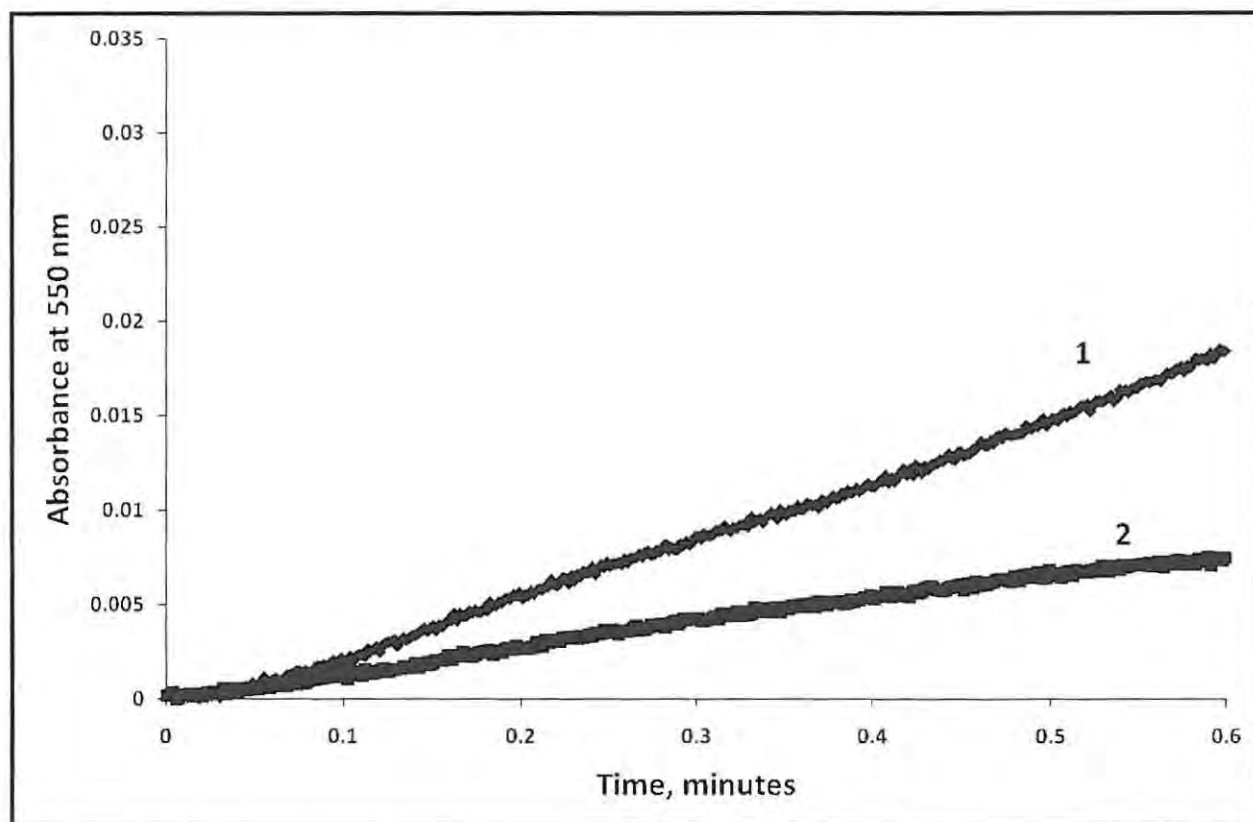
Fig. 7.2 McCord-Fridovich assay without (1) and with (2) (OH)MnPc(SCH$_2$Ph)$_4$ (**8b**, 0.05 μM) in a 50 mM PBS solution containing cytc (10 μM) + xanthine (20 μM) and xanthine oxidase (0.01 U.mL^{-1})

Fig. 7.3 shows the percentage inhibition as a function of the concentration of complex **8b**.
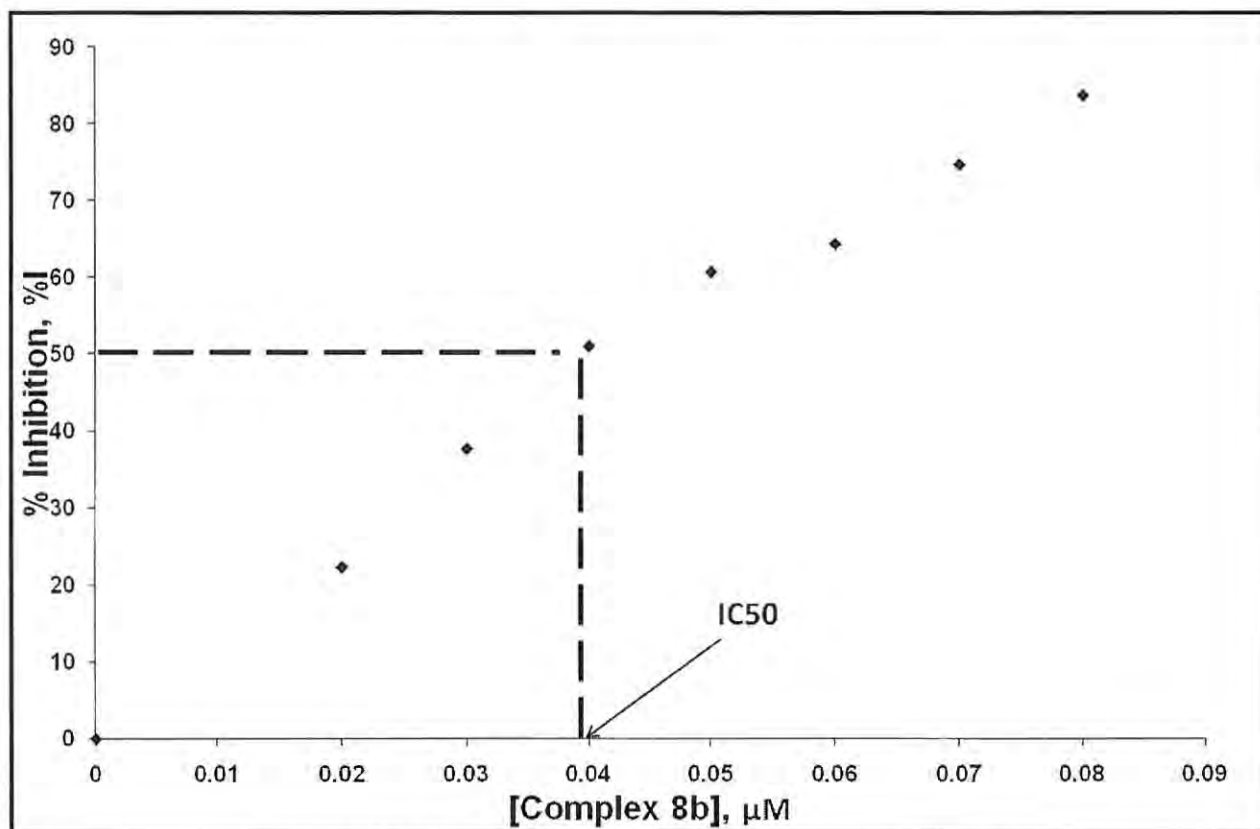
Fig. 7.3 Percentage inhibition of the reduction of cytochrome c as a function of the concentration of $(OH)MnPc(SCH_2Ph)_4$ (**8b**) and the IC50 determination each done over one minute

The inhibition increases as the concentration of the complex increases. The IC50 value can be read from the graph as shown in Fig. 7.3. Table 7.2 lists the IC50 and log k_{cat} values obtained in this work using complexes **6c**, **6d**, **6e**, **8b**, **8d**, **8e**, **8f**, **38**, and those reported in the literature for other porphyrinic Mn (III) complexes [361,369,409,419,501,503,504].

209

Table 7.2 SOD-like activity of Mn complexes determined by the McCord-Fridovich assay. Axial ligands have been omitted for simplicity

Complex	Identification of the complex	IC50 (μM)	Log k_{cat}	Ref.
MnSOD		-	9.26	[369]
$[Mn^{III}Cl_4TE\text{-}2\text{-}PyP]^{5+}$		0.0065	8.60±10%	[409]
Manganese (III) 2,(3) tetraphenylthio phthalocyanine: $[Mn^{III}TPTPc]^+$	6c	0.040	7.81	This work
Manganese (III) tetrakis (benzyl-mercapto) phthalocyanine: $[Mn^{III}TBMPc]^+$	8b	0.044	7.76	This work
$[Mn^{III}TE\text{-}2\text{-}PyP(OH)_2]^{5+}$		0.045	7.76±10%	[419]
$[Mn^{II}\{N,N\text{-}bis(2\text{-}pyridylmethyl)\text{-}(S)\text{-}histidinate\}(H_2O)]_2(ClO_4)_2$		0.289	6.95	[503]
Manganese (III) tetrasulfonated phthalocyanine: $[Mn^{III}TSPc]^{3-}$	8f	0.362	6.86	This work
Manganese (III) tetramethyl-tetra -1,(4)-tetra-(2-mercaptopyridine) phthalocyanine: $[Mn^{III}Tm1,4TMPyPc]^{5+}$	6e	0.450	6.76	This work
Quaternized manganese (III) 2,(3)-tetra-(2-mercaptopyridine)phthalocyanine: β-Q-(OH)MnTMPyPc	8e	0.464	6.68	This work
$Mn^{III}TrM\text{-}2\text{-}PyP^{4+}$		0.609	6.63±10%	[361]
Manganese (III) 2,(3)-tetra-(2-mercaptopyridine) phthalocyanine: $[Mn^{III}2,3\text{-}TMPyPc]^+$	8d	0.626	6.62	This work

Table 7.2 continues

Chapter 7: Superoxide dismutase studies

Table 7.2 continues				
Manganese (III) 1,(4)-tetra-(2-mercaptopyridine) phthalocyanine: [Mn^{III}1,4-TMPyPc]$^+$	6d	0.624	6.62	This work
[Mn^{III}TM-3-PyP]$^{5+}$		0.638	6.61±10%	[361]
Manganese (III) tetrakis (1-methyl-4-pyridyl) porphyrin: [Mn^{III}TMPyP]$^{5+}$	38	0.677	6.53	This work
		0.684	6.58±10%	[361]
MnBr$_8$TCPP		0.684	6.58	[501]
[Mn^{III}BM-2-PyP]$^{3+}$		0.785	6.52±10%	[361]
[Mn^{III}T-2,3-PyPz]$^+$		0.902	6.46±20%	[419]
[Mn^{III}T(TFTMA)P]$^{5+}$		2.483	6.02±10%	[361]
[Mn^{III}T(2,6-Cl$_2$-3-SO$_3$-P)P]$^{3-}$		2.600	6.00±10%	[361]
[Mn^{III}Pc]$^+$		4.027	5.81±20%	[419]
[Mn^{III}T(2,6-F$_2$-3-SO$_3$-P)P]$^{3-}$		8.035	5.51±10%	[361]
[Mn^{III}TCPP]$^{3-}$		9.286	5.45±10%	[504]
		72.610	4.56±10%	[361]
[Mn^{III}T(TMA)P]$^{5+}$		20.182	5.11±10%	[361]
[Mn^{III}T(PFP)P]$^+$		26.000	5.00±20%	[419]
[Mn^{III}TPP]$^+$		38.457	4.83±20%	[419]
[Mn^{III}T-4-PyP]$^+$		76.731	4.53±20%	[419]
[Mn^{III}T-2-PyP]$^+$		133.344	4.29±20%	[419]

List of abbreviations:

[Mn(III)TE-2-PyP(OH)$_2$]$^{5+}$: manganese (III) 5,10,15,20-tetrakis(N-ethylpyridinium-2-yl)porphyrin

[Mn(III)TrM-2-PyP]$^{4+}$: manganese (III) 5-(2-pryridyl)-10,15,20-tris(N-methylpyridinium-2-yl)

[Mn(III)TM-3-PyP]$^{5+}$: manganese (III) tetrakis (1-methyl-3-pyridyl)porphyrin

Mn(III)Br$_8$TBAP: manganese (III) β-octabromo-meso-tetrakis(4-carboxyphenyl)porphyrin

Chapter 7: Superoxide dismutase studies

$[Mn(III)BM-2-PyP]^{3+}$: manganese (III) 5,10,15,20-bis(2-pyridyl)-bis(N-methylpyridinium-2-yl)porphyrin

$[Mn^{III}T-2,3-PyPz]^{+}$: manganese (III) tetrakis (2,3-pyridino)porphyrazine

$[Mn(III)T(TFTMA)P]^{5+}$: manganese (III) 5,10,15,20-tetrakis(2,3,56-tetrafluoro-N,N,N-trimethylanilinium-4-yl)porphyrin

$[Mn(III)T(2,6-Cl_2-3-SO_3-P)P]^{3-}$: manganese (III) 5,10,15,20-tetrakis(2,6-dichloro-3-sulfonatophenyl)porphyrin

$[Mn(III)Pc]^{+}$: manganese (III) phthalocyanine

$[Mn(III)T(2,6-F_2-3-SO_3-P)P]^{3-}$: manganese (III) 5,10,15,20-tetrakis(2,6-difluoro-3-sulfonatophenyl)porphyrin

$[Mn(III)T(TMA)P]^{5+}$: manganese (III) 5,10,15,20-tetrakis(N,N,N-trimethylamilinium-4-yl)porphyrin

$[Mn(III)T(PFP)P]^{+}$: manganese (III) 5,10,15,20-tetrakis(pentflurophenyl)porphyrin

$[Mn(III)TPP]^{+}$: manganese (III) 5,10,15,20-tetrakis(phenyl)porphyrin

$[Mn(III)TCPP]^{3-}$: manganese (III) 5,10,15,20-tetrakis(4-benzoic acid)porphyrin

$[Mn(III)T-4-PyP]^{+}$: manganese (III) tetra(4-pyridyl)porphyrin

$[Mn(III)T-2-PyP]^{+}$: manganese (III) tetra(2-pyridyl)porphyrin

MnSOD: manganese superoxide dismutase

$[Mn^{III}Cl_4TE-2-PyP]^{5+}$: manganese (III) β-tetrachloro[34]-5,10,15,20-tetrakis(N-ethylpyridinium-2-yl)

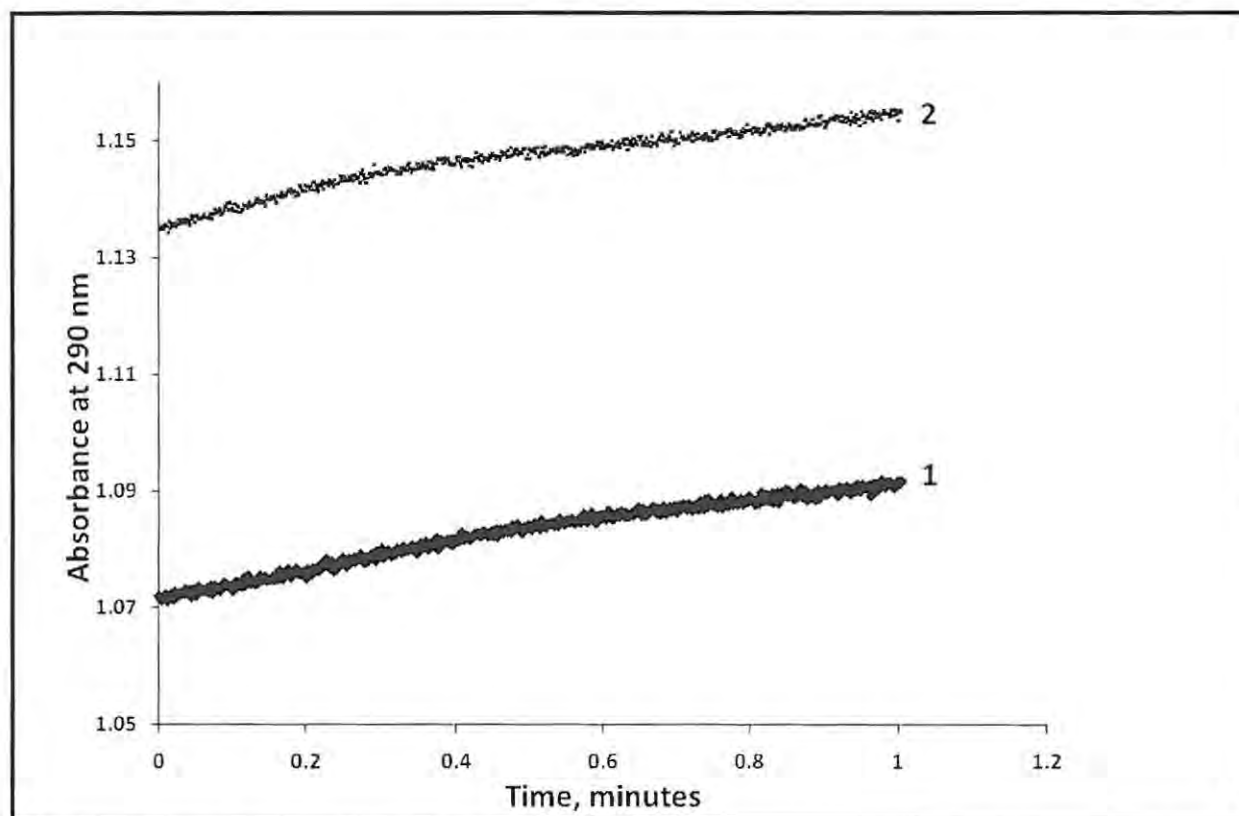$[Mn^{III}TrM-2-PyP]^{4+}$: manganese 5-(2-pyridyl)-10,15,20-tris(N-methylpyridinium-2-yl) porphyrin

The lower the IC50 value, the lower the concentration of SOD mimic needed to inhibit cytochrome c reduction, hence the more effective the SOD mimic. Therefore, from Table 7.2, it can be seen that the complexes reported in this work (especially **6c** and **8b**) performed well. This is confirmed by comparison of the log k_{cat} values which are independent of the concentration and nature of the marker. The higher the value of log k_{cat}, the more efficient the complex. As expected, natural MnSOD has the highest log k_{cat}. Of the complexes studied in this work, large k_{cat} values were obtained for the quaternized (positively charged) complexes **6e** and **8e** and also

for the negatively charged complex **8f**. This last result might appear surprising. Negatively charged complexes should display lower activity towards superoxide due to electrostatic effects [421], while earlier studies reported that no significant effect of charge was obtained on the catalytic rate constants for the dismutation of superoxide in the case of Mn (III) biliverdin complexes [419]. Table 7.2 also shows the reported activity of manganese (III) tetrakis (4-benzoic acid)porphyrin, a commercially available SOD mimic complex. A recently reported study disputes its SOD mimic activity claiming that it is not a SOD mimic when pure [505].

From the results obtained, all of the examined complexes exhibit a dismutation activity for superoxide. Yet, clear dependence of this activity on the redox potentials cannot be established. Although possible relationships between the redox potential of the Mn^{III}/Mn^{II} process of several porphyrins and their log k_{cat} have been reported [361,410,413,418,419,421], the developed biochemical assay allows only the overall k_{cat} to be measured so that the rate constants for the individual steps of the catalytic cycle cannot be determined and the possible effects of the redox potential cannot be properly examined. The influence of the complex structure on the acid dissociation constant of the pyrrolic nitrogens of the macrocycle sometimes affects the possible correlation. This difference has been explained by the contribution of kinetic as opposed to thermodynamic factors.

7.4. SOD-like activity towards extracellular and intracellular superoxide production by human leukemia cells

One major limitation of cytochrome c for superoxide detection is its inability to act on intracellularly generated superoxide. The detection of superoxide produced intracellularly by dihydroethidium (DHE) fluorescence thus offers an excellent alternative. Recent evidence by Zhao *et al* [506] indicates that DHE reacts with superoxide to form hydroxyethidium which has a fluorescence emission peak at 567 nm, is stable intracellularly, and is not produced by other reactive oxygen and nitrogen species. Although Benov *et al* [507] have suggested that the use of DHE for the quantitative measurement of the superoxide anion should be avoided because the stoichiometry of the reaction is unreliable, Peshavariya *et al* [508] recently demonstrated that hydroxyethidium fluorescence analysis can be used for the quantification of not only intracellular superoxide production in HL-60 cells but also the extracellular release of superoxide by those

cells. HL-60 cells are widely used as a superoxide-producing cell model when treated with DMSO. When activated with phorbol 12-myristate 13-acetate (PMA), these DMSO-treated cells produce superoxide that is detected extracellularly, but non-activated, intracellular superoxide production is also detectable. There was a significant increase in fluorescence when HL-60 cells were exposed to DHE, Fig. 7.4. In Fig. 7.4, HL-60 cells were incubated with DHE (25 μM) only, or after activation with PMA (100 ng.mL^{-1}). Extracellular production of superoxide was inhibited by addition of SOD (600 U.mL^{-1}). Also shown in Fig. 7.4 are the background fluorescences of DHE, PMA, or cells. Values (mean ± SEM, n = 3) represent fluorescence arbitrary unit.
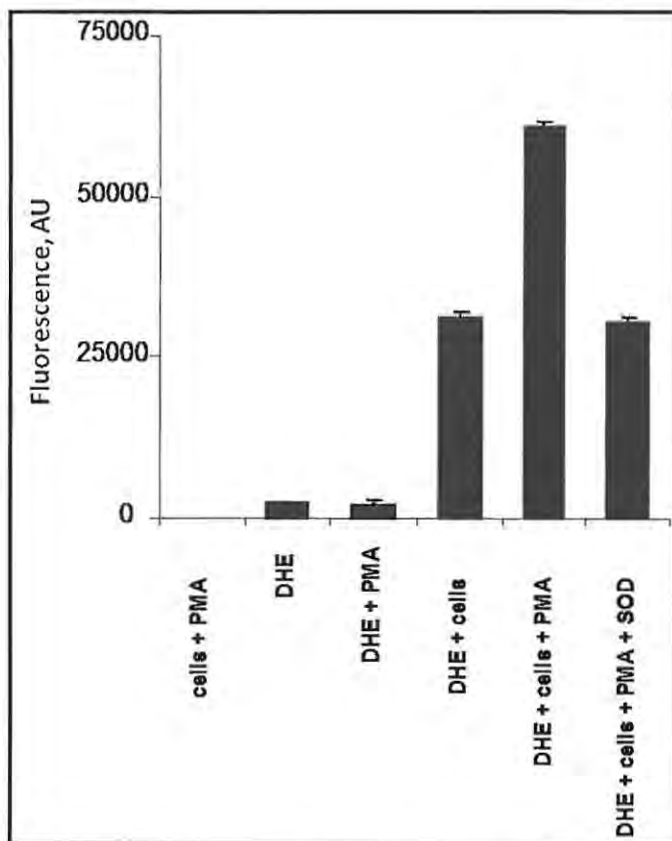
Fig. 7.4 Measurement of intracellular and extracellular superoxide of DMSO-differentiated HL-60 cells using DHE fluorescence

From Fig. 7.4, exposure of PMA-activated cells to DHE is seen to result in the highest increase in fluorescence intensity. This was decreased to the value of the fluorescence of the non-activated cells by the addition of cell impermeable SOD. The component of the fluorescence

inhibited by SOD is attributed to extracellular superoxide release from the cells into the solution. The results obtained correlate well with those recently reported by Peshavariya *et al* [508] using complex **38**, a commercially available Mn (III) porphyrin SOD mimic. The cells themselves produced no background fluorescence at the wavelengths used for superoxide detection, and background fluorescence caused by DHE in the absence of cells is negligible.

DHE fluorescence was used to evaluate the inhibition of superoxide production by the complexes. First, the inhibition of extracellular superoxide production was determined. The results obtained (data not shown) clearly indicate a good correlation between the McCord-Fridovich and DHE assays. The inhibition of intracellular superoxide production by the examined SOD mimics was then evaluated, as exemplified in Fig. 7.5 for complex **6e**. The experiment of Fig. 7.5 was done twice and the line of Fig. 7.5 represents the mean.
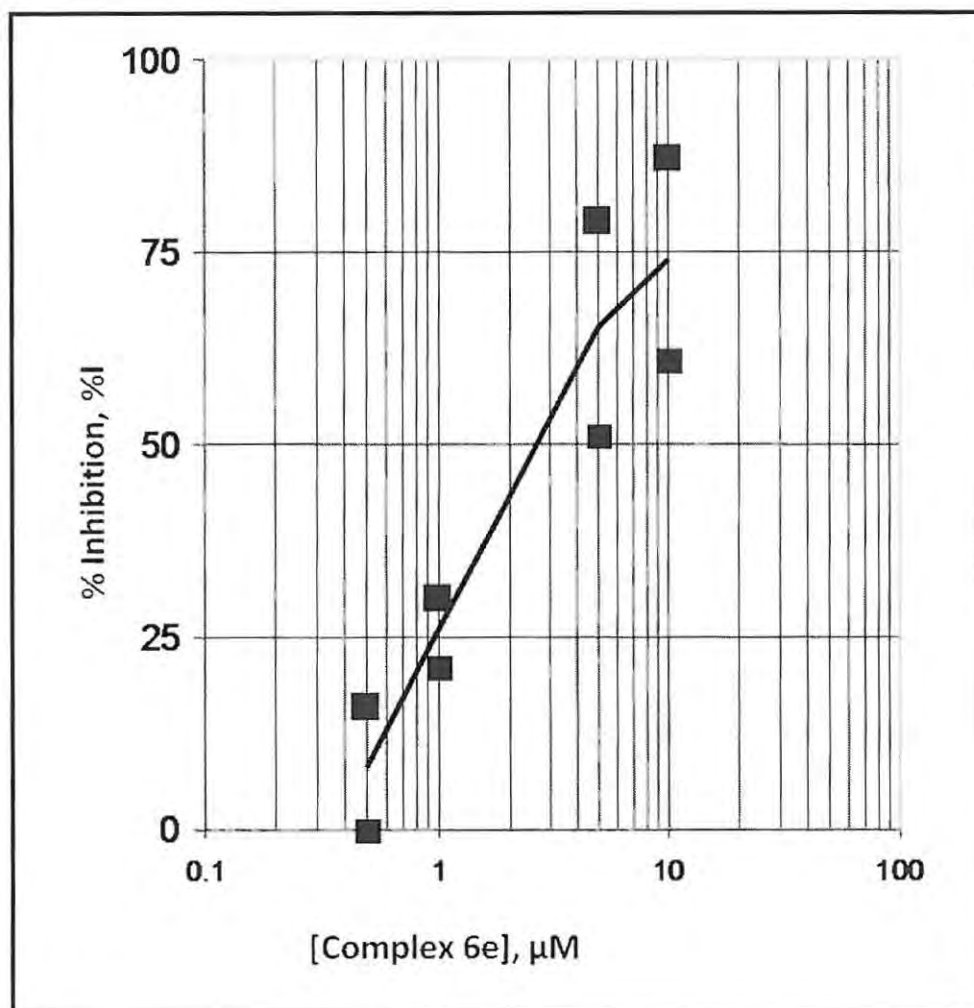
Fig. 7.5 Percentage inhibition as a function of the concentration of α-Q-(OH)MnTMPyPc (**6e**) for HL-60 intracellular production of superoxide using DHE fluorescence

Table 7.3 shows values of the percentage inhibition of intracellular superoxide formation for two fixed concentrations of all of the examined complexes.

Chapter 7: Superoxide dismutase studies

Table 7.3 Intracellular HL-60 SOD-like activity of Mn complexes at two fixed concentrations determined by fluorescence[a,b]

Complex	% Inhibition (mean ± SEM)	
	Concentration of the complex = 10 μM	Concentration of the complex = 50 μM
6c	93 ± 4.6	69 ± 0.8
6d	62 ± 1.5	27 ± 3.2
6e	39 ± 0.8	26 ± 5.0
8b	96 ± 0.7	104 ± 2.7
8d	59 ± 1.7	30 ± 3.0
8e	58 ± 3.2	38 ± 0.6
8f	94 ± 2.4	91 ± 1.4
38	66 ± 1.4	30 ± 3.5

[a]DHE assay, no PMA; studies done in triplicate; SEM = standard error of the mean

[b]**6c** = $(OH)MnPc(SPh)_4$; **6d** = α-$(OH)MnTMPyPc$; **6e** = α-Q-$(OH)MnTMPyPc$; **7a** = $CoPc(COOH)_4$; **8b** = $(OH)MnPc(SCH_2Ph)_4$; **8d** = β-$(OH)MnTMPyPc$; **8e** = β-Q-$(OH)MnTMPyPc$; **8f** = $(Na)_4(OH)MnPc(SO_3)_4$; **38** = manganese (III) tetrakis (1-methyl-4-pyridyl)porphyrin

The percentage of inhibition decreases with increasing concentration of the complex, Table 7.3. This is because, from Eq. 7.1, the IC50 (a form of percentage of inhibition) is inversely proportional to the k_{cat} (the apparent catalytic rate constant for the dismutation of superoxide): hence the lower the percentage of inhibition, the higher the k_{cat} (the better the dismutation of superoxide) which is expected for a higher concentration of SOD mimic complex (Table 7.3).

Values obtained in Table 7.3 can be used as an indirect measurement of the cell permeability to the studied mimics. Complexes **6c**, **8b**, and **8f** are unable to inhibit the intracellular superoxide production. Therefore, it can be hypothesised that these complexes:

- are not able to enter cells or
- cannot reach the appropriate subcellular location where superoxide is being generated, or
- may be metabolized in some way as to inactivate them.

Chapter 7: Superoxide dismutase studies

Although these complexes (**6c**, **8b**, and **8f**) were shown *in vitro* to have k_{cat} values similar (and even larger) than complex **6e** (Table 7.2), differences in intracellular pH may diminish their SOD activity. Conversely, complexes **6d**, **6e**, **8d**, and **8e** are as effective as the commercially available porphyrinic complex selected for this study (**38**), with complex **6e** being the most effective. Finally, viability of cells upon exposure to the examined complexes was assayed using the MTT test (explained in Chapter 2). The test was voluntarily limited to 2 hours which is the duration of the fluorescence measurement. Results of this study are recorded in Fig. 7.6. For Fig. 7.6, HL-60 cells were incubated with the SOD mimics **6c**, **6d**, **6e**, **8b**, **8d**, **8e**, **8f**, and **38** for 2 hours, and then cell viability was evaluated using the MTT test and represented as a percent (black bars) of the viability obtained with cells incubated with 10 μL of solvent (DMSO for **6c**, **6d**, **8b**, and **8d**; PBS for **6e**, **8e**, **8f**, and **38**). Viability of cells incubated with these solvents is shown (white bars), Fig. 7.6.
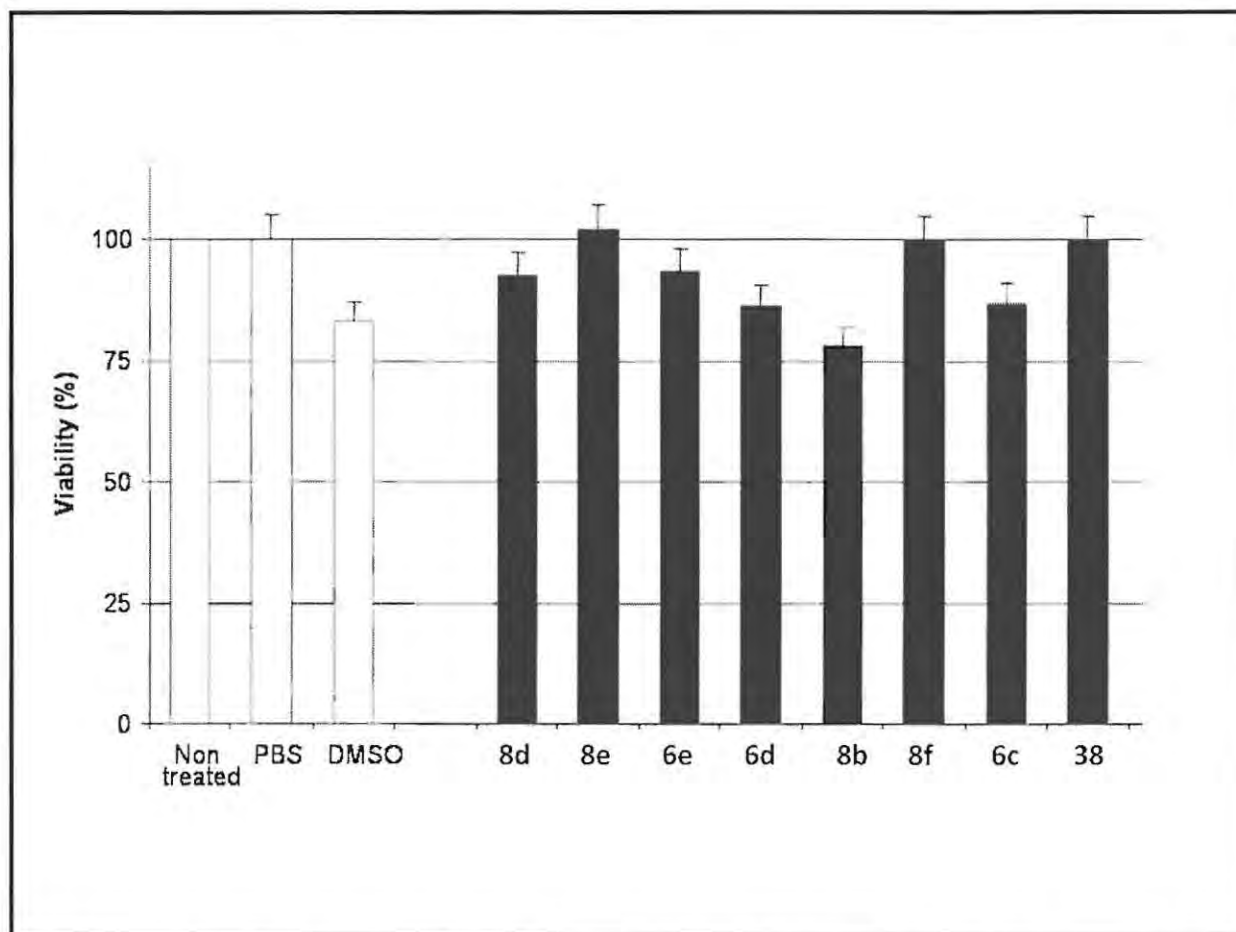
Fig. 7.6 Cell viability in the presence of 50 μM of complexes (OH)MnPc(SPh)$_4$ (**6c**), α-(OH)MnTMPyPc (**6d**), α-Q-(OH)MnTMPyPc (**6e**), (OH)MnPc(SCH$_2$Ph)$_4$ (**8b**), β-(OH)MnTMPyPc (**8d**), β-Q-(OH)MnTMPyPc (**8e**), (Na)$_4$(OH)MnPc(SO$_3$)$_4$ (**8f**), Manganese (III) tetrakis (1-methyl-4-pyridyl)porphyrin (**38**)

As seen in Figure 7.6, complexes which are soluble in PBS (**6e**, **8e**, **8f**, and **38**) show no toxicity, except a very slight toxicity for complex **6e** (93% viability). But, complexes which are not soluble in PBS (**6c**, **6d**, **8b**, **8d**), hence dissolved in DMSO, exhibit higher toxicity (around 70% viability) with the exception of **8d**. This underlines important features for the possible use of complexes **6d**, **6e**, **8d**, and **8e** as efficient SOD mimics, although limited side-effect toxicity is observed in some cases.

7.5. Conclusions

All of the manganese phthalocyanine complexes of this work acted as SOD mimics *in vitro*. Initially, SOD mimic studies were done using an enzymatic system of superoxide production i.e. xanthine-xanthine oxidase. They showed suitable efficiency in terms of the IC50 and k_{cat} values. From the cellular studies, four manganese complexes of this work (**6d**, **6e**, **8d**, **8e**) are cell permeable, act as intracellular SOD mimics, and have SOD-like activity comparable to the commercially available porphyrinic mimic (**38**). These results allow future evaluation of these complexes in cell-based and/or animal experimental protocols as antioxidant drugs.

CHAPTER 8: GENERAL CONCLUSIONS

This work illustrates the use of metallophthalocyanines as electrochemical sensors (electrocatalysts) and superoxide dismutase mimics.

Fe, Co, and Mn phthalocyanine complexes were synthesized and/or characterized. All complexes of this work are soluble in common organic solvents (e.g. DMF), with the quaternized MnPc derivatives (**6e** and **8e**) also being water soluble. The infrared spectra of all the synthesized complexes displayed characteristic bands proving the formation of the desired Pc from the starting material. The UV-visible spectra of the complexes displayed wavelength maxima between 657 nm (for **5g**) and 777 nm (for **8b**), showing the effect of the central Pc metal on the absorption maxima. Furthermore, most synthesized complexes displayed absorption maxima that were mostly red-shifted relative to their unsubstituted counterparts, primarily due to the electron-donating nature of the sulfur groups. The quaternized complexes (**6e** and **8e**) are blue-shifted compared to the corresponding unquaternized derivatives (**6d** and **8d**), due to the lowering of the electron-donating ability of the nitrogen groups on quaternization. The infrared and UV-visible spectra of **5g**, **7a**, and **10a** suggest that the COOH groups do have some effect on the properties of the Pc.

Two metal based redox processes ($M^{III}Pc^{-2}/M^{II}Pc^{-2}$ and $M^{II}Pc^{-2}/M^{I}Pc^{-2}$) were observed for **9b** and **10b**. Complex **9b** displayed four ring redox processes, whilst three such processes were obtained for complex **10b**. The potentials for first reduction of complexes **9b** and **10b** are much less negative than those of other thio substituted CoPc and FePc complexes. This suggests that the phenylthiol substituents confer ease of reduction on the CoPc and FePc species. Each of the MnPc complexes **6d**, **6e**, **8d**, and **8e** displayed three redox processes, two of which are metal based. This work reports the formation of a Mn(I)Pc species from the first reduction of $Mn^{II}Pc^{-2}$, depending on the nature of the substituents for the MnTMPyPc complexes.

For the first time, the coordination of a metallophthalocyanine (**7a**) to an electrode pre-modified with aryl radicals is reported in this work. The electrode is named **GCE-4**. The modification technique has the advantage that a stable electrode was formed with a readily available MPc complex, CoPc(COOH)₄ in this study, without the need for a complicated and lengthy synthesis.

221

Chapter 8: General conclusions

Of all of the analytes in this work, **GCE-4** could only detect thiocyanate at a potential and limit of detection comparable to that of published works. Also, because **GCE-4** can reliably detect thiocyanate in the mM range it can be used as a sensor in this range. A mechanism for the interaction of thiocyanate with the $CoPc(COOH)_4$ of **GCE-4** has been proposed based on UV-visible spectral observations, kinetics, and electrochemical behaviour.

The catalytic activity of the CoPc complexes is highly dependent on the substituent and hence this work compares the catalytic activity of cobalt phthalocyanine (CoPc, **5g**) with those of cobalt tetracarboxy phthalocyanine ($CoPc(COOH)_4$, **7a**) and cobalt octacarboxy phthalocyanine ($CoPc(COOH)_8$, **10a**), when adsorbed onto glassy carbon electrodes, for the electrocatalytic detection of nitrite, L-cysteine, and melatonin (the electrodes cannot detect thiocyanate). Electrodes modified with CoPc derivatives showed larger nitrite oxidation peaks at much lower oxidation potentials than with an un-modified GCE. CoPc and $CoPc(COOH)_4$ modified electrodes displayed nitrite oxidation at lowest potentials, but $CoPc(COOH)_8$ gave a slightly higher current response. $CoPc(COOH)_4$ had higher surface coverage but did not show larger nitrite oxidation currents. This shows that the number of ring substituents does affect the potential of nitrite oxidation. Good limits of detection of nitrite (10^{-7} M region) were obtained for all modified electrodes. From UV-visible spectral studies, addition of nitrite to CoPc and $CoPc(COOH)_8$ showed axial ligation of the MPc complexes, but for $CoPc(COOH)_4$ there was evidence of aggregation which may explain the unfavourable limits of detection obtained for the $CoPc(COOH)_4$ GCE. A mechanism for catalysis of nitrite oxidation using CoPc and $CoPc(COOH)_8$ has been proposed.

All of the electrodes adsorbed with the CoPc derivatives could detect L-cysteine, whereas an un-modified electrode could not. The limits of L-cysteine detection by the modified electrodes are in the 10^{-7} M region. The stability of the electrodes in detecting L-cysteine decreased with an increasing number of substituents on the CoPc, which indicates that the bulkiness of the substituents disturbs the stability. A mechanism for the catalysis of L-cysteine oxidation using CoPc and $CoPc(COOH)_8$ has been proposed.

The electrochemical detection of melatonin has not been extensively studied and this work presents for the first time the electrochemical detection of melatonin using electrodes with

Chapter 8: General conclusions

adsorbed MPcs. These modified electrodes detected melatonin at higher peak currents and lower peak potentials than an un-modified gold electrode. The limits of melatonin detection of the modified electrodes lay in the 10^{-7} to 10^{-6} M region. Electrode modification with specific CoPcs was shown to improve the long-term stability of the GCE for the detection of melatonin. A mechanism for the oxidation of melatonin by the CoPc derivatives was proposed in which: the axial ligation of the MPc complexes to melatonin occurs; the first one electron transfer is rate determining; and the total number of electrons transferred is two. The modified electrodes accurately measured the contents of capsule melatonin concentrations as specified by the supplier. With respect to biological sensing, all modified electrodes could differentiate between a mixture of melatonin, tryptophan, and ascorbic acid.

All modified electrodes of this work can reliably detect nitrite, L-cysteine, and melatonin in the 10^{-4} to 10^{-2} M region.

MPc complexes substituted with thio groups were used to form self assembled monolayers (SAMs). Voltammetry, impedance measurements, atomic force microscopy, and scanning electrochemical microscopy proved that all of the SAMs are well packed and act as selective and efficient barriers to ion permeability. Furthermore, surface coverage studies confirmed that the MPc macrocycles adsorb onto the gold electrode as monolayers. All of the MPc SAMs were successfully used as electrochemical sensors of nitrite and L-cysteine (thiocyanate and melatonin cannot be detected by these electrodes). The MPc SAMs showed larger nitrite oxidation peaks at much lower oxidation potentials than with an un-modified gold electrode. All MPc SAMs displayed linear relationships between the peak current and the nitrite ion concentration with the MnPcs doing so in a wider range than the $FePc(SCH_2Ph)_8$ and $CoPc(SCH_2Ph)_8$ SAMs. Nitrite sensitivities of all of the SAMs of this work are in the $mA.M^{-1}$ range. The MnPc SAMs displayed much better limits of detection of nitrite than the $FePc(SCH_2Ph)_8$ and $CoPc(SCH_2Ph)_8$ SAMs. All of the SAMs of this work showed good stability in analyzing nitrite solutions. Two electrons are involved in the electro-oxidation of nitrite by the MnPc SAMs. This value contrasts with the involvement of one electron for the $FePc(SCH_2Ph)_8$ and $CoPc(SCH_2Ph)_8$ SAMs. The $M^{III}Pc/M^{II}Pc$ process is possibly involved for the $FePc(SCH_2Ph)_8$ and the $CoPc(SCH_2Ph)_8$ SAMs whilst the $M^{IV}Pc/M^{III}Pc$ process may be involved for the MnPcs. Further studies are needed to

Chapter 8: General conclusions

verify this. A mechanism for the interaction of nitrite with the MPc SAMs has been proposed based on UV-visible spectral observations, kinetics, and electrochemical behaviour.

All of the SAM gold modified electrodes in this work can detect L-cysteine, whereas an unmodified gold electrode cannot. Linear relationships between the peak current and the L-cysteine concentration (10^{-4} - 10^{-2} M range) were obtained for all of the MPc SAMs. L-cysteine sensitivities of all of the SAMs of this work are in the mA.M^{-1} range. The MnPc SAMs displayed better limits of detection for L-cysteine than the FePc(SCH$_2$Ph)$_8$ and CoPc(SCH$_2$Ph)$_8$ SAMs. All of the SAMs of this work showed good stability in analyzing L-cysteine solutions, with MnPc SAMs being the best in this respect. UV-visible spectral observations, kinetics, and electrochemical behaviour studies enabled a mechanism to be proposed for the interaction of the MPcs with L-cysteine.

The manganese phthalocyanines **6c**, **6d**, **6e**, **8b**, **8d**, **8e**, and **8f** were used as superoxide dismutase (SOD) mimics for the dismutation of the superoxide radicals (O$_2$$^{\bullet-}$). Their performance was assessed using cyclic voltammetry, UV-visible spectrophotometry and fluorescence. The electrochemical analysis of the MnPcs allowed fine tuning of the redox potential of the Mn^{III}/Mn^{II} couple which is involved in the dismutation process. The behaviour of the MPcs as SOD mimics was evaluated using the O$_2$$^{\bullet-}$ produced from the xanthine-xanthine oxidase reaction, using cytochrome c and UV-visible spectrophometry (McCord-Fridovich assay). All of the manganese phthalocyanine complexes were fond not to interfere with the xanthine-xanthine oxidase reaction and hence efficiently dismutated O$_2$$^{\bullet-}$ with apparent overall catalytic rate constant values ranging from log k_{cat} = 7.81 to 6.62 and improved IC50 values (0.04 to 0.68 μM) compared to one commercially available Mn porphyrin based SOD mimic (manganese (III) tetrakis (1-methyl-4-pyridyl)porphyrin, **38**: k_{cat} = 6.53; IC50 = 0.677). DMSO-treated HL60 cells (human leukemia cells) were used as a model of O$_2$$^{\bullet-}$ production, either extracellular production with phorbol 12-myristate 13-acetate (PMA) stimulation or intracellular production without PMA stimulation. With these models, analysis of dihydroethidium fluorescence for the detection of superoxide production showed that the MnPcs examined acted as proficient superoxide dismutase mimics. The results obtained also showed that four of these MnPcs (**6d**, **6e**, **8d**, **8e**)

can infiltrate cells. Future evaluation of these complexes in cell-based and/or animal experimental protocols as antioxidant drugs can therefore be confidently done.

REFERENCES

1. A. G. Dandridge, S. W. Dunworth, H. A. E. Drescher, A. L. Thomas, Great Britain Patent 322169, ICI (1928).

2. R. P. Linstead, J. Chem. Soc. (1934) 1016.

3. G. T. Byrne, R. P. Linstead, A. R. Lowe, J. Chem. Soc. (1934) 1017.

4. R. P. Linstead, A. R. Lowe, J. Chem. Soc. (1934) 1022.

5. C. E. Dent, R. P. Linstead, J. Chem. Soc. (1934) 1027.

6. R. P. Linstead, A. R. Lowe, J. Chem. Soc. (1934) 1031.

7. C. E. Dent, R. P. Linstead, A. R. Lowe, J. Chem. Soc. (1934) 1033.

8. J. M. Robertson, J. Chem. Soc. (1935) 615.

9. J. M. Robertson, J. Chem. Soc. (1936) 1195.

10. J. M. Robertson, J. Chem. Soc. (1936) 1736.

11. J. M. Robertson, J. Chem. Soc. (1937) 219.

12. J. M. Robertson, J. Chem. Soc. (1940) 36.

13. R. P. Linstead, E. G. Noble, J. M. Wright, J. Chem. Soc. (1937) 911.

14. M. Durmuş, T. Nyokong, Tetrahedron 63 (2007) 1385.

15. C. C. Leznoff, A. B. P. Lever (eds.), Phthalocyanines: Properties and Applications, Vol. 2, VCH Publishers, Inc., Weinheim: New York, 1993.

16. M. J. Stillman, T. Nyokong, Phthalocyanines: Properties and Applications, C. C. Leznoff, A. B. P. Lever (eds.), Vol. 1. VCH Publishers, Inc., Weinheim: New York, 1989.

17. D. Dini, M. Hanack, The Porphyrin Handbook, Phthalocyanines: properties and materials, Vol. 17, K. M. Kadish, K. M. Smith, R. Guilard (eds.). Elsevier Science: Netherlands, 2003.

18. K. Ishii, N. Kobayashi, The Porphyrin Handbook, Phthalocyanines: Spectroscopic and Electrochemical Characterisation, Vol. 16, K. M. Kadish, K. M. Smith, R. Guilard (eds). Elsevier Science: Netherlands, 2003.

19. R. J. Jasinski, J. Electrochem. Soc. 112 (1965) 526.

20. R. J. Jasinski, Nature 201 (1964) 1212.

References

21. J. H. Zagal, Coord. Chem. Rev. 119 (1992) 89.

22. J. Obirai, T Nyokong, Electrochim. Acta 49 (2004) 1417.

23. K. Ozoemena, T. Nyokong, P. Westbroek, Electroanalysis 15 (2003) 1762.

24. B. Agboola, T. Nyokong, Talanta 72 (2007) 691.

25. S. A. Mikhalenko, L. I. Solov'eva, E. A. Luk'yanets, Russian J. Gen. Chem. 74 (2004) 451.

26. K. Sakamoto, E. Ohno, Prog. Org. Coat. 31 (1997) 139.

27. B. Agboola, K. I. Ozoemena, P. Westbroek, T. Nyokong, Electrochim. Acta 52 (2007) 2520.

28. S. Khene, A. Ogunsipe, E. Antunes, T. Nyokong, J. Porphyrins Phthalocyanines 11 (2007) 109.

29. J. H. Weber, D. H. Busch, Inorg. Chem. 4 (1965) 469.

30. P. Tau, T. Nyokong, Dalton Trans. 37 (2006) 4482.

31. N. Sehlotho, M. Durmuş, V. Ahsen, T. Nyokong, Inorg. Chem. Commun. 11 (2008) 479.

32. B. Agboola, T. Nyokong, Anal. Chim. Acta 587 (2007) 116.

33. K. Ozoemena, P. Westbroek, T. Nyokong, Electrochim. Acta 47 (2002) 4035.

34. K. Ozoemena, P. Westbroek, T. Nyokong, Electrochem. Commun. 3 (2001) 529.

35. G. Mbambisa, P. Tau, E. Antunes, T. Nyokong, Polyhedron 26 (2007) 5355.

36. K. Takahashi, M. Kawashima, Y. Tomita, M. Itoh, Inorg. Chim. Acta. 232 (1995) 69.

37. A. R. Özkaya, A. G. Gürek, A. Gül, Ö. Bekaroglu, Polyhedron 16 (1997) 1877.

38. I. Fridovich, J. Exp. Biol. 201 (1998) 1203.

39. I. Fridovich, Science 201 (1978) 875.

40. R. H. Felton, H. Linschitz, J. Am. Chem. Soc. 87 (1965) 4238.

41. N. McKeown, Phthalocyanine Materials: Synthesis, Structure and Function. Cambridge University Press: Cambridge, 1998.

42. N. McKeown, Chem. Ind. (London) 3 (1999) 92.

43. P. Gregory, J. Porphyrins Phthalocyanines 3 (1999) 468.

44. P. Gregory, J. Porphyrins Phthalocyanines 4 (2000) 432.

45. J. D. Spikes, Photochem. Photobiol. 43 (1986) 691.

References

46. J. R. Darwent, P. Douglas, A. Harriman, G. Porter, M. C. Richoux, Coord. Chem. Rev. 44 (1982) 83.

47. T. A. Temfonte, K. F. Schoch, J. Appl. Phys. 65 (1988) 1350.

48. B. D. Berezin, Coordination compounds of porphyrins and phthalocyanines, John Wiley and Sons Ltd.: New York, 1981.

49. G. Booth, The Chemistry of Synthetic Dyes, K. Venkataraman (ed.). Academic Press: New York, 1971.

50. A. B. P. Lever, Adv. Inorg. Radiochem. 27 (1965) 27.

51. M. Brewis, G. J. Clarkson, P. Humberstone, S. Makhseed, B. N. McKeown, Chem. Eur. J. 4 (1998) 1633.

52. B. N. McKeown, I. Chambrier, M. J. Cook, J. Chem. Soc., Perkin Trans. 1 (1990) 1169.

53. F. Baumann, B. Bienert, G. Rösch, H. Vollmann, W. Wolf, Agnew. Chem. 68 (1956) 133.

54. G. Pawlowski, M. Hanack, Synthesis (1980) 287.

55. M. Sommerauer, C. Rager, M. Hanack, J. Am. Chem. Soc. 118 (1996) 10085.

56. L. G. Tomilova, E. V. Chernykh, T. T. Ioffe, E. A. Luk'yanets, Zh. Obshch. Khim. 53 (1983) 2594; J. Gen. Chem. USSR (Engl. Transl.) 53 (1983) 2339.

57. P. A. Barrett, C. E. Dent, R. P. Linstead, J. Chem. Soc. (1936) 1719.

58. J. A. Thompson, K. Murata, C. D. Miller, J. L. Stanton, W. E. Broderick, B. M. Hoffman, J. A. Ibers, Inorg. Chem. 32 (1993) 3546.

59. I. Gürol, V. Ahsen, Ö. Bekaroglu, J. Chem. Soc., Dalton Trans. (1994) 497.

60. C. C. Leznoff, A. B. P. Lever, (eds.) Phthalocyanines: Properties and Applications, Vol. 1, VCH Publishers, Inc., Weinheim, New York, 1989.

61. H. Tomoda, S. Saito, S. Shiraishi, Chem. Lett. (1983) 313.

62. K.-W. Poon, Y. Yan, X. Y. Li, D. K. P. Ng, Organometallics 18 (1999) 3528.

63. A. H. Jackson, The Porphyrins, Vol. 1, D. Dolphin (ed.). Academic press: New York, 1977.

64. D. Wöhrle, G. Schrnurpfeil, G. Knothe, Dyes Pigm. 18 (1992) 91.

65. A. Kempa, J. Dobrowolski, Can. J. Chem. 66 (1988) 2553.

228

References

66. A. Shaabani, J. Chem. Res., Synop. 10 (1998) 672.

67. S. A. Mikhalenko, E. A. Luk'yanets, Zh. Obshch. Khim. 39 (1969) 2129; J. Gen. Chem. USSR (Engl. Transl.) 39 (1969) 2801.

68. J. Metz, O. Schneider, M. Hanack, Inorg. Chem. 23 (1984) 1065.

69. D. Wöhrle, M. Eskes, K. Shigehara, A. Yamada, Synthesis (1993) 194.

70. J. Silver, P. J. Lukes, P. K. Hey, J. M. O'Connor, Polyhedron 8 (1989) 1631.

71. M. Hanack, P. Vermehren, Chem. Ber. 124 (1991) 1733.

72. P. A. Barrett, D. A. Frye, R. P. Linstead, J. Chem. Soc. (1938) 1157.

73. M. A. Mohammad, P. Ottenbreit, W. Prass, G. Schnurpfeil, D. Wöhrle, Thin Solid Films 213 (1992) 285.

74. F. Henari, A. Davey, W. Blau, P. Haisch, M. Hanack, J. Porpyrins Phthalocyanines 3 (1999) 331.

75. H. Ali, R. Langlois, J. R. Wagner, N. Brasseur, B. Paquette, J. E. van Lier, Photochem. Photobiol. 47 (1988) 713.

76. R. D. George, A. W. Snow, J. Heterocyclic Chem. 32 (1995) 495.

77. N. Kornblum, L. Cheng, R. C. Kerber, M. M. Kestner, B. N. Newton, H. W. Pinnick, R. G. Smith, P. A. Wade, J. Org. Chem. 41 (1976) 1560.

78. J. R. Beck, J. Org. Chem. 37 (1972) 3224.

79. V. M. Vlasov, Russ. Chem. Rev. 72 (2003) 681.

80. J. G. Young, W. Onyebuagu, J. Org. Chem. 55 (1990) 2155.

81. A. Beck, K.-M. Mangold, M. Hanack, Chem. Ber. 124 (1991) 2315.

82. W. Eberhardt, M. Hanack, Synthesis (1995) 95.

83. C. C. Leznoff, S. M. Maruccio, S. Greenberg, A. B. P. Lever, K. B. Tomer, Can. J. Chem. 63 (1985) 623.

84. G. J. Clarkson, N. B. McKeown, K. E. Treacher, J. Chem. Soc., Perkin Trans. 1 (1995) 1817.

85. A. Tomoda, S. Saito, S. Shiraishi, Chem. Lett. (1980) 1277.

86. T. W. B. Healy, C. T. Ewins, J. Porphyrins Phthalocyanines 3 (1999) 522.

References

87. J. Mack, M. J. Stillman, The Porphyrin Handbook, Phthalocyanines: Spectroscopic and Electrochemical Characterisation, Vol. 16, K. M. Kadish, K. M. Smith, R. Guilard (eds.). Elsevier Science: Netherlands, 2003.

88. S. Khene, D. A. Geraldo, C. A. Togo, J. Limson, T. Nyokong, Electrochim. Acta 54 (2008) 183.

89. T. Nyokong, H. Isago, J. Porphyrins Phthalocyanines 8 (2004) 1083.

90. N. Kobayashi, J. Chem. Soc., Chem. Commun. (1991) 1203.

91. A. Meller, A. Ossko, Monatsh. Chem. 105 (1974) 405.

92. S. Liu, X. Jiang, G. Zhuo, New J. Chem. 31 (2007) 916.

93. A. K. Sobbi, D. Woehrle, D. Schlettwein, J. Chem. Soc. Perkin Trans. 2 (1993) 481.

94. N. A. Wiederkehr, Eclet. Quím. 24 (1999) 45.

95. R. D. George, A. W. Snow, J. S. Shirk, W. R. Barger, J. Porphyrins Phthalocyanines 2 (1998) 1.

96. M. J. Cook, J. McMurdo, D. A. Miles, R. H. Poynter, J. Mater. Chem. 4 (1994) 1205.

97. M. P. Somashekarappa, J. Keshavayya, Synth. React. Inorg. Met.-Org. Chem. 31 (2001) 811.

98. S. Dabak, G. Gumus, A. Gul, O. Bekaroglu, J. Coord. Chem. 38 (1996) 287.

99. M. J. Stillman, A. J. Thomson, Chem. Soc. Faraday Trans. II 70 (1974) 805.

100. A. B. P. Lever, M. R. Hempstead, C. C. Leznoff, W. Liu, M. Melnik, W. A. Nevin, P. Seymour, Pure Appl. Chem. 58 (1986) 1467.

101. K. Kasuga, M. Tsutsui, Coord. Chem. Rev. 32 (1980) 67.

102. R. Weiss, J. Fischer, The Porphyrin Handbook, Phthalocyanines: Spectroscopic and Electrochemical Characterisation, Vol. 16, K. M. Kadish, K. M. Smith, R. Guilard (eds.). Elsevier Science: Netherlands, 2003.

103. A. O. Ogunsipe, D. M. Maree, T. Nyokong, J. Mol. Struct. 650 (2003) 131.

104. W. F. Law, K. M. Lui, D. K. P. Ng, J. Mater. Chem. 7 (1997) 2063.

105. O. V. Dolotova, N. I. Bundina, O. L. Kaliya, E. A. Lukyanets, J. Porphyrins Phthalocyanines 1 (1997) 355.

106. J. Wang, Analytical Electrochemistry. VCH Publishers, Inc: USA, 1994.

References

107. C. M. A. Brett, A. M. O. Brett, Electrochemistry: Principles, Methods and Applications. Oxford University Press: USA, 1993.

108. D. B. Hibbert, Introduction to Electrochemistry. Macmillan: London, 1993.

109. Southampton Electrochemistry Group (R. Greef, R. Peat, L. M. Peter, D. Pletcher, J. Robinson), Instrumental methods in electrochemistry, (1985) Southampton Electrochemistry Group/ Ellis Horwood Limited, England.

110. R. G. Gale (ed.), Spectroelectrochemistry, Theory and practice. Plenum: New York, 1988.

111. C. Gutiérrez, C. Melendres (eds.), NATO ASI Series, Ser. C: Mathematical and Physical Sciences 320 (1990) 481.

112. P. A. Christensen, A. Hammnett, Techniques and mechanisms in electrochemistry. Blackie: Glasgow, 1994.

113. W. Plieth, G. S. Wilson, C. de la Fe, Pure Appl. Chem. 70 (1998) 1395.

114. B. Beden, Mater. Sci. Forum 192-4 (1995) 277.

115. P. Monk, Fundamentals of electroanalytical chemistry. John Wiley & Sons: Manchester, 2001.

116. Y.-H. Tse, A. Goel, M. Hu, C. C. Leznoff, J. E. Van Lier, A. B. P. Lever, Can. J. Chem. 71 (1993) 742.

117. Z. Jin, K. Nolan, C. R. McArthur, C. C. Leznoff, A. B. P. Lever, J. Organomet. Chem. 468 (1994) 205.

118. H. Isago, C. C. Leznoff, M. F. Ryan, R. A. Metcalfe, R. Davids, A. B. P. Lever, Bull. Chem. Soc. Jpn. 71 (1998) 1039.

119. N. Kobayashi, H. Lam, W. A. Nevin, P. Janda, C. C. Leznoff, A. B. P. Lever, Inorg. Chem. 29 (1990) 3415.

120. N. Nombona, T. Nyokong, Dyes Pigm. 80 (2009) 130.

121. A. B. P. Lever, E. R. Milaeva, G. Speier, Phthalocyanines: Properties and Applications, Vol. 3, C. C. Leznoff, A. B. P. Lever, (eds.). VCH Publishers, Inc., Weinheim: New York, 1993.

122. S. Fukuzumi, The Porphyrin Handbook, Vol. 8, K. M. Kadish, K. Smith, R. Guilard (eds.). Academic Press: San Diego, 2000.

References

123. M. L'her, A. Pondaven, The Porphyrin Handbook, Phthalocyanines: spectroscopic and electrochemical characterisation, Vol. 16, K. M. Kadish, K. M. Smith, R. Guilard (eds.). Elsevier Science: Netherlands, 2003.

124. C. Weiss, H. Kobayashi, M. Gouterman, J. Mol. Spectrosc. 16 (1965) 415.

125. M. Gouterman, G. H. Wagniere, L. C. Snyder, J. Mol. Spectrosc. 11 (1963) 2.

126. A. McHugh, M. Gouterman, J. Weiss, Theor. Chim. Acta 24 (1972) 346.

127. A. Henriksson, M. Sunborn, Theor. Chim. Acta 27 (1972) 213.

128. J. F. Myers, G. W. Rayner Canham, A. B. P. Lever, Inorg. Chem. 14 (1975) 461.

129. A. B. P. Lever, J. P. Wilshire, Inorg. Chem. 54 (1978) 1145.

130. A. B. P. Lever, P. C. Minor, J. P. Wilshire, Inorg. Chem. 20 (1981) 2550.

131. E. Bald, E. Anioska, G. Chatko, R. Glowacki, Talanta 50 (2000) 1233.

132. D. L. Pilloud, X. Chen, P. L. Dutton, C. C. Moser, J. Phys. Chem. B 104 (2000) 2868.

133. K. Ozoemena, P. Wesbroek, T. Nyokong, J. Porphyrins Phthalocyanines 6 (2002) 98.

134. S. Steinberg, Y. Tor, E. Sabatani, I. Rubenstein, J. Am. Chem. Soc. 113 (1991) 5176.

135. P. Vasudevan, N. Phougat, A. K. Shukla, Appl. Organometal. Chem. 10 (1996) 591.

136. N. Kobayashi, W. A. Nevin, Appl. Organometal. Chem. 10 (1996) 579.

137. S. Zecevic, B. Simic-Glavaski, E. Yeager, A. B. P. Lever, P. C. Minor, J. Electroanal. Chem. 196 (1985) 339.

138. R. W. Murray, A. G. Ewing, R. A. Durst. Anal. Chem. 59 (1987) 379A.

139. J. Zak, T. Kuwana, J. Electroanal. Chem. 150 (1983) 645.

140. R. P. Baldwin, K. N. Thomsen, Talanta 38 (1991) 1.

141. J. P. Collman, P. Denisevich, Y. Konai, M. Morocco, C. Koval, F. C. Anson, J. Am. Chem. Soc. 102 (1980) 6027.

142. E. Steckhan, T. Kuwana, Ber. Bunsenges. Phys. Chem. 78 (1974) 253.

143. S. L. Vilakazi, T. Nyokong, J. Electroanal. Chem. 512 (2001) 56.

144. M. Gulppi, S. Griveau, F. Bedioui, J. H. Zagal, Electrochim. Acta 46 (2001) 3397.

145. H. Aga, A. Aramata, Y. Hisaeda, J. Electroanal. Chem. 437 (1997) 111.

146. R. L. McCreery, Carbon Electrodes: Structural Effects on Electron Transfer Kinetics in Electroanalytical Chemistry, Vol. 18, A. J. Bard (ed.) Marcel Dekker: New York, 1991.

References

147. T. Shigemitsu, G. Matsumoto, Med. and Biol. Eng. and Comput. 17 (1979) 465.

148. G. M. Jenkins, K. Kawamura, L. Ban, Proc. Roy. Soc. A 327 (1972) 501.

149. G. M. Jenkins, K. Kawamura, Polymeric Carbons. Cambridge University Press: Cambridge, 1976.

150. G. M. Jenkins, Physics and Chemistry of carbon, Vol. 11, P. L. Walker (ed.). Dekker: New York, 1973.

151. P. Westbroek, G. Priniotakis, P. Kiekens, Analytical electrochemistry in textiles. Woodhead Publishing Limited: England, 2005.

152. T. Malinski, Z. Taha, Nature 358 (1992) 676.

153. S. Mesaros, S. Grunfeld, A. Mesarosova, D. Bustin, T. Malinski, Anal. Chim. Acta. 339 (1997) 265.

154. F. D'Souza, Y.-Y. Hsieh, H. Wickman, W. Kutner, Chem. Commun. (1997) 1191.

155. M. Biesaga, K. Pyrzynska, M. Trojanowicz, Talanta 51 (2000) 209.

156. Y. Ein-Eli, S. F. Mcdevitt, D. Aurbach, B. A. Markovsky, A. Schechter, J. Electrochem. Soc. 144 (1997) L180.

157. G.-J.Yang, J.-J. Xu, K. Wang, H.-Y. Chen, Electroanalysis 18 (2006) 282.

158. S. Radhakrishnan, S. D. Deshpande, Mater. Lett. 48 (2001) 144.

159. G. Milczarek, A. Ciszewski, Electroanalysis 17 (2005) 371.

160. J. Zagal, P. Herrera, Electrochim. Acta 30 (1985) 449.

161. M. J. Aquirre, M. Isaacs, F. Armijo, L. Basáez, J. Zagal, Electroanalysis 14 (2002) 356.

162. M. J. Cook, Pure Appl. Chem. 71 (1999) 2145.

163. J. Zhang, A. B. P. Lever, W. J. Pietro, Can. J. Chem. 73 (1995) 1072.

164. T. V. Magdesieva, T. Yamamoto, D. A. Tryk, A. Fujishima, J. Electrochem. Soc. 149 (2002) D89.

165. J. Zagal, J. Electroanal. Chem. 109 (1980) 389.

166. B. Filanovsky, Anal. Chim. Acta 394 (1999) 91.

167. S. Griveau, J. Pavez, F. Bedioui, J. Electroanal. Chem. 497 (2001) 75.

168. P. Janda, J. Weber, L. Dunsch, A. B. P. Lever, Anal. Chem. 68 (1996) 960.

169. I. Chambrier, M. J. Cook, D. A. Russell, Synthesis (1995) 1283.

References

170. M. P. Somashekarappa, J. Keshavayya, S. Sampath, Pure Appl. Chem. 74 (2002) 1609.

171. M. P. Somashekarappa, S. Sampath, Chem. Comm. (2002) 1262.

172. D. J. Revell, I. Chambrier, M. J. Cook, D. A. Russell, J. Mater. Chem. 10 (2000) 31.

173. S. Nitahara, N. Terasaki, T. Akiyama, S. Yamada, Thin Solid Films 499 (2006) 354.

174. M. A. Meineke, J. D. Gezelter, J. Phys. Chem. B 105 (2001) 6515.

175. D. Xie, Y. Jiang, J. Jiang, Z. Wu, Y. Li, Sensor. Actuator B: Chem. 77 (2001) 260.

176. D. T. Sawyer, J. L. Roberts, Experimental electrochemistry for chemists. Wiley-Interscience: New York, 1974.

177. R. C. Engstrom, Anal. Chem. 56 (1984) 890.

178. F. Patolsky, G. Tao, E. Katz, I. Willner, J. Electroanal. Chem. 454 (1998) 9.

179. J. Obirai, N. Pereira-Rodrigues, F. Bedioui, T. Nyokong, J. Porphyrins Phthalocyanines 7 (2003) 508.

180. N. Tromach, O. Hild, D. Schlettwein, D. Wöhrle, J. Mat. Chem. 12 (2002) 879.

181. R. W. Murray, Electroanal. Chem. 13 (1984) 191.

182. A. W. C. Lin, P. Yeh, A. M. Yacynych, T. Kuwana, J. Electroanal. Chem. 84 (1977) 411.

183. M. Noel, P. N. Anantharaman, Surf. Coat. Tech. 28 (1986) 161.

184. M. L. Bowers, B. A. Yenser, Anal. Chim. Acta 43 (1991) 243.

185. E. Fitzer, K. H. Geigl, W. Heitner, R. Weiss, Carbon 18 (1987) 389.

186. W. P. Hoffman, W. C. Curley, T. W. Owens, H. T. Phan, J. Mater. Sci. 26 (1991) 4545.

187. E. Fitzer, R. Weiss, Carbon 25 (1987) 455.

188. M. Delamar, R. Hitmi, J. Pinson, J. M. Savéant, J. Am. Chem. Soc. 114 (1992) 5883.

189. C. Bourdillion, M. Delamar, C. Demaille, R. Hitmi, J. Moiroux, J. Pinson, J. Electroanal. Chem. 336 (1992) 113.

190. P. Allongue, M. Delamar, B. Desbat, O. Fagebaume, R. Hitmi, J. Pinson, J.-M. Savéant, J. Am. Chem. Soc. 119 (1997) 201.

191. C. P. Andrieux, J. Pinson, J. Am. Chem. Soc. 125 (2003) 14801.

192. P. A. Brooksby, A. J. Downard, Langmuir 20 (2004) 5038.

References

193. S. Baranton, D. Bélanger, J. Phys. Chem. B 109 (2005) 24401.

194. A. J. Downard, Electroanalysis 12 (2000) 1085.

195. J. Pinson, F. Podvorica, Chem. Soc. Rev. 34 (2005) 429.

196. M. J. Weaver, F. C. Anson, J. Electroanal. Chem. 65 (1975) 711.

197. A. J. Appleby, M. Savy, Electrochim. Acta 21 (1976) 567.

198. A. J. Appleby, M. Savy, Electrochim. Acta 22 (1977) 1315.

199. L. Kreja, A. Plewka, Electrochim. Acta 27 (1982) 251.

200. A. A. Tanaka, C. Fierro, D. Scherson, E. B. Yeager, J. Phys. Chem. 91 (1987) 3799.

201. H. Yamada, H. Imohari, Y. Nishimura, I. Yamazaki, T. K. Ahn, S. K. Kim, D. Kim, S. Fukuzumi, J. Am. Chem. Soc.125 (2003) 9129.

202. Z. Li, M. Leiberman, Inorg. Chem. 40 (2001) 932.

203. H. O. Finklea, Encyclopedia of Analytical Chemistry: Applications, Theory and Instrumentations, R. A. Meyers (ed.). Wiley: New York, 2000.

204. M. Lackinger, T. Mweller, T. G. Gopakumar, F. Mueller, F. Heitschold, G. W. Flynn, J. Phys. Chem. B 108 (2004) 2279.

205. P. N. Mashazi, K. I. Ozoemena, D. M. Maree, T. Nyokong, Electrochim. Acta 51 (2006) 3489.

206. G. Kalyuzhny, A. Vaskevich, G. Ashkenaasy, A. Shanzer, I. Rubinstein, J. Phys. Chem. B 104 (2000) 8238.

207. E. Solomon, T. Angot, N. Papageorgioi, J. M. Layet, Surface Sci. 596 (2005) 74.

208. K. Ozoemena, T. Nyokong, Michrochem. J. 75 (2003) 241.

209. Z. Li, M. Lieberman, Supramol. Sci. 5 (1998) 485.

210. T. Akiyama, S. Nitahara, S. Inoue, S. Yamada, Photochem. Photobiol. Sci. 3 (2004) 26.

211. H. O. Finklea, Electroanalytical Chemistry, Vol. 13, A. J. Bard, I. Rubenstein (eds.). Marcel Dekker: New York, 1996.

212. E. Katz, D. D. Schlereth, H.-L. Schmidt, J. Electroanal. Chem. 367 (1994) 59.

213. H. A. Biebuyck, C. D. Bain, G. M. Whitesides, Langmuir 10 (1994) 1825.

214. C. E. D. Chidsey, Science 251 (1991) 919.

215. W. Yang, J. J. Gooding, D. B. Hibbert, J. Electroanal. Chem. 516 (2001) 10.

References

216. I. Willner, R. Blonder, A. Dagan, J. Am. Chem. Soc. 115 (1994) 4935.

217. G. Che, Z. Li, H. Zhang, C. R. Cabrera, J. Electroanal. Chem. 453 (1998) 9.

218. H. O. Finklea, Electroanalytical Chemistry, Vol. 3, A. J. Bard, I. Rubenstein (eds.). Marcel Dekker: New York, 1996.

219. E. Sabatani, I. Rubinstein, J. Phys. Chem. 91 (1987) 6663.

220. Z. Li, M. Lieberman, Fundamental Aspects of Chemically Modified Surfaces, J. P. Blitz, C. B. Little (eds.). Royal Soc. Chem. Lettchworth: UK, 1999.

221. Z. Li, M. Lieberman, W. Hill, Langmuir 17 (2001) 4887.

222. D. D. Macdonald, Electrochim. Acta 51 (2006) 1376.

223. J. R. Macdonald, W. B. Johnson, Impedance Spectroscopy Theory, Experiment, and Applications, 2nd edition, E. Barsoukov, J. R. Macdonald (eds.). Wiley-Interscience: USA, 2005.

224. A. J. Bard, M. Stratmann (eds.), Encyclopedia of Electrochemistry, Vol. 3, P. R. Unwin (ed). WILEY-VCH Verlag GmbH & Co. KGaA: Weinheim, 2003.

225. R. P. Janek, W. R. Fawcett, Langmuir 14 (1998) 3011.

226. J. E. B. Randles, Disc. Faraday Soc. 1 (1947) 11.

227. E. Sabatani, J. Cohen-Boulakia, M. Bruening, I. Rubinstein, Langmuir 9 (1993) 2974.

228. R. Ehret, W. Baumann, M. Brischwein, A. Schwinde, K. Stegbauer, B. Wolf, Biosens. Bioelectron. 1 (1997) 29.

229. M. M. Musiani, Electochim. Acta 35 (1990) 1665.

230. P. Delahay, Double Layer and Electrode Kinetics. Interscience Publisher and John Wiley & Sons: New York, 1965.

231. W. R. Fawcett, M. Opallo, Agnew. Chem., Int. Ed. Engl. 33 (1994) 2131.

232. C. J. Miller, P. Cuendet, M. Gatzel, J. Phys. Chem. 95 (1991) 877.

233. H. O. Finklea, D. A. Snider, J. Fedyk, Langmuir 9 (1993) 3660.

234. J. E. B. Randles, Trans. Faraday Soc. 48 (1952) 828.

235. C. Saby, B. Ortiz, G. Y. Champagne, D. Belanger, Langmuir 13 (1997) 6805.

236. P. N. Mashazi, K. I. Ozoemena, T. Nyokong, Electrochim. Acta 52 (2006) 177.

References

237. A. Lasia, Electrochemical Impedance Spectroscopy and its Applications in Modern Aspects of Electrochemistry, Vol. 32, B. E. Conway, J. Brockris, R. E. White (eds.). Kluwer Academic/Plenum Publishers: New York, 1999.

238. I. D. Raistrick, D. R. Franceschetti, J. R. Macdonald, Impedance Spectroscopy Theory, Experiment, and Applications, 2nd Edition, E. Barsoukov, J. R. Macdonald (eds.). Wiley-Interscience: USA, 2005.

239. G. Binnig, H. Rohrer, Ch. Gerber, E. Weibel, Phys. Rev. Lett. 49 (1982) 57.

240. G. Binnig, C. F. Quate, Ch. Gerber, Phys. Rev. Lett. 56 (1986) 930.

241. T. Junno, S. B. Carlsson, H. Xu, L. Montelius, L. Samuelson, Appl. Phys. Lett. 72 (1998) 548.

242. Y. Okada, S. Amano, Y. Iuchi, M. Kawabe, J. S. Harris, Electron. Lett. 34 (1998) 1262.

243. S. Sasa, T. Ikeda, M. Akahori, A. Kajiuchi, M. Inoue, Japanese J. Appl. Phys., Part 1: Regular Papers and Short Notes and Review Papers 38(2B) (1999) 1064.

244. P. S. Dobson, J. M. R. Weaver, M. N. Holder, P. R. Unwin, J. V. Macpherson, Anal. Chem. 77 (2005) 424.

245. R. E. Gyurcsanyi, G. Jagerszki, G. Kiss, K. Toth, Bioelectrochemistry 63 (2004) 207.

246. Z. F. Ding, B. M. Quinn, A. J. Bard, J. Phys. Chem. B 105 (2001) 6367.

247. M. V. Mirkin, M. Arca, J. Bard, J. Phys. Chem. 97 (1993) 10790.

248. M. Arca, M. V. Mirkin, A. J. Bard, J. Phy. Chem. 98 (1994) 9106.

249. R. W. Murray, Electroanalytical Chemistry, Vol. 13, A. J. Bard (ed.). Marcel Dekker: New York, 1984.

250. G. Inzelt, in: A. J. Bard (Ed.), Electroanalytical Chemistry, Vol. 18. Marcel Dekker: New York, 1994.

251. J. J. Jortner, M. A. Ratner, Molecular Electronics. Blackwell: Oxford, 1997.

252. B. Liu, A. J. Bard, M. V. Mirkin, S. E. Creager, J. Am. Chem. Soc. 126 (2004) 1485.

253. H. Xiong, J. D. Guo, S. Amemiya, Anal. Chem. 79 (2007) 2735.

254. W. Zhan, A. J. Bard, Anal. Chem. 78 (2006) 5046.

255. O. D. Uitto, H. S. White, K. Aoki, Anal. Chem. 74 (2002) 4577.

256. Y. F. Yang, G. J. Denuault, Electroanal. Chem. 418 (1996) 99.

References

257. C. A. Nijhuis, J. K. Sinha, G. Wittstock, J. Huskens, B. J. Ravoo, D. N. Reinhoudt, Langmuir 22 (2006) 9770.

258. E. Volker, C. G. Inchausspe, E. Calvo, J. Electrochem. Commun. 8 (2006) 179.

259. A. C. Bastos, A. M. Simoes, S. Gonzalez, Y. Gonzalez-Garcia, R. M. Souto, Prog. Org. Coat. 53 (2005) 177.

260. P. Sun, F. Li, Y. Chen, M. Q. Zhang, Z. Q. Zhang, Z. Gao, Y. H. Shao, J. Am. Chem. Soc. 125 (2003) 9600.

261. Y. H. Shao, M. V. Mirkin, J. Phys. Chem. B 102 (1998) 9915.

262. M. Komatsu, K. Yamashita, K. Uchida, H. Kondo, S. Takaenaka, Electrochim. Acta 51 (2006) 2023.

263. J. Wang, F. Song, F. Zhou, Langmuir 18 (2002) 6653.

264. C. G. Zoski, N. Simjee, O. Guenat, M. Koudelka-Hep, Anal. Chem. 76 (2004) 62.

265. X. Q. Lu, L. M. Zhang, M. R. Li, X. Q. Wang, Y. Zhang, X. H. Liu, G. F. Zuo, Chem. Phys. Chem. 7 (2006) 854.

266. C. Lee, J. Kwak, A. J. Bard, Proc. Natl. Acad. Sci. U. S. A. 87 (1990) 1740.

267. A. J. Bard, F.-R. F. Fran, J. Korean Son. Anal. Sci. 8 (1995) 69.

268. F. Forouzan, A. J. Bard, M. V. Mirkin, Isr. J. Chem. 37 (1997) 155.

269. G. Wittstock, R. Heese, W. Schuhmann, Electroanalysis 9 (1997) 746.

270. T. Wilhelm, G. Wittstock, Microchim. Acta 133 (2000) 1.

271. L. Svobodova, M. Snejdarkova, K. Toth, R. E. Gyurcsanyi, T. Hianik, Bioelectrochemistry 63 (2004) 285.

272. F.-M. Boldt, N. Baltes, K. Bogwarth, J. Heinze, Surf. Sci. 597 (2005) 51.

273. D. Burshtain, D. Mandler, J. Electroanal. Chem. 581 (2005) 310.

274. B. Liu, A. J. Bard, C.-Z. Li, H.- B. Kraatz, J . Phys. Chem. B 109 (2005) 5193.

275. J. F. Silva, S. Griveau, C. Richard, J. H. Zagal, F. Bedioui, Electrochem. Commun. 9 (2007) 1629.

276. M. Kropf, F. Steinbach (eds.), Katalyse und Phthalocyaninen. Thieme: Stuttgart, 1973.

277. J. Manassen, Catal. Rev. Sci. Eng. 9 (1974) 223.

278. L. J. Boucher, Coordination Chemistry of Macrocyclic Compounds, G. A. Melson (ed.). Plenum Press: New York, 1979.

References

279. J. H. Zagal, C. Fierro, E. Muñoz, R. Rozas, S. Ureta, Electrocatalysis, The Electrochemical society symposium series, W. E. O'grady, P. N. Ross, F. G. Will (eds.), 1982, p. 389.

280. M. J. Chen, J. W. Rathke, Phthalocyanines: Properties and Applications, Vol. 4, C. C. Leznoff, A. B. P. Lever, (eds.). VCH Publishers, Inc., Weinheim: New York, 1996.

281. R. de Saja, J. Souto, M. L. Rodriguez-Mendez, J. A. de Saja, Mater. Sci. Eng. C 8-9 (1999) 565.

282. S. Komorsky-Lovrić, M. Lovrić, F. Scholz, Michrochim. Acta 127 (1997) 95.

283. S. Maree, T. Nyokong, J. Electroanal. Chem. 492 (2000) 120.

284. S. Griveau, F. Bedioui, Electroanalysis 13 (2001) 253.

285. J. H. Zagal, C. Paez, Electrochim. Acta 34 (1989) 243.

286. J. H. Zagal, M. Gulppi, M. Isaacs, G. Cardenas-Jiron, M. J. Aguirre, Electrochim. Acta 44 (1998) 1349.

287. G. I. Cardenas-Jiron, M. A. Gulppi, C. A. Caro, R. del Rio, M. Paez, J. H. Zagal, Electrochim. Acta 46 (2001) 3227.

288. C. Shi, F. C. Anson, Inorg. Chem. 37 (1998) 1037.

289. A. B. P. Lever, J. Porphyrins Phthalocyanines 3 (1999) 488.

290. F. Beck, J. Appl. Electrochem. 7 (1977) 191.

291. N. Grootboom, T. Nyokong, Anal. Chim. Acta 432 (2002) 49.

292. J. H. Zagal, M. A. Gulppi, G. Cáedenas-Jirón, Polyhedron 19 (2000) 2255.

293. C. A. Caro, F. Bedioui, M. A. Páez, G. Cáedenas-Jirón, J. H. Zagal, J. Electrochem. Soc. 151 (2004) E32.

294. A. Ciszewski, E. Kubaszewski, M. Łożyński, Electroanalysis 8 (1996) 293.

295. S. Trevin, F. Bedioui, J. Devynck, Talanta 43 (1996) 303.

296. M. Sekota, T. Nyokong, Electroanalysis 9 (1999) 1257.

297. N. Sonoyama, M. Kirii, T. Sakata, Electrochem. Commun. 1 (1999) 213.

298. N. Nombona, D. A. Geraldo, J. Hakuzimana, A. Schwarz, P. Westbroek, T. Nyokong, J. Appl. Electrochem. 39 (2009) 727.

299. T. Nyokong, N_4-Macrocyclic Metal Complexes, J. H. Zagal, F. Bedioui, J.-P. Dodelet (eds.). Springer: United States of America, 2006.

References

300. I. V. Zhdanova, Clin. Pharmacol. Ther. 57 (1995) 552.

301. R. Hardeland, Endocrine 27 (2005) 119.

302. R. J. Reiter, Exp. Biol. Med. 230 (2005) 104.

303. A. Carrillo-Vico, J. Guerrero, P. Lardone, R. Reiter, Endocrine 27 (2005) 189.

304. R. J. Reiter, D. Acuña-Castroviejo, D. Tan, S. Burkhardt, Ann. N. Y. Acad. Sci. 939 (2001) 200.

305. W. Qi, Environ. Health Perspect. 108 (2000) 399.

306. E. Arushanian, E. Beier, Eksp. Klin. Farmakol. 65 (2002) 73.

307. G. Maestroni, Adv. Exp. Med. Biol. 467 (1999) 217.

308. D. E. Blask, J. Neural. Transm. 21 (1986) 433.

309. X. Wang, J. Zhang, X. Yu, L. Han, Z. Zhou, Y. Zhang, J. Wang, Shengli Xuebao 57 (2005) 7.

310. R. J. Reiter, J. Robinson, Melatonin. Bantam Books: USA and Canada, 1995.

311. W. Qu, F. Wang, S. Hu, D. Cui, Microchim. Acta 150 (2005) 109.

312. A. Radi, G. E. Bekhiet, Bioelectrochem. Bioenerg. 45 (1998) 275.

313. A. K. Sinhababu, A. K. Ghosh, R. T. Borchardt, J. Med. Chem. 28 (1985) 1273.

314. A. Alonso, B. Etxaniz, M. D. Martinez, Food Addit. Contam. 9 (1992) 111.

315. S. S. Mirvish, Cancer Lett. 93 (1995) 17.

316. C. I. Walters, Oncology 37 (1980) 289.

317. K. K. Choi, K.W. Fung, Analyst 105 (1980) 241.

318. S. Arias-Negrete, L. A. Jimenez-Romero, M. O. Soliis-Martinez, J. Ramiirez-Emiliano, E. E. Avila, P. Cuella-Mata, Anal. Biochem. 328 (2004) 14.

319. C. A. Caro, F. Bedioui, J. H. Zagal, Electrochim. Acta 47 (2002) 1489.

320. B. O. Agboola, K. I. Ozoemena, T. Nyokong, Electrochim. Acta 51 (2006) 6470.

321. M. K. Amini, S. Shahrokhian, S. Tangestaninejad, Anal. Lett. 32 (1999) 2737.

322. J. A. Cox, T. Gray, Anal. Chem. 60 (1988) 1710.

323. D. Gao, J.-Z. Li, R.-Q. Yu, Anal. Chem. 66 (1994) 2245.

324. A. Abbaspour, M. A. Kamyabi, A. R. Esmaeilbeig, R. Kia, Talanta 57 (2002) 859.

325. J. H. Zagal, F. Bedioui, J.-P. Dodelet (eds.), N_4-Macrocyclic Metal Complexes. Springer: United States of America, 2006.

References

326. D. Nkosi, K. I. Ozoemena, J. Electroanal. Chem. 621 (2008) 304.

327. L. S. Stryer, Biochemistry (3rd edition). W. H. Freeman and Co.: New York, 1988.

328. http://www.lef.org/protocols/prtcl-004.shtml

329. J. Zagal, C. Fierro, R. Rozas, J. Electroanal. Chem. 119 (1981) 403.

330. F. J. Cookson, T. D. Smith, J. F. Boas, P. R. Hicks, J. R. Pilbrow, J. Chem. Soc. Dalton Trans. (1977) 109.

331. D. M. Wagnerova, E. Schertnerova, J. Veprek-Šiska, Collect. Czech. Chem. Commun. 38 (1973) 756.

332. N. N. Kundo, N. P. Keir, G. V. Glazneva, E. K. Mamaeva, Kinet. Katal. 8 (1966) 1119.

333. R. O. Lezna, S. Juanto, J. H. Zagal, J. Electroanal. Chem. 452 (1998) 221.

334. H. Alt, H. Binder, G. Sandstede, J. Electroanal. Chem. 31 (1971) 19.

335. M. Savy, P. Andro, C. Bernard, G. Magner, Electrochim. Acta 18 (1973) 191.

336. A. Kozawa, V. E. Zillinois, R. J. Brodd, J. Electrochem. Soc. 11 (1970) 1470.

337. R. K. Sen, J. Zagal, E. Yeager, Inorg. Chem. 16 (1977) 3379.

338. H. Behret, M. Binder, G. Sanstede, G. G. Scherer, J. Electroanal. Chem. 117 (1981) 29.

339. F. van den Brink, W. Visscher, E. Barendrecht, J. Electroanal. Chem. 172 (1984) 301.

340. J. A. R. van Veen, Electrochim. Acta 27 (1982) 1403.

341. A. Kozawa, V. E. Zillinois, R. J. Brodd, J. Electrochem. Soc. 11 (1970) 1474.

342. J. Zagal, P. Bindra, E. Yeager, J. Electrochem. Soc. 127 (1980) 1506.

343. F. van den Brink, W. Visscher, E. Barendrecht, J. Electroanal. Chem. 175 (1984) 279.

344. J. A. R. van Veen, J. F. van Baar, C. J. Kroese, J. G. F. Coolegem, N. de Wit, H. A. Colljn, Ber. Bunsenges, Phys. Chem. 85 (1981) 693.

345. M. R. Tarasevich, K. A. Radyushkina, S. I. Andruseva, Bioelectrochem. Bioenerg. 4 (1977) 18.

346. J. A. R. van Veen, C. Visser, Electrochim. Acta 24 (1979) 921.

347. L. Hua, H. Han, X. Zhang, Talanta 77 (2009) 1654.

348. X. Yao, Y. Wang, G. Chen, Biomed. Chrom. 21 (2007) 520.

References

349. M. M. Ardakani, P. Rahimi, P. Karami, P. E. Ebrahimi, H. R. Zare, H. Naeimi, Sens. Actuators, B: Chemical B123 (2007) 763.

350. P. N. Mashazi, P. Westbroek, K. I. Ozoemena, T. Nyokong, Electrochim. Acta 53 (2007) 1858.

351. A. Favier, Ann. Biol. Clin. 55 (1997) 9.

352. K. I. Ozoemena, T. Nyokong, Electrochim. Acta 51 (2006) 2669.

353. I. Fridovich, Ann. Rev. Biochem. 64 (1995) 97.

354. J. A. Imlay, S. Linn, Science 240 (1988) 1302.

355. J. C. Fantone, S. H. Phan, Free Radic. Biol. Med. 4 (1988) 399.

356. B. Halliwell, J. M. C. Gutteridge, Arch. Biochem. Biophys. 246 (1986) 501.

357. J. M. McCord, N. Engl. J. Med. 312 (1985) 159.

358. R. J. Reiter, FASEB J. 9 (1995) 526.

359. A. C. Maritim, R. A. Sanders, J. B. Watkins III, J. Biochem. Mol. Toxicol. 17 (2003) 24.

360. S. L. Church, J. W. Grant, L. A. Ridnour, L. W. Oberley, P. E. Swanson, P. S. Meltzer, J. M. Trent, Proc. Natl. Acad. Sci. USA 90 (1993) 3113.

361. I. Batinic-Haberle, I. Spasojevic, R. P. Hambright, L. Benov, A. L. Crumbliss, I. Fridovich, Inorg. Chem. 38 (1999) 4011.

362. B. Chance, H. Sies, A. Boveris, Physiol. Rev. 59 (1979) 527.

363. R. Sifert, G. Schultz, Rev. Physiol. Biochem. Pharmacol. 117 (1991) 1.

364. K. A. Prictchard Jr., L. Groszek, D. M. Smalley, W. C. Sessa, M. Wu, P. Villalon, M. S. Wolin, M. B. Stemmerman, Cir. Res. 77 (1995) 710.

365. G. Rotilio, R. C. Bray, E. M. Fielden, Biochim. Biophys. Acta 268 (1972) 605.

366. D. Klug, J. Rabani, I. Fridovich, J. Biol. Chem. 247 (1972) 4839.

367. F. Lavelle, M. E. McAdam, E. M. Fielden, E. M. Roberts, P. B. Roberts, K. Puget, A. M. Michelson, Biochem. J. 161 (1977) 3.

368. J.-L. Hsu, Y. Hsieh, C. Tu, D. O'Connor, H. S. Nick, D. N. Silverman, J. Biol. Chem. 271 (1996) 17687.

369. D. C. Richardson, Superoxide and superoxide dismutase. Academic Press: London, 1977.

References

370. J. M. McCord, I. Fridovich, J. Biol. Chem. 243 (1968) 5753.

371. J. M. McCord, I. Fridovich, J. Biol. Chem. 244 (1969) 6049.

372. T. Mann, D. Keilin, Proc. R. Soc. Ser. B126 (1938) 303.

373. L. Pauling, Trend Biochem. Sci. 4 (1979) N270.

374. P. F. Knowles, J. F. Gibson, F. M. Pick, R. C. Bray, Biochem. J. 111 (1969) 53.

375. W. Huber, T. L. Schulte, S. Carson, R. E. Goldhammer, E. E. Vogin, Toxicol. Appl. Pharmacol. 12 (1968) 308.

376. B. M. Babior, R. S. Kipnes, J. T. Curnutte, J. Clin. Invest. 52 (1973) 741.

377. M. L. Salin, J. M. McCord, J. Clin. Invest. 56 (1975) 1319.

378. J. M. McCord, Science 185 (1974) 529.

379. G. E. O. Borgstahl, H. E. Parge, M. J. Hickey, W. F. Beyer Jr., R. A. Hallewell, J. A. Tainer, Cell 71 (1992) 107.

380. P. J. Hart, M. M. Balbirnie, N. L. Ogihara, A. M. Nerissian, M. S. Weiss, J. S. Valentine, D. Eisenberg, Biochemistry 38 (1999) 2167.

381. M. S. Lah, M. M. Dixon, K. A. Pattridge, W. C. Stallings, J. A. Fee, M. L. Ludwig, Biochemistry 34 (1995) 1646.

382. M. Leone, A. Cupane, V. Militello, M. E. Stroppolo, A. Desideri, Biochemistry 37 (1998) 4459.

383. D. L. Sorkin, D. K. Duong, A.-F. Miller, Biochemistry 36 (1997) 8202.

384. J. A. Trainer, E. D. Getzoff, J. S. Richardson, D. C. Richardson, Nature 306 (1983) 284.

385. E. D. Getzoff, J. A. Trainer, P. K. Weiner, P. A. Kollman, J. S. Richardson, D. C. Richardson, Nature 306 (1983) 287.

386. C. X. Zhang, S. J. Lippard, Curr. Opin. Chem. Biol. 7 (2003) 481.

387. D. Salvemini, C. Muscoli, D. P. Riley, S. Cuzzocrea, Pulm. Pharmacol. Ther. 15 (2002) 439.

388. C. Policar, S. Durot, F. Lambert, M. Cesario, F. Ramiandrasoa, I. Morgenstern-Badarau, Eur. J. Inorg. Chem. (2001) 1807.

389. S. Durot, C. Policar, F. Cisnetti, F. Lambert, J.-P. Renault, G. Pelosi, G. Blain, H. Korri-Youssoufi, J.-P. Mahy, Eur. J. Inorg. Chem. 17 (2005) 3513.

References

390. S. Cuzzocrea, E. Mazzon, R. D. Paola, T. Genovese, C. Muia, A. P. Caputi, D. Salvemini, Arthritis Rheum. 52 (2005) 1929.

391. R. D'agata, G. Grasso, G. Iacono, G. Spoto, G. Vecchio, Org. Biomol. Chem. 4 (2006) 610.

392. C. W. Munroe, C. Kingsley, A. Durazo, E. B. Gralla, J. A. Imlay, C. Srinivasan, J. S. Valentine, J. Inorg. Biochem. 101 (2007) 1875.

393. F. Cisnetti, A. S. Lefèvre, R. Guillot, F. Lambert, G. Blain, E. Anxolabéhère-Mallart, C. Policar, Eur. J. Inorg. Chem. 28 (2007) 4472.

394. E. A. Lewis, H. H. Khodr, R. C. Hider, J. R. Lindsay-Smith, P. H. Walton, J. Chem. Soc. Dalton Trans. 2 (2004) 187.

395. E. A. Lewis, J. R. Lindsay-Smith, P. H. Walton, S. J. Archibald, S. P. Foxo, G. M. P. Giblin, J. Chem. Soc. Dalton Trans. 8 (2001) 1159.

396. D. P. Riley, Chem. Rev. 99 (1999) 2573.

397. W. H. Koppenol, F. Levine, T. L. Hatmaker, J. Epp, J. D. Rush, Arch. Biochem. Biophys. 251 (1986) 594.

398. S. Delagrange, R. Delgado, F. Nepveu, J. Inorg. Biochem. 81 (2000) 65.

399. W. C. J. Barrette, D. T. Sawyer, J. A. Fee, K. Asada, Biochemistry 22 (1983) 624.

400. J. Stein, J. P. Fackler, G. J. McClune, J. A. Fee, L. T. Chan, Inorg. Chem. 18 (1979) 3511.

401. J.-L. Pierre, Regard sur la Biochimie (2000) 17.

402. S. Imaizumi, V. Woolworth, R. A. Fishman, P. H. Chan, Stroke 21 (1990) 1312.

403. M. Wiedau-Pazos, J. J. Goto, S. Rabizadeh, E. B. Gralla, J. A. Roe, M. K. Lee, J. S. Valentine, D. E. Bredsen, Science 271 (1996) 515.

404. P. A. Egner, T. W. Kensler, Carcinogenesis 6 (1985) 1167.

405. J. P. Collman, X. Zhang, J. V. Lee, E. S. Uffelman, J. I. Brauman, Science 261 (1993) 1404.

406. P. K. S. Tsang, D. T. Sawyer, Inorg. Chem. 29 (1990) 2848.

407. A. Harriman, G. Porter, J. Chem. Soc. Faraday Trans. 275 (1979) 1532.

408. K. M. Faulkner, S. I. Liochev, I. Fridovich, J. Biol. Chem. 269 (1994) 23471.

409. R. Kachadourian, I. Batinić-Haberle, I. Fridovich, Inorg. Chem. 38 (1999) 391.

References

410. I. Batinić-Haberle, I. Spasojević, R. D. Stevens, P. Hambright, P. Neta, A. Okado-Matsumoto, I. Fridovich, Dalton Trans. (2004) 1696.

411. H. Sheng, J. Enghild, R. Bowler, M. Patel, C. L. Calvi, I. Batinić-Haberle, B. J. Day, R. D. Pearlstein, J. D. Capro, D. S. Warner, Free Radical Biol. Med. 33 (2002) 947.

412. G. B. Mackensen, M. Patel, H. Sheng, C. L. Calvi, I. Batinić-Haberle, B. J. Day, L. P. Liang, I. Fridovich, J. D. Capro, R. D. Pearlstein, D. S. Warner, J. Neurosci. 21 (2001) 4582.

413. I. Batinić-Haberle, I. Spasojević, R. D. Stevens, P. Hambright, I. Fridovich, J. Chem. Soc., Dalton Trans. (2002) 2689.

414. A. Okado-Matsumoto, I. Batinić-Haberle, I. Fridovich, Free Radical Biol. Med. 37 (2004) 401.

415. O. C. Farokhzad, S. Jon, A. Khademhosseini, T. N. Tran, D. A. Lavan, R. Langer, Cancer Res. 64 (2004) 7668.

416. G. Kaul, M. J. Amiji, Drug Target. 12 (2004) 585.

417. K. Hyoudouy, M. Nishikawa, Y. Umeyama, Y. Kobayashi, F. Yamashita, M. Hashida, Clin. Cancer Res. 10 (2004) 7685.

418. B. J. Day, I. Batinić-Haberle, J. D. Crapo, Free Radic. Biol. Med. 26 (1999) 730.

419. I. Spasojević, I. Batinić-Haberle, Inorg. Chim. Acta 317 (2001) 230.

420. A. S. Fernandes, J. Gaspar, M. F. Cabral, C. Caneiras, R. Guedes, J. Rueff, M. Castro, J. Costa, N. G. Oliveira, J. Inorg. Biochem. 101 (2007) 849.

421. J. S. Reboucas, G. DeFreitas-Silva, I. Spasojevic, Y. M. Idemori, L. Benov, I. Batinić-Haberle, Free Rad. Bio. Med. 45 (2008) 201.

422. F. Bellot, R. Hardré, G. Pelosi, M. Thérisod, C. Policar, Chem. Commun. (2005) 5414.

423. J. R. J. Sorenson, V. Kishore, A. Pezeshk, L. W. Oberley, S. W. C. Leuthauser, T. D. Oberley, Inorg. Chim. Acta 91 (1984) 285.

424. L.-P. Liang, J. Huang, R. Fulton, B. J. Day, M. Patel, J. Neurosci. 27 (2007) 4326.

425. A. D. Ross, H. Sheng, D. S. Warner, C. A. Piantadosi, I. Batinic-Haberle, B. J. Day, J. D. Crapo, Free Radic. Biol. Med. 33 (2002) 1657.

426. M. Faraggi, Oxygen Radicals in Chemistry and Biology, W. Bors, M. Saran, D. Tait (eds.). Walter de Gruyter, Publishers: Berlin, Germany, 1984.

References

427. R. F. Pasternack, A. Barth, J. M. Pasternack, C. S. Johnson, J. Inorg. Biochem. 15 (1981) 261.

428. T. Matsubara, M. Ziff, M. Ziff, J. Cell. Physiol. 127 (1986) 207.

429. U. P. Steinbrecher, Biochim. Biophys. Acta 959 (1988) 20.

430. R. H. Weiss, A. G. Flickinger, W. J. Rivers, M. M. Hardy, K. W. Aston, U. S. Ryan, D. P. Riley, J. Biol. Chem. 268 (1993) 23049.

431. J. Butler, W. H. Koppenol, E. Margoliash, J. Biol. Chem. 257 (1982) 10747.

432. C. Privat, S. Trevin, F. Bedioui, J. Devynck, J. Electroanal. Chem. 436 (1997) 261.

433. B. H. J. Bielski, D. E. Campbell, R. L. Arudi, A. B. Ross, J. Phys. Chem. Ref. Data 14 (1985) 1041.

434. T. Finkel, N. J. Holbrook, Nature 408 (2000) 239.

435. F. Lisdat, B. Ge, E. Ehrentreich-Förster, R. Reszka, F. W. Scheller, Anal. Chem. 71 (1999) 1359.

436. P. Manning, C. J. McNeil, J. M. Cooper, E. W. Hillhouse, Free Radical Biol. Med. 24 (1998) 1304.

437. C. J. McNeil, D. Athey, W. O. Ho, Biosens. Bioelectron. 10 (1995) 75.

438. C. J. McNeil, K. R. Greenough, P. A. Weeks, C. H. Self, J. M. Cooper, Free Radic. Res. Commun. 17 (1992) 399.

439. J. M. Cooper, K. R. Greenough, C. J. McNeil, J. Electroanal. Chem. 347 (1993) 267.

440. M. K. Beissenhirtz, F. W. Scheller, F. Lisdat, Anal. Chem. 76 (2004) 4665.

441. S. Shleev, J. Wetterö, K.-E. Magnusson, T. Ruzgas, Biosens. Bioelectron. 22 (2006) 213.

442. B. Ge, F. W. Scheller, F. Lisdat, Biosens. Bioelectron. 18 (2003) 295.

443. S. Mesaros, Z. Vankova, A. Mesarosova, P. Tomcik, S. Grunfeld, Bioelectrochem. Bioenerg. 46 (1998) 33.

444. S. Mesaros, Z. Vankova, S. Grunfeld, A. Mesarosova, T. Malinski, Anal. Chim. Acta 358 (1998) 27.

445. K. Tanaka, F. Kobayashi, Y. Isogai, T. Iizuka, Bioelectrochem. Bioener. 26 (1991) 413.

References

446. C. Privat, O. Stepien, M. David-Dufilho, A. Brunet, F. Bedioui, P. Marche, J. Devynck, M.-A. Devynck, Free Radic. Biol. Med. 27 (1999) 554.

447. L. M. Ellerby, D. E. Cabelli, J. A. Garden, J. S. Valentine, J. Am. Chem. Soc. 118 (1996) 6556.

448. J. S. Beckman, J. P. Crow, Biochem. Soc. Trans. 21 (1993) 330.

449. H. Ischiropoulos, L. Zhu, J. S. Beckman, Arch. Biochem. Biophys. 298 (1992) 446.

450. P. J. Pagano, K. Tornheim, R. A. Cohen, Am. J. Physiol. 265 (1993) H707.

451. N. W. Kooy, J. A. Royall, Arch. Biochem. Biochem. Biophys. 310 (1994) 352.

452. J. Vásquez-Vivar, J. Joseph, H. Karoui, H. Zhang, J. Miller, P. Martásek, Analusis 28 (2000) 487.

453. D. Simão, H. Alves, D. Belo, S. Rabaça, E. B. Lopes, I. C. Santos, V. Gama, T. Duarte, R. T. Henriques, H. Novais, M. Almeida, Eur. J. Inorg. Chem. (2001) 3119.

454. N. P. Farrell, A. J. Murray, J. R. Thornback, D. H. Dolphin, B. R. James, Inorg. Chim. Acta 28 (1978) L144.

455. A. J. Bard, L. R. Faulkner, Electrochemical Methods: fundamentals and applications. John Wiley & Sons Inc.: USA, 2001.

456. J. Hua, T. Hasebe, A. Someya, S. Nakamura, K. Sugimoto, I. Nagaoka, J. Leukocyte Biol. 68 (2000) 216.

457. K. Ozoemena, P. Westbroek, T. Nyokong, J. Porphyrins Phthalocyanines 3 (2002) 529.

458. M. Kandaz, M. N. U. Yaraşir, A. Koca, Ő. Bekaroğlu, Polyhedron 21 (2002) 255.

459. M. J. Stillman, T. Nyokong, Phthalocyanines. Properties and Applications, C. C. Leznoff, A. B. P. Lever (eds.), Vol. 1. VCH Publishers: New York, 1989.

460. M. N. Golovin, P. Seymour, K. Jayaraj, Y. S. Fu, A. B. P. Lever, Inorg. Chem. 29 (1990) 1719.

461. R. Baker, D. P. Wilkinson, J. Zhang, Electrochim. Acta 54 (2009) 3098.

462. K. Ban, K. Nishizawa, K. Ohta, H. Shirai, J. Mater. Chem. 10 (2000) 1083.

463. M. J. Stillman, Phthalocyanines. Properties and Applications, C. C. Leznoff, A. B. P. Lever (eds.), Vol. 3. VCH Publishers: New York, 1993.

References

464. C. C. Leznoff, L. S. Black, A. Heibert, P. W. Causey, D. Christendat, A. B. P. Lever, Inorg. Chim. Acta 359 (2006) 2690.

465. C. -L. Lin, C. -C. Lee, K. -C. Ho, J. Electroanal.Chem. 524 - 525 (2002) 81.

466. M. O. Liu, C.-H. Tai, M.-Z. Sain, A. T. Hu, F. Chou, J. Photochem. Photobiol. A: Chem. 164 (2004) 131.

467. Z. Grabarek, J. Gergely, Anal. Biochem. 185 (1990) 131.

468. N. S. DeSilva, Am. J. Respir. Cell. Mol. Biol. 29 (2003) 757.

469. J. V. Staros, R. W. Wright, D. M. Swingle, Anal. Biochem. 156 (1986) 220.

470. D. Sehgal, I. K. Vijay, Anal. Biochem. 218 (1994) 87.

471. L. Jiang, A. Glidle, A. Griffith, C. J. McNeil, J. M. Cooper, Bioelectrochem. Bioenerg. 42 (1997) 15.

472. J. M. Tedder, A. Nechvatal, A. W. Murray, J. Carnduff, Basic Organic Chemistry. Wiley-Interscience: New York, 1972.

473. H. Lund, M. M. Baizer (eds.), Organic Electrochemistry. Marcel Dekker: New York, 1991.

474. M. Delamar, G. D´esarmot, O. Fagebaume, R. Hitmi, J. Pinson, J.-M. Sav´eant, Carbon 35 (1997) 801.

475. B. Ortiz, C. Saby, G. Y. Champagne, D. Belanger, J. Electroanal. Chem. 455 (1998) 75.

476. J. E. Hutchison, T. A. Postlethwaite, R. W. Murray, Langmuir 9 (1993) 3277.

477. N. Kobayashi, P. Janda, A. B. P. Lever, Inorg. Chem. 31 (1992) 5172.

478. J. H. Zagal, M. A. Guilppi, C. Depretz, D. Lelievre, J. Porphyrins Phthalocyanines 3 (1999) 355.

479. K. Shimizu, R. A. Osteryoung, Anal. Chem. 53 (1981) 2350.

480. M. E. G. Lyons, C. A. Fitzgerald, M. R. Smyth, Analyst 119 (1994) 855.

481. M. H. Pournaghi-Azar, H. Dastangoo, J. Electroanal. Chem. 567 (2004) 211.

482. V. Lakshminarayanan, U. K. Sur, Pramana 61 (2003) 361.

483. N. Nombona, P. Tau, N. Sehlotho, T. Nyokong, Electrochim. Acta 53 (2008) 3139.

484. P. Tau, T. Nyokong, J. Electroanal. Chem. 611 (2007) 10.

485. B. Wermeckes, F. Beck, Electrochim. Acta 30 (1985) 1491.

References

486. K. Ozoemena, N. Kuznetsova, T. Nyokong, J. Photochem. Photobiol. A: Chem. 139 (2001) 217.

487. Z.-H. Wen, T.-F. Kang, Talanta, 62 (2004) 351.

488. T. J. O'Shea, S. M. Lunte, Anal. Chem. 66 (1994) 307.

489. D. Robinson, J. E. Anderson, J. L. Lin, J. Phys. Chem. 94 (1990) 1003.

490. F. J. Farrell, T. G. Spiro, Inorg. Chem. 10 (1971) 1606.

491. C.-Z. Li, J. H. T. Luong, Anal. Chem. 77 (2005) 478.

492. S. G. Hickey, D. J. Riley, Electrochem. Commun. 1 (1999) 116.

493. M. D. Porter, T. B. Bright, D. Allara, C. E. D. Chidsey, J. Am. Chem. Soc. 109 (1987) 3559.

494. B. Agboola, P. Westbroek, K. Ozoemena, T. Nyokong, Electrochem. Commun. 9 (2007) 310.

495. P. Tau, T. Nyokong, Electrochim. Acta 52 (2007) 4547.

496. W. J. R. Santos, A. L. Sousa, R. C. S. Luz, F. S. Damos, L. T. Kubota, A. A. Tanaka, S. M. C. N. Tanaka, Talanta 70 (2006) 588.

497. J.-M. Zen, A. Senthil Kumar, M.-R. Chang, Electrochim. Acta 45 (2000) 1691.

498. F. Bedioui, S. Griveau, T. Nyokong, A. J. Appleby, C. A. Caro, M. l. Gulppi, G. Ochoa, J. H. Zagal, Phys. Chem. Chem. Phys. 9 (2007) 3396.

499. L. Qingwen, G. Hong, W. Yiming, L. Guoan, M. Jie, Electroanalysis, 13 (2001), 1342.

500. Z. Chen, H. Zheng, C. Lu, Y. Zu, Langmuir 23 (2007) 10816.

501. R. Kachadourian, M. M. Flaherty, A. L. Crumbliss, M. Patel, B. J. Day, J. Inorg. Biochem. 95 (2003) 240.

502. A. M. C. Herath, R. M. G. Rajapakse, V. Karunarathne, A. Wicramasinghe, Electrochim. Acta. 51 (2005) 2890.

503. K. Yamato, I. Miyahara, A. Ichimura, K. Hirotsu, Y. Kojima, H. Sakurai, D. Shiomi, K. Sato, T. Takui, Chem. Lett. 4 (1999) 295.

504. P. J. F. Gauuan, M. P. Trova, L. Gregor-Boros, S. B. Bocckino, J. D. Crapo, B. J. Day, Bioorg. Med. Chem. 10 (2002) 3013.

505. J. S. Reboucas, I. Spasojevic, Y. M. Idemori, L. Benov, I. Batinić-Haberle, J. Biol. Inorg. Chem. 13 (2008) 289.

References

506. H. Zhao, S. Kalivendi, H. Zhang, J. Joseph, K. Nithipatikom, J. Vasquez-Vivar, B. Kalyanaraman, Free Radic. Biol. Med. 34 (2003) 1359.

507. L. Benov, L. Sztejnberg, I. Fridovich, Free Radic. Biol. Med. 25 (1998) 826.

508. H. M. Peshavariya, G. J. Dusting, S. Selemidis, Free Radic. Res. 41 (2007) 699.